Low temperature kinetics measurements for reactions of astrochemical relevance

Myriam Drissi

▶ **To cite this version:**

Myriam Drissi. Low temperature kinetics measurements for reactions of astrochemical relevance. Physics [physics]. Université de Rennes, 2023. English. ⟨NNT : 2023URENS109⟩. ⟨tel-05583750⟩

HAL Id: tel-05583750

https://theses.hal.science/tel-05583750v1

Submitted on 8 Apr 2026

HAL is a multi-disciplinary open access archive for the deposit and dissemination of scientific research documents, whether they are published or not. The documents may come from teaching and research institutions in France or abroad, or from public or private research centers.

L'archive ouverte pluridisciplinaire **HAL**, est destinée au dépôt et à la diffusion de documents scientifiques de niveau recherche, publiés ou non, émanant des établissements d'enseignement et de recherche français ou étrangers, des laboratoires publics ou privés.

HAL Authorization

COLLEGE SCIENCES DE LA MATIERE
DOCTORAL DES MOLECULES
BRETAGNE ET MATERIAUX

Université de Rennes

THÈSE DE DOCTORAT DE

L'UNIVERSITÉ DE RENNES

ÉCOLE DOCTORALE 638
Sciences de la Matière, des Molécules et Matériaux
Spécialité : *Physique : atomes, molécules et surfaces*
Spécialité secondaire : Chimie Physique, Chimie Théorique

Par
Myriam DRISSI

Low Temperature Kinetics Measurements for Reactions of Astrochemical Relevance

Thèse présentée et soutenue à Rennes, le 09-11-2023
Unité de recherche : Institut de Physique de Rennes UMR 6251

Rapporteurs avant soutenance :

Mitchio OKUMURA Professeur, Caltech, Pasadena, California, État-Unis
Lam NGUYEN Maîtresse de Conférences (HDR), Université Paris-Est Créteil

Composition du Jury :

Président :	François LIQUE	Professeur, Université de Rennes
Examinateurs :	Jean-Christophe LOISON	Directeur de recherche, Université de Bordeaux
	Lam NGUYEN	Maîtresse de Conférences (HDR), Université Paris-Est Créteil
	Mitchio OKUMURA	Professeur, Caltech, Pasadena, California, État-Unis
Dir. de thèse :	Ian SIMS	Professeur, Université de Rennes

À mon Père, pour m'avoir inspiré et guidé jusqu'ici

Acknowledgements

And here it goes, the end of a three-year journey towards reaching my goal of becoming a researcher. The path was long and not as expected, but I must say, I don't regret any of the choices I made that led me here today. Doing this PhD has been not only a professional challenge but also a personal one. I guess that's why I chose to pursue this path, it was a fantastic opportunity for growth. Of course, this thesis would have never been the same without all the wonderful people I had the chance to meet along the way. You've all inspired me in a different way and I must say that I was lucky to work every day in such a pleasant environment. I would like to thank all the people who have contributed to this work both directly and indirectly.

First and foremost, I would like to express my gratitude to my supervisor Prof. Ian Sims, for giving me the opportunity to join the CRESUCHIRP project. I am grateful for your support and guidance through these three intense years and I really enjoyed all our scientific discussions.

This adventure could have never been better without the wonderful CRESUCHIRP team. Words cannot express my gratitude to Théo, Divita, Ilsa, Brian and Omar for guiding me through the first year of my PhD. Then the two last years of my PhD could have never been better without you Alberto (I already miss playing tennis with you !). Each of you has inspired me to get better and become the researcher I am today. I am grateful to have the opportunity to work with all of you.

Je souhaite également remercier tous le personnel du département de physique moléculaire. Particulièrement Jonathan Courbe et Jonathan Thiévin pour leur soutien technique et pour m'avoir sortie de pas mal de galère sur le projet. Mais aussi Sophie, Lucile, Robert, Ludovic, Abdessamad, André et Erwann, pour m'avoir accueilli comme il se doit au sein du département. Autant pour les discussions scientifiques qu'informelles sur le temps du midi. Plus généralement, je tiens à remercier l'équipe de l'atelier, des gestionnaires et de direction de l'IPR pour leurs aides et disponibilité tout au long de ma thèse.

Qu'aurait été cette aventure sans Amélie, Julien (le L), Julien (le M), Romain, Solène, Marion, Maxime, Elliot et toutes nos bêtises ! Mention spéciale pour Amélie et tous nos brunchs du samedi midi, à quand le prochain ?! J'ai de la chance de vous avoir non seulement comme collègues mais aussi comme amis, vous avez grandement participé à rendre ces années de thèse inoubliable, alors merci à tous (Et non vous n'avez pas encore fini de me voir à Rennes !!).

Je tiens également à remercier tous les autres non-permanents de l'IPR que j'ai pu côtoyer de près ou de loin. Sans oublier mes stagiaires, Jacques et Aditi.

Pour finir j'aimerais remercier comme il se doit mes amis et ma famille. Plus particulièrement Alexis, merci pour ton aide et ton soutien pendant ces trois années de thèse. Papa, Maman, merci pour vos encouragements permanents. Vos précieux conseils m'ont mené jusqu'ici et continuent de me guider toujours plus loin, merci pour tout. Papa, c'est grâce à toi que j'ai postulé pour cette thèse, merci de m'avoir encouragé et d'avoir toujours cru en moi. J'aurai tant aimé t'avoir à mes côtés pour partager ce moment.

Résumé détaillé

L'astrochimie est un domaine relativement récent, ayant débuté dans les années 40 avec la première détection moléculaire de CH et CN [1,2]. Auparavant, la communauté scientifique pensait que seuls les atomes existaient dans l'espace entre les étoiles. À ce jour, plus de 300 molécules[3] avec une structure plus ou moins complexe ont été détectées dans le milieu interstellaire, ce qui témoigne d'une chimie riche malgré les conditions de faible température et de faible densité. Plus généralement, le domaine de l'astrochimie vise à étudier la formation, la destruction et l'excitation des molécules dans les milieux astronomiques et leur influence sur la structure, la dynamique et l'évolution de ces derniers. Atteindre cet objectif nécessite une collaboration entre les observateurs, les théoriciens et les expérimentateurs, qui abordent chacun des aspects distincts et complémentaires de l'astrochimie. Chacun de ces domaines comporte de nombreux défis techniques à relever afin d'affiner notre compréhension des processus chimiques fondamentaux

Le milieu interstellaire est connu pour abriter de nombreuses molécules malgré les basses températures. Une grande variété de molécules de taille différente, a été détectée au cours des dernières décennies. Leurs structures peuvent être aussi simples que le CO, le méthanol (CH_3OH), ou plus complexes comme le benzonitrile, voire même jusqu'à des structures de plus de 10 atomes comme les fullerènes (C_{60} et C_{70} [4]). Le nuage moléculaire du Taureau (TMC-1) est particulièrement connu pour abriter une grande variété de cyano-polyynes (HC_nN, n= 3,5,7,..) [5] et de molécules cycliques telles que le cyano-cyclopentadiène [6] ou l'oxirane [7]. D'autres molécules contenant du soufre, du phosphore ou du silicium ont également été détectées.

Les planètes et les lunes présentent également une chimie intéressante. Si elles sont suffisamment massives pour avoir une atmosphère, un riche réseau chimique peut s'y développer. L'une des atmosphères les plus explorées, après la Terre, est celle de Titan, la plus grande lune de Saturne. Plusieurs missions spatiales ont confirmé la présence de N_2, H_2, et CH_4 en tant que composants dominants de l'atmosphère de Titan. L'interaction avec le rayonnement UV/solaire ainsi que l'exposition aux particules lourdes chargées électriquement provenant de

[1]Swings and Rosenfeld (1937). Considerations Regarding Interstellar Molecules. The Astrophysical Journal, 86:483–486.

[2]McKellar (1940). EVIDENCE FOR THE MOLECULAR ORIGIN OF SOME HITHERTO UNIDENTIFIED INTERSTELLAR LINES. Publications of the Astronomical Society of the Pacific, 52(307):187.

[3]Müller et al. The Cologne Database for Molecular Spectroscopy, CDMS: a useful tool for astronomers and spectroscopists. Journal of Molecular Structure, 742(1-3):215–227.

[4]Cami et al. (2010). Detection of C60 and C70 in a Young Planetary Nebula. Science, 329(5996):1180–1182.

[5]Freeman and Millar (1983). Formation of complex molecules in TMC-l.

[6]McCarthy et al. (2021). Interstellar detection of the highly polar five-membered ring cyanocyclopentadiene. Nature Astronomy, 5(2):176-180.

[7]Barnum et al. (2022). A Search for Heterocycles in GOTHAM Observations of TMC-1. The Journal of Physical Chemistry A, 126(17):2716–2728.

la magnétosphère de Saturne induisent une chimie complexe résultant de la photolyse de ces principaux constituants atmosphériques. La mission Cassini a notamment permis d'observer de nombreux nitriles et hydrocarbures comme C_2H_2, HC_3N, ou C_2H_3CN [8]. L'atmosphère de Titan est particulièrement connue pour sa brume due à la formation d'aérosols qui sont d'un grand intérêt pour la communauté astrochimique [9].

Parmis les objets d'étude, les comètes revêtent un intérêt particulier en tant que fossiles de l'ère de la formation des planètes. Les noyaux des comètes se composent de débris rocheux, de glace et de gaz gelés. Lorsqu'elles s'approchent suffisamment de leurs étoiles, la couche glacée se sublime, créant deux queues distinctes autour du noyau. La première est constituée de poussières libérées lors du processus de sublimation, tandis que la seconde est composée d'espèces gazeuses. La queue gazeuse est principalement riche en ions en raison du rayonnement ultraviolet (UV) émis par l'étoile. La couche de glace est principalement composée d'eau, de CO et de CO_2. Étant donné que la température de sublimation de ces trois composants diffère, la chimie de l'atmosphère cométaire est principalement influencée par le constituant majoritaire en fonction de la distance par rapport à l'étoile. De nombreuses molécules ont été détectées dans la queue gazeuse, telles que divers hydrocarbures, de petits HAP comme le benzène [10], ainsi que des molécules azotées, soufrées, et bien d'autres [11]. La glycine, le plus simple des acides aminés, a également été détectée dans un échantillon de poussière de la mission Stardust provenant de la comète 81P/Wild2 [12].

Les molécules actuellement détectées et les connaissances sur la cinétique des réactions soulèvent de multiples questions fondamentales en astrochimie. La taille croissante des structures carbonées n'est pas complètement expliquée et suscite de nombreuses recherches sur la formation des espèces aromatiques polycycliques (HAP) [13]. La brume caractéristique de Titan fait également l'objet de diverses investigations, en mettant particulièrement l'accent sur le processus de formation des tholines [14]. Ces composants ont été formés lors de la célèbre expérience de Miller et Urey [15] visant à comprendre l'apparition de la vie sur Terre et réalisée

[8]Vuitton et al. (2006). The Nitrogen Chemistry of Titan's Upper Atmosphere Revealed. The Astrophysical Journal, 647(2):L175.

[9]Waite et al. (2007). The Process of Tholin Formation in Titan's Upper Atmosphere. Science, New Series, 316(5826):870–875.

[10]Schuhmann et al. (2019). Aliphatic and aromatic hydrocarbons in comet 67P/Churyumov-Gerasimenko seen by ROSINA. Astronomy & Astrophysics, 630:A31.

[11]Biver et al. (2022). Chemistry of comet atmospheres. arXiv:2207.04800 [astro-ph].

[12]Elsila et al. (2009). Cometary glycine detected in samples returned by Stardust. Meteoritics & Planetary Science, 44(9):1323–1330.

[13]Reizer et al. (2022). Formation and growth mechanisms of polycyclic aromatic hydrocarbons: A mini-review. Chemosphere, 291:132793.

[14]Dubois et al. (2019). In situ investigation of neutrals involved in the formation of Titan tholins. Icarus, 317:182–196.

[15]Miller and Urey (1959). Organic compound synthesis on the primitive earth. Science (New York, N.Y.),

dans des conditions similaires à l'atmosphère de Titan. De manière générale, la formation des molécules prébiotiques est un sujet d'actualité qui est au cœur de nombreuses recherches. En particulier, les scientifiques s'efforcent de comprendre où et dans quelles conditions les acides aminés peuvent se former. L'origine de l'homochiralité observée dans les organismes vivants est également un sujet de recherche actuel [16]. Pour répondre à ces questions, il est nécessaire de comprendre les processus réactionnels se produisant dans des conditions extrêmes. Ces données permettront de construire des modèles décrivant l'évolution des objets astronomiques et ainsi d'aider à élucider la formation de toutes ces espèces.

La cinétique d'une réaction chimique peut être décrite par deux paramètres : le coefficient de vitesse, qui quantifie la disparition des réactifs, et le rapport de branchement, qui caractérise l'efficacité des différentes voies qu'une réaction peut emprunter. Ces deux paramètres dépendent de la température, cependant, la simple connaissance de la vitesse globale de la réaction ne suffit pas à déterminer la vitesse d'apparition de chaque produit. Ainsi, les rapports de branchement s'avèrent indispensables pour modéliser avec précision un réseau chimique.

Le manque de données expérimentales à basse température découle des multiples défis auxquels sont confrontées les expérimentateurs dans ce domaine. Ces types de mesures impliquent le suivi de l'évolution de la concentration dans le temps d'une ou plusieurs espèces. Pour ce faire, il est impératif d'éviter les réactions croisées susceptibles de perturber les mesures, ainsi que la condensation des molécules due aux basses températures. De plus, en ce qui concerne la détermination des rapports de branchement, la technique de détection utilisée doit être soit une méthode de détection multiplexe, permettant de détecter simultanément différentes espèces, soit une méthode capable de mesurer des concentrations absolues. Enfin, la production du réactif en question n'est pas nécessairement une tâche aisée. De nombreuses molécules présentes dans l'espace présentent des structures assez exotiques et sont instables, ce qui les rend difficiles à produire en laboratoire. L'ensemble de ces divers aspects crée des contraintes lors de la réalisation des expériences et requiert la recherche d'un équilibre adéquat pour caractériser expérimentalement chaque nouveau système réactif.

L'objectif de cette thèse est de fournir des coefficients de vitesse et des rapports de branchement à basse température pour des réactions pertinentes dans divers milieux astrophysiques, tels que les nuages moléculaires ou les atmosphères planétaires et cométaires.

Pour effectuer des mesures de coefficients de vitesse et de rapports de branchement, la technique CRESU (Cinétique de Réaction en écoulement supersonique uniforme) a été associée à la spectroscopie micro-onde à impulsions chirpées (chirped pulse). Les tuyères de Laval, utilisées

130(3370):245–251.

[16] Hadidi et al. (2021). Conformer-dependent vacuum ultraviolet photodynamics and chiral asymmetries in pure enantiomers of gas phase proline. Communications Chemistry, 4(1):1–14.

pour générer des flux CRESU, créent un environnement offrant des conditions uniformes de température et de densité. La technique chirped pulse quant à elle permet une détection spécifique des molécules, y compris les rotamères, dès lors que la molécule possède un moment dipolaire. Pour ces travaux, un spectromètre en bande E a été utilisé (60-90 GHz).

La première partie de cette thèse est consacrée à la détermination des rapports de branchement de la réaction du radical CN avec le propène. Cette réaction est supposée être la voie principale de formation des isomères de cyanopropène. Ces molécules font partie de la famille des cyanopolyynes, présumées jouer un rôle essentiel dans la formation des précurseurs d'acides aminés, la croissance des chaînes carbonées et la formation d'aérosols dans l'atmosphère de Titan. Récemment, les isomères du cyanopropène ont été détectés dans TMC1 [17], chacun présentant une abondance similaire. Cependant, les études actuelles sur la réaction du radical CN avec le propène réalisées à température ambiante ont montré qu'un des isomères du cyanopropène est formé de manière négligeable par rapport aux deux autres. Ce constat souligne la nécessité de réaliser des mesures à basse température pour affiner notre compréhension de ce système et établir sa contribution aux modèles astrochimiques.

Dans ce travail, le rapport de branchement du produit principal de la réaction entre CN et propène a été déterminé à 35 et 52 K. Les résultats expérimentaux sont présentés et comparés aux calculs théoriques effectués avec MESMER. Il s'agit de la première détection expérimentale d'un produit de cette réaction à une température inférieure à la température ambiante. La fraction de branchement pour le cyanure de vinyle a été déterminée à l'aide d'une réaction de calibration. Bien que les tentatives d'observation d'autres produits issus de cette réaction n'aient pas été couronnées de succès, des limites supérieures ont été établies pour tous les isomères du cyanopropène. Le cyanure de vinyle s'est avéré être le produit principal de cette réaction jusqu'à 35 K. Aucune preuve de dépendance en pression pour ce chemin réactionnel n'a été trouvée à 52 K dans les limites de l'incertitude expérimentale. Les calculs théoriques effectués à l'aide de MESMER concordent avec les valeurs mesurées. Ils fournissent des preuves supplémentaires expliquant la non-détection des autres produits de réaction. En effet, les limites supérieures déterminées pour les produits de réaction sont supérieures aux rapports de branchement théoriques calculés, expliquant ainsi l'impossibilité de les détecter avec le dispositif expérimental actuel. Pour poursuivre ce travail, il est donc nécessaire d'améliorer la sensibilité du spectromètre. Cela pourrait se faire en développant des flux CRESU pulsés, permettant ainsi une plus grande flexibilité dans les conditions de conception des tuyères. Une autre possibilité consisterait à utiliser une méthode d'analyse différente, telle que l'empilement

[17] Cernicharo et al. (2022). Discovery of five cyano derivatives of propene with the QUIJOTE line survey. Astronomy & Astrophysics, 663:L5.

spectral [18]. Cette méthode est couramment utilisée en astronomie pour détecter les faibles transitions de rotation et pourrait être employée dans ce contexte. Dans l'ensemble, cette étude semble indiquer que les isomères du cyanopropène ne sont pas formés en quantités égales à basse température, malgré les observations actuelles dans TMC1. La raison n'en est pas encore claire, mais pourrait être due aux conditions hors équilibre thermique des nuages moléculaires, affectant potentiellement la répartition des produits. Les isomères de cyanopropènes pourraient également être formés selon d'autres voies de réaction qui ne sont pas encore prises en compte.

La deuxième partie de cette thèse est consacrée à la détermination des coefficients de vitesse pour la formation d'hétérodimères entre l'acide formique et le CO_2. Le processus de nucléation est la première étape d'une transition de phase. Cette transformation se produit par la formation de liaisons non covalentes entre les molécules. La nucléation a un large éventail d'applications car ce processus est omniprésent dans la nature et joue un rôle essentiel dans de nombreux domaines tels que la biologie, les nanotechnologies ou les sciences de l'atmosphère [19]. En astrochimie, ce type de processus est important pour les atmosphères planétaires et cométaires, ainsi que pour la formation des particules de poussière [20].

L'acide formique, le plus simple des acides carboxyliques, présente un grand intérêt pour les études atmosphériques et astrochimiques. Il a été détecté dans divers environnements astrophysiques, tels que les nuages moléculaires, les atmosphères planétaires et cométaires [21], [22]. Le CO_2 quant à lui peut devenir constituant principal d'atmosphère cométaire selon la distance par rapport à son étoile. Si la densité est suffisamment élevée, la complexation entre CO_2 et l'acide formique pourrait devenir pertinente pour ces environments, et la mesure du taux de dimérisation pourrait donc être introduite dans leurs modèles. L'étude du système acide formique-CO_2 a également pour objectif de servir de référence pour la caractérisation de la formation d'hétérodimères combinant les flux du CRESU et la spectroscopie micro-onde à impulsions chirpées.

Dans ce travail, le coefficient de vitesse de la réaction entre l'acide formique (FA) et le CO_2 a été directement mesuré en suivant la décroissance du réactif dans des conditions de pseudo-premier ordre à 52 K. L'évolution du produit au fil du temps a également été suivie et s'est

[18] Loomis et al. (2021). An investigation of spectral line stacking techniques and application to the detection of HC11N. Nature Astronomy, 5(2):188-196.

[19] Zhang et al. (2012). Nucleation and Growth of Nanoparticles in the Atmosphere. Chemical Reviews, 112(3):1957–2011. Publisher: American Chemical Society.

[20] Gobrecht et al. (2022). Bottom-up dust nucleation theory in oxygen-rich evolved stars - I. Aluminium oxide clusters. Astronomy & Astrophysics, 658:A167. Publisher: EDP Sciences.

[21] Zuckerman et al. (1971). Microwave Detection of Interstellar Formic Acid. The Astrophysical Journal, 163:L41. ADS Bibcode: 1971ApJ...163L..41Z

[22] Favre et al. (2018). First Detection of the Simplest Organic Acid in a Protoplanetary Disk. The Astrophysical Journal, 862:L2. ADS Bibcode: 2018ApJ...862L...2F.

avérée être en accord avec la vitesse mesurée. Le principal défi ce type de mesure consiste à éviter les autres processus de complexation, tels que la formation d'homodimères à partir des réactifs et la formation d'hétérodimères avec le gaz tampon. La formation d'homodimères peut être évitée en introduisant les réactifs à la densité appropriée. Cette densité maximale peut être déterminée par un "test de cluster" en suivant l'évolution de l'intensité du signal de la molécule d'intérêt (ou d'une approximation si la molécule n'a pas de moment dipolaire) pour différentes densités moléculaires. Il s'agit toutefois d'une limite expérimentale, car les densités maximales doivent être suffisamment importantes pour permettre des mesures. La formation d'hétérodimères avec le gaz tampon sera quant à elle influencée par les conditions d'écoulement et la nature du gaz tampon. Il est donc possible de les éviter en jouant sur la tuyère utilisée. L'influence du complexe formé avec le tampon a été observée dans ce travail avec une tuyère d'azote à 38 K. Le coefficient de vitesse mesuré était plus rapide d'un ordre de grandeur que dans la tuyère d'argon à 52 K. Malgré les conditions d'écoulement légèrement différentes, cela semble peu probable. Les calculs de l'énergie de Gibbs pour la formation de ce complexe ont été effectués et fournissent des preuves supplémentaires d'un mécanisme de chaperon où un premier complexe avec l'acide formique et l'azote est formé avant de réagir avec le CO_2.

Cette première étude couplant les flux du CRESU avec la spectroscopie micro-onde à impulsions chirpées montre les capacités de cette installation à mesurer les coefficients de vitesse absolus. La technique de détection utilisée ici a l'avantage d'être hautement spécifique et permet donc de distinguer les différents isomères du dimère. La suite de ce travail consistera à effectuer davantage de mesures à différentes températures et à explorer la dépendance à la pression du processus de dimérisation avec des tuyères de même température et de pressions différentes. Cela pourrait impliquer l'utilisation de différents gaz tampons, étant donné que le complexe formé avec celui-ci pourrait ouvrir une nouvelle voie pour la formation du complexe FA-CO_2. Enfin, des calculs théoriques sont en cours pour modéliser ces mesures expérimentales.

Contents

List of figures viii

List of tables ix

1 Introduction to astrochemistry 1
- 1.1 Interstellar media . . . 2
  - 1.1.1 The different types of environments . . . 2
  - 1.1.2 Observing molecules in space . . . 3
  - 1.1.3 Chemistry in space . . . 5
- 1.2 Reaction kinetics . . . 8
  - 1.2.1 Characteristic parameters . . . 8
  - 1.2.2 Theories of reaction kinetics . . . 16
  - 1.2.3 Kinetics parameters determination . . . 21
  - 1.2.4 Astrochemical models . . . 25
- 1.3 Outline of the thesis . . . 26

2 Experimental methodology 27
- 2.1 Introduction . . . 27
- 2.2 CRESU flows . . . 28
  - 2.2.1 Flow characteristics . . . 28
  - 2.2.2 Nozzle design and characterisation . . . 30
  - 2.2.3 Comparison with other cooling techniques . . . 33
- 2.3 CRESU chambers . . . 34
  - 2.3.1 CRESU-Chirp . . . 34
  - 2.3.2 Reactant introduction and generation using a precursor . . . 35
- 2.4 Chirped pulse microwave spectroscopy . . . 42
  - 2.4.1 Theoretical aspects . . . 42
  - 2.4.2 Coupling chirped pulse with CRESU flows: the SKISURF setup . . . 46
  - 2.4.3 Spectrometers developed in Rennes . . . 47
  - 2.4.4 Data acquisition . . . 50
  - 2.4.5 Data analysis . . . 52

3 Measurement of low temperature branching ratio for the CN + propene reaction 55
- 3.1 Introduction . . . 55
- 3.2 Experimental methodology . . . 58
- 3.3 Theoretical Methodology . . . 60
- 3.4 Results and discussion . . . 61
  - 3.4.1 Experimental Results . . . 61
  - 3.4.2 Theoretical Results . . . 70
- 3.5 Conclusion . . . 75

4 Heterodimer formation: formic acid – CO_2 dimer kinetics **77**
4.1 Introduction 77
4.2 Experimental method 80
4.2.1 Setup description 80
4.2.2 Experimental procedure and analysis method for the FA-CO_2 system . 83
4.3 Results and discussion 86
4.4 Conclusion 89

5 Conclusion and perspectives **91**

Bibliography **97**

Appendix **109**

A Laval nozzles **109**

B CN + propene **119**
B.1 Full data sets 121
B.2 Igor Pro code for branching ratio calculation 123
B.3 VAR and INT files for the cyanopropene isomers 125
B.4 Optimized geometries 128
B.5 Direct mechanisms for CN and propene reaction 133

C Formic acid and CO_2 dimerisation **137**
C.1 Argon 52K data set 138
C.2 Nitrogen 38K data set 140

List of Figures

1.3 Cumulative number of known interstellar molecules over time. From McGuire [2022]. . . . 4
1.5 Rho Ophiuchi (NIRCam image). Credit: NASA, ESA, CSA, STScI, Klaus Pontoppidan (STScI), processing Alyssa Pagan (STScI) . . . 6
1.6 Reaction coordinate diagram as a function of Gibbs energy. . . . 11
1.7 Scheme representing Maxwell-Boltzmann distribution of speeds for different temperatures. . . . 12
1.8 General cases for exothermic reactions. The upper panel shows a scheme of the potential energy of the system as the reaction takes place. The lower panel shows the corresponding log of the rate coefficient in the function of the inverse of temperature. From Sims [2013] . . . 13
1.9 Potential energy as a function of AB radius to illustrate the stabilisation by collision with a third body. . . . 14
1.10 Pressure dependence schematic as described by Lindemann-Hinshelwood mechanism. Adapted from Carstensen and Dean [2007]. . . . 15
1.11 Hard sphere collision schematic for the collision theory. . . . 17
1.12 Scheme of the influence of the impact parameter b and the collision outcome. From Zhang and Willitsch [2017]. . . . 18
1.13 Illustration of a PES connecting an initial state and a final state via different pathways. The minima are the initial and final state and the saddle point are the transition states. From Liu et al. [2022]. . . . 24
1.14 Fractional abundances of propargyl (CH_2CCH) as a function of time calculated with gas-phase chemical network RATE12 from the UMIST database and adaptation from the authors (see article). The dashed line corresponds to the calculated abundance of CH_2CCH when the reactions of this radical with O and N atoms were removed. Abundances observed in TMC-1 are indicated by dotted horizontal lines. Adapted from Agúndez et al. [2021]. . . . 25

2.1 Scheme of the expansion from a reservoir in a vacuum chamber through a Laval nozzle with a 2D simulated temperature map. From Gupta [2021] . . . 28
2.2 Isentropic flow and boundary layers arising from the real nozzle profile. From Fournier et al. [2017] . . . 29
2.3 Pitot measurement setup for Laval nozzle characterisation. Left hand side, picture of the setup, front view, installed in CRESU-LIF chamber. Right hand side, schematic of the pitot measurement setup in CRESU flow. . . . 31
2.4 Pitot characterisation of an argon Laval nozzle with an average temperature of 35 K. Reservoir pressure = 52.7 mbar and chamber pressure = 0.28 mbar . . 31
2.5 2D Mach number profile simulation of a nitrogen nozzle with 770 mbar in reservoir and 0.05 mbar in the chamber. Computed using Ansys fluent software. From Abdelkader Khedaoui [2022] . . . 32

2.6 Picture of both chambers in the laboratory. The pumping group is located in the basement and is connected between the two chambers. The CRESU-Chirp chamber is connected to the E-band spectrometer described in section 2.4. On this picture, The CRESU-LIF chamber is connected to the calibration vessels used for Mass flow controller calibration (see section 2.3.2) 34
2.7 CRESU-Chirp chamber schematic. (A) Reaction region (B) Movable reservoir, (C) Skimmer chamber, pumped by a turbo molecular pump, (D) 4-way cross connecting the chamber with CRESU-LIF and the pumping group. From Guillaume [2021] 35
2.8 Setup used for gas introduction in the reservoir. Left hand side, thermal mass flow controller system. Right hand side, ozone generator connected to the precursor line. 36
2.9 Calibration of Thermal mass flow controller. 37
2.10 Setup used for liquid introduction in the reservoir. 38
2.11 Picture of setup for gas mixture preparation. 39
2.12 UV-visible spectrometer scheme. From Gupta [2021] 40
2.13 ICN density measurement from UV-visible setup. 41
2.14 Chirped-pulse schematic principle. (1) A chirp is sent to polarise the molecular sample in a first step. (2) Then the FID signal is recorded in the time domain. (3) Finally, the signal is fast Fourier Transformed (FFT) to give the final spectrum in the frequency domain. 45
2.15 Schematic of signal up-conversion using a mixer and then a bandpass filter. . 46
2.16 Experimental FIDs for the J=6-5 transition over the experimental pressure range for a fixed partial pressure of OCS of 5.10^{-5} mbar in He buffer gas between 0.005 - 0.320 mbar in a flow cell. From Hays et al. [2020]. 46
2.17 Comparison of vinyl cyanide signal in an argon 30 K flow under CRESU conditions (orange) and skimmer conditions using the 4 mm skimmer (red). Right: Frequency spectrum. Left: corresponding FIDs in the time domain. The stars refer to spurs from the spectrometer electronics. From Abdelkader Khedaoui [2022]. 47
2.18 Scheme of the E-band spectrometer using digitizer as the acquisition device. From Hays et al. [2020]. 48
2.19 Picture of E-band spectrometer. (A) From top to bottom, DDG, computer (with acquisition card), oscilloscope and AWG. (B) Transmitter side. (C) Receiver side. 49
2.20 Scheme of an acquisition frame using the digitizer. From Guillaume [2021]. . . 50
2.21 Scheme of a multicolour pulses sequence. Credit: Ilsa R. Cooke. 51
2.22 Comparison between the multicolour and multifrequency pulses. Left, FFT of the FID after the pulse. Right, FFT of the excitation pulse. On acrylonitrile (VCN) transitions between 75.5 and 77 GHz in the skimmer chamber with an Ar 30K nozzle (Pressure reservoir = 23.24 mbar and Pressure chamber = 0.082 mbar). VCN density in the flow = $1 \times 8\ 10^{13}$ cm^{-3}. Scan averaged 10^4 times. . . 52
2.23 Acquisition scheme in case of reactions involving excimer laser. 53
2.24 Acquisition scheme in case of complex formation experiments, here showing loss in monomer signal. 54

3.1 CN radical and propene reaction pathways. 57
3.2 Scheme of the SKISURF setup used for the experimental measurements. Credits: Ilsa R. Cooke 59
3.3 Rotation diagram using the line intensities of the vinyl cyanide spectrum for argon 52 K high pressure nozzle. Probing: chirp 73-78 GHz, duration 200 ns, 250 000 accumulations, LO = 74 GHz, Flow VCN = 0.2 $g.h^{-1}$. 61
3.4 Vinyl cyanide spectrum used for rotational diagram analysis. Probing: chirp 73-78 GHz, duration 200 ns, 250 000 accumulations, LO = 74 GHz, Flow VCN = 0.2 $g.h^{-1}$. 62
3.5 Measurement of propene rotational transition intensity as a function of the density of propene in the flow at 35 K. Probing: 80 ns single frequency pulse with 100 000 accumulations, LO = 68 GHz. 62
3.6 Spectrum averaged between 250-530 µs after the excimer laser pulse compared with the simulated spectra (9 K) of the products using SPCAT. 63
3.7 Intensity evolution of the rotational feature from vinyl cyanide from the reaction of CN + propene. The time stamps indicate the delay from the excimer laser pulse/start of the reaction. The top inset shows the time dependence of the line intensity. Probing: 80 ns single frequency pulse at 66198.36 MHz (J=$7_{0,7}$ ← $6_{0,6}$) with 1 million accumulations (4 scans of 250,000 accumulations averaged together), LO = 74 GHz. 64
3.8 Vinyl cyanide rotational line intensity from reactions of CN with ethene and propene as a function of time measured at (a) 35 K (b) 52 K at low pressure and (c) 52 K at high pressure. Probing for vinyl cyanide: 80 µs single frequency pulse at 66198.36 MHz (J=$7_{0,7}$ ← $6_{0,6}$) with 250,000 accumulations, LO = 74 GHz. Probing for ozone: 80 ns single frequency pulse at 67 3562 MHz (J= $6_{0,6}$ ← $5_{1,5}$) with 10,000 accumulations, LO = 68 GHz. The blue shaded zones indicate the measurements used to calculate the branching fraction. 65
3.9 Measurements of branching fractions of vinyl cyanide channel with associated error. The dashed line represents the non-weighted average of all these values for each nozzles. (a) Argon 35 K nozzle (b) Argon 52 K low pressure nozzle (c) Argon 52 K high pressure nozzle. Experimental conditions for all these measurements are provided in appendix B.3. 67
3.10 Relative enthalpy scheme with ZPE correction for the CN propene reaction. Solid and dotted lines represent the different reactive channels while dashed lines represent the isomerisation channels. 70
3.11 Schematic of the entrance channel for the addition of CN onto the propene double bond. 71
3.12 Scheme of the isomerisation pathway to go from C1a-1 to C3-1 via the large initial barrier. 72

4.1 Gibbs free energy of cluster formation as a function of the cluster size for different degrees of saturation S. 78

4.2 Rotational diagram acquired with 0.2 g/h of vinyl cyanide in the flow. The flow of the nitrogen 38 K nozzle was sampled using a 4mm skimmer. $P_{reservoir}$ = 470 mbar and $P_{chamber}$ = 0.39 mbar $P_{skimmer}$= 8 µbar. Probing: 200 ns chirp between 73-78 GHz with 250 000 accumulations, LO = 74 GHz. 81
4.3 Schematic of the experimental setup for rate coefficient measurement of heterodimer formation. 81
4.4 N_2O (8×10^{13} cm^{-3} in the flow) signal intensity as a function of the reservoir position. Probing conditions: 75 369 MHz frequency, pulse length = 170 µs with 10,000 accumulations, LO=74 GHz. Acquired in nitrogen 38 K nozzle with 4 mm skimmer. Reservoir between 16 and 52 cm with 2 cm steps. 82
4.5 Frequency spectrum of trans (left panel) and cis (right panel) formic acid. Acquired in argon 35 K nozzle. 84
4.6 Signal intensity as a function of the formic acid density. Probing conditions: 67 291 MHz transition ($3_{0,3} \leftarrow 2_{0,2}$), pulse length = 170 µs with 100,000 accumulations, LO = 68 GHz. Acquired in argon 52 K nozzle with 3 mm skimmer. . 85
4.7 Signal intensity as a function of the formic acid density. Probing conditions: 75 369 MHz ($3 \leftarrow 2$), pulse length = 170 µs with 100,000 accumulations, LO = 74 GHz. Acquired in argon 52 K nozzle with 3 mm skimmer. 86
4.8 Kinetics data obtained in argon nozzle at 52 K with a 3 mm skimmer. The left panel shows the formic acid decay at a 24 cm position fit with a single exponential decay function (black dotted line). The right panel shows the second-order kinetics plot where the pseudo-first order rate coefficients are plotted as a function of CO_2 concentration. The black dotted line shows the fit yielding the second-order rate coefficient. 87
4.9 Kinetics data obtained in argon nozzle at 52 K with a 3 mm skimmer showing the FA-CO_2 complex growth at a 16 cm position and fitted using equation 4.5 (black dotted line). Probing: single frequency pulse at 65 738 MHz, 170 ns, LO = 68 GHz, 250 000 accumulations, FA density = 8×10^{11} cm^3. 87
4.10 Kinetics data obtained in N_2 nozzle at 38 K with a 4 mm skimmer. The left panel shows the formic acid decay at a 45 cm position fit with a single exponential decay function (black dotted line). The right panel shows the second-order kinetics plot where the pseudo-first order rate coefficients are plotted as a function of CO_2 concentration. The black dotted line shows the fit yielding the second-order rate coefficient. 88

5.1 2D radial temperature profile of the nitrogen 23.5 K nozzle ($P_{reservoir}$ = 773.5 mbar and $P_{chamber}$ = 0.12 mbar). Obtained using CFD simulation with Ansys Fluent. The probing region of a 4 mm diameter skimmer is represented in white. The two black dashed lines show the region covered by the horn antennas in the CRESU environment. From Abdelkader Khedaoui [2022]. 92
5.2 1D temperature and density measurement along flow axis using a Pitot probe of He 6 K nozzle ($P_{reservoir}$ = 676.5 mbar and $P_{chamber}$ = 0.04 mbar, motor speed = 2500 RPM) 93
5.3 2D temperature measurement along flow axis using a Pitot probe of He 6 K nozzle ($P_{reservoir}$ = 676.5 mbar and $P_{chamber}$ = 0.04 mbar, motor speed = 2500 RPM) 93

5.4 Picture of the inside of the pulsed system reservoir. 94

A.1 1D temperature and density measurement along flow axis using a Pitot probe of Ar 35K nozzle (see conditions in table A.1) 109
A.2 2D density measurement along and lateral to the flow axis using a Pitot probe of Ar 35K nozzle (see conditions in table A.1) 110
A.3 Rotation diagram using the line intensities of the vinyl cyanide spectrum for the argon 35 K nozzle. Probing: 200 ns chirp between 73-78 GHz with 250 000 accumulations, LO=74 GHz, Flow VCN = 0.2g/h. 110
A.4 1D temperature measurement along flow axis using a Pitot probe of Ar 50K 0.3 nozzle (see conditions in table A.1) 111
A.5 1D density measurement along flow axis using a Pitot probe Ar 50K 0.3 nozzle (see conditions in table A.1) 111
A.6 2D temperature measurement along and lateral to the flow axis using a Pitot probe Ar 50K 0.3 nozzle (see conditions in table A.1) 112
A.7 Rotation diagram using the line intensities of the propene spectrum for argon 52 K low pressure nozzle. Probing: chirp 73-78 GHz, duration 200 ns, LO=74GHz, Flow VCN = 0.2g/h. 113
A.8 1D temperature measurement along flow axis using a Pitot probe Ar 50K 0.7 nozzle (see conditions in table A.1) 113
A.9 1D density measurement along flow axis using a Pitot probe Ar 50K 0.7 nozzle (see conditions in table A.1) 114
A.10 2D temperature measurement along and lateral to the flow axis using a Pitot probe Ar 50K 0.7 nozzle (see conditions in table A.1) 114
A.11 1D temperature measurement along flow axis using a Pitot probe N2 38K nozzle (see conditions in table A.1) 115
A.12 2D density measurement along and lateral to the flow axis using a Pitot probe N2 38K nozzle (see conditions in table A.1) 115
A.13 Rotation diagram using the line intensities of the propene spectrum for nitrogen 38 K nozzle. Probing: chirp 73-78 GHz, duration 200 ns, LO = 74 GHz. . . . 116

B.1 Ar 50 K low pressure data. 119
B.2 Ar 50 K high pressure data. 120
B.3 Ar 35 data. 121

C.1 NO_2 (5 sccm) signal intensity in function of the reservoir position. Probing conditions: 75 369 MHz conditions, pulse length = 170 µs with 10,000 accumulations, LO=74 GHz. Acquired in argon 52 K nozzle with 3mm skimmer. reservoir between 8 and 52 cm with 2 cm steps. 137
C.2 Kinetics data obtained in argon nozzle at 52 K with a 3 mm skimmer. Formic acid decay fitted with a single exponential decay function (black dotted line). . 138
C.3 Kinetics data obtained in argon nozzle at 52 K with a 3 mm skimmer. Formic acid-CO_2 complex signal fitted with a model described in chapter 4 (black dotted line). 139

C.4 Kinetics data obtained in nitrogen nozzle at 38 K with a 4 mm skimmer. Formic acid decay fitted with a single exponential decay function (black dotted line). . 140

List of Tables

3.1 Summary of previous branching ratio measurements for the CN + propene reaction. *Errors represent a combination of statistical uncertainty (2σ) and an estimate of possible systematic errors. **Errors are reported as 2σ incorporating the uncertainties in both the fit and the photoionization crosssections. 58
3.2 Experimental conditions for the CN radical and propene reaction. 59
3.3 Details of the multicolour pulse used for monitoring the products from the reaction CN + propene. 63
3.4 Summary of experimental results of branching ratio measurement of the CN + propene reaction. Uncertainties are quoted at 95% confidence with an estimated 10% possible systematic error added in quadrature. 69
3.5 Summary of theoretical results of product branching fractions for the CN + propene reaction calculated using MESMER. The results at 298 K are extracted from Trevitt et al. [2009, 2011]. The data at 52 and 35 K are extrapolated from the calculated data. Values in parenthesis consider the same probability to form C1a-1 and C3-1 complexes after the reactant collision. 74

4.1 Summary of calculated Gibbs energies and equilibrium constant calculated with CBS-QB3 thermochemistry method. Calculations performed by Sándor Demes. 88

A.1 Nozzle conditions. 117
A.2 Vinyl cyanide line list used for rotational diagram analysis 118

B.1 Experimental conditions for the CN radical and propene reaction in argon 52 K nozzle. Propene density 1×10^{14} cm^{-3}, total flow density 5.15×10^{16} cm^{-3}. Experimental uncertainties are estimated at the $\pm 2\sigma$ level. 119
B.2 Experimental conditions for the CN radical and propene reaction with argon 52 K high pressure. Propene density 5×10^{13} cm^{-3}, total flow density 10.3×10^{16} cm^{-3}. Experimental uncertainties are estimated at the $\pm 2\sigma$ level. 120
B.3 Experimental conditions for the CN radical and propene reaction with argon 35 K nozzle. Propene density 5×10^{13} cm^{-3}, total flow density 5.26×10^{16} cm^{-3}. Experimental uncertainties are estimated at the $\pm 2\sigma$ level. 122

C.1 Ar 52 K data set. Fitting range for k_{1st} determination: $[CO_2] = 1.4 \times 10^{14} - 1.6 \times 10^{15}$ cm^{-3}. 139
C.2 Nitrogen 38 K data set. Fitting range for k_{1st} determination: $[CO_2] = 1 \times 10^{13} - 6.5 \times 10^{13}$ cm^{-3}. 140

Chapter 1

Introduction to astrochemistry

Rien ne se perd, rien ne se crée, tout se transforme.

– Antoine Lavoisier

Astrochemistry is a young field that started in the 40s with the first molecular detection of CH and CN [McKellar, 1940, Swings and Rosenfeld, 1937]. Beforehand, only atoms were thought to exist in space, and the area between stars was thought to be empty. Advances in radioastronomy in the 60-70s allowed the detection of many new molecules and the repertoire of interstellar molecules has not stopped growing since then. More than 300 molecules (CDMS [Müller et al., 2005]) with varying degrees of complexity in their structure have been detected to date in the interstellar medium (ISM), highlighting a rich chemistry despite the low temperature and density conditions. Overall, the astrochemistry field aims to study the formation, destruction, and excitation of molecules in astronomical media and their influence on the structure, dynamics, and evolution of astronomical objects. This objective requires collaborative work between observers, theoreticians, and experimentalists, as they each address distinct and complementary aspects of astrochemistry. Each of these fields includes many technical challenges to be met in order to refine our understanding of fundamental chemical processes.

This thesis focuses on the experimental aspect of astrochemistry. In this introductory chapter, the context and implications of this work will be presented. To give a general background, the different types of environments will be described along with their physical conditions. The various ways to observe molecules will be discussed along with the current knowledge on the chemistry of these media. Then, the different experimental and theoretical aspects relating to the kinetics of chemical processes will be discussed, to give a sense of the necessary data to describe a reaction and the challenges in this field. The impact of these parameters on the accuracy of astrochemical models will be discussed, emphasising the importance of kinetics measurements at low temperatures.

1.1 Interstellar media

1.1.1 The different types of environments

A wide variety of environments can be found in space, each with its own set of physical conditions of pressure, density, and temperature. These different media can be summarised by looking at the life cycle of a star (figure 1.1).
The process starts with the diffuse cloud state, where gas and dust from old stars collapse inward to form a cloud. The temperature ranges from 50 to 100 K and densities are very low around $< 10^3$ cm^{-3} compared to Earth's atmosphere at around 10^{20} cm^{-3}. After further collapsing, it will enter the dark cloud stage. The accumulation of tiny dust makes them opaque, hence their name, and acts as a shield from dissociating UV radiation. An ice layer starts to form on the dust grains due to the cold temperatures from 10 - 100 K. The molecular density is slightly higher from 10^3 to 10^6 cm^{-3}. As collapse progresses, the central part, forming the protostar, becomes so dense that radiation cannot escape anymore, causing a warming up of this region to 100-300 K. An outflow of matter is generated, forming the protoplanetary disk. A gradient of temperature can be observed in this disk, from warm temperatures close to the protostar, causing the melting of ice, to colder temperatures in the outer region where ice layer remains. When the protostar reaches a critical temperature, the fusion process of hydrogen can start, making it an actual star. Inside the disk, particles will eventually form increasing size aggregates to create planets, comets, and asteroids. The physical conditions on these planets will vary depending on their mass and distance to the central star. The temperature of the surface and the presence of an atmosphere as well as the main chemical component of the planet will influence greatly its chemical evolution. When the star runs out of fuel, it will explode and collapse, releasing its material once again into the interstellar media. Depending on its mass, several other objects can be formed like neutron stars, black holes or white dwarfs.

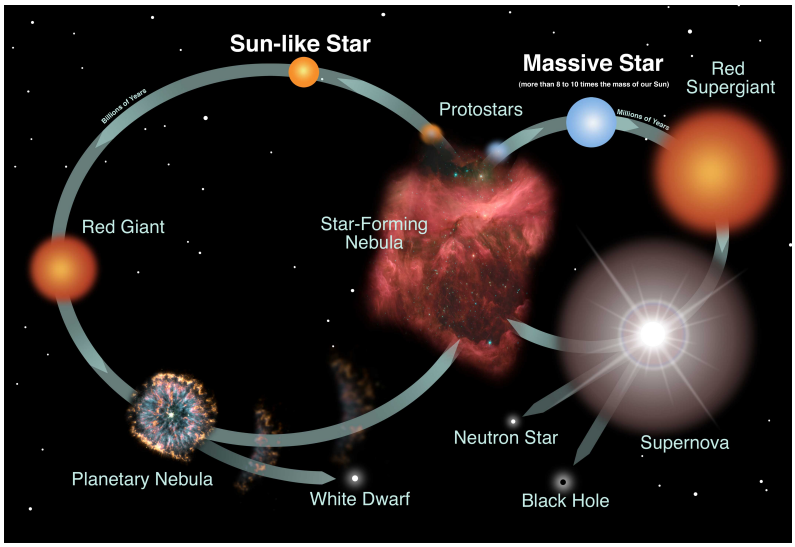

Figure 1.1: Life cycle of a star. Image credits: NASA and the Night Sky Network. [1]

[1] source: https://webbtelescope.org/contents/media/images/4190-Image (accessed: 28/09/2023)

1.1.2 Observing molecules in space

The observation of molecules is based on their interaction with electromagnetic radiation. The energy levels accessible for a molecule are quantized and can be divided into three types: rotational, vibrational and electronic. Looking at the absorption or emission of photons will give information on the transition between states of a molecule and allow its identification. Each type of transition corresponds to a range of the light spectrum, rotational transitions can be probed in microwave and far infrared, vibrational in infrared, and electronic in UV-visible.

Earth's atmosphere is composed of many molecules that absorb radiation coming from space. Only a little part of this spectrum can pass through as figure 1.2 shows. The largest accessible window is located in the radio wave ($\sim$ 10 MHz - 1 THz), which allows the probing of rotational transitions directly from the ground.

The first single-dish telescopes were constructed with the advances in radio telecommunications. The dish is made to collect and focus the light on a receiver which then amplifies and converts the signal coming from astronomical objects. Yebes[2], for instance, is a telescope with a 40m dish located in Castilla-La Mancha in Spain. It can probe frequencies from 4.9 to 90 GHz. With this kind of telescope, the ability to observe fine details, so-called angular resolution, is defined by the observed wavelength and the size of the antenna. Since the observable range from Earth is already on the long wavelength part of the light spectrum, enormous dishes of hundreds of meters are required to observe the sky with a similar resolution to optical telescopes. A compromise was found by combining multiple small dish telescopes using interferometry. NOEMA[3], for instance, is an array located in the French Alps, composed of 12 dishes of 15m each. The frequency range from 80 to 370 GHz. These two types of telescopes are complementary to probe different size objects.

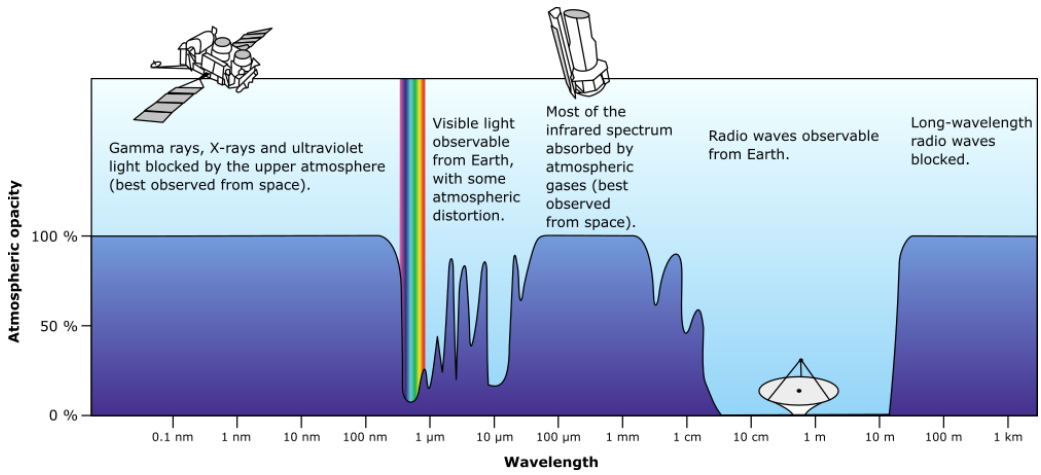

Figure 1.2: Absorption of the light spectrum by Earth atmosphere. Image credits: NASA. [4]

Though Earth telescopes are very practical for observing molecules in space, they do not

[2]https://rt40m.oan.es/ (accessed: 28/09/2023)
[3]https://iram-institute.org/observatories/noema/ (accessed: 28/09/2023)
[4]source: https://commons.wikimedia.org/wiki/File:Atmospheric_electromagnetic_opacity.svg (accessed: 28/09/2023)

cover all possibilities. Rotational transitions can only be probed for molecules possessing a dipole moment, meaning that highly symmetric molecules will not be observable. Moreover, as molecules increase in size, their rotational constants become smaller, thus they will have closely spaced energy levels with transitions at lower frequencies. The partitioning of population among these numerous energy levels will result in a lower number of molecules absorbing or emitting at a given frequency, making their detection more difficult. Finally, the detection of molecules in the condensed phase is not possible as they do not possess free rotational motions. These drawbacks underline the need to observe molecules directly from space in order to access other parts of the light spectrum. Various space missions have been launched for this purpose since the 50s. Each space telescope has various instruments to probe a specific wavelength range and has contributed to significant findings. The Cassini mission, for instance, was focused on the study of Saturn and its moons. One particular probe, Huygens, was dedicated to the study of Titan's atmosphere and has totallyn Earth changed our perspectives on its chemical model [Lopes et al., 2019, Vuitton et al., 2006]. The recently launched James Webb telescope (JWST) was built in the infrared range to study the early universe, star formation, and exoplanet composition. The first observational results are currently being published and will certainly broaden our understanding of the chemistry of astrophysical media, opening new interesting questions [Berné et al., 2023, Kamp et al., 2023].

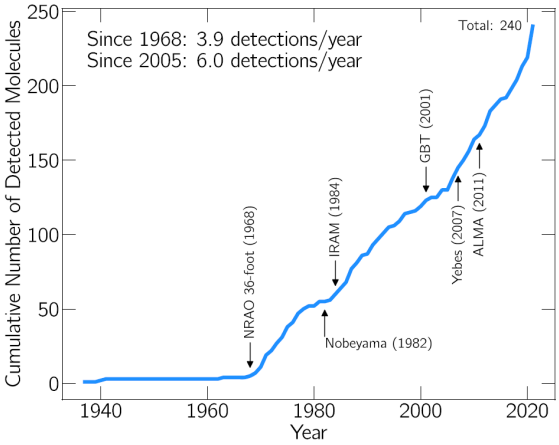

Figure 1.3: Cumulative number of known interstellar molecules over time. From McGuire [2022].

Since the first detection of space molecules, significant progresses have been made, and the tally now stands at approximately 300 molecules detected in the interstellar medium or circumstellar shells. The increasing rate of molecular detection is closely linked to instrumentation advances (figure 1.3). By increasing the sensitivity and bandwidth of the detectors, weaker lines, either from molecules in small quantities or very distant objects are becoming accessible. For the assignment of transition to represent a firm detection, it requires various criteria to be met as described by Herbst and Van Dishoeck [2009]. In particular, the frequencies need to be known with enough accuracy from laboratory measurements or high-precision theoretical models. This criteria itself already represents a challenge for experimentalists and theoreticians. Overall, technical progresses and new detections keep pushing our knowledge further every day, revealing a large panel of possible reactions between the molecules known in space.

1.1.3 Chemistry in space

The "Astronomer's periodic table" varies drastically from that on Earth. In space, hydrogen represents around 90% of the cosmic element abundance followed by helium with around 8%. The rest is spread between oxygen, carbon and nitrogen as well as a few other atoms (figure 1.4). For this reason, astronomers usually quote the atomic abundances compared to hydrogen and molecular abundances compared to H_2, the most abundant molecule. It is important to note that the definition of a complex molecule differs from typical usage in organic chemistry. For astronomers, any molecule containing at least 6 atoms is considered a complex organic molecule (COM) [Herbst and Van Dishoeck, 2009].

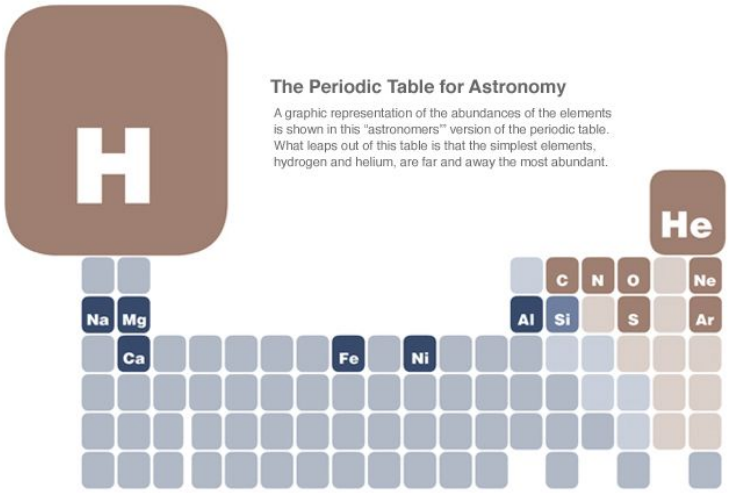

Figure 1.4: The periodic table for astronomy. From NASA [5]

To elucidate the chemistry of a given environment, two factors must be taken into account. The first one is the physical conditions of the astronomical object which play a vital role in determining the feasible reactions. The second one is the formation history of the object which influences its primary chemical constituents, ultimately shaping the overall chemistry. As a result, commonalities may emerge in the chemistry of two objects of the same type, while certain groups of molecules may prevail, serving as signatures of their uniqueness.

The ISM (figure 1.5), for instance, is known to host a rich chemical repertoire despite the cold temperatures. A wide variety of different-sized molecules from 2 to 12 atoms [McGuire, 2022] were detected during the past decades. Their structures can be as simple as CO, methanol (CH_3OH), or more complex like the cyclic benzonitrile, up to few molecules with more than 12 atoms like fullerenes (C_{60} and C_{70} [Cami et al., 2010]). The Taurus molecular cloud (TMC-1) is particularly known for hosting a wide variety of cyano-polyynes (HC_nN, n= 3,5,7,..) [Freeman and Millar, 1983] and cyclic molecules such as cyano-cyclopentadiene [McCarthy et al., 2021] or oxirane [Barnum et al., 2022]. Other molecules containing sulfur, phosphor or silicon were also detected.

Planets and satellites have been showing interesting chemistry as well. If they are massive enough to have an atmosphere, a rich chemical network can develop. One of the most explored

[5] source: https://chandra.harvard.edu/resources/flash/periodic_tables.html (accessed: 28/09/2023)

atmospheres other than Earth is Titan, the largest moon of Saturn. Various space missions have revealed N_2, H_2 and CH_4 as its main components. The UV/solar radiation and electrically charged heavy particles from Saturn's magnetosphere induce a rich chemistry with the photolysis of the main atmosphere components. Cassini's mission allowed the observation of many nitriles and hydrocarbons like C_2H_2, HC_3N, or C_2H_3CN[Vuitton et al., 2006]. Titan's atmosphere is particularly known for its haze due to the formation of aerosols which are of great interest to the astrochemistry community [Waite et al., 2007].

Cometary environments are of significant interest as they are fossils from the era of planet formation. The comet's nuclei are made from leftover rocky debris, ice and frozen gases. When it gets close enough to its star, the icy layer sublimates, forming two distinct comas around the nucleus. The first is composed of dust released from the sublimation process and the second with gaseous species. The gas tail is mainly composed of ions due to the ultraviolet (UV) radiation emitted by the star. The ice layer is mainly composed of water, CO and CO_2. As the sublimation temperature of these three components is different, the chemistry of the cometary atmosphere will be mainly driven by one of them, depending on the distance to the star. Many molecules have been detected in the volatile coma such as various hydrocarbons, small polycyclic aromatic hydrocarbons (PAH) like benzene [Schuhmann et al., 2019], nitrogen and sulphur-bearing molecules among many others [Biver et al., 2022]. Even glycine amino acid has been detected in the dust sample from the Stardust mission to comet 81P/Wild2 [Elsila et al., 2009].

Figure 1.5: Rho Ophiuchi (NIRCam image). Credit: NASA, ESA, CSA, STScI, Klaus Pontoppidan (STScI), processing Alyssa Pagan (STScI)

The structural complexity and diversity of the detected molecules suggest overall a rich chemistry. Given the extreme conditions in the observed media, this raises the question of how these molecules were formed. Molecules usually need a certain amount of energy for a reaction to proceed, named the activation barrier. This amount varies in function of the reactants implied. On one hand, the temperature of a medium defines the additional energy possessed by a molecule, thus constraining the possible processes. On the other hand, the environment

density constrains the number of reactants involved in a reaction. In the case of low density environment, only unimolecular and bimolecular reactions are considered as reactions involving three bodies are unlikely to happen. These two points will be discussed in depth in section 1.2. This thesis work is focused on low temperatures and low density media, therefore, only bimolecular reactions will be discussed.

In cold environments, two types of processes can be distinguished, the ice-phase and the gas-phase. At the grain surface, an ice layer can form with the right temperature conditions. Molecules in the gas phase can collide with these grains and get adsorb on the ice layer. They may be able to move at the surface and eventually meet other components and react. Species adsorb at the surface can be released in the gas phase through various processes like thermal desorption or photodesorption. The gas-phase processes, on the other side, can be divided into four main categories :

(i) Ion-neutral reactions: the long-range interaction induced by the charged ionic species allows them to attract other species despite the low densities. Most of these processes are barrierless or have submerged barriers, thus requiring no additional energy to proceed.

$$A + BC^+ \rightarrow AB^+ + C$$

(ii) Neutral-neutral reactions: typically they involve at least one radical (species with one or more unpaired electrons). These processes are characterised by the formation of a lower energy complex which can proceed to products without additional energy (barrierless or submerged barrier processes).

$$A + B \rightarrow C + D$$

(iii) Radiative association reactions: The two reactants can form an excited intermediate which relaxes with the emission of a photon.

$$A + B \rightarrow AB + h\nu$$

(iv) Dissociative recombination reactions: An ion can collide with an electron, forming an excited neutral intermediate, which then dissociates in fragments, releasing kinetic energy.

$$AB^+ + e^- \rightarrow A + B$$

The current detected molecules and knowledge on reaction kinetics raise multiple fundamental questions in astrochemistry. The increasing size of carbonaceous structures remains elusive and is the subject of multiple research on the formation of PAH [Leger and Puget, 1984, Reizer et al., 2022]. Titan's characteristic haze is also the center of various investigations. The

process of formation of tholins is especially puzzling [Dubois et al., 2019, Waite et al., 2007]. These components were formed during the famous Miller and Urey [1959] experiment, aiming to understand the appearance of life on Earth and was performed under conditions which are similar to Titan's atmosphere. In general, the formation of prebiotic molecules is a burning topic that is at the center of many projects. In particular, scientists are trying to understand where and under which conditions amino acids can be formed [Carl et al., 2023, Sanz-Novo et al., 2022]. The origin of homochirality observed in living organisms is also questioned [Hadidi et al., 2021, Kaiser et al., 2022].

Replying to these questions requires a deep understanding of reaction processes in extreme conditions to build accurate models that could describe the evolution of astronomical objects and help unravel the formation of all these species.

1.2 Reaction kinetics

Understanding the kinetics behind a chemical process is crucial when it comes to modelling and predicting the evolution of a system. The following section presents in depth the different aspects and theories behind the determination of the kinetics parameters of a reaction. The rate law and branching fractions will be defined along with their temperature and potential pressure dependencies. Additionally, the experimental and theoretical methods to determine these coefficients will be described. Finally, the use of the kinetics parameters in astrochemical models will be discussed.

1.2.1 Characteristic parameters

The kinetics of a chemical reaction can be described by two parameters, the rate coefficient, which describes the disappearance of the reactants, and the branching ratio, which characterise the efficiency of the different path a reaction can follow.

Consider a general single channel reaction :

$$aA + bB \rightarrow cC + dD \tag{1.1}$$

Where upper case letter stands for a molecule and lower case letter stands for the stoichiometry of the molecule in the considered reaction.

The rate of a reaction is related to how fast the reactant disappears or the products appears. The rate of change of concentration of C, for instance, can be written as $\frac{d[C]}{dt}$. Thus, the rate of a reaction can be written as

$$rate = -\frac{1}{a}\frac{d[A]}{dt} = -\frac{1}{b}\frac{d[B]}{dt} = \frac{1}{c}\frac{d[C]}{dt} = \frac{1}{d}\frac{d[D]}{dt} \tag{1.2}$$

In general, the rate can also be expressed as the product of a coefficient named k and the

product of the concentrations of the reactants raised to some power (here named m and n) (equation 1.3). The overall order of the reaction is defined as the sum of individual powers, order = m + n. The form of the rate law and the order give clues on the mechanism of the reaction.

$$rate = k[A]^m[B]^n \tag{1.3}$$

In the case of elementary reactions, the orders, m and n, are equal to the stoichiometry factor of the species. Elementary processes can be defined as reactions proceeding in a single step. They include unimolecular and bimolecular processes. As mentioned in section 1.1.3, the media of interest for this thesis are at very low densities, thus only these types of processes are accounted for.

Consider a first-order reaction for the elementary process $A \rightarrow products$. The rate law can be defined as

$$-\frac{d[A]}{dt} = k[A] \tag{1.4}$$

This equation can be rearranged and integrated over time, giving

$$ln\frac{[A(t)]}{[A]_0} = -kt \tag{1.5}$$

Where $[A]_0$ is defined as the initial concentration of A and [A(t)] is the concentration at time t. By exponentiating both sides, it gives the final rate law

$$[A(t)] = [A]_0 exp(-kt) \tag{1.6}$$

Consider now a second-order reaction for the elementary process $A + B \rightarrow products$. The rate law can be defined as

$$-\frac{d[A]}{dt} = k[A][B] \tag{1.7}$$

The concentration of both reactants are now needed to be able to determine the rate of the reaction. As it can be difficult to follow the evolution of two species experimentally, one of the reactants can be injected in excess compared to the other. Its concentration can thus be considered as a constant. These conditions are called pseudo-first order or isolation conditions.

By considering $[B]_0 \gg [A]_0$, the rate law becomes,

$$-\frac{d[A]}{dt} = k[A][B]_0 \tag{1.8}$$

This equation can be rearranged and integrated over time, to give the final rate law

$$[A(t)] = [A]_0 exp(-k[B]_0 t) \tag{1.9}$$

The pseudo-first order rate coefficient can be defined as $k_{1st} = k[B]_0$. By measuring the k_{1st} coefficient for various $[B]_0$ concentrations, the overall rate coefficient k can be derived. This method is commonly used in kinetics measurements involving methods such as laser-induced fluorescence (LIF). In this work, this principle was used to measure dimerisation rate coefficient using chirped-pulse microwave spectroscopy (Chapter 4).

While the rate coefficient gives information on the reactant's evolution over time, it can be more complicated for products. In fact, when a reaction can lead to different sets of products, the efficiency of each cannot be retrieved solely from the overall rate coefficient value.

Consider a multi-channel reaction

$$\begin{aligned} \text{A + B} &\xrightarrow{1} \text{C + D} \\ &\xrightarrow{2} \text{E + F} \\ &\xrightarrow{3} \text{G + H} \end{aligned}$$

In this case, the overall rate coefficient k is now expressed as

$$k(T) = k_1(T) + k_2(T) + k_3(T) \tag{1.10}$$

where T is the temperature. The product branching ratio α can be defined as

$$\alpha_1 = \frac{k_1}{k} \quad ; \quad \alpha_2 = \frac{k_2}{k} \quad ; \quad \alpha_3 = \frac{k_3}{k} \tag{1.11}$$

As the proportion of each path may also depend on temperature, both the overall rate coefficient and branching ratios are necessary to model accurately a chemical network. The experimental measurement of these coefficients is more challenging as it requires a detection method not only highly sensitive, but also either multiplex, to detect different species simultaneously, or able to measure absolute concentrations.

Temperature dependence

To understand the temperature dependence of the rate coefficient, let us consider the basic concepts behind the transition state theory (TST), a widely used theory first developed by Henry Eyring, Meredith Gwynne Evans and Michael Polanyi [Evans and Polanyi, 1935, Eyring, 1935]. This theory proposes that the reactants goes through an activated complex form, named the transition state, before going to the products. The reaction can be written as:

$$A + B \rightleftharpoons AB^{\ddagger} \longrightarrow P \tag{1.12}$$

For a system to go from the reactant to the product, it requires therefore additional energy as the reactants need to rearrange in space, eventually creating and forming bonds to give the products. This additional energy needed to reach the transition state can be seen as a "barrier" for the reaction to proceed (figure 1.6).

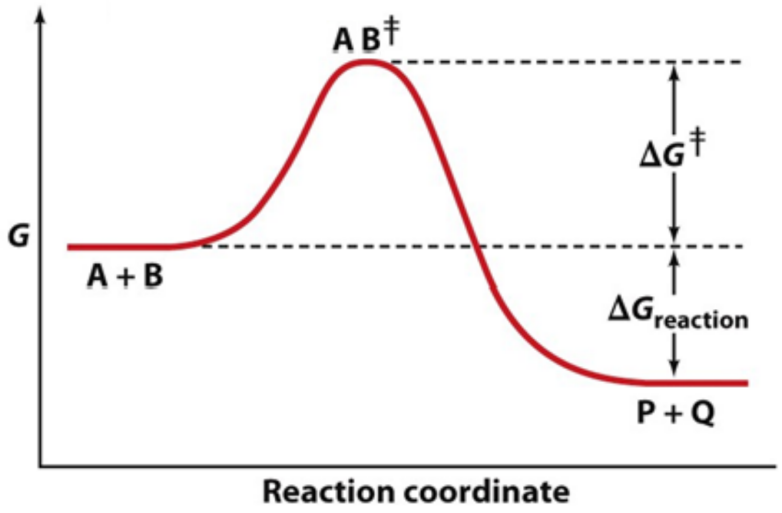

Figure 1.6: Reaction coordinate diagram as a function of Gibbs energy.

The change in Gibbs energy from the reactant to the activated complex is noted $\Delta G^{\ddagger}$, where Gibbs energy can be written as a function of enthalpy H, entropy S and temperature T.

$$dG = dH - TdS \tag{1.13}$$

Depending on the difference in enthalpy between the reactant and the product, the reaction will either be endothermic (ΔH>0) or exothermic (ΔH<0). In low-temperature environments, only exothermic processes are considered as there is no energy available to drive forward endothermic processes.

For an ideal gas, temperature can be seen as a measure of molecular agitation as speed and temperature are linked by the following equation

$$< v^2 >= \frac{3k_B T}{m} \tag{1.14}$$

where k_B is the Boltzmann's constant, equal to the ratio between the ideal gas constant (R), the Avogadro number (N_a) and m is the mass of the molecule. At a given temperature, each molecule in the gas phase does not have the same speed. The molecular speeds follow instead a Maxwell-Boltzmann distribution which defines the proportion of molecules that will have enough energy to overcome the barrier. As temperature rises, the distribution curve maximum gets shifted to higher speeds. This will also stretch the width of the curve, giving a broader speed distribution (figure 1.7). More molecules will have enough energy to overcome the reaction barrier and the rate increases.

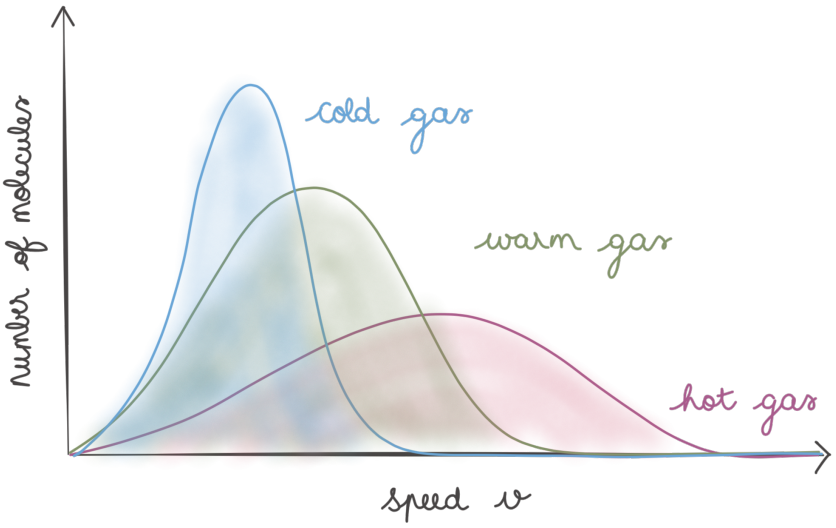

Figure 1.7: Scheme representing Maxwell-Boltzmann distribution of speeds for different temperatures.

At a certain temperature, the molecules will also have enough energy to cross the barrier in the other direction, an equilibrium is established between the reactant and the products. When a reaction can lead to different products, a competition between the various pathways takes place. Some products might be less stable but have a smaller barrier, named the kinetic product, as it can be formed faster. Some other products might be more stable but have a higher barrier, named the thermodynamic product. Depending on temperature, some paths will be more accessible than others and the efficiency of each path changes accordingly as the system tries to find the best compromise between stability and entropy.

To understand how some reactions can speed up at low temperatures, let us now consider the three general cases that can be encountered in exothermic reactions (figure 1.8). Throughout this discussion, the case (a) was presented, where a substantial potential energy barrier exists between the reactants and the products. This is the classic Arrhenius behaviour, where the rate rapidly drops as the temperature is lowered. A slight curvature is expected at the end as the pre-exponential factor is slightly temperature-dependent and because quantum tunnelling can lead the system to cross the barrier directly to products. The details behind the empirical Arrhenius model will be further discussed in section 1.2.2. When the two reactants are radicals, a different behaviour can be observed such as case (b). The unpaired electrons of each radical can be combined, forming a molecular bond. A lower energy intermediate complex is thus formed and no additional energy is needed to proceed to products. This type of reaction is often faster at low temperatures [Hickson and Bergeat, 2012]. A combination of these two behaviours gives the final case (c). The system can form an initial weakly bound complex which goes by a submerged barrier leading to the final products. At high-temperatures, a positive activation energy is observed, but as temperatures fall, the rate coefficient passes through a minimum before increasing again. It was shown experimentally and theoretically that at high temperatures, it is the submerged barrier that controls the reaction rate, while at low temperatures it is the initial "capture" with the formation of an initial complex that controls the rate. This explains the turnover in the rate coefficient as the rate-controlling step switches mecha-

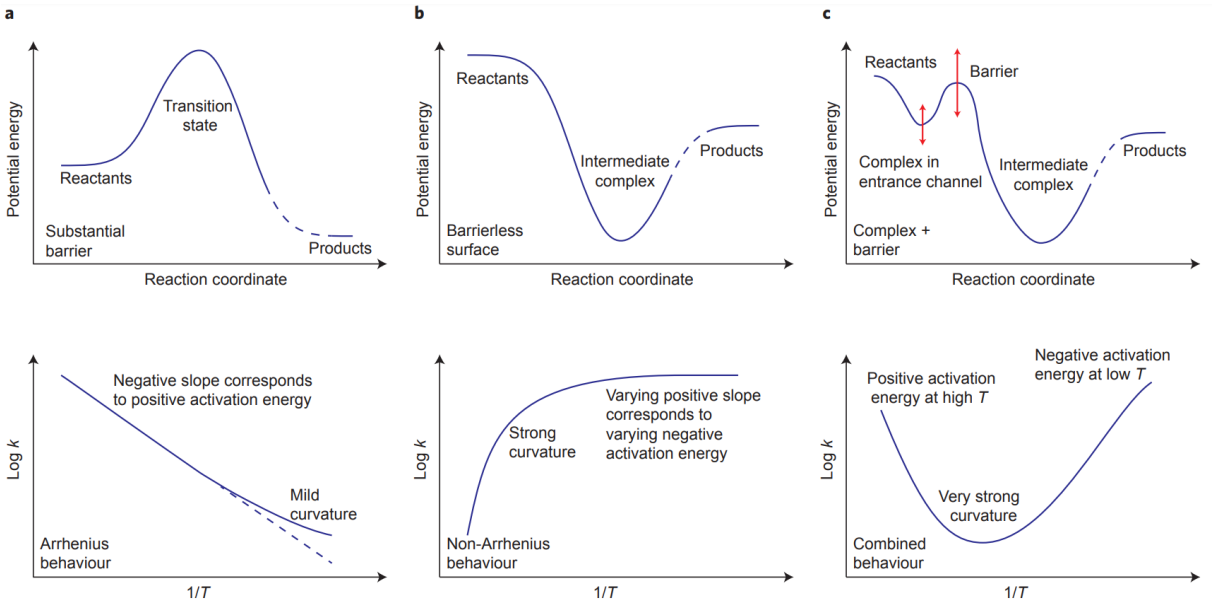

Figure 1.8: General cases for exothermic reactions. The upper panel shows a scheme of the potential energy of the system as the reaction takes place. The lower panel shows the corresponding log of the rate coefficient in the function of the inverse of temperature. From Sims [2013]

nisms [Gerlich and Rox, 1989, Olkhov and Smith, 2007]. Many radical-molecule reactions fall in this category [Heard, 2018, Smith, 2006]. The rate coefficient curvature depends strongly on the initial well depth and the barrier height. Therefore, some systems might not show a particular curvature but have a rather constant rate coefficient in the low-temperature range [Cooke et al., 2020, Messinger et al., 2020]. Depending on the reaction mechanism, quantum tunnelling could also affect the temperature dependence of the rate coefficient on top of the behaviour mentioned above.

The reaction mechanism plays therefore an important role in the rate coefficient temperature dependence. This highlights not only the necessity to characterise this dependency, with experimental measurements and theoretical calculations but also the importance of understanding the mechanism behind these processes.

Pressure dependence

Some reactions can show a pressure dependence on top of the temperature one. To achieve accurate rate predictions, they both need to be taken into account in the models. This type of reaction usually includes radical-radical recombination reactions, radical addition to multiple bonds, elimination, dissociation and isomerisation reactions. In these processes, a first step involves the formation of an excited molecule, which then is relaxed in a second step. This excess energy is removed with a collision in a bath gas to stabilise the final product. The model proposed by Lindemann and Hinshelwood allows to quantitatively describe this pressure dependency.

Consider the following reaction :

$$\mathrm{A + B} \underset{k_{-1}}{\overset{k_1}{\rightleftharpoons}} \mathrm{AB^*}$$

$$\mathrm{AB^* + M} \xrightarrow{k_2} \mathrm{AB + M}$$

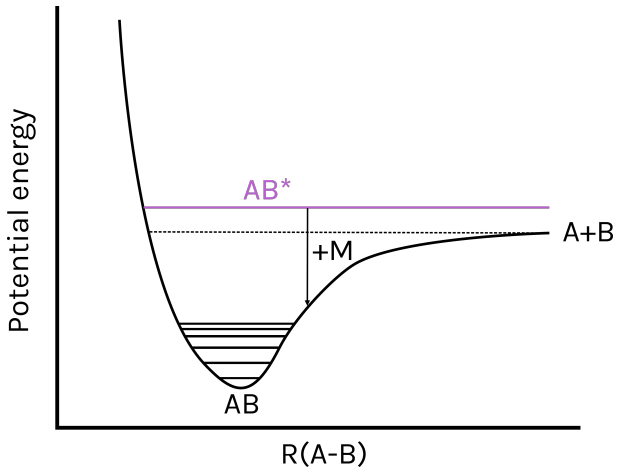

Figure 1.9: Potential energy as a function of AB radius to illustrate the stabilisation by collision with a third body.

The two reactants form an activated complex AB* which can either redissociate to A and B or stabilise via collisions with the buffer gas M (figure 1.9). The energy of the initial excited AB* is determined by two contributions, the energy released from the bond formation and the thermal energy content of both reactants.

After a short time, the formation and consumption of AB* will reach a steady state, thus its concentration can be considered constant. This assumption is named the steady-state approximation. Assuming that this time is short compared to the reaction time, the rate law for this reaction can be derived as :

$$\frac{d[AB]}{dt} = k_2[AB^*][M] = \frac{k_1 k_2 [A][B][M]}{k_2[M] + k_{-1}} \tag{1.15}$$

Two limiting cases arise from this equation:

(i) When [M] $\rightarrow$ 0, called the low-pressure limit. The stabilisation rate is much less than the dissociation one, $k_2[M] \ll k_{-1}$, the rate coefficient becomes:

$$\frac{d[AB]}{dt} = \frac{k_1 k_2 [A][B][M]}{k_{-1}} \tag{1.16}$$

The rate coefficient is directly proportional to the buffer gas concentration. A rise in pressure affects therefore drastically the rate.

(ii) When [M] $\rightarrow \infty$, called the high-pressure limit. As [M] is large, $k_2[M] \gg k_{-1}$, the concentration of M and k_2 can be cancelled out and the rate coefficient becomes:

$$\frac{d[AB]}{dt} = k_1[A][B] \tag{1.17}$$

A further increase in pressure will therefore have no impact on the rate of the overall reaction.

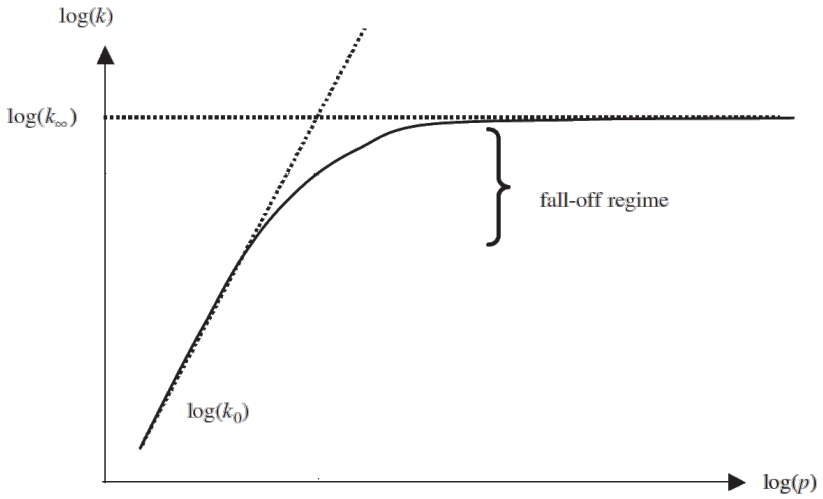

Figure 1.10: Pressure dependence schematic as described by Lindemann-Hinshelwood mechanism. Adapted from Carstensen and Dean [2007].

The transition between the two regimes is called the fall-off region (figure 1.10). As the rate for the individual steps are temperature dependent, the fall-off region location is also affected. Characterizing the pressure dependence of these types of processes is therefore essential to ensure accurate modelling, especially in these low-density media where the lower-pressure regime can have a drastic effect on the rate.

1.2.2 Theories of reaction kinetics

The determination of reaction rates is often complex, particularly under extreme conditions. In such cases, theoretical models are not only useful to understand the physical processes behind but also to predict the rates when no experimental values are available. Building a theoretical model implies a certain level of approximation and thus some limits arise in their application. Their knowledge is important to choose the appropriate theory depending on the application and level of precision required.

This section will go through the most common theories of reaction kinetics used to predict the reaction rate. Their basic principles and limitations will be presented to have a better understanding of the interplay between theory and experiments.

Arrhenius empirical equation

By far, the most well-known equation when it comes to kinetics is due to Arrhenius. At the end of the 19$^{\text{th}}$ century, based on his experiments and on Van't Hoff equation for the temperature dependence of reversible reactions, he proposed the following equation

$$k(T) = A \ \ exp(\frac{-E_a}{RT}) \tag{1.18}$$

where A is the pre-exponential factor, R the ideal gas constant, E_a the activation energy and T the temperature.

In this equation, the term E_a can be identified (approximately) with the barrier for the reaction to take place. Additionally, the pre-exponential factor takes into account the number of collisions with the proper orientation for the reaction to proceed. Usually, these factors are determined experimentally and used to extrapolate the rate coefficient to a broader temperature range. From this equation, reactions are supposed to slow down as the temperature is lowered. While this assumption agrees quite well with a large panel of reactions, some show discrepancies at low temperatures. In fact, the pre-exponential factor is also slightly temperature-dependent and gave rise to a modified version of the Arrhenius equation

$$k(T) = \alpha(\frac{T}{300})^{\beta} exp(\frac{-\gamma}{RT}) \tag{1.19}$$

Here the α, β and γ parameters can be adjusted to fit properly the experimental data.

Despite the empirical nature of the Arrhenius equation, it was found to be a useful representation for a wide range of reactions and temperatures. When it comes to lower temperature processes, it reaches however some limits. In particular, it doesn't take into account the pressure dependence of some processes and various quantum effects such as tunnelling or the molecular rotation that could affect the rate. The modified version can still be used as a tool to extrapolate $k(T)$, however, experimental measurements are needed.

Collision theory

The collision theory is the simplest approach to predict a reaction rate. It is based on the hard-sphere model of collisions. The reaction is considered to take place if, during a collision, the molecule has enough energy to overcome the barrier height. Molecules are considered as hard spheres, thus no other interaction effects are considered. The perpendicular distance between the two initial velocity vectors of each molecule is named the impact parameter b (figure 1.11) A collision occurs if the distance between two molecules, of radius r_1 and r_2, is equal or smaller than the sum of their two radii. Thus b_{max} can be defined as the maximum value of the impact parameter for a reaction to occur ($b_{max} = r_1 + r_2$).

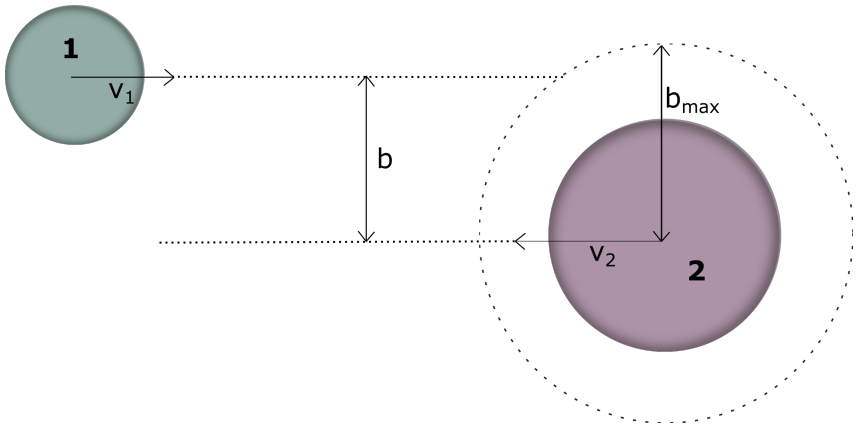

Figure 1.11: Hard sphere collision schematic for the collision theory.

As the molecules follow the Maxwell-Boltzmann distribution of speeds, the collision frequency (Z) can be derived as

$$Z = \pi b_{max}^2 n_1 n_2 \sqrt{\frac{8 k_B T}{\pi \mu}} \tag{1.20}$$

Where T is the temperature, k_B the Boltzmann constant, n is the number of density and $\mu = \frac{m_1 m_2}{m_1 + m_2}$ is the reduced mass.

From the energy distribution, the fraction of molecules with enough energy to go over the barrier can be defined as $exp(\frac{-E_a}{RT})$. Thus the rate coefficient can be expressed with

$$k(T) = \pi b_{max}^2 n_1 n_2 \sqrt{\frac{8 k_B T}{\pi \mu}} exp(\frac{-E_a}{RT}) \tag{1.21}$$

The pre-exponential factor is expressed here as the number of collisions between the two species. However, this simple model doesn't take into account the orientation of the reactant during the process, which impacts the outcome. A modified version of this equation takes this effect into account by multiplying the rate with an empirical steric factor ρ (<1).

Capture models

As explained above, the Arrhenius equation no longer holds true for various types of reactions, in particular for barrierless processes. It is the case of many ion-neutral reaction systems, where the process is in fact dominated by the long-range attractive forces generated by the ion. For these reactions, the rate is determined by the "capture" rate, when the two reactants form an intermediate. A major assumption of this theory is that the reactant has a zero probability of reverting back if the reactant has enough energy to go over the initial centrifugal barrier.

The capture theory was first developed by Langevin [1905]. Here the molecule is assumed to be spherical and the ion a point charge. The effective potential is expressed by :

$$V_{eff}(r) = -\frac{1}{2}\frac{\alpha q^4}{r^4} + \frac{L^2}{2\mu r^2} \tag{1.22}$$

Where q is the charge of the ion, α is the polarisability of the ion, r is the distance between the two species, L is the orbital angular momentum and μ is the reduced mass

It defines the energy needed to cross the centrifugal barrier and accounts for the long-range forces in the first term as well as the centrifugal forces in the second term. The distance between the ion and the molecule is defined by a parameter b. When it reaches a critical value b_{max} (equation 1.23), the molecule will spiral inward to collide with the ion. If the collision energy (E_{col}) is equal or bigger than the effective potential, the reaction can proceed, otherwise, the ion is rejected (figure 1.12).

$$b_{max} = (\frac{2\alpha q^2}{E_{col}})^{1/4} \tag{1.23}$$

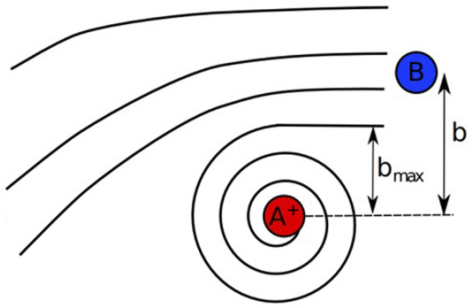

Figure 1.12: Scheme of the influence of the impact parameter b and the collision outcome. From Zhang and Willitsch [2017].

As every collision is assumed to be reactive, the rate coefficient can finally be expressed as equation 1.24. It can be noticed here that the Langevin rate coefficient is independent of molecular speed and therefore temperature.

$$k_L = 2\pi\sqrt{\frac{\alpha q^2}{\mu}} \tag{1.24}$$

This classical capture theory, however, does not take into account short-range interactions. Here only the likelihood of a reaction to form an initial complex is considered. Thus no information on the products can be inferred. Furthermore, since all collisions are considered reactive, the capture model can best be seen as an upper limit for the rate coefficient. Finally, since ions are treated as point dipoles or quadrupoles, the predictions are less accurate for large polyatomic molecules. Variations of the capture model take into account some quantum effects such as rotational states, Stark effect or quantum tunnelling and lead to more precise description of the reaction kinetics.

In the case of radical-neutral reactions, the simple Langevin theory fails to describe the kinetics, as the attractive forces are much smaller than for ions. Some semi-empirical methods were developed to compare with experimental measurements [Faure et al., 2009]. For these reactions, the isotopic dispersion contribution is considered dominant in the long-range interaction. In particular, the electrostatic potential, like the dipole-dipole, becomes dominant as demonstrated by Stoecklin et al. [1991]. This gives a new expression for the capture rate constant where the dispersion coefficient is determined with the London formula.

$$k(T) = 2\sqrt{\frac{2\pi}{\mu}}\Gamma(\frac{2}{3})(2C_6)^{1/3}(k_B T)^{1/6} \tag{1.25}$$

$$C_6^{London} = \frac{2}{3}\frac{I_1 I_2}{I_1 + I_2}\alpha_1\alpha_2 \tag{1.26}$$

Where k_B is the Boltzmann constant, $\Gamma(x)$ the gamma function, I is the ionisation potential and α the polarisability of the reactants. C_6^{London} usually underestimates the dispersion, thus C_6 in equation 1.25 is taken as twice C_6^{London}.

To apply this semi-empirical method, the system needs first to be chosen according to two criteria proposed by Smith et al. [2006]: (i) the room temperature rate coefficient (experimental or theoretical) needs to be at least of the order of magnitude 10^{-11} cm^3 s^{-1} and (ii) the difference between the ionization energies of the molecular reagent and the electron affinity of the radical needs to be greater than 8.5 eV. Then the capture rate equation can be used to calculate couple rate coefficients at low temperatures. These values and the measured room temperature rate coefficient can finally interpolated using the modified Arrhenius equation to give a model of the temperature dependence for the reaction.

Transition state theory

Various important concepts of transition state theory (TST) were introduced in the temperature dependence section. The development of TST combines the various approaches described throughout this section. It includes aspects of thermodynamics, collision theory and statistical mechanics. Some later versions also include quantum mechanics.

While TST builds on the principles of collision theory, it provides a more refined view by considering the transition state as the critical configuration for reaction. In particular, the calculation of the rate is linked with the potential energy surface (PES). The PES describes the

potential energy evolution of a system in function of the reactant coordinates. The reactants and products are located in a valley and the transition state, or activated complex, is a saddle point, linking these two valleys. The reaction is considered to proceed in two steps (see figure 1.6). Consider the following reaction

$$\text{A + B} \quad \underset{k_{-1}}{\overset{k_1}{\rightleftharpoons}} \quad \text{AB}^{\ddagger} \quad \xrightarrow{k_2} \quad \text{products}$$

The transition state (TS) is considered to be in a dynamic equilibrium with the reactants. Its thermodynamic properties can be derived using this equilibrium constant and statistical mechanics. In particular, the partition function gives the expected number of occupied microstates under given thermodynamic conditions and thus can be used to determine various thermodynamic properties of the transition state. The equilibrium constant for the reaction is expressed by

$$K = \frac{Q_{TS}}{Q_{reactants}} exp(-\frac{E_a}{RT}) \tag{1.27}$$

where E_a is the activation energy, R the ideal gas constant, T the temperature and Q_{TS} and $Q_{reactants}$ are the partition functions of the transition state and the reactants, respectively. The rate can finally be derived as

$$k = \frac{k_B T}{h} \frac{Q_{TS}}{Q_{reactants}} exp(-\frac{E_a}{RT}) \tag{1.28}$$

where k_B is the Boltzmann constant and h the Planck's constant.

While providing a better view of the link between the rate and the reaction mechanism, the TST has various limitations. In particular, it assumes that reactions are reversible on a microscopic level, meaning that the transition state can revert back to reactants with the same probability as it proceeds to products. This main assumption is also a fundamental flaw in this theory. In reality, the molecule might cross and turn around multiple times on the surface before reacting. In the case of multistep reaction, the theory fails also as it assumes that each intermediate is long-lived enough to apply the Boltzmann distribution of energies. Problems also appear in the case of extreme temperatures. At high temperatures, higher vibrational energy modes will be populated, the molecular motion becomes so complex that the collision may lead to a transition state far away from the low energy one considered in the PES. At low temperatures, the possibility of quantum tunnelling can become important which is not taken into account with this classical view. Different variants of the TST have been developed to address these flaws such as the microcanonical TST or Rice–Ramsperger–Kassel–Marcus (RRKM) theory.

1.2.3 Kinetics parameters determination

The various theories described in the previous section provide a good starting point to understand and predict the reaction rate. However, none of them is perfect. They all show limits when the system complexity increases and in extreme temperature conditions. This highlights the interplay between theory and experiments. On the one hand, theory needs experiments to refine the rate model and provide more accurate predictions. On the other hand, experiments need theory to target the most interesting system and understand the processes behind. Together they help us to unravel the fundamental principles behind the reaction kinetics and dynamics.

The following section reviews various molecular detection methods that can be used to measure low temperature rate coefficient and branching ratios. Then, the typical theoretical method used for kinetics parameters determination of neutral-neutral reaction is presented.

Experimental methods

The measurement of kinetics parameters requires following the time evolution of the concentration of one or more species. The detection technique in use needs thus to be sensitive and specific enough to distinguish the different molecules. In the case of branching ratio measurements, it requires either an absolute concentration measurement or a simultaneous detection which complicates even more the task. Various methods can be used for that purpose and all show different strengths and shortcomings. In this section, a brief outline of the frequently used techniques to determine rate coefficients and branching ratios at low temperatures will be provided to give a general perspective of the subject.

Laser-induced fluorescence (LIF) is commonly used for that purpose. The fluorescence measurement allows us to follow the evolution of a targeted species over time. In the case of reaction involving radical, a pump-probe variation is used. A first laser will generate the radical by laser photolysis of a suitable precursor and then a second will be used to probe the radical fluorescence signal. The delay between the lasers can be adjusted to increase the reaction time. This technique has the advantage of being very sensitive but does not provide an absolute concentration value. It is thus widely used for rate coefficient measurement but requires a calibration reaction for branching ratios [Gannon et al., 2007, West et al., 2019].

Another widely used technique is mass-spectrometry. Coupled with tunable vacuum ultraviolet synchrotron radiation, it becomes a powerful tool to distinguish different species using photoionisation. This technique is highly sensitive, however, the photoionisation spectrum can sometimes be difficult to measure or interpret in the case of isomers. Various groups have used this technique for branching ratio measurements at room temperature and demonstrated its capabilities [Bouwman et al., 2013, Trevitt et al., 2011]. Mass-spectrometry can also be used without synchrotron radiation in the case of products with different masses. In particular, it has been coupled with CRESU flows for branching ratio measurements of ion-neutral reactions at low temperatures [Bourgalais et al., 2016a, Joalland et al., 2019].

Cavity Ring-Down Spectroscopy (CRDS) is also an interesting technique for kinetics measurements. A ring-down time is measured in an optical cavity with and without the molecule of

interest. By comparing these two timings, the absolute concentration of the species can be derived. The high sensitivity due to the cavity and the absolute concentration measure makes it a promising tool for branching ratio measurements. In particular, this technique has been coupled to CRESU flow by Suas-David et al. [2019]. This setup was recently used to measure the low temperature rate coefficient of the reaction between vibrationally excited CN radical and butadiene [Thawoos et al., 2023]. Even if this technique is not coupled to a broadband source, the absolute concentration measurement can still be exploited for branching ratio measurements. The light source used in the cavity is usually in the infrared range, thus it might not be able to distinguish all isomers such as conformers.

Frequency combs have also been developed recently for chemical kinetics measurements. These ultra-fast lasers produce simultaneously various wavelengths all locked in phase. It offers a coherent broadband light source which can be used as a high-sensitivity detection technique when coupled with a cavity. Various groups have already demonstrated its good capabilities at room temperature [Bjork et al., 2016, Roberts et al., 2020]. These kinds of lasers are typically available in the IR range and thus present the same drawback mentioned earlier for isomer differentiation. Its broadband characteristics make it however a promising tool for branching ratio measurement at low temperatures.

Finally, the recently developed Chirped Pulse Fourier Transform millimeter Wave spectroscopy technique (CP-FTmmW) have been showing interesting aspects for branching ratio measurements at low temperature. This rotational spectroscopy technique has the advantage of being highly specific. As long as molecules have a permanent dipole moment, they possess a distinct rotational signature, even isomers and conformers. This technique was first coupled with CRESU flows by Arthur Suits, Robert Field and Ian Sims [Abeysekera et al., 2014, Oldham et al., 2014]. The CPUF (Chirped-Pulse in Uniform Flow) setup already showed interesting results for rate coefficient and branching ratio measurements [Abeysekera et al., 2015, Dias et al., 2018, Gurusinghe et al., 2022b]. In this technique, the main challenge is the pressure broadening of the line induced by the high-collisional environment of CRESU flows. This point was addressed by decoupling the reaction and probing region using airfoils or skimmers [Abdelkader Khedaoui, 2022, Gurusinghe et al., 2022a, Soorkia et al., 2011]. Increasing the sensitivity of the technique remains however the main challenge for this experimental method. The different aspects behind the development and application of the CPUF technique will be discussed in detail throughout this manuscript.

Theoretical methods

The standard kinetics theories were outlined in section 1.2.2. The conversation revolved around their fundamental principles, mainly from a classical mechanics standpoint. This initial approach is suitable for small systems and at room temperature, but as the size of the molecules increases or under extreme conditions, the mechanism becomes more complex and these simple models break down. The small scale of molecules requires a quantum mechanical approach to take into account other effects that will impact the reaction mechanism. This section will provide a brief introduction to the theoretical methods based on transition state theory that are used to calculate rate coefficients and branching ratios. It is the most common method for kinetics studies of neutral-neutral reactions.

The TST approach starts with the calculation of the potential energy surface (PES). It describes the evolution of the potential energy of a molecule as a function of certain geometrical parameters, in general, the position of atoms. In the case of a reaction, the PES comprises all the different configurations that the two reactants can have during the chemical process, constituting a general "landscape." The PES is utilised to locate the minimum energy geometries that will be involved in the reaction pathways. These stationary points are defined by

$$\frac{\partial E}{\partial r} = 0 \tag{1.29}$$

Where E is the energy and r the geometric parameter. They include minima, maxima, first-order saddle points (transition state) and higher-order saddle points (figure 1.13). This allows to determine the minimum-energy reaction pathway of the reaction which will be used in the next steps.

The potential energy values are calculated using quantum mechanics. As the Schrödinger equation is only solvable for small molecules, some ab initio computational methods are needed for bigger systems. These methods will introduce a certain level of approximations to the fundamental principle of quantum chemistry to derive the Hamiltonian (energy operator). The method used is referred to as the level of theory. It includes various semi-empirical methods, Density Functional Theory (DFT) or post-Hartree Fock methods. For each method, a basis set is necessary as well. This is a set of mathematical functions used to build the wavefunction of the system. The basis set will specify the region of space where each electron is restricted and will impact the accuracy of the results. Both the level of theory and the basis set need to be chosen carefully as they will impact the result accuracy and the computational time of the calculation. These calculations can be performed with various software packages such as Gaussian [**?**] or MOLPRO [Werner et al., 2012].

After constructing the PES, the kinetics parameters can be calculated using the transition state theory, its general principles were presented in section 1.2.2. Multiple variations of this theory exist and rely on different approaches to treat the energy exchange of the system during the chemical reaction.

The canonical approach considers the system in contact with a bath gas at a constant temperature. Thus the system is assumed to follow a Maxwell-Boltzmann distribution. It considers that the activated complex is in equilibrium with the reactant, therefore the steady state ap-

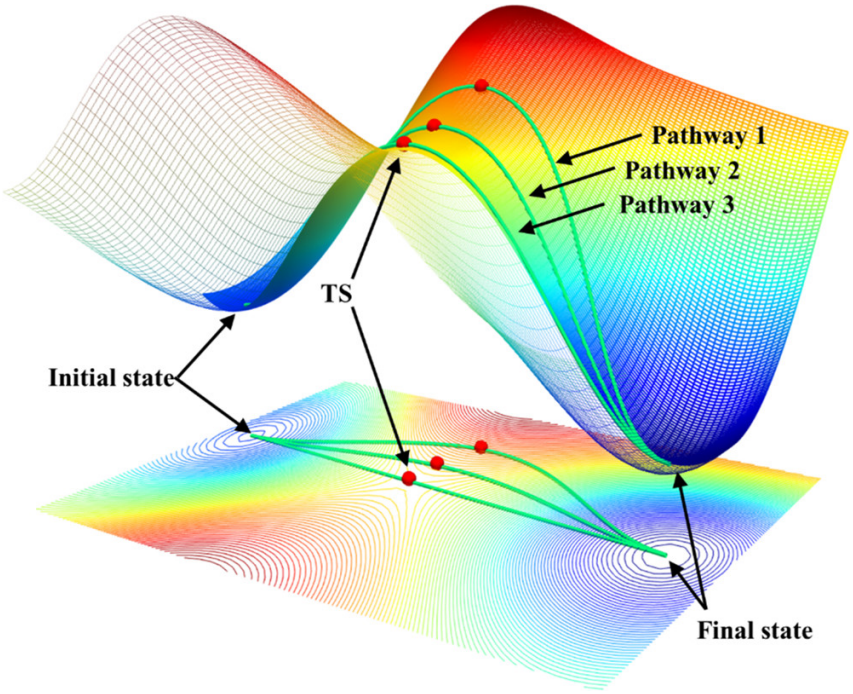

Figure 1.13: Illustration of a PES connecting an initial state and a final state via different pathways. The minima are the initial and final state and the saddle point are the transition states. From Liu et al. [2022].

proximation applies. This approach of the TST works well for systems for which the relaxation time is faster than the reaction time. These types of reactions usually have a single well.

For multi-well reactions, the relaxation time of the transition state can be of the same order as the reaction time, the steady-state approximation thus no longer holds true and a competition between the two needs to be considered. A first way to deal with this is the microcanonical approach. Here the system is considered isolated thus the energy is conserved during the reaction process. The reaction rates are calculated by considering the density of states and energy distribution of the reactant, transition state and the products. A second way is to use the RRKM theory which also accounts for the density of states and energy transfer but was specifically designed for unimolecular reactions and assumes a statistical distribution of energy. In these two approaches, the master equation can be used to describe the transition probability between different states. This mathematical framework is well-suited to describe the stochastic (random probability distribution) behaviour as the energy distribution no longer follows a Maxwell-Boltzmann distribution.

For this work, the MESMER (Master Equation Solver for Multi-Energy Well Reactions) [Glowacki et al., 2012] software was used to calculate the branching ratios of the CN radical and propene reaction (chapter 3). Here the competition between the relaxation and the reaction is treated with a stochastic energy grained master equation (EGME) using the microcanonical TST and collisional energy transfer model.

1.2.4 Astrochemical models

Throughout this introductory chapter, the basics of chemistry in astrophysical environments and the fundamental questions surrounding current observations have been discussed. The models of these environments are important for understanding and predicting their chemical evolution. To build them, the physical conditions, observed molecules and available experimental data are examined to choose the reactions considered in the model. Then the time dependence of molecular abundances and column densities can be calculated by integrating a system of coupled, nonlinear differential rate law equations. An example of model output is shown in figure 1.14. Here, the observed abundance of propargyl (dotted horizontal line) is plotted with the calculated abundance using two models.

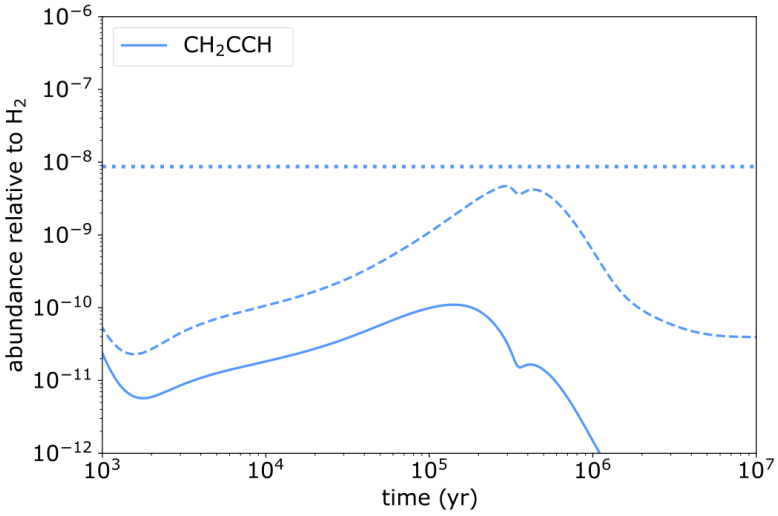

Figure 1.14: Fractional abundances of propargyl (CH_2CCH) as a function of time calculated with gas-phase chemical network RATE12 from the UMIST database and adaptation from the authors (see article). The dashed line corresponds to the calculated abundance of CH_2CCH when the reactions of this radical with O and N atoms were removed. Abundances observed in TMC-1 are indicated by dotted horizontal lines. Adapted from Agúndez et al. [2021].

Achieving accurate models requires the collaborative work of observation, theory and experiment. Observational data allow to derive the abundance of the molecules and help to constrain models as well as target potential missing reactions. Experiments are necessary to provide input data for the model and molecular spectrum for the detection of new molecules. The theory provides a framework for understanding and predicting the processes and evolution in a chemical network. Various quantum tools can be used to calculate data, either to provide a starting point to target the systems that might be of interest or too difficult to measure experimentally at that time. These models and calculations can be refined with experimental data.

The accuracy of a model is influenced by three main factors. Firstly, there is the uncertainty from the reactions which are not taken into account because of the lack of data or ignorance. They lead to systematic errors and are complicated to assess due to their inherent nature. Secondly, uncertainties arise from the kinetics data at low temperatures, which mainly come from the methods employed but are more easily identifiable and quantifiable. Finally, uncertainty

remains regarding data extrapolated to lower temperatures. The estimation of associated uncertainty is rather complex. Hébrard et al. [2006] proposed a method for this purpose, but it does not replace direct measurement under relevant temperature and pressure conditions.

Overall to reduce efficiently the uncertainty in models, what matters is to determine the critical reactions that will influence most the abundance of molecules. Key reactions can be identified by performing a sensitivity analysis where the rates are randomly varied within their uncertainty limits and calculating the associated time-dependent abundance and column densities [Dobrijevic et al., 2003, Lebonnois, 2005, Vasyunin et al., 2008]. Working on the identification of missing reactions is also essential but more difficult to perform. The detection of new molecules or experimental and theoretical data could help to that extent but is of course limited.

The lack of experimental data at low temperatures is due to the many challenges encountered in the field. These types of measurements require following the time evolution of the concentration of one or more species. It implies avoiding cross-reactions which could perturbate the measurement or condensation due to low temperatures. The detection techniques need to be highly sensitive and for branching ratio measurement, they need also to be multiplex or provide absolute concentration measurement. Finally, producing the reactant of interest is not necessarily an easy task. Many molecules in space have quite exotic structures and are unstable, making them difficult to produce in the laboratory. All these different aspects contribute to fixing constraints in experiments and necessitate finding the right compromise to characterise experimentally each new reactive system.

1.3 Outline of the thesis

The aim of this thesis is to provide rate coefficients and branching ratios at low temperatures for reactions relevant to various astrophysical media such as dark clouds, planetary and cometary atmospheres.

Chapter 2 introduces the experimental method used for this work along with the associated challenges that it poses. The CRESU technique, used to reach low temperatures, is discussed and compared to other experimental cooling techniques. Then the chirped-pulse spectroscopy technique for molecular detection is presented along with the experimental adjustments needed to be coupled with CRESU flows.

Chapter 3 presents the experimental results of the branching ratio measurement of the CN and propene reaction at low temperatures. Then Chapter 4 presents the rate coefficient measurement of the hetero-complexation process between formic acid and CO_2.

Finally, Chapter 5 summarises the conclusions and future perspectives for this experimental setup.

Chapter 2

Experimental methodology

Il ne suffit pas de dire: je me suis trompé;
il faut dire comment on s'est trompé

– Claude Bernard

2.1 Introduction

Conducting experimental measurements under extreme conditions relevant to astrophysical media poses a significant technical challenge. Replicating the low temperature and low density conditions of dark clouds for instance would not be viable in the laboratory as too few collisions happen at the human time scale. As discussed in chapter 1 section 1.2, kinetic parameters are temperature and sometimes pressure-dependent. Therefore, exact replication of the environmental conditions becomes unnecessary as long as these parameters can be accurately measured. In the context of this work, several criteria must be considered when selecting the experimental method. First and foremost, a suitable uniform medium is essential for the reaction to occur. Additionally, care must be taken to avoid the formation of clusters or condensation as the temperature is lowered. Lastly, a highly sensitive detection method is required to monitor the various reactants and products over time. Meeting these criteria demands not only the identification of appropriate experimental methods but also the ability to strike the right compromise between them.

This chapter will discuss in detail the methods chosen to perform low temperature kinetic measurements. The first part describes the CRESU technique, used to reach low temperatures. It explores the characteristics of this technique and compares it with other cooling methods. The second part describes in detail the introduction of reactants in this setup and underlines the associated limitations. Lastly, the chapter outlines the spectroscopic technique used for this thesis, the chirped pulse microwave spectroscopy for branching ratio and rate coefficient measurement.

2.2 CRESU flows

CRESU is a French acronym which stands for "Reaction Kinetics in Uniform Supersonic Flow". The idea is to generate a supersonic gas expansion by using Laval nozzles. It provides a uniform medium with well-defined temperature and density conditions, making it an ideal environment for reaction kinetics measurement. Laval nozzles were invented by Gustaf Laval in 1888 and found application in rocket motors. A century later, they were first applied to ion-molecule reaction kinetics measurement by Rowe et al. [1984], marking a new era in low-temperature kinetics studies.

2.2.1 Flow characteristics

CRESU flow are generated by an isentropic expansion through a Laval nozzle with a specific convergent-divergent design. The gas goes from a high-pressure region (typically tens to hundreds of millibars) to a lower-pressure region (less than a millibar) through the nozzle (figure 2.1). The gas in the reservoir is considered static as its volume is large compared with the internal volume of the nozzle. In the convergent part, as the cross-section gets smaller, the gas accelerates from zero to a Mach number (M) of one at the throat. The Mach number is defined as the ratio between the velocity of the flow and the speed of the sound in the propagating medium. When the flow reaches this particular condition at the throat, it can further expand in the divergent part and reach a higher Mach number. If the pressure in the lower pressure region is the same as the pressure at the exit of the nozzle, the right conditions are met to have a collimated flow with well-defined temperature and density conditions.

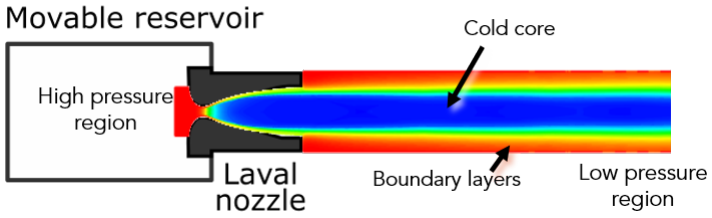

Figure 2.1: Scheme of the expansion from a reservoir in a vacuum chamber through a Laval nozzle with a 2D simulated temperature map. From Gupta [2021]

The flow is described using a variation of Bernoulli's equation 2.1. It relates the reservoir conditions, where the gas is considered static, to any point in the expansion. The effect of gravity can be neglected as the nozzle size is small.

$$C_P T_{flow} + \frac{v_{flow}^2}{2} = C_P T_0 \tag{2.1}$$

where C_P is the heat capacity at constant pressure, v the fluid velocity and T the temperature of the fluid. The index "0" refers to any point from the reservoir and the index "$flow$" to any point in the expansion.

For an ideal gas, since the expansion is isentropic (reversible and adiabatic), equation 2.2 can be applied in the nozzle.

$$PV^{\gamma} = constant \tag{2.2}$$

where P is the pressure in the flow, V the occupied volume and γ the ratio of heat capacity at constant volume ($\gamma = \frac{C_P}{C_V}$). C_V is the specific heat capacity at constant volume.

Equation 2.3 can be used to calculate the flow speed.

$$v_{flow} = \sqrt{\frac{\gamma RT}{M_m}} \tag{2.3}$$

where $R = C_P - C_V$, and M_m is the molar mass of the gas.

The temperature of the flow can finally be derived by replacing equation 2.3 in equation 2.1.

$$T_{flow} = T_0(1 + \frac{\gamma - 1}{2}M^2)^{-1} \tag{2.4}$$

For real flows, the fluid viscosity is never zero and a small heat exchange occurs with the outer layers. The process is therefore not strictly adiabatic and gives rise to boundary layers of thickness δ (figure 2.2).

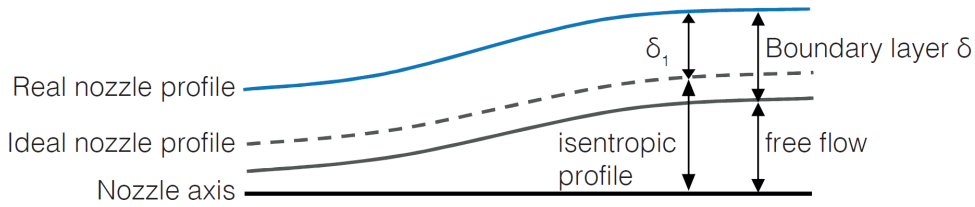

Figure 2.2: Isentropic flow and boundary layers arising from the real nozzle profile. From Fournier et al. [2017]

The flow conditions can be tweaked by modifying the buffer gas and the nozzle geometry. This will change the final temperature and density, as well as the flow length and the boundary layer thickness. The accessible conditions remain however constrained by the pumping capacity of the experimental set-up. In Rennes, this technique allows to have supersonic flow temperatures from around 10 to 220 K and densities around 10^{16} to 10^{18} cm^{-3}, without initial pre-cooling. The common buffer gases used for designing a nozzle are helium, argon, nitrogen and hydrogen. When used for kinetics measurement purposes, the reactants are introduced in less than 1% of the total flow to ensure the designed hydrodynamic conditions. Depending on the specificities of the target system, the nozzle will be chosen, with attention to eventual cluster formation, relaxation efficiency and expected speed of the reaction.

2.2.2 Nozzle design and characterisation

The nozzle profiles are computed using a program developed in Turbo Basic by Marquette [1988]. The profile is numerically tested with computational fluid dynamics calculation using Ansys Fluent software. After profile confirmation, the nozzle can be machined either in the university workshop, using stainless steel, or 3D printed using the Form 2 printer (Formlabs) with a light-activated resin (usually GreyPro). The machining process is quite delicate as any significant imperfection in the nozzle profile can alter the supersonic flow. In particular, the convergent region is critical for reaching a Mach number of one at the throat. Without this condition, the supersonic expansion cannot take place. Moreover, defects in the divergent part may cause a detachment of the boundary layers, affecting the flow collimation. The final nozzle needs therefore to be experimentally tested using a Pitot probe to record the final flow conditions.

The Pitot probe is placed in parallel to the CRESU flow propagation. As the supersonic flow enters in contact with the tip of the static probe, a shock wave is created. As the impact pressure (P_i) is related to the reservoir pressure (P_0) with equation 2.5, the Mach number (M) can be determined. The latter can be used to calculate the corresponding pressure (P), temperature (T) and density (n) in the isentropic core (equations 2.6, 2.7 and 2.8).

$$P_i = P_0(\frac{\gamma+1}{2})^{\frac{\gamma+1}{\gamma-1}} M^{\frac{2\gamma}{\gamma-1}} (\gamma M - \frac{\gamma-1}{2})^{\frac{1}{1-\gamma}} \tag{2.5}$$

$$\frac{P_0}{P} = \frac{T_0}{T}^{\frac{\gamma}{\gamma-1}} \tag{2.6}$$

$$\frac{T_0}{T} = 1 + \frac{\gamma-1}{2} M^2 \tag{2.7}$$

$$\frac{n_0}{n} = \frac{T_0}{T}^{\frac{1}{\gamma-1}} \tag{2.8}$$

where T_0 is the reservoir temperature and n_0 the reservoir number density.

The Pitot probe used here is a 10cm long hollow tube with 1/8 inch diameter. The tube is connected to a Brooks capacitance manometer (10-100 mbar) for impact pressure measurement. The set-up is mounted on a motorised platform allowing spatial characterisation in two directions (figure 2.3). The Pitot probe is aligned along the flow axis using a HeNe laser (Thorlabs).

A LabVIEW program is used to record the impact, chamber and reservoir pressure at various positions. The temperature, density and pressure in the flow are then calculated using equations 2.6 2.7 and 2.8 as mentioned previously. These equations only apply to the isentropic flow, thus all values for the boundary layers on the 2D Pitot map are not physically correct. Typically, the step size is 0.5 cm along the flow axis and 0.1 cm lateral to the flow axis. The 2D Pitot map is then interpolated using the IgorPro software. Figure 2.4 shows an example of 1D and 2D characterisation maps for an argon Laval nozzle. The 1D profiles are used to determine

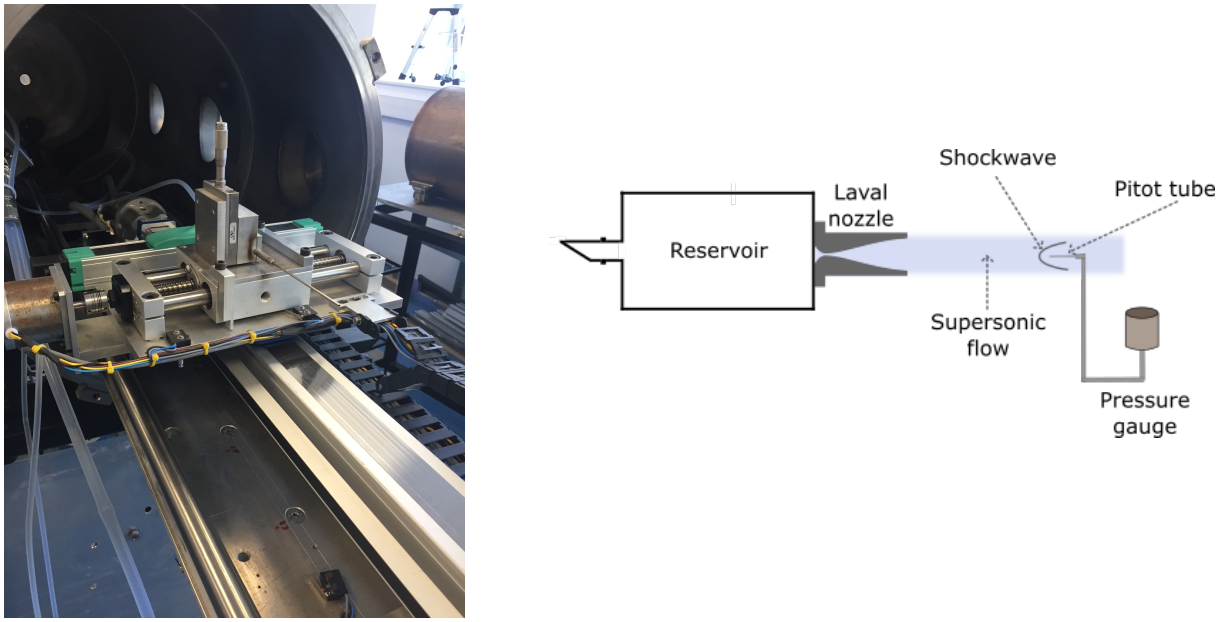

Figure 2.3: Pitot measurement setup for Laval nozzle characterisation. Left hand side, picture of the setup, front view, installed in CRESU-LIF chamber. Right hand side, schematic of the pitot measurement setup in CRESU flow.

the average temperature, density and uniform flow length. The velocity can be derived from the measured Mach number and used to calculate the total accessible hydrodynamic time. The hydrodynamic time corresponds here to the time needed for the gas to go from the end of the nozzle to a given position in the flow. Thus the total hydrodynamic time for a nozzle is defined as the time until the flow is no longer uniform. This information is essential for choosing the right nozzle when studying time-dependent processes. The 2D profiles are used to determine both the isentropic core size and uniformity deviation along the flow.

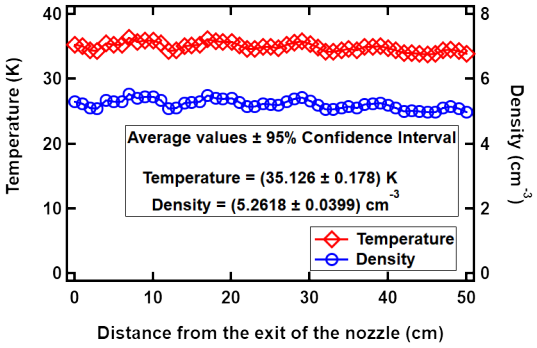

(a) 1D temperature and density measurement along the flow axis using a Pitot probe

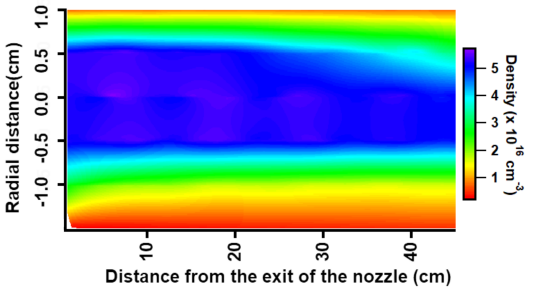

(b) 2D density measurement along and lateral to the flow axis using a Pitot probe

Figure 2.4: Pitot characterisation of an argon Laval nozzle with an average temperature of 35 K. Reservoir pressure = 52.7 mbar and chamber pressure = 0.28 mbar

After machining, the new nozzles are first characterised using their theoretical conditions. The reservoir and chamber pressures can then be adjusted to fine-tune the flow conditions keeping in mind that the ratio between the stagnation pressure and the chamber pressure ($\frac{P_{ch}}{P_{res}}$) needs to reach a critical value to ensure a Mach number of one at the nozzle throat to have a proper expansion. Then, the flow uniformity is influenced by the difference between the chamber and the nozzle exit pressures. Three cases can be encountered (figure 2.5):

(a) Underexpanded flow: the chamber pressure is lower than nozzle exit pressure.
(b) Overexpanded flow: the chamber pressure is higher than than nozzle exit pressure. The flow is compressed inwards, creating oblique shockwaves. The flow can reexpand under the low-pressure conditions of the chamber and collapse again. This process can happen several times until the flow fades away, giving this characteristic shock diamond shape.
(c) Ideal flow: The two pressures are equal. The flow can maintain its uniformity for several tens of centimeters.

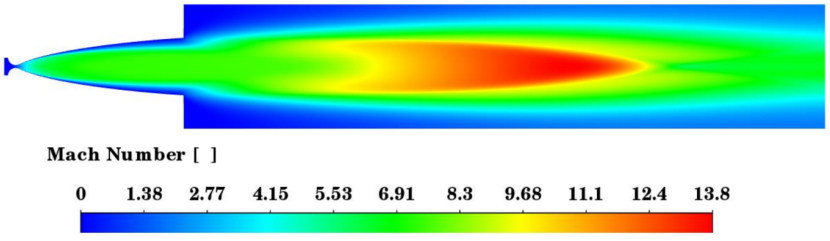

(a) Underexpanded flow profile

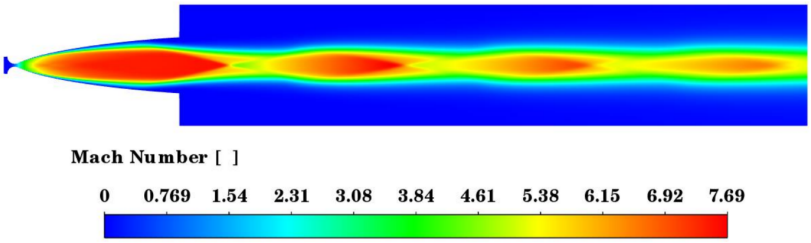

(b) overexpanded flow profile

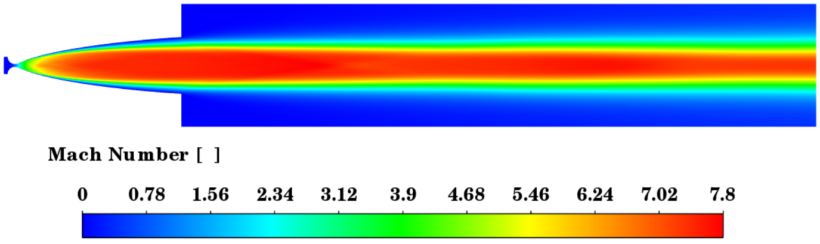

(c) Ideal flow profile

Figure 2.5: 2D Mach number profile simulation of a nitrogen nozzle with 770 mbar in reservoir and 0.05 mbar in the chamber. Computed using Ansys fluent software. From Abdelkader Khedaoui [2022]

2.2.3 Comparison with other cooling techniques

Various experimental techniques have been used in the literature to reach low temperatures. Each displays its own advantages and drawbacks, making them more or less suited for certain applications.

In particular, kinetics measurements require following the time evolution of the concentration with accuracy. As the temperature is lowered, molecules can form clusters or stick to a surface much more easily, impacting the reliability of molecular concentrations. Techniques such as cryogenic cooling, where species are cooled by collision with the walls of a reactor are very sensitive to this experimental issue. It requires working with pressure below the vapour pressure of the different species (at the temperature of the wall) in order to avoid any condensation of adsorption on the walls. The accessible temperature range for this technique therefore varies with the targeted species.

Kinetics measurements also require a uniform media for the reaction to take place. In the case of free jet expansions, low temperature can be reached via a gas expansion through a pinhole or a slit. This creates a low temperature and density region, called the zone of silence, followed by a shock wave, named the Mach disk. This technique presents however a large velocity distribution and a strong gradient of density and temperature along the main axis. This can be improved by adding a skimmer in the zone of silence to generate a molecular beam. Followed by a collimator it can help to narrow the velocity distribution. This version is particularly often used for crossed-beam experiments. Nevertheless, these types of expansions have low densities and therefore require a very sensitive spectroscopy technique.

The CRESU technique has the particularity to generate a uniform wall-less cooled environment, limiting considerably condensation issues. The flow isentropic core offers a media with uniform temperature, density and velocity distribution conditions. The frequent collisions inside the flow ensure local thermodynamic equilibrium (LTE) conditions. All these characteristics make CRESU flows an ideal environment to measure absolute rate coefficients and collisional energy transfer processes. For the flow to sustain itself and LTE conditions to be reached, it requires however enough collisions. This factor together with the pumping capacity of the experimental setup, constrains the accessible pressure conditions. Therefore, it can be difficult to determine the fall-off region (see section 1.2) for pressure-dependent processes. The size of the isentropic core could also matter depending on the reaction of interest and the sensitivity of the detection technique. Studies involving lasers for instance can benefit greatly from having a bigger interaction region with the flow. The size of the core is mainly influenced by the size of the nozzle and will scale up the gas quantities needed. This last point can be addressed with the development of a pulsed CRESU flow and will be discussed in more detail in chapter 5.

Each cooling technique has its own set of strengths and shortcomings, making them all complementary in a sense. With the CRESU technique, the absolute density in the flow is known. This method allows therefore to measure absolute rate coefficients which do not require relative scaling or normalization. The absolute density is more complicated to measure with other cooling techniques such as cryogenic cooling or crossed-beam, thus the rate coefficient will be expressed in different units or relative scales (e.g., normalized by the collision frequency). The study of each new system requires therefore finding the best compromise between the flow

conditions, the detection technique used and measurement objectives.

2.3 CRESU chambers

This section will present the chamber used for this experimental work (figure 2.6). The CRESU-Chirp chamber is coupled to a home-built microwave spectrometer which will be covered in more detail in section 2.4. This chamber is connected with a 4-way cross to the pumping group and the CRESU-LIF chamber. This second chamber is coupled with a photo-multiplier tube for pulsed-laser photolysis laser-induced fluorescence (PLP-LIF) experiments. The pumping group includes a primary and 4 roots blower pumps connected in series, allowing a total pumping capacity of 30,000 m^3hr^{-1}. The pumping capacity can be adjusted using a butterfly valve depending on the nozzle conditions in use.

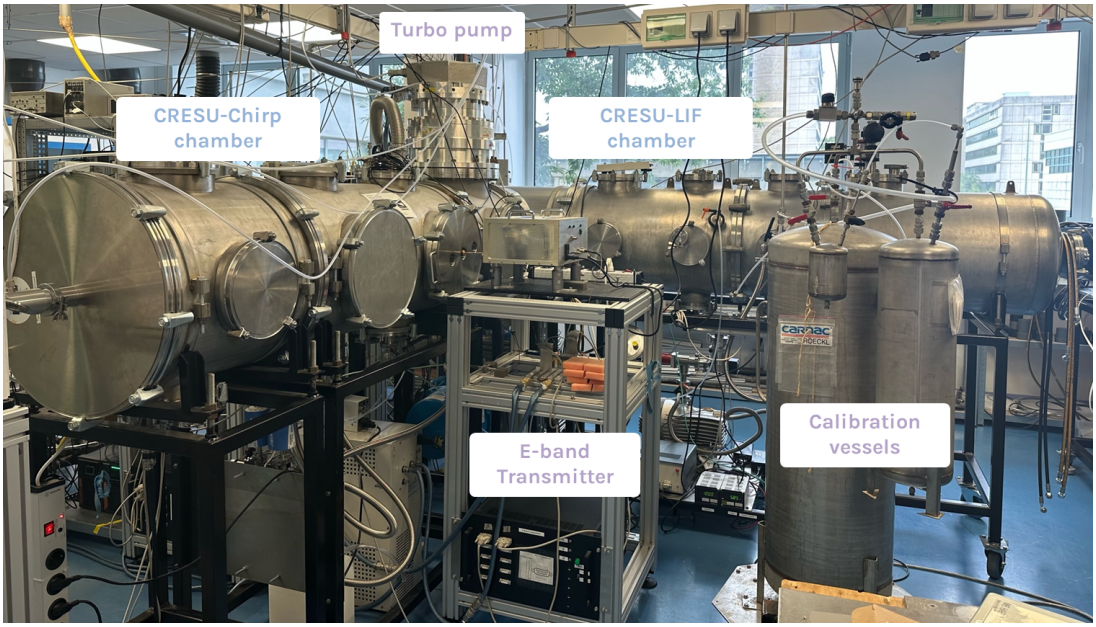

Figure 2.6: Picture of both chambers in the laboratory. The pumping group is located in the basement and is connected between the two chambers. The CRESU-Chirp chamber is connected to the E-band spectrometer described in section 2.4. On this picture, The CRESU-LIF chamber is connected to the calibration vessels used for Mass flow controller calibration (see section 2.3.2)

2.3.1 CRESU-Chirp

The CRESU-Chirp chamber was built under the ERC funded CRESUCHIRP project. The chamber consists of a 3m long and 0.5m diameter stainless tube. It is connected to the pumping group (Pfeiffer Vacuum) via a 4-way cross (MDC Vacuum product) and a butterfly valve (Pro-axiss) allowing for pumping capacity adjustment or complete isolation. The cross is also connected to the CRESU-LIF chamber and two Brewster windows for laser beam entrance.

Figure 2.7 shows in more detail the different parts of the chamber. Section (A) includes a movable reservoir mounted on a translation table. The distance from the nozzle exit to the probing region can be adjusted using a braked stepper motor. The reservoir (11 L) is Teflon-coated and has a Teflon-coated aluminium diffusing plate to ensure proper gas mixing. It includes two separate inputs for buffer gas and precursor entrance. A Brewster window can also be mounted to the reservoir and has a separate gas input for purging.

Section (C) includes a secondary expansion chamber connected to a turbo molecular pump (Osaka Vacuum TGkine3300M). This smaller chamber is aligned in the flow axis and is fitted with a skimmer holding plate in the front and a Brewster window in the back. The inside of the skimmer chamber is covered in microwave-absorbing foam to avoid reflections. The design of the secondary expansion chamber is described in more detail by Abdelkader Khedaoui [2022]. The connection to the spectrometer receiver and transmitter parts will be described in section 2.4.

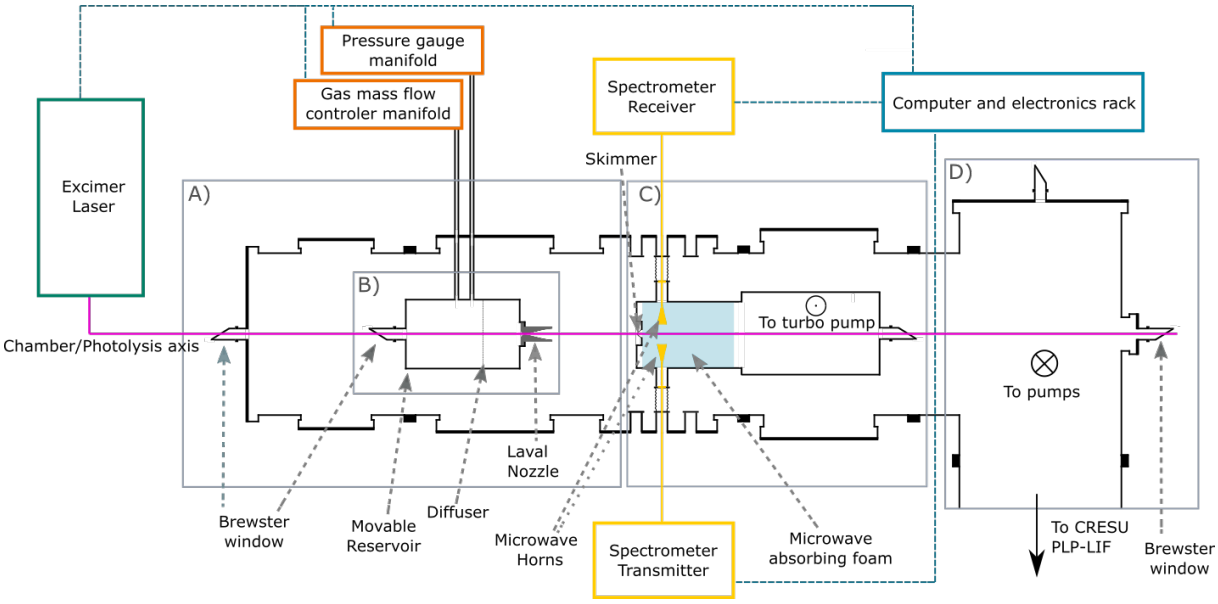

Figure 2.7: CRESU-Chirp chamber schematic. (A) Reaction region (B) Movable reservoir, (C) Skimmer chamber, pumped by a turbo molecular pump, (D) 4-way cross connecting the chamber with CRESU-LIF and the pumping group. From Guillaume [2021]

2.3.2 Reactant introduction and generation using a precursor

To conduct kinetic studies, the chamber requires the controlled introduction of various reactants. The subsequent section will detail how buffer and reactants from gas bottles are introduced using thermal mass flow controllers (MFCs). Additionally, the method of liquid sample introduction will be presented, using either a controlled evaporating mixer (CEM) or pre-made gas mixtures. Lastly, the setup employed to introduce solid samples will be described. In the case of pre-made gas mixtures and solid samples, accurate determination of reactant concentrations is needed. This can be achieved using a UV-visible spectrometer, also explained in this section. Furthermore, the generation of radicals, a key focus of this thesis, will be presented.

Mass flow controller system

Multiple MFCs are mounted on an aluminium rack to ensure a high-accuracy flow rate to the reservoir (figure 2.8). The main buffer gas (Air Liquide He $\geq$99.995%, N_2 $\geq$99.995%, Ar $\geq$99.998%) is delivered through (Brooks SLA 5800 series) 100 SLM flow controller. The reactant and precursor are introduced via various flow controllers (Brooks GF series) of different ranges (20 and 100 sccm or 1, 2 and 5 SLM). As mentioned in the description of the CRESU-Chirp chamber (section 2.3.1), the precursor entrance in the reservoir is separate from other gases to avoid any prior mixing and limit potential cross-reactions. All Brooks MFCs are connected to a power supply controller box (Serv'instrumentation) linked to the computer.

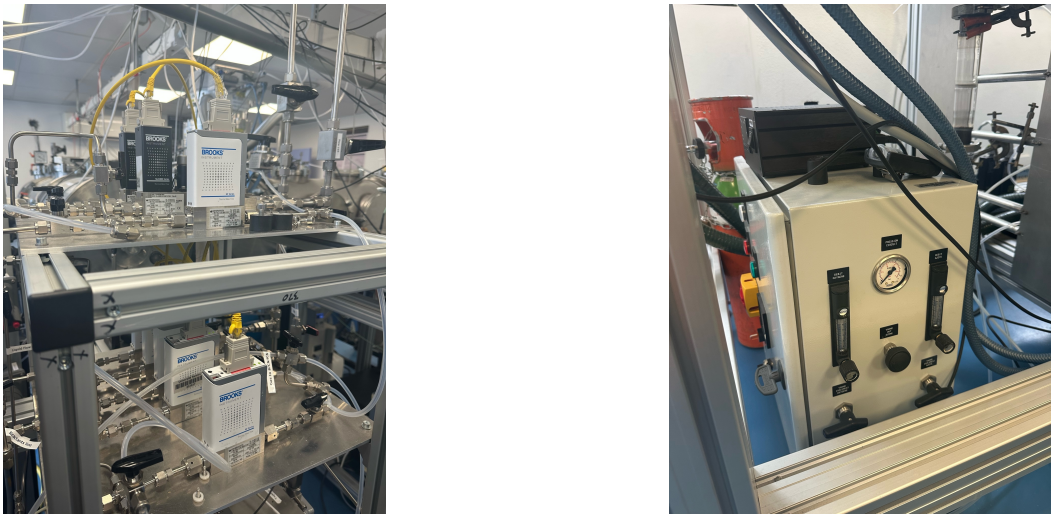

Figure 2.8: Setup used for gas introduction in the reservoir. Left hand side, thermal mass flow controller system. Right hand side, ozone generator connected to the precursor line.

Every 2 to 3 years, the MFCs' calibration are controlled in-house to ensure accurate flow rates (figure 2.9b). The system is composed of three different size tanks (150, 30 and 1,3L) which are chosen depending on the MFC scale to ensure a decent measurement time. The real flow is measured by following the pressure of the tank as a function of time. This procedure can be done either by filling or emptying the container. In the case of this experiment, the MFCs have a constant pressure upstream. Therefore, the filling method was used to stay closer to the real usage. The pipes' volume to the tank is measured for a precise calibration. This matters especially with the smallest container.

The acquisition of the tank's pressure (typically from 0 to 1 bar) as a function of time is performed using a LabVIEW program. Each curve is linearly fitted to extract the real flow. This procedure is repeated for multiple flow settings. The correction factor is finally determined with a linear fit of the real flow as a function of the set flow (figure 2.9a). Since the calibration is performed with N_2 buffer gas, a conversion factor will be applied to read any other gas flow.

An ozone generator (OZONE-SERVICE, model OS OA-10FLab) can also be used for ozone introduction via the precursor line (figure 2.8). The generator has two separate gas inputs, one for buffer gas and one for oxygen (Air liquid O_2 $\geq$99.995%). To ensure a high-accuracy flow rate, the generator's in-built flow meters are left open, and the flow rate is controlled upstream by MKS mass flow controllers (2 SLM and 5 SLM for buffer and oxygen, respectively). The flow

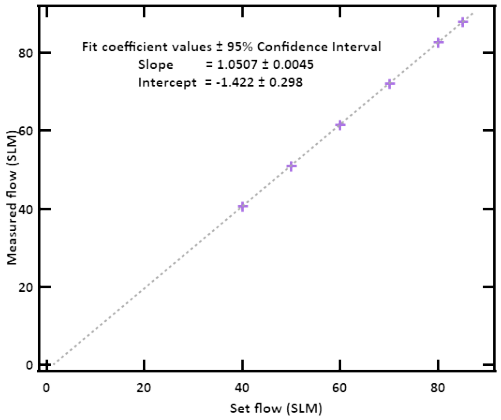

(a) Second order calibration plot, measured flow in function of flow settings for 100 SLM Thermal mass flow controller.

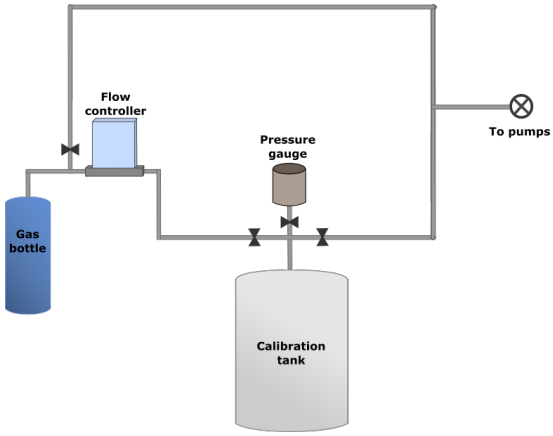

(b) Scheme of the MFC calibration setup.

Figure 2.9: Calibration of Thermal mass flow controller.

meters are controlled by an external MKS multi gas controller box (647C). The pressure in the generator can be adjusted using a needle valve. A minimum pressure of 0.35 bar is required to start the ozone generation. The electrical power of the generator can also be modified to adjust the ozone production efficiency.

This ozone generator uses the corona discharge method to produce ozone (O_3). An electrical discharge is applied to break oxygen molecules (O_2) into single oxygen atoms. These atoms can react with other O_2 molecules to give ozone. The generator output is connected to the UV-visible spectroscopic measurement setup for precise ozone density measurement before entering the reservoir (see section 2.3.2).

Liquid flow controller

For liquid samples, a CEM is used to ensure an accurate flow rate (figure 2.10). The CEM has two separate inputs, one for the buffer gas and one for the liquid. The addition of buffer gas is controlled with a thermal mass flow controller (Bronkhorst EL-FLOW Prestige, 5 SLM). The liquid introduction is done via a Coriolis liquid flow meter (Bronkhorst mini CORI-FLOW ML120V00). The latter is connected to four different liquid vessels, each filled with the liquid of choice and then pressurized with 3 bars of buffer gas (figure 2.10a). The liquid flow meter calibration process is explained in Gupta [2021]. The liquid is mixed with the buffer gas and evaporated inside the CEM before being delivered to the reservoir.

(a) Picture of the liquid flow system in the laboratory

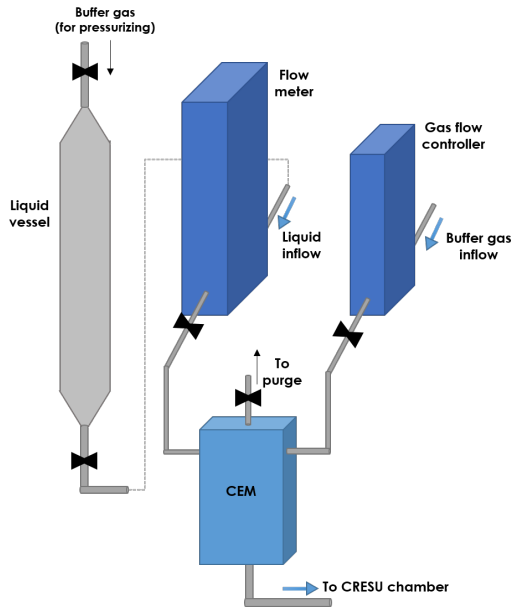

(b) Liquid setup scheme. From Gupta [2021]

Figure 2.10: Setup used for liquid introduction in the reservoir.

Gas mixture preparation

The CEM described above can flow accurately a minimum of 0.1 $g.h^{-1}$. When a smaller quantity of liquid is needed, a gas mixture is used instead. The mixture is prepared in a Teflon-coated stainless-steel container. The liquid of choice is vaporized in the tank through an home-made setup (figure 2.11). It consists of a glass tube with seven separate inputs. One is connected to a dry scroll pump (Edwards nXDS 6i) for purging. Two are for pressures gauges (100 and 1000 mbar MKS Baratron gauge type 626). To check the vacuum conditions and potential leaks, another input is for a vacuum gauge (Edwards Active Pirani vacuum gauge APG100-XM). Two connections are dedicated to the liquid glass container. Finally, a input is used for the mixture tank. Each connection can be closed with greaseless valves (vacuum compatible from J Youngs).

A good vacuum needs to be reached in the line ($\sim 10^{-3}$ mbar) to start the process. All impurities dissolved in the liquid need first to be removed. This is done by performing multiple "pump-freeze-throw" cycles. After freezing the sample using liquid nitrogen, the valve is opened to the pump to remove any air and residues until the sample starts to vaporise again. At this stage, the pressure in the line needs to be followed carefully to avoid sample loss. The line is then isolated from the pump and the liquid vessel is opened to the mixture tank. At this stage, the maximum partial pressure in the vessel is limited by the vapour pressure of the liquid. The tank is finally pressurised using buffer gas to get the desired dilution percentage.

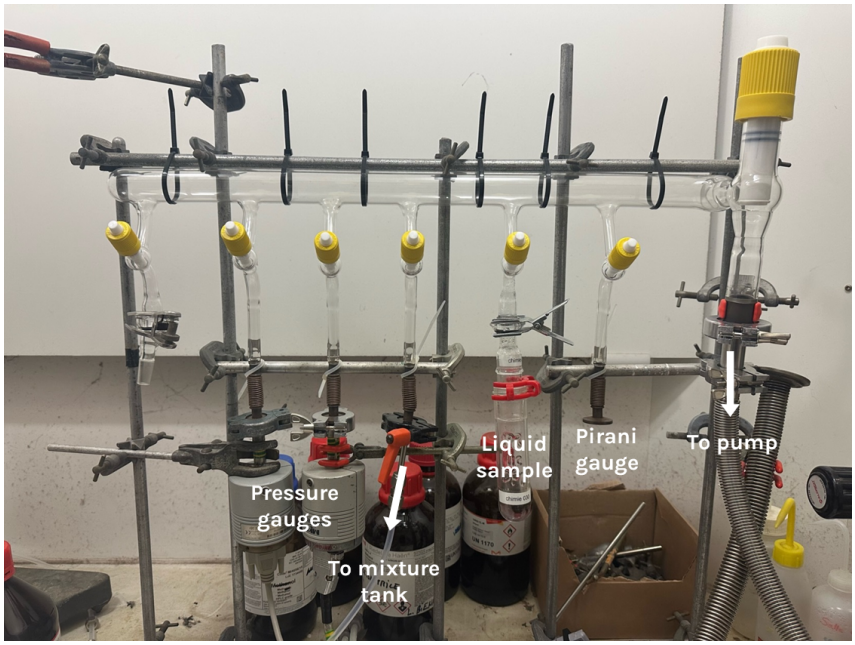

Figure 2.11: Picture of setup for gas mixture preparation.

Solid sample introduction

Solid samples can also be vaporized to be introduced into the system. The setup consists of a 30cm long glass vessel with a glass frit in the middle, where the solid compound is placed (figure 2.12). The vessel is connected to the main system via quick connectors (Swagelok). The buffer gas is flowed from the top to carry the solid vapour. The vapour density introduced in the system can be measured with a UV-visible setup placed prior to the reservoir. For ICN density measurement, a custom heating pad and a thermocouple (Omicron technologies) were added around the glass vessel. It allowed maintaining the temperature of the vessel a couple of degrees above room temperature, ensuring a more constant ICN vaporization.

UV-visible spectrometer setup

When the quantity of a compound cannot be known with accuracy due to its introduction method, the density in the flow can be measured using a UV-visible spectrometer. In this work, it was used to measure the density of ICN (precursor used for CN radical generation), ozone and formic acid pre-made mixtures.

The setup (figure 2.12) is composed of a 63 cm long, 3.5 cm diameter stainless steel cylinder with two quartz windows, followed by collimating lenses at its ends. On one side, an optic fiber (QP600-2-XSR) is used to transmit the light from the source (Ocean Insight DH2000-DUV). The latter is equipped with two lamps, a deuterium and a halogen lamp to cover the range of 190-2500 nm. The second side is connected to another optic fiber, linked to a Maya2000-Pro spectrometer, fitted with an Ocean Optics H5 grating (0.16 nm resolution), to collect the light after absorption by the compound. Two pressure gauges (MKS Baratron gauge type 626, 1000

torr) are placed before and after the UV-vis cell.

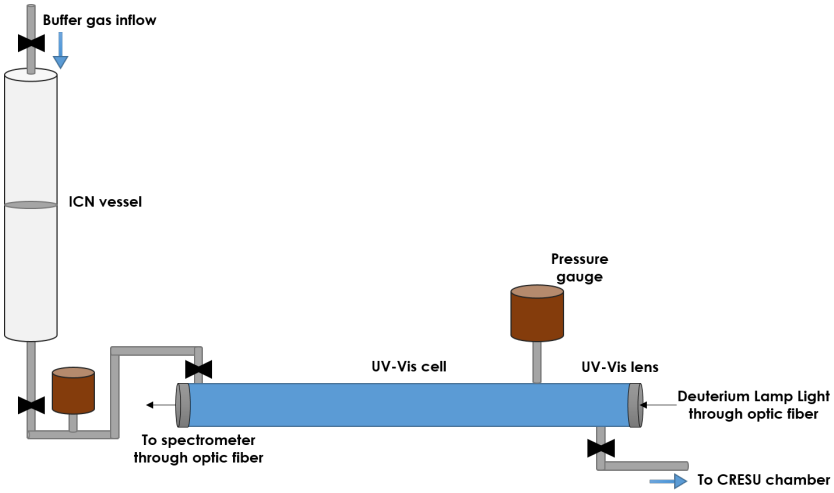

Figure 2.12: UV-visible spectrometer scheme. From Gupta [2021]

The molecular density inside the UV-vis cell is calculated using the Beer-Lambert law (equation 2.9). The number density is average over a given wavelength range, adjusted in function of the molecule cross-section. The final density in the CRESU flow can be deduced using equations 2.10 and 2.11.

$$ln(\frac{I - I_{off}}{I_0 - I_{off}}) = \sigma N l \tag{2.9}$$

Where I_{off} is the background intensity with the lamp off, I_0 is the intensity with the light on and no sample and I is the light intensity with the sample. σ is the absorption cross-section measured in the literature, N is the number density in cm^{-3} and l is the length of the UV-vis cell.

$$flow_i = \frac{N_i}{N_{UVtotal}} flow_{UVtotal} \tag{2.10}$$

$$N_{i,CRESU} = \frac{flow_i}{flow_{total}} N_{total,CRESU} \tag{2.11}$$

Where the index "i" stands for the target species.

Figure 2.13 shows an example of ICN density measurement using the UV-visible spectrometer. The ICN density in the CRESU flow is calculated with an average from the individual values in the range of 235 to 269 nm.

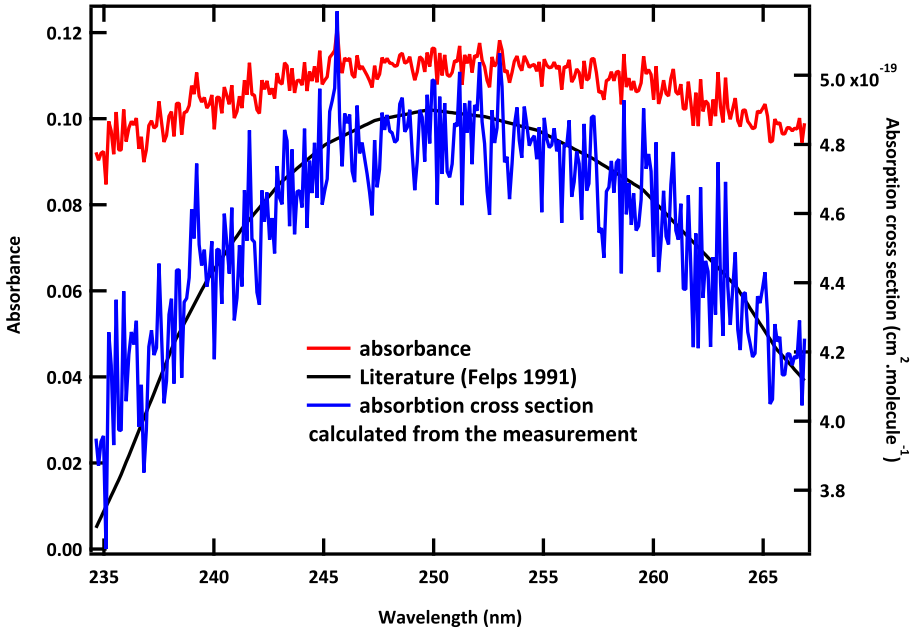

Figure 2.13: ICN density measurement from UV-visible setup.

Radical generation

The common techniques used for radical generation are photolysis, microwave discharge and flash vacuum pyrolysis. As kinetics measurement requires avoiding cross-reaction, the methods need to produce side-reactive products as little as possible. In the case of this work, additional care must be taken to not affect the flow temperature. Techniques such as flash vacuum pyrolysis are therefore excluded as they will warm up the environment. For the various reasons mentioned above, the photolysis method was chosen for this work. In particular, an excimer laser (Coherent LPXPro 210) was employed. It has a maximum repetition rate of 100 Hz and can generate 3 different wavelengths (193, 248 and 351 nm) depending on the gas mixture used in the cavity. The laser enters the chamber via multiple Brewster windows and photolyses the precursor of choice along the flow propagation. As radicals are only generated in the cold region of the CRESU flow, the warm boundary layers will not affect the detection technique of choice.

For this work, the 248 nm wavelength was used to photolyse the ICN precursor and produce CN radicals. The laser is triggered from the back of the reservoir to the skimmer chamber, thus the beam size in the flow is limited by the nozzle throat. For a beam diameter of 7 mm, the interaction area is 0.38 cm^2 and provides a laser fluence of around 7×10^{16} $photon.pulse^{-1}.cm^{-2}$.

2.4 Chirped pulse microwave spectroscopy

Throughout the first part of this chapter, the discussion has revolved around a key constraint imposed by reaching low temperatures: the upper limit on the density of reactants that can be introduced into the experiment. In the context of CRESU flows, the reactants can constitute no more than 1% of the total flow density to ensure the hydrodynamic conditions of the nozzle. Depending on the nozzle this means a maximum density between 1×10^{14} and 1×10^{15} cm^{-3}. These low densities imply the use of a highly sensitive detection technique while keeping a high specificity to distinguish the different molecules. For branching ratio measurements, another aspect enters into play, the simultaneous probing or absolute concentration measurements. In the case of rotational spectroscopy, each molecule, even isomers, possesses distinct rotational transitions. This allows unambiguous assignment as long as the molecule has a permanent electric dipole. Multiple transitions can even be detected simultaneously when a particular kind of pulse, called chirp, is used. For these various reasons, the chirped-pulse microwave technique was coupled to CRESU flow to tackle the challenges in low-temperature kinetic parameter measurements.

This section will first explore the basic theoretical aspects behind rotational spectroscopy and more specifically using chirped pulses. The challenges encountered in coupling this technique with CRESU flows will be discussed along with the spectrometers used in this work. Finally, the data acquisition and processing protocols will be presented to provide a complete view of the experimental procedure employed in this work.

2.4.1 Theoretical aspects

Molecular rotation

Determining the rotational spectrum of a molecule requires expressing its angular momentum to derive the rotational energy levels. The angular momentum is expressed as the product between the angular velocity and the moment of inertia. The latter is crucial as it describes the repartition of mass in an object and influences greatly its ability to rotate along a particular axis. For a molecule, the moment of inertia (I) can be expressed as

$$I = \sum_i m_i r_i^2 \tag{2.12}$$

where m_i and r_i are the mass and the distance of the i^{th} atom to the rotational axis.

In the case of molecular rotation, the moment of inertia is defined along three main orthogonal axes passing through the center of mass, a, b and c. By convention, the a axis corresponds to the smallest moment of inertia and c the greatest, thus $I_a \leq I_b \leq I_c$.

Molecules can be classified depending on their rotational symmetries. Four main categories can be distinguished :

(i) Spherical molecules, for which all moments of inertia are equal (e.g., CH_4). These species

are highly symmetric and thus present no dipole moment

$$I_a = I_b = I_c \tag{2.13}$$

(ii) Linear molecules, such as HCN for which

$$I_a = 0 \ \ and \ \ I_b = I_c \tag{2.14}$$

(iii) Symmetric tops molecules, for which two cases can be distinguished, the prolate case ($I_a < I_b = I_c$) and the oblate case ($I_a = I_b < I_c$).

(iv) Asymmetric top molecules, for which all moments of inertia are unequal (e.g., CH_2O).

$$I_a \neq I_b \neq I_c \tag{2.15}$$

To understand the principles behind molecular rotation, the simplest model is the rigid rotor approximation. Let's consider a simple diatomic molecule. Under this approximation, the atoms are considered as two masses attached together with a fixed distance. The solution of the Schrödinger equation allows to derive the Hamiltonian with the different rotational energy levels. When neglecting the centrifugal distortion, the levels $E(J)$ are given by

$$E(J) = \frac{h}{8\pi^2 cI} J(J+1) = BJ(J+1) \tag{2.16}$$

Where h is Planck's constant, c the light velocity, B the rotational constant and J the rotational quantum number, linked to the total angular momentum of the object.

In the case of symmetric top molecule, the two moments of inertia lead to two distinct rotational constants. It becomes necessary to introduce a new quantum number K which corresponds to the projection of the angular momentum along the a or c axis for oblate and prolate case, respectively. The energy levels are thus noted J_{Ka} or J_{Kc}. The equation 2.16 to express the energy levels becomes

$$E(J) = BJ(J+1) + (A-B)K^2 \tag{2.17}$$

Where A and B are the rotational constants associated with the moment of inertia I_a and I_b respectively, for a prolate molecule.

In the case of asymmetric top molecules, there are now three rotational constants as the moments of inertia are different along the three axes. Both Ka and Kc need to be mentioned to distinguish the rotational levels. They give the projection of angular momentum along each axis. The levels are noted $J_{Ka,Kc}$. The J quantum number can have integer values and K is always smaller or equal to J. In this case, the Hamiltonian cannot be factored in a simple expression for the energy levels.

This simple model offers a good starting point to understand the description of molecular rotation, however, it neglects various aspects impacting the prediction accuracy. In particular,

the centrifugal distortion needs to be taken into account as it affects considerably the rotational motion. In many cases, molecules such as symmetric tops or asymmetric tops require a more rigorous quantum treatment for accurate predictions. The SPFIT/SPCAT program suites, developed by Pickett [1991], are commonly used to that end. SPFIT is used to fit experimental data and derive the various spectroscopic constants, while SPCAT takes these parameters as input and calculates the different energy levels. Molecular transitions and associated parameters can be found in various catalogues such as the Cologne Database for Molecular Spectroscopy (CDMS, Müller et al. [2005]) or the Jet Propulsion Laboratory (JPL, [Pickett et al., 2003]). In the case of this work, SPCAT is used to predict the line intensities at low temperatures in order to target the best transitions in given experimental conditions.

Chirped-pulse microwave spectroscopy

Rotational spectroscopy is a powerful tool as it allows extracting information on the molecular structure. The bond lengths and angle as well as the energy barrier to internal rotation can be derived by looking at the rotational transitions. In this work, rotational spectroscopy is used as a fingerprint to identify and quantify the molecules in presence during a reaction. In most cases, the targeted transitions are already well-known or can be extrapolated with enough accuracy.

Traditional microwave spectrometers use single frequency pulses coupled with a Fabry-Perot cavity. While this technique allows the acquisition of a high-resolution spectrum, it is very slow. New technological developments in electronic components allowed the invention by Pate and co-workers [Brown et al., 2008] of broadband chirped-pulse spectrometers. This technique has the advantage of probing a wide range of frequencies while being very fast. The excitation pulse, called chirp, consists of a linear frequency sweep which will polarize microscopically molecules possessing transitions within the frequency range of the chirp. The chirp generates an electromagnetic field for a short period of time which will excite the higher rotational states, inducing a phase-coherent rotation. As the chirp stops, the excited molecules will lose this coherence and relax back to their initial state by emitting a Free Induction Decay (FID) signal. This electromagnetic response can be recorded in the time domain and then Fourier-Transformed in the frequency domain to extract the molecular spectrum (figure 2.4). The signal (S) emitted during the FID from a chirped excitation can be derived from the Bloch equation [McGurk et al., 1974], giving

$$S \propto \omega \mu^2 E_{pulse} \Delta N_0 (\frac{\pi}{\alpha})^2 \tag{2.18}$$

where ω is the frequency, μ the transition dipole moment, E_{pulse} the electric field magnitude, ΔN_0 the population difference at equilibrium and α the sweep rate.

The FID signal is affected by the decay of coherence induced by the relaxation to lower energy levels and by energy transfer through molecular collisions. To reflect even more experimental conditions, the Doppler contribution in the profile can also be taken into account in the Bloch equation. This effect arises from the different velocities in the gas sample relative to the microwave beam. Each molecule will see a slightly different frequency, thus affecting the decay of coherence [Schwendeman, 1978]. In the SKISURF setup, the pressure is usually very low, around 8 µbar, thus the pressure broadening can be neglected in the line profile (discussed in

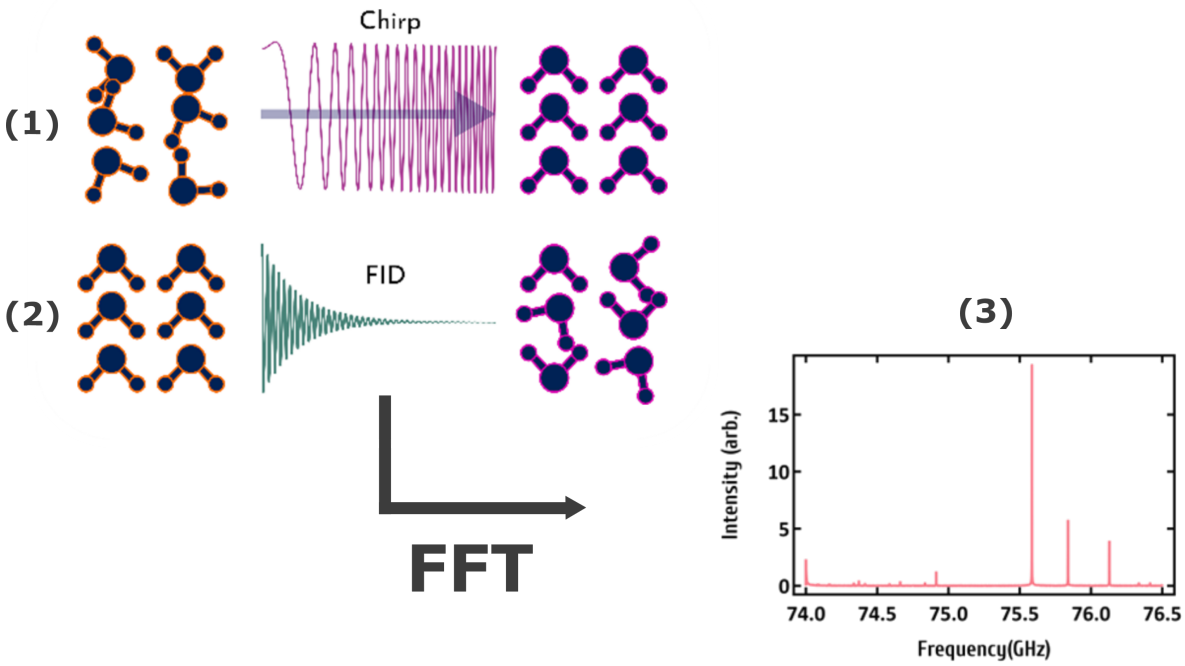

Figure 2.14: Chirped-pulse schematic principle. (1) A chirp is sent to polarise the molecular sample in a first step. (2) Then the FID signal is recorded in the time domain. (3) Finally, the signal is fast Fourier Transformed (FFT) to give the final spectrum in the frequency domain.

the next section). Furthermore, the probing is performed perpendicularly to the flow direction thus the Doppler effect can be neglected, only the thermal Doppler component remains.

Current electronic technologies do not allow the generation of frequencies directly in the microwave domain. Performing rotational spectroscopy thus requires different frequency up-conversion steps based on the superheterodyne receiver principle. In this method, the key step is the signal conversion to higher frequency using a mixer. It takes two entrance frequencies, one is named the input frequency and the second local oscillator (LO). In chirped pulse configuration, the LO is usually a fixed sine wave and the input frequency will vary to give the chirp. The mixer will produce the sum and the difference between the two input frequencies. The desired upper frequency can then be selected using a bandpass filter, removing all other components (figure 2.15). The signal can be further multiplied, modulated or amplified to reach the final frequency range. Various filtering stages can be added to remove undesirable frequency components added during the different steps. The latest improvements in electronic components, of arbitrary waveform generators, broadband amplifiers and fast acquisition cards, made possible the design of these fast chirped pulse spectrometers. The design and specification of the spectrometer used in this work will be described in the following section.

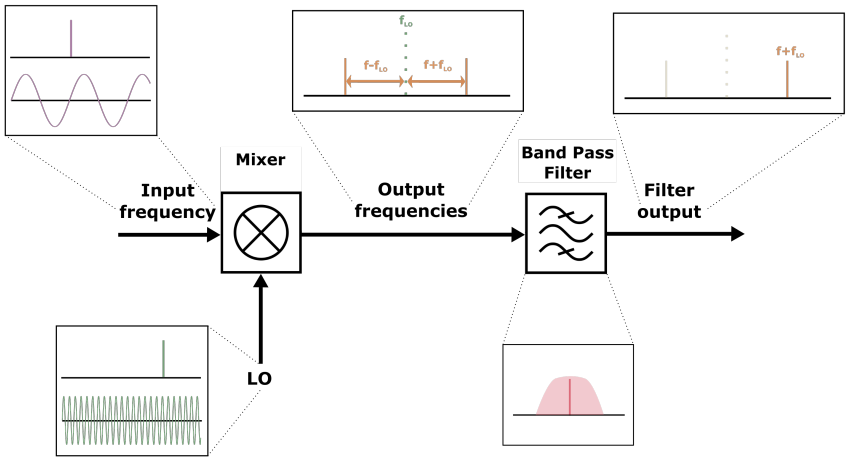

Figure 2.15: Schematic of signal up-conversion using a mixer and then a bandpass filter.

2.4.2 Coupling chirped pulse with CRESU flows: the SKISURF setup

While kinetic studies in CRESU flows require enough collisions to proceed in a reasonable time, rotational spectroscopy in emission is very sensitive to pressure. In fact, during a collision, the excited molecules will be relaxed via non-radiative transfer processes instead of radiative emission. This contributes to a significant diminution in the signal-to-noise ratio (SNR). As figure 2.16 shows, with increasing pressure, this effect becomes predominant and affect considerably the FID profile. To tackle this compatibility issue, the reaction region, in CRESU flow, and the probing region, with the chirped pulse, were decoupled.

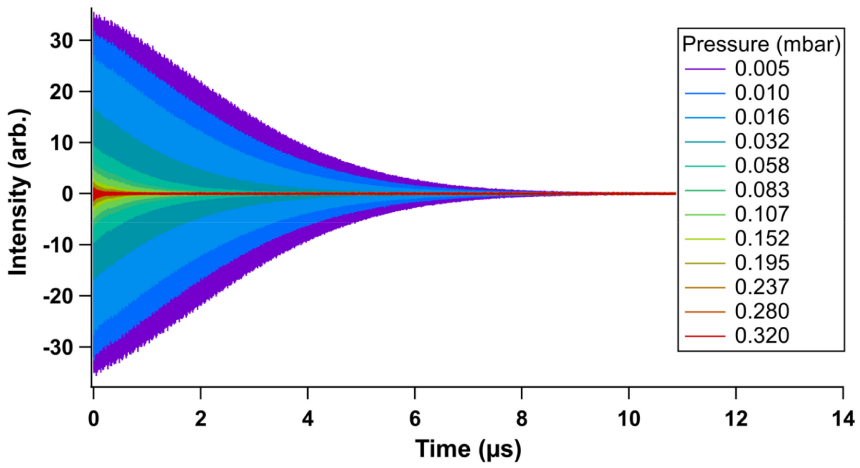

Figure 2.16: Experimental FIDs for the J=6-5 transition over the experimental pressure range for a fixed partial pressure of OCS of 5.10^{-5} mbar in He buffer gas between 0.005 - 0.320 mbar in a flow cell. From Hays et al. [2020].

The CRESU flow is sampled with a skimmer in a lower-pressure chamber (described in 2.3.1). This second expansion allows reaching lower pressure and temperature in the probing re-

gion. Both the lower collision rate and depopulation of the higher energy state contribute to a strengthening in the molecular signal. The probing region collision rate is considered too low for the reaction to proceed, thus reaction products are considered to be formed only under the CRESU flow conditions.

The setup constructed in Rennes, named SKISURF (Skimmed uniform Supersonic Flow) is described in detail by Abdelkader Khedaoui [2022]. The development of this setup is based on similar methods using airfoil to sample the flow employed by Gurusinghe et al. [2022a] and Soorkia et al. [2011].

Figure 2.17 shows a comparison between the signal taken in the CRESU flow and in the skimmed flow. A clear improvement in the FID size, in the time domain, and the line strength and shape, in the frequency domain, can be noticed. Less reflections are also observed, which was an issue in the initial setup. The secondary expansion chamber coupled with a skimmer has therefore considerably improved the acquisition conditions. This setup was used for the experimental work of this thesis. The associated limitations will be discussed in detail in the following chapters.

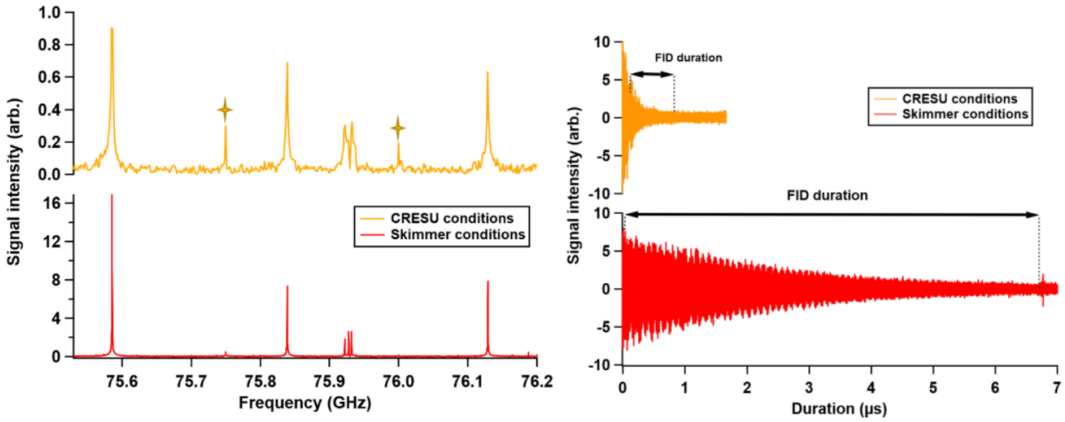

Figure 2.17: Comparison of vinyl cyanide signal in an argon 30 K flow under CRESU conditions (orange) and skimmer conditions using the 4 mm skimmer (red). Right: Frequency spectrum. Left: corresponding FIDs in the time domain. The stars refer to spurs from the spectrometer electronics. From Abdelkader Khedaoui [2022].

2.4.3 Spectrometers developed in Rennes

Two spectrometers were constructed under the ERC funded CRESUCHIRP project, a Ka-band spectrometer (25-40 GHz) and an E-band spectrometer (60-90 GHz). Their construction and performances are described in Hearne et al. [2020] and Hays et al. [2020] respectively. The experimental work of this thesis was conducted only with the E-band spectrometer, a scheme of the electronics configuration is shown in figure 2.18.

The spectrometer is constructed in two distinct stages: the transmission stage, to generate the pulse at the right frequencies, and the receiver stage, to record the emitted molecular signal and

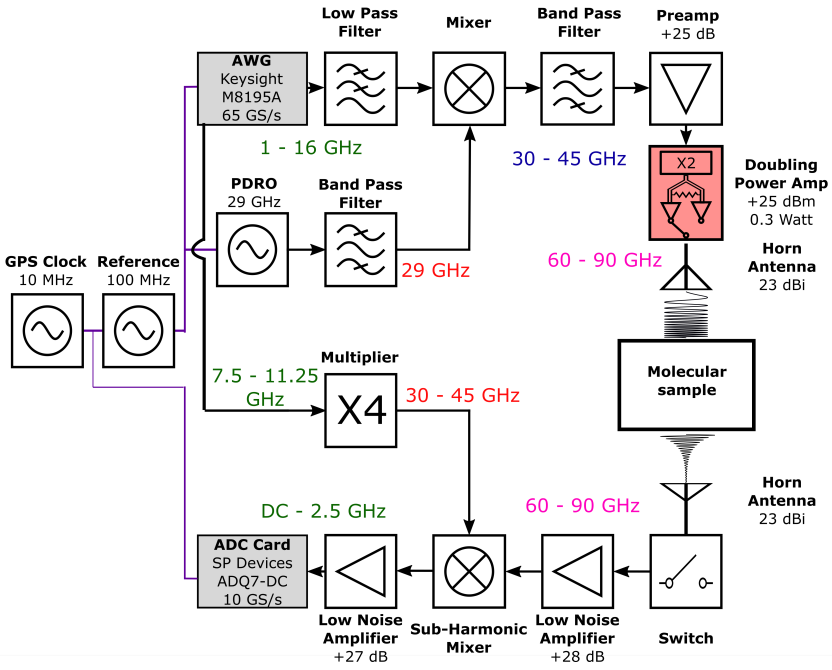

Figure 2.18: Scheme of the E-band spectrometer using digitizer as the acquisition device. From Hays et al. [2020].

down-convert it to be readable by the acquisition card. Each stage is mounted on independent aluminium tables shown in figure 2.19.

Electronic components are mounted on heat-sink blocks to maintain a constant temperature at 25±0.1°C by a water chiller (ACCEL series 250 PHP), allowing a stable response throughout the experiment. The electronic assemblies are mounted on optical breadboards and optical posts for a precise waveguide alignment in the chamber. The spectrometer is coupled to the secondary expansion chamber via a waveguide bulkhead connected to 150 mm long waveguides and horn antennas at the end. Vacuum is ensured by homemade 100 micron thick Teflon sheet windows clamped between the two waveguide flanges. Between individual waveguide elements, gaskets shaped for waveguide flanges (SAS Industries Inc., 1056-7407) were added as well. The two horns are separated by about 10 cm to probe the skimmed flow. The interior wall of the skimmer chamber is covered in absorbing foam (Eccosorb HR-10 Laird) to reduce microwave reflection which could affect the recorded signal.

To produce the desired frequency, the process starts in the transmitter side with an arbitrary waveform generator (AWG Keysight M8195, 64 GS/s) which can generate a frequency in the range 1-16 GHz. The signal is then mixed with a local oscillator (LO) from a phase-locked dielectric resonator oscillator (PDRO, Microwave Dynamics PLO-2070-29.00) by entering a mixer (Marki M11850H). This will generate two components by adding and subtracting the two input frequencies. The upper-side band, in the range 30-45 GHz, is selected using a broadband high-pass filter (Reactel 9HS-X30/45G-K11R). Then the signal is amplified with a Quinstar preamplifier (QPW-205020525-J0). Finally, for the signal to reach its frequency range (60-90 GHz), it goes through a doubling power amplifier (Quinstar integrated system QPW-205020525-J0). The latter has two millimeter wave amplifiers used either to reach 60-75 GHz or 75-90 GHz. An

electro-mechanical switch is used to select the one in use. The amplifiers are controlled with TTL signals for fast turn-on and turn-off times of less than 20 ns. The microwave radiation is fed in the chamber via a 20 dBi gain horn antenna (Quinstar QWH-EPRR00).

The molecular signal is then recorded with the emission side of the spectrometer. The emitted frequencies are collected with the same antenna as the transmission stage, followed by a variable attenuator (Quinstar QAL-E00000). It allows monitoring the pulse power during experiments. The signal then enters a fast single pole-single throw PIN switch in 60-90 GHz range (Millimeter Wave product 911E/387TTL). This switch is here to protect the low noise amplifier (LNA) from the initial exciting pulse. The signal is amplified by the LNA (Millitech LNA-12-02,350) and then down-convert with a subharmonic mixer (Virginia Diodes WR12SHM) and a LO signal from the PDRO or from another channel of the AWG sent through a quadrupler (Quinstar QMM-38,150,504J). The LO source is chosen depending on the acquisition method described below. The output signal goes through a final amplifying stage with another LNA (Mitech AFS4-0 0,101,800-25-S-4).

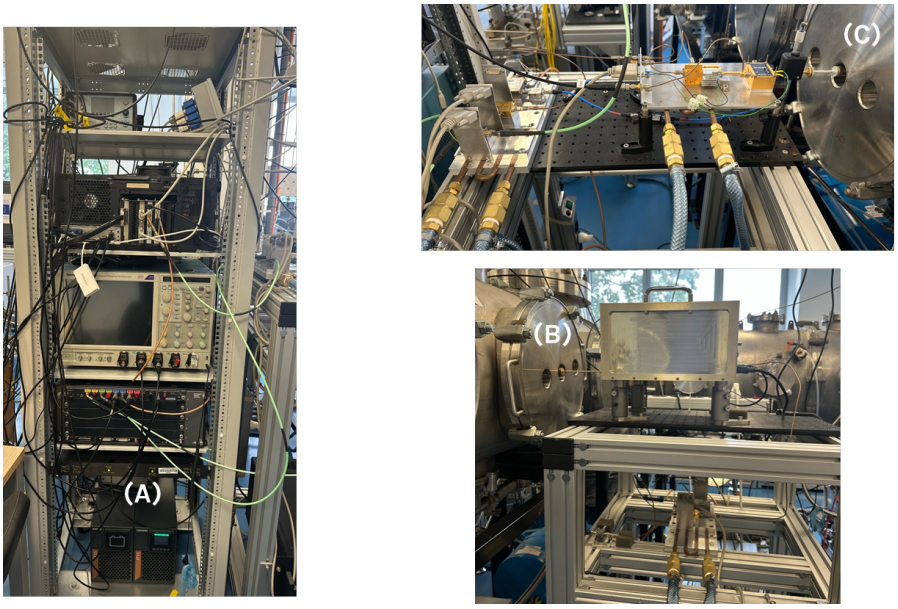

Figure 2.19: Picture of E-band spectrometer. (A) From top to bottom, DDG, computer (with acquisition card), oscilloscope and AWG. (B) Transmitter side. (C) Receiver side.

Data acquisition is ensured by either a digitizer (Teledyne SP devices ADQ7DC-PCIE) or an oscilloscope (Tektronix DPO 71604C). The digitizer card is running at 10 GS/s with a 2.5 GHz 3 dB bandwidth. This method is used during usual experiments. The oscilloscope is mostly used for troubleshooting and instrument characterisation. The acquisition device is triggered by a pulse from an AWG marker channel. The other components, including the excimer laser, are triggered by a digital pulse delay generator (DDG) (BNC 577), triggered by another AWG marker channel. All instrument's timings are synchronized paying attention to protecting the LNA from the exciting pulse, as it is very sensitive to the input signal power. The oscilloscope, digitizer, AWG and PDRO are synchronised with a 100 MHz oven-controlled crystal oscillator (Precision Test Systems GPS10-eR-50), locked to a GPS-disciplined Rb clock (Stanford Research Systems FS740) at 10 MHz. The higher frequency ensures better phase stability than the Rb

clock alone. The DDG is synchronized to the 10 MHz clock alone as it doesn't require this extra stability.

2.4.4 Data acquisition

The data acquisition protocol is described in detail in Guillaume [2021]. This section will present the particular scheme used for this work.

The acquisition sequence starts as follows, an excitation microwave pulse is transmitted through the horn antenna. The switch on the receiver side is closed during this time to protect the sensitive electronic components. The pulse will excite the molecular species of interest. As the pulse stops, the molecule will relax and emit a FID. At that time, the switch is opened to record the signal on the receiver side. The delay between the end of the exciting pulse and the opening of the switch is carefully chosen to avoid any powerful reflections that could damage the electronic parts while ensuring the maximum recorded time. This frame is repeated a maximum of times until the acquisition card is full (2 million points), this constitutes the complete acquisition scheme. Typical experiments comprise 80 frames. At the beginning of one frame in the sequence, the laser can be triggered to study reactions involving radicals. This acquisition scheme can be repeated and averaged on the card multiple times (number of acquisitions) (figure 2.20). The acquisition card has a sample rate of 10 GS/s. When operating at full speed, it gives a maximum recorded time of 200 µs. The card can however skip points to record longer timings. Depending on the excited frequencies, this can cause signal aliasing but should not affect the line intensity. For each experiment, all the above parameters are optimised to the system of interest.

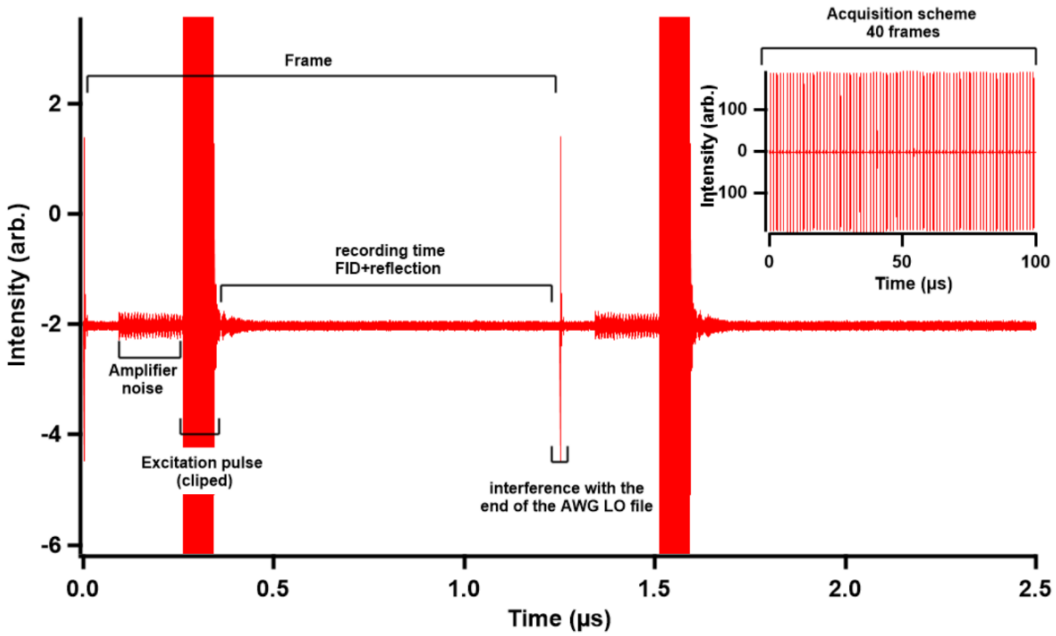

Figure 2.20: Scheme of an acquisition frame using the digitizer. From Guillaume [2021].

The exciting pulse was initially a chirp as it allows the simultaneous detection of different

species. This excitation mode poses however few constraints with the typical experimental conditions. During the linear frequency sweep of the chirp, the polarizing power is spread over the different frequencies. In contrast to a single-frequency pulse, where the polarizing power is concentrated on one particular transition. The duration of this single pulse can be adjusted to achieve the maximum polarization ($\pi/2$ conditions). This optimal time can be determined by performing a Rabi cycle experiment [Park et al., 2011]. In the case of this work, the molecular densities are usually so small that using chirps for molecular detection is not always the best option. Single-frequency pulses can be used instead which allows a better SNR but loses the broadband characteristic. To overcome this issue, a "multicolour" acquisition pulse sequence, based on Broderick et al. [2018], was developed. Various single-frequency pulses are sent one after the other, each with optimal timings, before the switch opening. Multiple transitions can therefore be probed, allowing a compromise between the chirp and the single-frequency pulses. This stacked transmission sequence implies however a careful post-processing analysis. As the total FID recording starts at the end of the last pulse, part of the signal of the previous pulses is lost. This could matter in the case of branching ratio determination where, at least, two transitions need to be compared. This effect can be corrected in post-processing by choosing the appropriate analysis window (see following section).

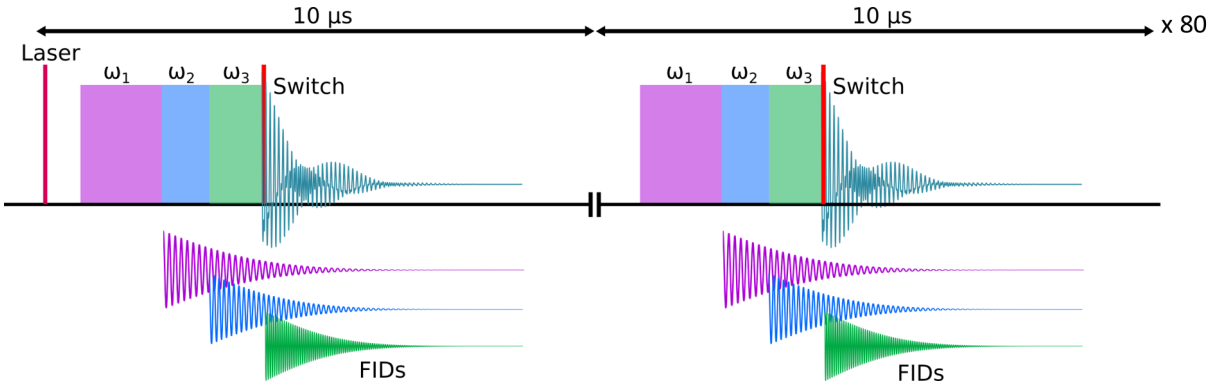

Figure 2.21: Scheme of a multicolour pulses sequence. Credit: Ilsa R. Cooke.

A drawback of the multicolour excitation pulse is that the molecules could relax completely before the recording starts. A way around this problem would be to stack the pulses on top of each other by generating an excitation pulse with the sum of the different sine waves at different frequencies, giving a "multifrequency" pulse. The multicolour and multifrequency pulses were tested on various vinyl cyanide transitions as presented in figure 2.22. The left panel presents the FFT of the FID and the right panel the FFT of the excitation pulses. The FFT of the pulses in both multicolour and multifrequency should be mathematically the same, however, the experimental results show clearly that in the up-conversion stage, something might not be reacting well for the multifrequency pulse and result in a weaker excitation field. This leads to a significant decrease in the molecular response in the FID. For this reason, the multicolour pulse sequence was chosen over the multifrequency pulse.

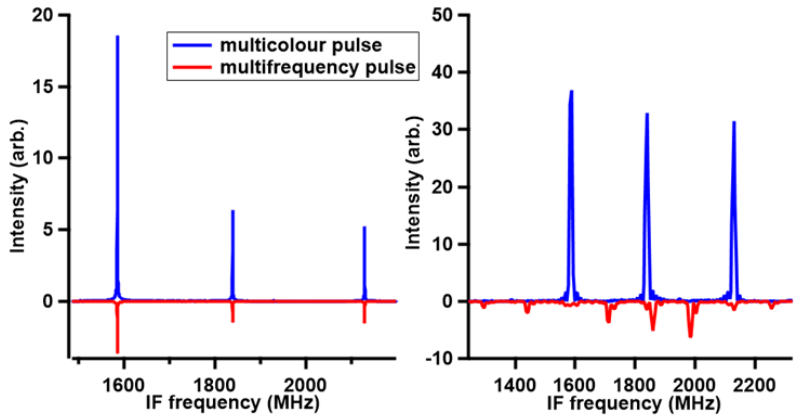

Figure 2.22: Comparison between the multicolour and multifrequency pulses. Left, FFT of the FID after the pulse. Right, FFT of the excitation pulse. On acrylonitrile (VCN) transitions between 75.5 and 77 GHz in the skimmer chamber with an Ar 30K nozzle (Pressure reservoir = 23.24 mbar and Pressure chamber = 0.082 mbar). VCN density in the flow = $1 \times 8\ 10^{13}$ cm^{-3}. Scan averaged 10^4 times.

2.4.5 Data analysis

The collected data are processed using the Igor Pro software (Igor Pro 8, Wavemetrics) with routines developed mainly by Théo Guillaume and Brian M Hays. Most procedures are provided and explained in Guillaume [2021]. The particular procedures used for this work will be presented in this section.

The signal recorded in the time domain can comprise various undesirable components such as reflections, electronic noise, spurs from the clock or LO bleed-through. Microwave reflections can not only be attenuated using absorbing foam but also subtracted using post-processing methods. Here, a few frames at the beginning of the sequence can be averaged and subtracted to all other frames to clean the data. Electronic noise and spurs are treated using a pattern filter. This method is based on the recording and subtraction of the coherent noise. In the acquisition frame, the signal is recorded a little more time than the length of the FID for this purpose. This signal portion is averaged and then subtracted from all other frames. This pattern filter is however not effective on intermodulation spurs coming from signal mixed with impurities of the LO source. These parasitic frequencies are usually well separated or the LO can be adjusted to avoid any interference in the analysis.

A phase drift between successive frames can sometimes be observed. The origin of this phenomenon is not well known. It affects the quality of background subtraction, thus impacting the final SNR and spur removal. To tackle this issue, a program was developed to calculate the phase of each frame and then rotate them using their complex Fourier transform, so they all are in phase. This method based on Park et al. [2011] ensures a coherent background subtraction.

After the signal is cleaned with these various filtering steps in the time domain, it can be Fourier-transformed (FFT) in the frequency domain to give the final spectrum. To follow the time dependence of the signal, each frame can be individually transformed in the frequency

domain. The FFT window is adjusted to allow a maximum signal intensity or to correct the losses from the multicolour acquisition sequence. As the intensity of the FID is proportional to the amount of species, it can be linked to the transition intensity in the frequency domain. The line SNR for the different frames is plotted as a function of time to give the signal time dependence. This procedure is only possible when the laser is triggered, as it serves as a timestamp for the beginning of the reaction. With the SKISURF setup, 10 µs frames are used, which is the maximum time resolution for this type of experiment. Figure 2.23 summarise the acquisition scheme using the laser as a trigger for the reaction.

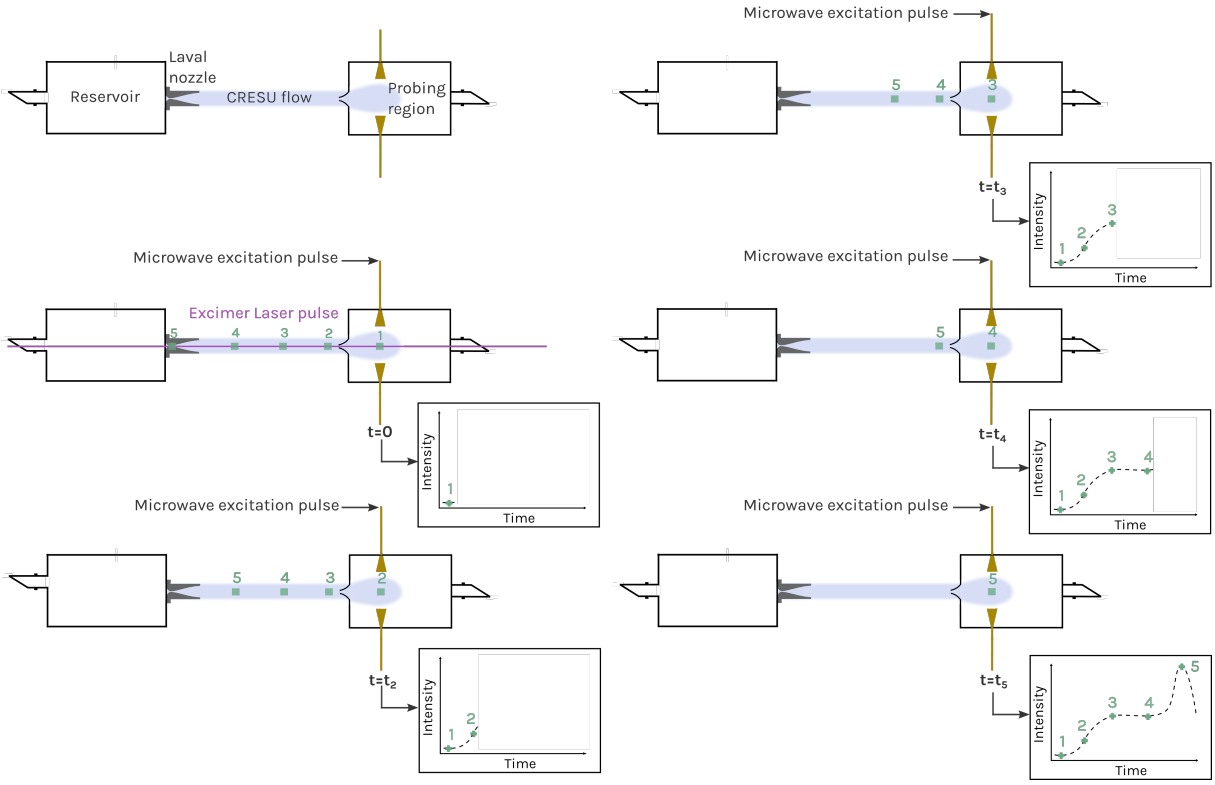

Figure 2.23: Acquisition scheme in case of reactions involving excimer laser.

In the context of this work, an analysis routine for branching ratio measurement was also developed when a calibration reaction is used. The analysis procedure is described in detail in chapter 3.

In the case of complex formation experiments, only stable species are injected into the system, thus the reservoir position serves as a time stamp. The velocity of the uniform flow and the distance between the nozzle tip and the probing region give the available complexation time. As the reservoir moves further away, the targeted molecule will have more time to form complexes. For each reservoir position, a spectrum of the targeted species is acquired. In this case, all frames can be averaged together as there is no time dependence in this signal. The reservoir position is converted in time and thus the intensity of the targeted line can be plotted as a function of time (figure 2.24). The data acquisition procedure and reservoir motion were automatised with a LabVIEW program. The analysis procedure is described in detail in chapter 4.

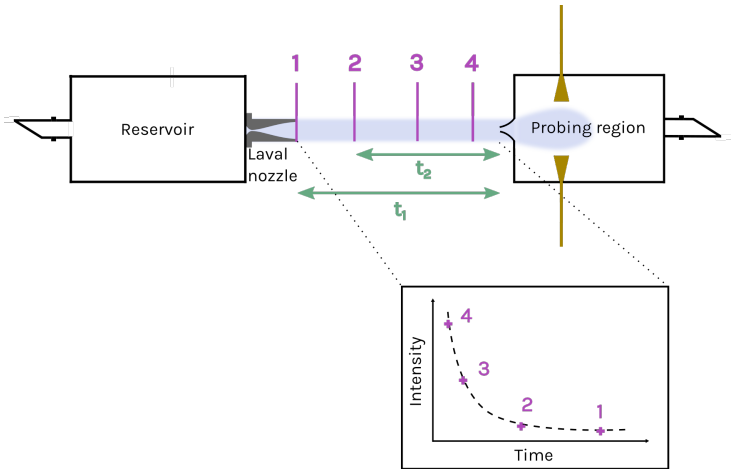

Figure 2.24: Acquisition scheme in case of complex formation experiments, here showing loss in monomer signal.

Chapter 3

Measurement of low temperature branching ratio for the CN + propene reaction

Les difficultés croissent à mesure qu'on approche du but.

– Johann Wolfgang von Goethe

Reaction rates and branching ratios of thousands of reactive systems are missing in the databases to predict accurately the abundances of molecules. As discussed throughout the two previous chapters, the measurement of these coefficients at low temperatures are subject to multiple challenges in the experimental field. This chapter presents the application of the SKISURF setup developed specifically for low temperatures kinetics measurements. Here the results of experimental and theoretical product branching fractions for the CN propene reaction down to 35 K are presented and the astrochemical implications are discussed.

3.1 Introduction

The multiplicity of detected nitrogen-bearing molecules along with their relatively high abundances [McGuire, 2022] highlights a rich gas-phase chemistry for this category of molecules. The cyanopolyynes group, part of the nitrile compounds, can be formed by reactions of CN radicals with hydrocarbons. Some of these reactions are known for more than 30 years to remain rapid at cold temperatures [Morales et al., 2010, Sims et al., 1993]. The C-N group in cyanopolyyne molecules has multiple interests in astrochemistry. In particular, they can be potential building blocks for amino acids and nucleobases. These compounds and the related polyyne species are also presumed to play a role in PAH growth, for which a bottom-up approach is suggested with small hydrocarbons as key intermediates given the recent increase and variety of cyclic and long hydrocarbon chains detected in the ISM [McGuire, 2022]. Waite et al. [2007] also highlights the importance of nitriles and hydrocarbons for the formation of

tholins. These molecules could form aerosols and explain the haze of Titan's atmosphere. Altogether, the study of cyanopolyynes at low temperatures has various interests and can help refine our understanding of various processes taking place in astrophysical media.

Propene ($CH_3CH=CH_2$) is a small hydrocarbon detected in TMC1 at a relative of 4×10^{-9} [Marcelino et al., 2007] and in Titan's upper atmosphere [Waite et al., 2007] and stratosphere [Nixon et al., 2013]. The reaction of CN radical with propene is already known to remain fast at low temperatures. The rate coefficient was measured from 23-298 K by pulsed laser photolysis-laser induced fluorescence (PLP-LIF) in CRESU flows [Morales et al., 2010] and was found to stay constant over the temperature range with an order of magnitude 10^{-10} $cm^3 \times s^{-1}$. This behaviour is characteristic of barrierless or submerged barrier reactions and underlines its importance in the chemistry of the ISM and planetary atmospheres. Recently, Cernicharo et al. [2022] reported the discovery of five cyaonopropene isomers. The reaction of the CN radical with propene is expected to be the primary route for the formation of these molecules. The detected isomers all displayed similar abundances which are, relative to propene, two orders of magnitude less, however, they are not explained by the current experimental data on the CN propene system [Gannon et al., 2007, Gu et al., 2008, Huang et al., 2009, Trevitt et al., 2009, 2011]. Since these isomers have a large energy difference, the authors state that the similar abundances further supports a chemistry driven by kinetics in cold dark cloud rather than thermodynamics where considerations such as the minimum energy principle [Lattelais et al., 2010] would apply. These recent observations highlight therefore the need for new experimental measurements of branching ratios at low temperatures to establish the role of this reaction in astrochemical models.

Various groups have studied the CN radical and propene reaction both experimentally and theoretically. Figure 3.1 summarises the different reaction pathways. Gannon et al. [2007] studied the branching ratios at room temperature using calibrated PLP-LIF of H-atom yield. The H-atom channels were found to be pressure dependent in the range of 2 to 200 Torr. In particular, a fraction of 0.48 ± 0.05 was found for H-elimination channels at 2 Torr. A potential energy surface (PES) was calculated at the G3X//UB3LYP level of theory and used to run master equation calculations to compute the theoretical branching fractions. Excellent agreement was found with their experimental data, therefore, the H and CH_3 yields were extrapolated at low temperatures and pressures relevant to Titan from 90 to 300 K and 0.5 to 5 Torr. In both cases, the channels were found to be pressure dependent across the range of conditions.

Using the crossed molecular beam technique, Gu et al. [2008] gave more insight into the product repartition for H-elimination channels. The experiments were performed under single collision conditions for the reaction of ground state CN radicals with propene and two deuterated isotopologues of propene at a collision energy of (25.5 ± 1.3) kJ mol^{-1}. The results with deuterated isotopologues suggest a repartition of 0.75 for the cis/trans 1-cyanopropene isomer and 0.25 for the 3-cyanopropene isomer. Huang et al. [2009] later performed the calculation associated with this experimental work. A PES was calculated at the unrestricted B3LYP/cc pVTZ level of theory and refined using CCSD(T)/cc-pVTZ. RRKM calculations were performed to determine the rate constants at 0 kcal/mol for the possible paths. They found 3-cyanopropene, trans-1-cyanopropene, and mostly vinyl cyanide as the major products.

Time-resolved mass spectrometry method with tunable synchrotron photoionization was also used to study the product repartition of this system in two studies performed by Trevitt et al.

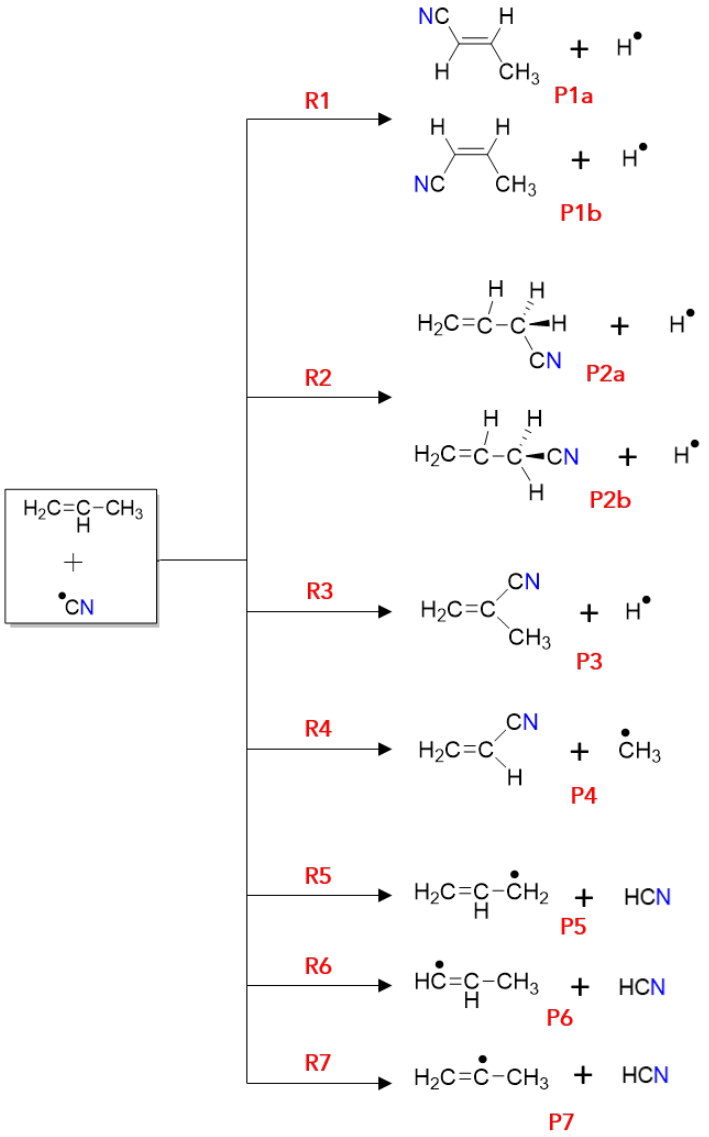

Figure 3.1: CN radical and propene reaction pathways.

[2009, 2011]. The measurements were carried out at room temperature and 4 Torr. In their first study, they found vinyl cyanide as the major route with a yield of 75%. The other 25% was attributed to H elimination channels which form cyanopropene isomers. The latter includes 57% of 1-cyanopropene and 43% of 2-cyanopropene. An upper limit of 15% of 3-cyanopropene was calculated from their measurements. For all reaction channels, no pressure dependence was found in the range of 1 to 6 Torr. Since this result was in contradiction with Gu et al. [2008] and Huang et al. [2009], the authors decided to further explore the reaction in a second study, this time using experimentally measured photoionization spectra for all isomers. Due to similarities in photoionization spectra, an unequivocal assignment remains difficult. In their best fit, 1-cyanopropene appears as the main contributor, the second contribution is more ambiguous. Measurements from equivalent deuterated species provide further evidence of the 3-cyanopropene isomer as the second main contributor to the H-elimination channel. In both

studies, no evidence of HCN formation was found.

All these studies present acrylonitrile as the major product (table 3.1). For the H-elimination channel, if ambiguities remain regarding the contribution of the different isomers, studies all agree on their non-equal ratio. However, the pressure dependence of the two main channels remains a point of disagreement between these different studies despite the similar pressure conditions. Finally, the H-abstraction channel was not reported in any of these papers.

Table 3.1: Summary of previous branching ratio measurements for the CN + propene reaction. *Errors represent a combination of statistical uncertainty (2σ) and an estimate of possible systematic errors. **Errors are reported as 2σ incorporating the uncertainties in both the fit and the photoionization crosssections.

Reaction channel	Gannon* et al. (2007)	Master equation Gannon et al. (2007)	RRKM Huang et al. (2009)		EXPT Trevitt** et al. (2008)	EXPT Trevitt** et al. (2010)
	298 K - 2 Torr	90 K - 0.5 Torr	0 kcal.mol^{-1}	5 kcal.mol^{-1}	293 K - 4 Torr	293 K - 4 Torr
Vinyl cyanide + CH_3	-	0.52	0.7	0.57	0.75 ± 0.15	0.59 ± 0.15
Cis/trans crotonitrile + H			0.12	0.16	0.14 ± 0.03	0.20 ± 0.05
Methyl acrylonitrile + H	0.478 ± 0.045	0.48	~ 0	~ 0	0.10 ± 0.03	~ 0
Cis/trans/gauche allylcyanide + H			0.18	0.26	< 0.03	0.20 ± 0.1
Radical + HCN	-	-	-	-	-	-

Overall, whereas experimental and theoretical results present one of the isomers as negligible, observational data detect them in similar abundances. This underlines the need for data at low temperatures to refine our understanding of this system and its contribution to astrochemical models. In this work, the product channels of CN radical and propene reaction were explored down to 35 K using CP-FTMW spectroscopy. The experimental results are presented and compared with the theoretical calculations made using MESMER.

3.2 Experimental methodology

The reaction products of CN + propene were monitored by chirped pulse microwave spectroscopy at 35 and 52 K. An E-band (60–90 GHz) spectrometer, as described in section 2.4, was used to monitor the spectra from the possible products. A dilute mixture (∼0.1%) of propene (99.5%; Air Liquide) and ICN (Acros Organics, 98%), the CN radical precursor, in a buffer gas (Ar (99.998%)); Air Liquide) was expanded isentropically through a Laval nozzle to generate a cold supersonic flow. All the gases, including Ar and propene, were introduced into the CRESU flow using Brooks gas flow controllers (see section 2.3.2).

The reaction between CN and propene is initiated by ICN photolysis at 248 nm using a KrF excimer laser (Coherent LPXPro 210) with a laser fluence in the reaction zone of ∼49.5 mJ cm^{-2} pulse $^{-1}$ (6.18×10^{16} photons pulse^{-1} cm^{-2}). Photodissociation of ICN at 248 nm produces CN radicals primarily ($\geq$93%) in the ν=0 level of the $X^2\Sigma^+$ state [O'Halloran et al., 1987] and rapid rotational relaxation is ensured by frequent collisions due to the high density of the buffer gas. The ICN concentration was measured using a UV-Vis spectrometer in the range of 200–250 nm, as described in section 2.3.2. An estimated concentration of CN radicals in the flow was calculated using the laser fluence measured inside the chamber and the absorption cross-section

measured by Felps et al. [1991]. Table 3.2 summarises the conditions of the different nozzles along with the reactant densities. The CN concentration is lower than the concentration of propene by at least a factor of one hundred to ensure pseudo-first order conditions.

The CRESU flow is then expanded into a secondary chamber via a 4 mm diameter wide molecular beam skimmer (figure 3.2), which cools the chemical species in the flow, including the formed products, down to around 9 K for all nozzles used in this work. The distance between the nozzle exit and skimmer entry was maintained at 20 cm, providing an approximate reaction hydrodynamic time of ∼500 µs, including the region inside the nozzle after the throat. Based on the acquisition scheme provided in section 2.4.4, the reaction time could be observed at a time step of ∼10 µs. At the beginning of the sequence, 50 µs are used before the laser pulse for background and baseline. An 80 µs delay after the excimer laser pulse for the reaction products to enter the skimmer chamber is to note as well. The chemical species were monitored using either single-frequency or multicolor pulses, to follow the strongest (at 9 K) rotational transition in the 60–90 GHz range, for each product simultaneously (see section 2.4.4). For a reaction scan, 100,000 acquisitions at 100 Hz were collected in ∼16 minutes. Other scans which did not use the excimer laser were run at ∼2 kHz frequency, as there was no limitation from the excimer laser.

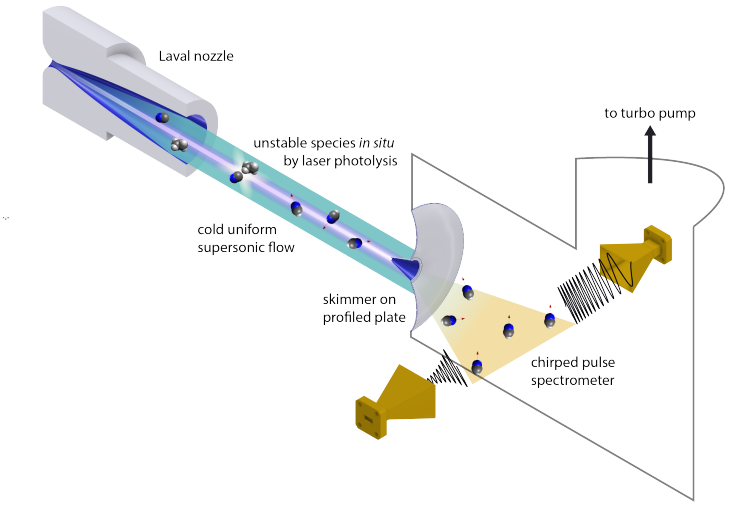

Figure 3.2: Scheme of the SKISURF setup used for the experimental measurements. Credits: Ilsa R. Cooke

Table 3.2: Experimental conditions for the CN radical and propene reaction.

Buffer gas	Temperature (K)	Pressure (mbar)	Total molecular density (cm^{-3})	Propene and ethene density (cm^{-3})	ICN density (cm^{-3})	CN radical density (cm^{-3})
Ar	35	0.295	5.26×10^{16}	5×10^{13}	$\sim 4 \times 10^{12}$	$\sim 1 \times 10^{11}$
Ar	52	0.390	5.15×10^{16}	1×10^{14}	$\sim 2 \times 10^{12}$	$\sim 7 \times 10^{10}$
Ar	52	0.782	10.3×10^{16}	5×10^{13}	$\sim 4 \times 10^{12}$	$\sim 1 \times 10^{11}$

3.3 Theoretical Methodology

The possible channels for the reaction between CN and propene (figure 3.1) were investigated using Gaussian 09 software [Frisch et al., 2009] to identify the different stationary points (minima, complexes, and transition states). All the species, including the reaction complexes and transition states were optimized at the (U)B3LYP/cc-pVTZ and (U)M06-2X/cc-pVTZ levels and zero-point corrected energies were calculated for each. Both addition-elimination channels (R1—R4), leading to cyano-substituted products, and abstraction channels (R5–R7), leading to HCN formation, were considered here. Reactions involving the CN radical may produce both cyano- and isocyano-species, however only the cyano-product pathways were considered in these calculations.

The MESMER software package [Glowacki et al., 2012] was used to calculate the temperature- and pressure-dependent branching ratios of this multichannel reaction. The conversion between the different stationary points (reactants, intermediates, products) of the PES is described using microcanonical rate coefficients calculated with the Inverse Laplace transformation (ILT) for the barrierless entrance process and using the RRKM approach for isomerisation channels. Tunneling is also taken into account using the Eckart approach. As collisions also occur during the process, the energy transfers between molecules are taken into account using the energy grained master equation approach (EGME). Here rovibrational states of similar energy are bundled together into grains. Then, the master equation is used to describe the energy transfer between these grains. This approach is used since describing the transfer of every level in a polyatomic system would be computationally too expensive. Solving these equations gives the full microcanonical description for every energy grain in the system as a function of time. To extract the final phenomenological rate coefficients which link the reactant to the product and extract the related branching ratios, a procedure based on Bartis and Widom [1974] and Miller and Klippenstein [2006] is finally used.

For ME calculations, the average energy transferred ($\langle \Delta Ed \rangle$) in a deactivating collision was taken into account because the collision between the intermediate species with the bath gas could play an important role in controlling the velocities of a reaction and therefore the product branching ratios. Since the probabilities of stabilization of the complex depend on the nature of the colliding gas, He and Ar were used as buffer gas at different pressures. The experimental conditions for the title reaction were used to facilitate comparisons both for the results shown in this work and the results taken from Gannon et al. [2007], Trevitt et al. [2009, 2011].

The Lennard-Jones parameters for He and Ar used in this work were σ = 2.55 Å, ε = 10 K and σ = 3.47 Å, ε = 114 K, respectively. To calculate the energy transfer $\langle \Delta Ed \rangle$, the single exponential down model was used with a temperature dependency given by $A(T/300)^n$, with A = 200 cm^{-1} and n = 0.95 and 0.75 for He and Ar, respectively [Ye et al., 2015]. The Lennard-Jones parameters for all the intermediate complexes were chosen from the similarities in the structures and nature of the functional groups. For σ, the number of atoms in the chain is more important than their nature. For this reason, the same value between the σ of pentane and neo-pentane was used (σ = 5.81 Å). It is the opposite for the ε parameter, which means that to represent the influence of the nitrogen atom in the molecule-molecule interaction, it is important to consider the presence of a more electronegative atom in the chain. In this case, the same value between propanol and iso-propanol was used (ε = 468.1 K) [Mourits and

Rummens, 1977]. For the ILT, an Arrhenius pre-exponential factor $A = 1 \times 10^{-10}$ cm^3 s^{-1} and E_a = 0 were used. The energy grain and the energy above the dissociation threshold were set to 80 cm^{-1} and 20 k_B, respectively, where k_B is the Boltzmann constant.

3.4 Results and discussion

3.4.1 Experimental Results

Rotational diagram

The rotation diagram analysis method was used to characterize the temperature of molecules in the secondary expansion chamber where reaction products are probed. This technique is commonly used in astronomy to derive the rotational temperature (T_{rot}) of the observed species using the intensity of the different rotational lines. Here, the spectrum of vinyl cyanide was recorded in the range 73–78 GHz. The transitions used for the rotational diagrams along with the rotational transitions are provided in appendix A.2. Figure 3.3 shows the rotational diagram for the argon 52 K high pressure nozzle and figure 3.4 the associated vinyl cyanide spectrum. The other rotational diagrams for the argon 35 and 52 K low pressure nozzles are provided in appendix A.3 and A.7 respectively. For all nozzles, a rotational temperature of $\sim$ 9 K was measured in the skimmer chamber. Measuring the rotational temperature inside the skimmer chamber is also a way to check that the sampling of the CRESU flow occurs properly without creating any shock waves. The rotational temperature needs to be lower than the isentropic core one to ensure a proper expansion. The pressure inside the skimmer chamber is also compared with the calculated one to further attest to the sampling conditions.

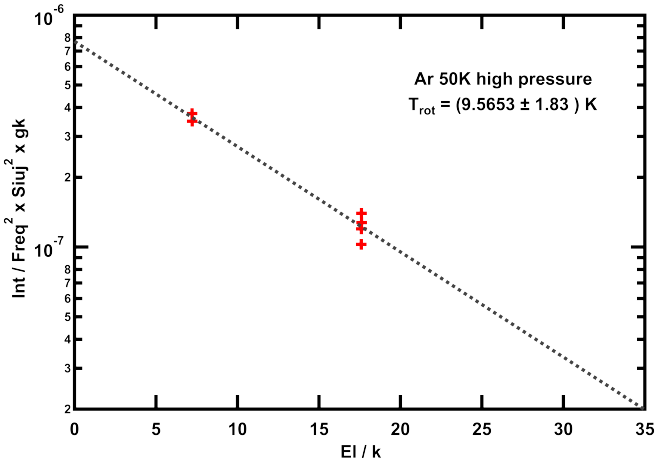

Figure 3.3: Rotation diagram using the line intensities of the vinyl cyanide spectrum for argon 52 K high pressure nozzle. Probing: chirp 73-78 GHz, duration 200 ns, 250 000 accumulations, LO = 74 GHz, Flow VCN = 0.2 g.h^{-1}.

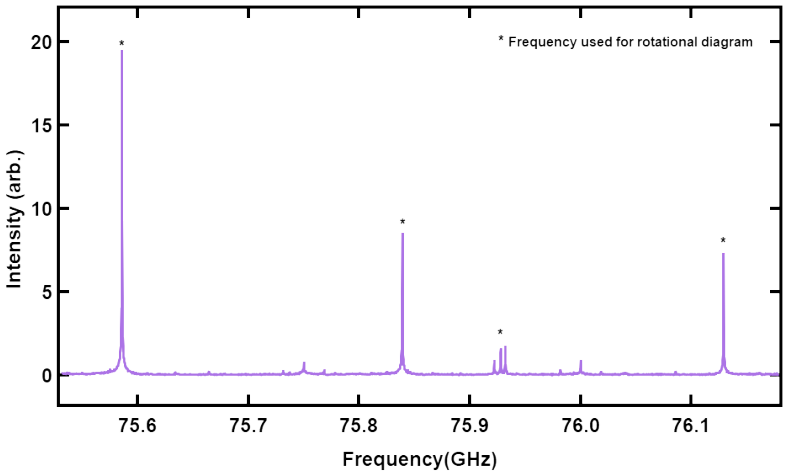

Figure 3.4: Vinyl cyanide spectrum used for rotational diagram analysis. Probing: chirp 73-78 GHz, duration 200 ns, 250 000 accumulations, LO = 74 GHz, Flow VCN = 0.2 g.h^{-1}.

Cluster regime

To avoid possible reactions of the CN radical with the dimers/clusters of propene, it is essential that the concentration of propene is maintained below its dimerization limit. A test was performed by following the intensity of the propene spectral line at 69483.72 MHz ($4_{0,4} \leftarrow 3_{0,3}$) for a series of propene concentrations in the flow. The results for the 35 K nozzle are shown in figure 3.5. A deviation from linearity can be observed at concentrations higher than $\sim 1 \times 10^{14}$ cm^{-3}, thus the concentration of propene used in the reaction scans was maintained at 5×10^{13} cm^{-3}. At 52 K, no deviation was observed up to the maximum density allowed by both nozzles (1% of total density). Therefore, the density was calculated to give a reaction half-life time of the order of 50 µs to ensure a long enough integration time of product signal.

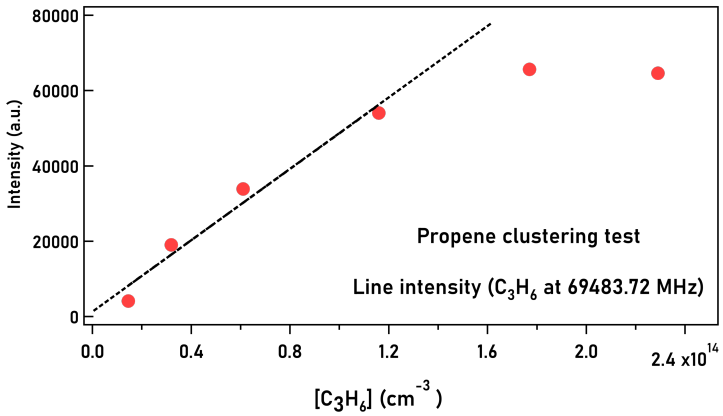

Figure 3.5: Measurement of propene rotational transition intensity as a function of the density of propene in the flow at 35 K. Probing: 80 ns single frequency pulse with 100 000 accumulations, LO = 68 GHz.

Multiproduct detection attempt

The multicolour pulse technique was used to monitor the products from the reaction channels (R1—R4). The details for the multicolour pulse used are given in table 3.3. For 3-cyanopropene, the two stable conformers were considered: cis (synperiplanar) and gauche (anticlinal). While the pulse lengths for trans/cis 1–cyanopropene and vinyl cyanide were optimized using their spectra collected from the pure samples, intuitive guesses based on their known dipole moments were made for the remaining possible products.

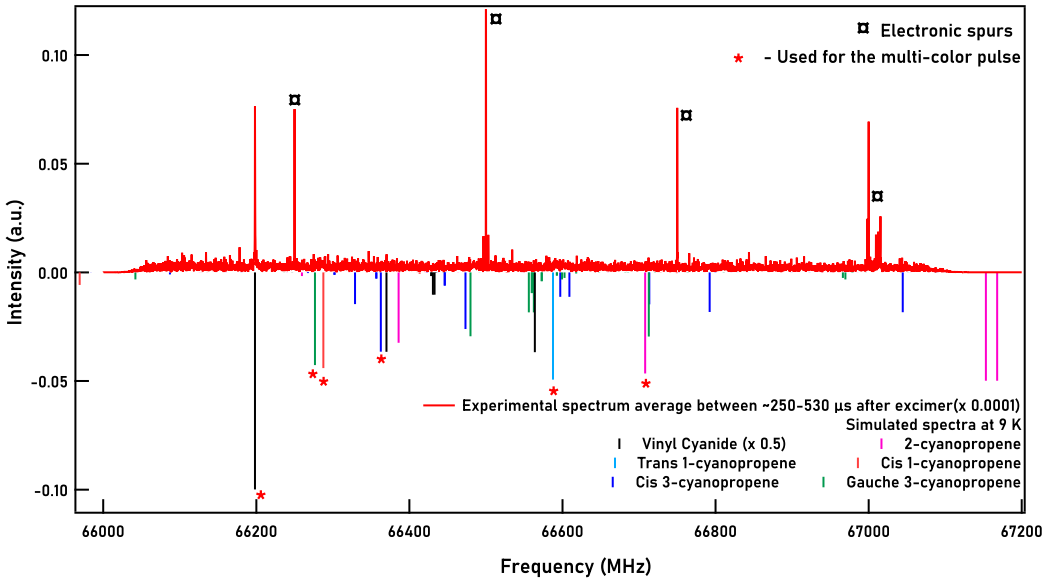

Figure 3.6: Spectrum averaged between 250-530 µs after the excimer laser pulse compared with the simulated spectra (9 K) of the products using SPCAT.

Chemical species	Product label	Frequency (MHz)	Duration of pulse (ns)
trans 1–cyano propene	P1a	66587.66	50 ns
cis 1–cyano propene	P1b	66285.63	90 ns
2–cyano propene	P3	66708.10	70 ns
gauche 3–cyano propene	P2b	66277.00	90 ns
cis 3–cyano propene	P2a	66362.63	110 ns
vinyl cyanide	P4	66198.36	80 ns

Table 3.3: Details of the multicolour pulse used for monitoring the products from the reaction CN + propene.

Figure 3.6 shows the spectrum averaged between 250-530 µs after the excimer laser pulse along with the simulated spectral lines (at 9 K) for all the three cyanopropene isomers and vinyl cyanide. The VAR and INT files used for simulating the spectra for all species are provided

in appendix B.3. Only one product, vinyl cyanide (P4) at 66198 MHz was observed from the reaction. Single-frequency pulses of the different cyanopropene isomers were also used for product monitoring, however, no detection could be confirmed from these attempts.

The figure 3.7 shows the spectral feature of vinyl cyanide rising as reaction time progresses, with the delay time from the excimer laser pulse indicated on top of each trace. Four scans of 100,000 acquisitions each were averaged, giving a SNR of 8.1 for the vinyl cyanide product. The SNR is calculated from the ratio of the line intensity to 2σ of the noise level next to the line.

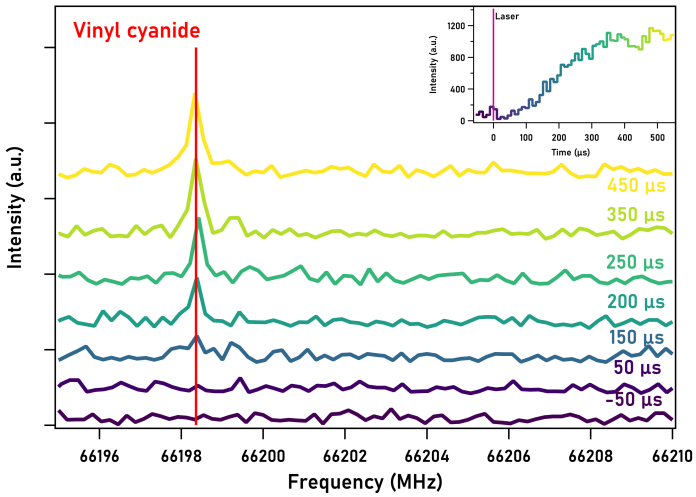

Figure 3.7: Intensity evolution of the rotational feature from vinyl cyanide from the reaction of CN + propene. The time stamps indicate the delay from the excimer laser pulse/start of the reaction. The top inset shows the time dependence of the line intensity. Probing: 80 ns single frequency pulse at 66198.36 MHz (J=$7_{0,7} \leftarrow 6_{0,6}$) with 1 million accumulations (4 scans of 250,000 accumulations averaged together), LO = 74 GHz.

For the H abstraction channel, the only spectral signature observable for HCN product in the 60–90 GHz range under our experimental conditions is at 88631.6 MHz (for the $\mathcal{J}$= 1-0 transition) and could not be monitored at the same time owing to the spectrometer bandwidth limitations. A separate multicolor pulse for HCN and vinyl cyanide was attempted but no signal for HCN could be conclusively found.

Vinyl cyanide branching fraction

Since only one product was detected, a calibration was performed using vinyl cyanide produced from the reaction of CN with ethene. For this reaction, it has been suggested that the main reaction channel leads to vinyl cyanide ($H_2C=CHCN$) and atomic hydrogen. In particular, Choi et al. [2004] measured an H atom branching ratio for this channel of 100 %, while Balucani [2009] and Trevitt et al. [2009] estimate less than a 1% and 2% contributions from the other possible channel producing HCN.

The time dependence of vinyl cyanide (VCN) line intensity for the reactions of CN with ethene

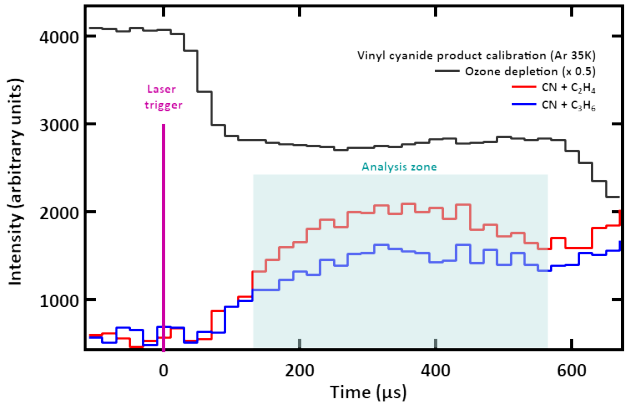

(a)

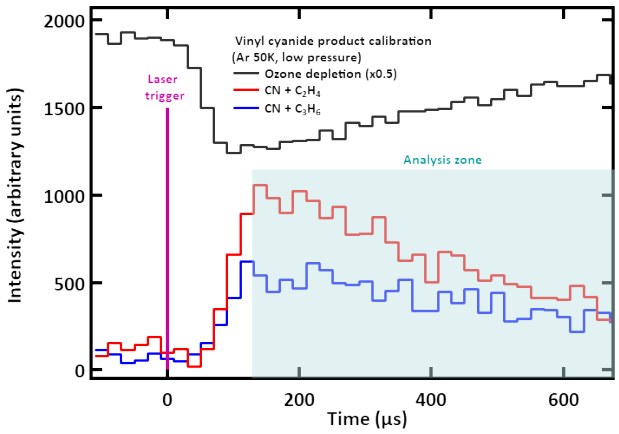

(b)

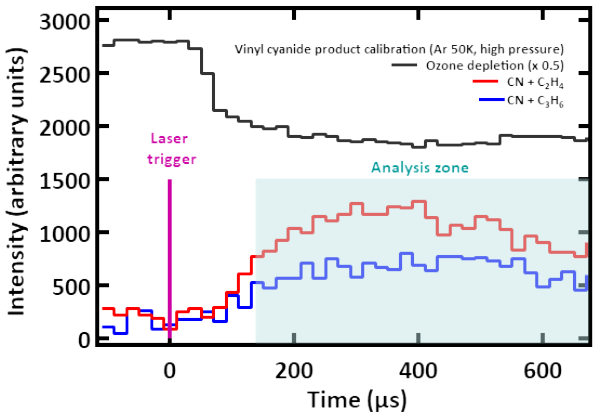

(c)

Figure 3.8: Vinyl cyanide rotational line intensity from reactions of CN with ethene and propene as a function of time measured at (a) 35 K (b) 52 K at low pressure and (c) 52 K at high pressure. Probing for vinyl cyanide: 80 µs single frequency pulse at 66198.36 MHz (J=$7_{0,7}$ $\leftarrow$ $6_{0,6}$) with 250,000 accumulations, LO = 74 GHz. Probing for ozone: 80 ns single frequency pulse at 67 3562 MHz (J= $6_{0,6}$ $\leftarrow$ $5_{1,5}$) with 10,000 accumulations, LO = 68 GHz. The blue shaded zones indicate the measurements used to calculate the branching fraction.

and propene are shown in figure 3.8. Since the product signal in both cases comes from reaction, similar rovibrational relaxation and diffusion in the flow can be supposed. In this case, the signals from ethene and propene reactions are linked by a proportionality factor. As the calibration signal represents 100% of vinyl cyanide, the proportionality factor becomes the branching fraction (BF) of the CN and propene reaction after scaling using the CN concentration (equation 3.1).

$$signal_{propene} = BF \times signal_{ethene} \times \frac{[CN]_{propene}}{[CN]_{ethene}} \tag{3.1}$$

The data analysis method used for each data set (consisting of one reaction scan with ethene and one with propene) proceeds as follows: first, for each nozzle, the analysis zone for which the equation applies must be determined. This depends on the position of the reservoir, which is chosen according to the total hydrodynamic time of the nozzle and the reaction rate. A quick calculation gives an estimate of this value but then an ozone depletion scan was used to experimentally verify the best analysis zone. For this, ozone is introduced in the flow (as described in section 2.3.2) and photolysed at 248 nm with an excimer laser. The signal can be followed over time during the process and gives the black trace in figure 3.8. The plateau observed after the laser trigger corresponds to the zone that can be used for analysis, where the product will be formed. Then, the raw signal from the reaction needs to be scaled for the equation to be applied. This scaling step is necessary as the CN radical density varies slightly with time. For this, the propene scan is multiplied by the ratio between the CN radical density in the propene over the ethene scans. Fluctuations in the laser fluence are negligible as the two scans to be compared are taken one after the other. Finally, the absolute intensity of the VCN signal is calculated by subtracting the averaged pre-laser trigger background from the relative intensity of the transition. Each signal point in this zone follows the equation 3.1, thus the branching fraction can be estimated by averaging the individual BF values for each point. The Igor procedure used for these calculations is provided in appendix B.2.

The results for the three nozzles used are shown in figure 3.8. The reaction was explored at 35 and 52 K and at two different pressures at 52 K (experimental conditions available in table 3.2). Each figure shows the two reaction scans with ethene and propene along with the ozone depletion used to determine the analysis zone. After the laser trigger, there is a 80 µs delay for the product to enter the skimmer chamber and be detected. Then the vinyl cyanide signal rises until it reaches a plateau before slightly diminishing again until the end of the flow uniformity. This reduction is certainly related to diffusion or alignment. For the lower-pressure nozzle at 52 K, a particular behaviour can be observed. The ozone depletion shows a non-flat depletion after the laser trigger. This effect could be due to the diffusion of the probed molecule, the laser and skimmer alignment or a detachment of the boundary layers. However, this tendency remains constant over time and since a calibration method was used, the two reaction scans account for these effects and should not impact the branching fraction calculation.

The error estimation for the measurement of each nozzle includes the statistical uncertainties of branching fraction for repeated measurements (with 95% confidence limits, 2σ) and an estimation of the systematic error. The statistical uncertainty is related to the precision of the measurement and comes mainly from experimental fluctuation. In the case of the SKISURF setup, the measurement precision is mainly affected by the SNR and the ICN density which

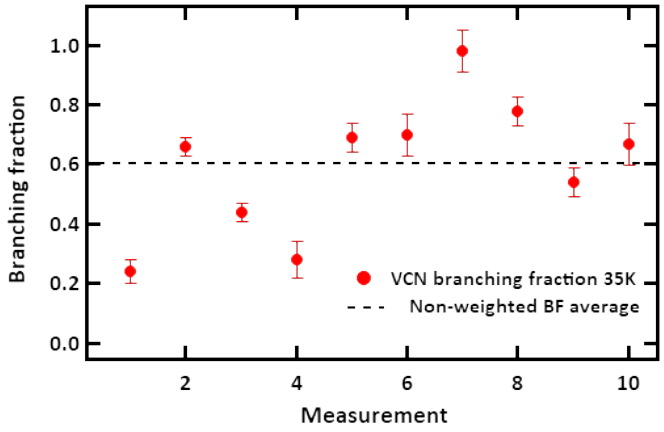

(a)

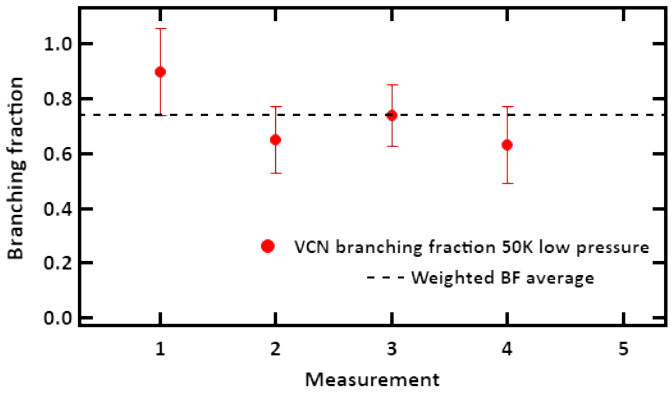

(b)

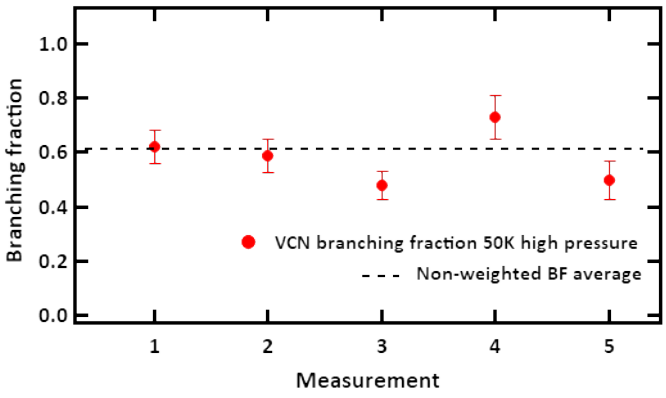

(c)

Figure 3.9: Measurements of branching fractions of vinyl cyanide channel with associated error. The dashed line represents the non-weighted average of all these values for each nozzles. (a) Argon 35 K nozzle (b) Argon 52 K low pressure nozzle (c) Argon 52 K high pressure nozzle. Experimental conditions for all these measurements are provided in appendix B.3.

is subject to fluctuation during the sublimation process. For one run, the branching fraction is determined by averaging the proportionality factor of each point in the analysis zone. The uncertainty of this run can thus be determined with the propagation of error formula taking into account the standard error of the branching fraction and ICN density. The BF measurement for each nozzle was repeated several times. All these values can be combined using a weighted average in order to balance out the importance of each measurement according to its individual uncertainty. However, this requires that the measurements are consistent, i.e. that the discrepancy between the measurements is not much greater than their combined uncertainties. The different measurement points for each nozzle are shown in figure 3.9 together with their individual uncertainties. Here the measurement for the higher pressure nozzle at 52 K shows agreement between all the measurement points, so the data have been combined using a weighted average. In contrast, the other two nozzles show discrepancies between the individual BF measurements. The 35 K measurement was repeated several times in an attempt to reduce this uncertainty, but it is clear that there must be other sources of external error that have not been identified. The fluctuation due to pressure gauges and flow controllers should already be minimal, other sources of external error could come from the laser alignment, diffusion or the flow collimation. The latter could result from boundary layer detachment, thus affecting the flow direction or uniformity. From the nozzle profiles (available in appendix A.2 and A.6), this effect is not noticeable. However, the 2D map is taken at the centre of the flow, so this effect may not be directly visible here, perhaps a 3D pitot map could help to explore this hypothesis. Finally, it is important to note that the high-pressure 52 K data have a lower signal-to-noise ratio than the two other nozzles. Thus each point has a larger error and could explain that all data are consistent. This difference in SNR is due to various factors such as the maximum ICN density that can be introduced, the density of the flow and the pressure in the skimmer chamber.

The likely sources of systematic error affecting this experiment are difficult to estimate. A systematic error of 10 % was added to the final error of the measurements. The random error and the systematic error were combined in quadrature. The final results are given in table 3.4.

For the two branching fractions measured at 52 K, similar values were found within the error range, thus no pressure dependence can be deduced for the vinyl cyanide channel (R4). This appears in contrast with Gannon et al. [2007] theoretical calculation which reported the H atom product yields and CH_3 channels as pressure dependent in the range 0.5 to 5 Torr. The other study from Trevitt et al. [2009] did not report any pressure dependence in the range 1–6 Torr. Since the two measurements at 50 K overlap within their error bars, nothing can be concluded at this point on the pressure dependence of this channel.

Results at both 35 K and 52 K show a similar branching fraction value, pointing to (R4) as the major product of this reaction. This is in accordance with the previous studies at room temperature in the literature on this system [Gannon et al., 2007, Huang et al., 2009] and [Trevitt et al., 2009, 2011]. This suggests that the product branching fraction is temperature independent.

Based on the simulated intensities for the remaining products at 9 K and assuming $\pi/2$ pulse conditions were achieved, the upper limits for the branching fraction for the reaction channels (R1–R3) were estimated to be: 22.17 % for 1-cyanopropene (R1) with 9.56 % and 12.61 % for the trans and cis isomer respectively, 23.90 % for 3-cyanopropene (R2) with 10.42 % and 13.48 %

for the cis and gauche conformer respectively, and 8.50 % for 2-cyanopropene (R3). The upper limits provided for the reaction channels are based on the assumption that all the products formed would be vibrationally relaxed, however since the products explored in this work are large polyatomics, 10–atom species, this assumption may no longer hold true. In these experimental conditions, the vibrational states couldn't be probed and could contribute to the reason why these species were not seen in the recorded spectra.

Table 3.4: Summary of experimental results of branching ratio measurement of the CN + propene reaction. Uncertainties are quoted at 95% confidence with an estimated 10% possible systematic error added in quadrature.

Reaction channel	**Experiments**		
	35 K - 0.295 mbar	**52 K - 0.39 mbar**	**52 K - 0.782 mbar**
Vinyl cyanide + CH_3	60 ± 18 %	71 ± 7 %	58 ± 14 %
Cis/trans 1-cyanopropene + H	$< 22\%$	-	-
2-cyanopropene + H	$< 9\%$	-	-
Cis/gauche 3-cyanopropene + H	$< 24\%$	-	-
C_3H_5 + HCN	-	-	-

3.4.2 Theoretical Results

Note: The PES was calculated by Divita Gupta and the MESMER calculations were done by Rafael A. Jara Toro.

A potential energy surface for the CN propene reaction calculated at the (U)B3LYP/cc-pVTZ level is shown in figure 3.10. All the addition-elimination channels (R1–R4) show a submerged barrier, preceded by a stable complex formation. While the R1 pathway was considered by Gannon et al. [2007], they did not take the two isomers separately into account in their calculations and did not explore the reaction channel R2, leading to 3-cyanopropene. In their study, Huang et al. [2009] found a barrier at CCSD(T)/cc-pVTZ//B3LYP/cc-pvTZ level for the HCN abstraction channel, R5, in contrast with this work where a submerged barrier of -7.8 kcal/mol was found. The two other possibilities for HCN channel leading to R6 and R7 were not located. More efforts to locate the transition states/any possible reaction barriers might be needed as Huang et al. [2009] also show a barrier for both these channels. This would necessitate further accurate energy calculations to establish the role of the HCN abstraction channels at low temperatures.

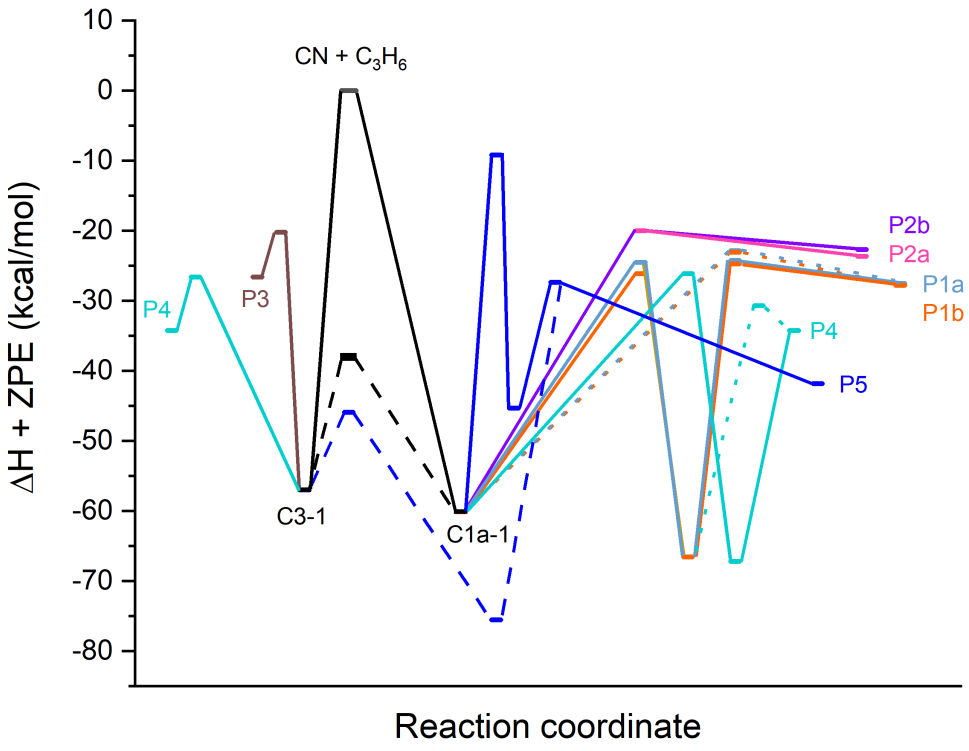

Figure 3.10: Relative enthalpy scheme with ZPE correction for the CN propene reaction. Solid and dotted lines represent the different reactive channels while dashed lines represent the isomerisation channels.

For the entrance channel, C_3H_6 has two accessible sites for the addiction of CN and produces two isomers (C1a-1 and C3-1 in figure 3.10 and 3.11). The addition of CN onto the terminal carbon of the double bond forming the complex C1a-1 should be more favourable because this terminal C is more electronegative and will stabilise more the radical formed on the secondary carbon. This complex also requires less energy to induce changes in the C_3H_6 geometry compared to the addition in the middle carbon (giving C3-1), which is an important criterion at very low temperatures. Therefore, the C1a-1 complex can be presumed to be formed predominantly. In these calculations, both entrance channels were still taken into account as the branching ratio could depend on the isomer formed during the collision process.

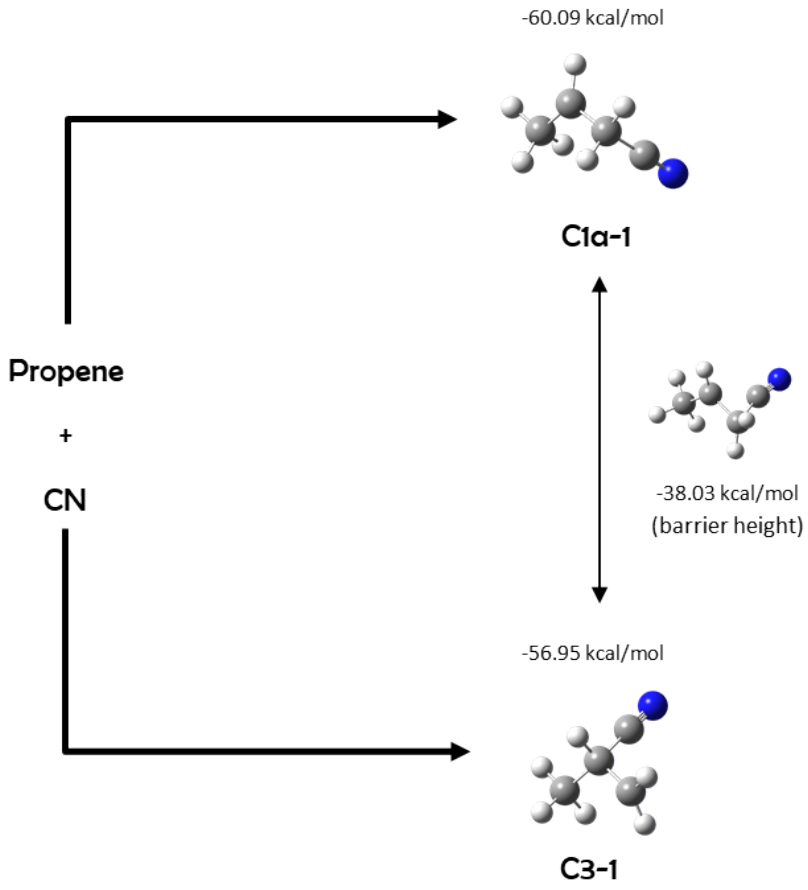

Figure 3.11: Schematic of the entrance channel for the addition of CN onto the propene double bond.

Figure 3.10 shows that the production of HCN + C_3H_5 (P5) is the most exoergic channel. However, there is a larger barrier from the favoured entrance channel forming C1a-1. This barrier could be crossed via tunnelling, leading to a complex that can form either P5 or another complex which could then form C3-1 (figure 3.12). Nevertheless, the difference in energy between P5 and the complex is very large, thus despite the tunnelling, the formation towards the C3-1 complex will be favoured and inhibit the production of P5.

Following the exoergicity presented in figure 3.10, a competition between the P1a, P1b, P3 and P4 channels can be noticed as they are almost iso-energetic. The major product is CH_3

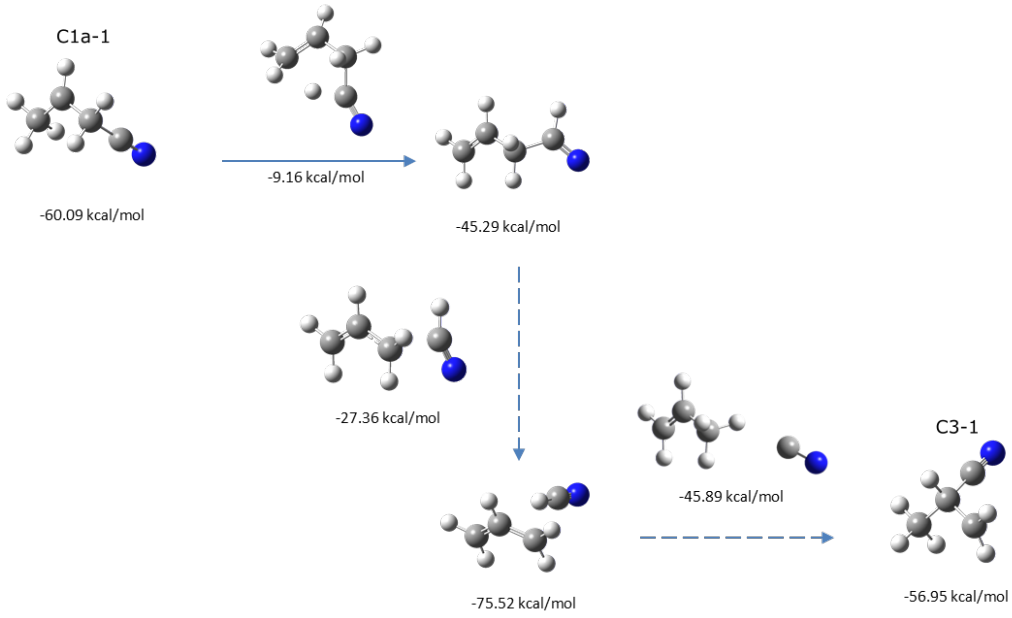

Figure 3.12: Scheme of the isomerisation pathway to go from C1a-1 to C3-1 via the large initial barrier.

+ cyanoethene (P4) as all the intermediate barriers for this reaction path are lower than for the other reaction paths. This was also observed experimentally at different temperatures and pressures and is consistent with the fact that the P5 channel is inhibited by the isomerisation process.

The channels leading to the formation of P2a, P2b and P3 have almost the same energy pathways (barriers previous to the products). Thus the proportion of each product channel is mainly determined by the entrance channel forming C1a-1 or C3-1. For example, if the entrance channel producing C3-1 is more probable than the C1a-1 production and the thermal equilibrium is not reached, the production of P3 will be faster than the P2a and P2b productions because these last processes involve multiple steps. The contrary will be observed if C1a-1 production is more frequent.

This mechanism was tested using the master equations implemented in the MESMER program to compute the branching ratios for the different products. Due to the impossibility of calculating the rate coefficients at temperatures lower than 55 K, the branching ratios were computed in the 300 – 55 K range using results from previous studies and then extrapolated to the experimental temperatures (35 K and 52 K). As there was no significant influence of the pressure in the calculated BF with the two experimental pressures, only the 0.295 mbar pressure was used for all the calculations at different temperatures.

The results of the calculations are provided in table 3.5 for two extreme cases: (i) addition of CN only to the terminal carbon and (ii) equal probability for the addition to both C. The CH_3 + cyanoethene (P4) channel was found dominant with a fraction of 74.04 % and 74.26 % at 52K and 35K, respectively. The H elimination channels forming trans- and cis-1-cyanopropene (P1a and P1b) provided branching fraction of 18.41 % (trans = 9.23, cis = 9.18) and of 18.33 % (trans =

9.19 %, cis = 9.14 %) and the formation of cis- and gauche-3-cyanopropene (P2a and P2b) show a fraction of 6.19 % (cis = 3.11, gauche = 3.08) and the 6.12 % (cis = 3.08 %, gauche = 3.04 %) at 52 K and 35 K respectively. The production of 2-cyanopropene (P3) was found to be negligible (2×10^{-2} % and 3×10^{-2} %) in all cases which is in accordance with the previous studies by Huang et al. [2009], Trevitt et al. [2011]. Finally, for the HCN + C_3H_5 (P5) exit channel, branching fractions of 1.34 % and 1.26 % were calculated at 52 K and 35 K respectively.

All the calculated branching fractions are in good agreement with the experimental measurements. The cyanopropene isomers are found to be formed at less than 10 % yield, considering the distinction between the different isomers. The upper limits derived for these molecules being around 20%, it explains the impossibility of observing them in the current experimental conditions. The same observation goes for the HCN abstraction channel.

The current abundances measured in TMC1 by Cernicharo et al. [2022] are however not consistent with these calculations. The three isomers were observed in similar abundances while this study and previous room temperature measurements show the 2-cyanopropene isomer as negligible. This could come from the extrapolation at lower temperatures which no longer holds true. This system being quite complex, it remains difficult to state the veracity of this hypothesis. Dark clouds usually have temperatures down to 10 K and the LTE conditions usually are not attained. A final possibility would be that the 2-cyanopropene isomer is produced from another chemical reaction.

Table 3.5: Summary of theoretical results of product branching fractions for the CN + propene reaction calculated using MESMER. The results at 298 K are extracted from Trevitt et al. [2009, 2011]. The data at 52 and 35 K are extrapolated from the calculated data. Values in parenthesis consider the same probability to form C1a-1 and C3-1 complexes after the reactant collision.

T (K)	P (Torr)	Vinyl cyanide + CH_3	2-cyanopropene + H	trans 1-cyanopropene + H	cis 1-cyanopropene + H	cis 3-cyanopropene + H	gauche 3-cyanopropene + H	HCN + C_3H_5
298	4 (He)	75	43	57		<15		-
			25					
298	4 (He)	59	-	50		50		-
			41					
300	4 (He)	70.49 (70.54)	0.01 (0.01)	10.74 (10.65)	10.51 (10.43)	4.06 (4.03)	4.04 (4.00)	0.16 (0.34)
			29.35 (29.12)					
300	4 (Ar)	70.48 (70.52)	0.01 (0.02)	10.72 (10.61)	10.49 (10.38)	4.06 (4.01)	4.03 (3.99)	0.22 (0.48)
			29.30 (29.01)					
300	0.59 (Ar)	70.34 (70.25)	0.03 (0.06)	10.33 (9.83)	10.11 (9.63)	3.90 (3.71)	3.88 (3.68)	1.41 (2.85)
			28.25 (26.91)					
300	0.22 (Ar)	70.13 (69.88)	0.07 (0.13)	9.67 (8.72)	9.48 (8.55)	3.65 (3.27)	3.62 (3.25)	3.38 (6.19)
			26.49 (23.93)					
250	0.22 (Ar)	71.06 (70.77)	0.05 (0.10)	9.61 (8.79)	9.44 (8.65)	3.52 (3.21)	3.49 (3.18)	2.83 (5.29)
			26.11 (24.94)					
200	0.22 (Ar)	71.91 (71.63)	0.04 (0.08)	9.53 (8.89)	9.40 (8.78)	3.40 (3.16)	3.38 (3.14)	2.34 (4.32)
			25.75 (24.05)					
160	0.22 (Ar)	72.54 (72.25)	0.03 (0.07)	9.47 (8.88)	9.36 (8.78)	3.32 (3.10)	3.29 (3.08)	1.99 (3.85)
			25.47 (23.90)					
110	0.22 (Ar)	73.27 (73.00)	0.03 (0.05)	9.38 (8.89)	9.30 (8.82)	3.22 (3.04)	3.19 (3.02)	1.62 (3.18)
			25.11 (23.83)					
105	0.22 (Ar)	73.34 (73.07)	0.03 (0.05)	9.37 (8.89)	9.29 (8.82)	3.21 (3.04)	3.18 (3.01)	1.59 (3.12)
			25.07 (23.81)					
70	0.22 (Ar)	73.80 (73.54)	0.02 (0.04)	9.29 (8.86)	9.22 (8.80)	3.14 (2.98)	3.11 (2.96)	1.42 (2.80)
			24.78 (23.66)					
55	0.59 (Ar)	74.21 (74.13)	0.01 (0.02)	9.47 (9.29)	9.41 (9.23)	3.19 (3.12)	3.16 (3.10)	0.54 (1.12)
			25.24 (24.75)					
55	0.22 (Ar)	74.01 (73.74)	0.02 (0.04)	9.23 (8.81)	9.17 (8.76)	3.10 (2.95)	3.08 (2.93)	1.34 (2.77)
			24.59 (23.49)					
52	0.22 (Ar)	74.04 (73.78)	0.02 (0.04)	9.23 (8.81)	9.18 (8.76)	3.11 (2.95)	3.08 (2.93)	1.34 (2.67)
			24.48 (23.36)					
35	0.22 (Ar)	74.26 (74.00)	0.03 (0.04)	9.19 (8.77)	9.14 (8.73)	3.08 (2.92)	3.04 (2.90)	1.26 (2.53)
			24.48 (23.36)					

3.5 Conclusion

This is the first experimental detection of vinyl cyanide from the reaction between CN radicals and propene below room temperature. The branching fraction was measured for the vinyl cyanide product channel (R4) using a calibration reaction. While attempts to observe other products from this reaction were not successful, upper limits for all the cyanopropene isomers were established. The vinyl cyanide product channel (R4) was found to be a major channel for this reaction down to 35 K. No evidence of pressure dependence for this channel was found at 52 K within experimental uncertainty. The theoretical calculations using MESMER are in accordance with the measured values. They provide further evidence on why the various cyanopropene isomers and HCN channels could not be detected. The current sensitivity of the spectrometer, which can be defined with the calculated upper limits, corresponds with the theoretical branching fractions estimation, thus the signal-to-noise ratio is currently insufficient. The future direction for this work would be to achieve a higher signal-to-noise ratio by improving the experimental setup. This could be done with the development of pulsed CRESU flows, which would allow more flexibility in the nozzle designed conditions. Another possibility to increase the SNR would be to use a different analysis method such as spectral stacking [Loomis et al., 2021]. This method is commonly used in astronomy to detect weak rotational lines and could be explored to this extent. Finally, the apparent external error source should be explored to reduce it to a minimum. This will help to reduce the overall error in the measured branching fraction and may allow a proper pressure dependence study for the vinyl cyanide channel. Overall, this study supports that the cyanopropene isomers are not formed in equal amounts at low temperatures, despite the current observation in TMC1. The reason for this is not clear yet but might be due to the non-thermal equilibrium conditions in dark clouds which could potentially affect the product repartitions or due to the formation of 2-cyanopropene isomer through another chemical reaction.

Chapter 4

Heterodimer formation: formic acid – CO_2 dimer kinetics

On dit de plus en plus souvent « c'est complexe » pour éviter d'expliquer. Ici il faut faire un véritable renversement et montrer que la complexité est un défi que l'esprit doit et peut relever

– Edgar Morin

Note: These measurements were performed in collaboration with postdoctoral fellow Dr Alberto Macario Farto.

4.1 Introduction

The nucleation process is the first step of a phase transition. This transformation occurs through the formation of non-covalent bonds between molecules. Nucleation has a large panel of applications as this process is ubiquitous in nature and plays an important role in many fields such as biology, nanotechnology or atmospheric sciences [Li and Signorell, 2021, Zhang et al., 2012]. In astrochemistry, this type of process is relevant for planetary and cometary atmospheres and in the formation of dust particles [Gobrecht et al., 2022].

The nucleation process is characterized by both a decrease in enthalpy and entropy. Thus despite being thermodynamically favourable, the decrease in entropy does not necessarily make this type of reaction spontaneous. A Gibbs energy barrier will often be involved and need to be overcome before the cluster growth becomes spontaneous. This barrier (ΔG_k) can be expressed as the difference in chemical potential between the condensed phase and the vapour phase ($\Delta\mu$) and the cluster surface energy ($F(k)$), where k refers to the number of

molecules contained in the cluster.

$$\Delta G_k = k\Delta\mu + F(k) \tag{4.1}$$

As the saturation S of the medium increases, $k\Delta\mu$ becomes negative but the surface energy of the cluster might still be positive, resulting in a barrier. As the cluster grows, the surface energy will decrease until it becomes equal to the difference in chemical potential, the process will therefore become barrierless (figure 4.1). The size of the cluster for which the process becomes spontaneous is called the critical cluster size.

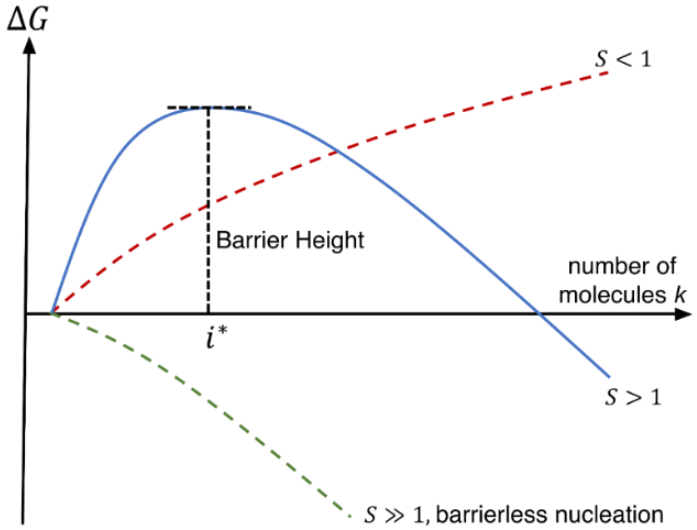

Figure 4.1: Gibbs free energy of cluster formation as a function of the cluster size for different degrees of saturation S.

The classical nucleation theory (CNT) is often used to describe nucleation processes. This theory is easy to implement as it only requires bulk material properties and allows to extract rates for the critical cluster size formation. These rates can also be measured experimentally with a condensation chamber such as the CERN CLOUD [Wang et al., 2022]. The CNT however fails when the critical cluster size is small. In this case, theory accounting for molecular interactions is required. For instance, the kinetics of cluster formation can be derived using the Becker and Döring [1935] model, for which the growth of clusters is considered via a sequence of association and dissociation of monomers. During the process, there is a critical cluster size for which the dissociation rate is equal to the association rate. At this point, for larger clusters, the association rate will be greater than the dissociation rate, therefore, the formation of increasing size particles becomes spontaneous. For this reason, the evaluation of the nucleation rate passes by the determination of this critical cluster size. The latter is influenced by the supersaturation of the medium and temperature. The degree of saturation (S) is defined as $S = P_{cond}/P_{eq}(T)$, where P_{cond} is the partial pressure of the condensable species and $P_{eq}(T)$ is the equilibrium vapour pressure of the condensable species at temperature. The system is described as supersaturated when S > 1. Under sufficiently highly supersaturated conditions, the dimerisation process can become the rate-determining step [Bourgalais et al.,

2016b, Kalikmanov and Hagmeijer, 2019, Li et al., 2021]. In this case, the growth of clusters becomes kinetically controlled rather than thermodynamically controlled as there are no reverse processes to bring about equilibration. As the temperature is lowered, the vapour pressure of many molecules can be less than a millibar, thus supersaturation conditions can be reached easily depending on the density of the media.

The dimerisation process is still poorly understood due to the experimental difficulties that it brings and results in a lack of studies on the subject. This process can be viewed with the Lindemann-Hinshelwood mechanism presented in chapter 1. The two molecules collide forming an excited complex which then needs a third body collision to relax in the ground state and form a stable complex. To measure experimentally the dimerisation rate coefficient, the absolute densities of the reactant or products need to be followed over time. This implies a proper media where the concentrations of molecules can be followed with accuracy while reaching the supersaturation conditions and avoid other complex formations such as with the buffer gas for instance.

Most direct studies on dimerisation have been performed for homodimers, where both monomers are the same molecule, and employed the CRESU technique as it provides a cold environment where supersaturation conditions are easily reached. These studies were performed coupling CRESU flows with LIF [Hamon et al., 2000] or with mass-spectrometry [Biennier et al., 2011, Bourgalais et al., 2019, 2016b, Li et al., 2021, Sabbah et al., 2010]. The kinetics of homodimerisation follows a second-order rate law and implies an absolute measurement of the concentration of monomer in order to determine the absolute rate coefficient. In the case of experiments performed with Laval nozzles, the throat represents a limitation for absolute concentration measurement. In this region, the conditions are not exactly known, the temperature has already gone down and the high pressure conditions make it an ideal environment for the formation of clusters prior to the start of the uniform region of the flow. Therefore the absolute concentration cannot be measured in these conditions. For this reason, the studies on homodimerisation usually provide an estimation of the rate and are measured indirectly.

The kinetics of heterodimer formation on the other hand, where monomers are two different molecules, can be simplified by introducing one of the reactants in excess and allow a determination of the absolute rate coefficient under pseudo-first order conditions without absolute concentration measurement of one of the species. The formation of heterodimers is widely thought to be more efficient and predominant in most of the environments where pre-existing particles are present [Lavvas et al., 2011]. Among the few studies on this kind of process, the acetaldehyde-water formation rate was estimated indirectly by measuring the rate of the OH and acetaldehyde reaction using laser-induced fluorescence in CRESU flows [Neeman et al., 2021]. Another study by Li et al. [2021] measured the nucleation enhancement between some organic molecules such as toluene, propanol or water with CO_2 using soft photoionisation in CRESU flow to measure cluster distributions and estimate rates via fits to a model. Finally, Satterthwaite et al. [2023] claimed to have measured the rate coefficient of the heterodimer formation of ethanol and methanol in a cryogenic cell using microwave spectroscopy. While these studies start to bring more insight into the heterodimer formation, a lot of work remains to provide exhaustive kinetics parameters that can be used in models.

In the case of heterodimer formation, the ability to distinguish different conformers or isomers becomes important as it can possibly influence the different reaction products. For this

reason, the chirped-pulsed spectroscopy technique is particularly appropriate as it allows the differentiation of all molecules. In this study, it was coupled with CRESU flow which provides a low temperature medium where supersaturated conditions can be easily reached.

This chapter presents some work performed on the kinetics measurement of the formation of the formic acid (FA) and CO_2 complex. FA is the simplest carboxylic acid, which has a wide range of interest both in atmospheric and astrochemical studies. In particular, it was detected in various astrophysical environments such as dark clouds, planetary and cometary atmospheres [Favre et al., 2018, Zuckerman et al., 1971]. As briefly discussed in the introduction chapter 1, CO_2 can become the main constituent of the cometary comae depending on the distance to its star. In this case, the chemistry will be mainly driven by this component [Biver et al., 2022]. If the density is high enough, the complexation between CO_2 and FA might become relevant for cometary and planetary atmospheres, thus the dimerisation rate measurement could be input in their models. The FA-CO_2 system was also chosen for this study to serve as a benchmark for heterodimer formation combining CRESU flows with chirped pulse microwave spectroscopy.

4.2 Experimental method

4.2.1 Setup description

The dimerisation reaction between FA and CO_2 was monitored by chirped pulse microwave spectroscopy at 38 and 52 K. The E-band spectrometer (60-90 GHz), described in chapter 2 section 2.4, was used to monitor the FA decay and FA-CO_2 complex appearance. A dilute mixture of CO_2 (Air liquide, 99.995%) and formic acid (Merck, 99.8%) in a buffer gas (argon, 99.998% or nitrogen, 99.995%; Air Liquide) was expanded isentropically through a Laval nozzle to generate a uniform supersonic flow. The formic acid was either introduced via a controlled evaporation mixer (see section 2.3.2) or via Brooks gas flow controllers using a pre-made mixture of FA and buffer gas (see section 2.3.2).

The SKISURF setup (see chapter 2 section 2.4.2) was used to measure the reaction kinetics. Here the CRESU flow is sampled into a secondary expansion chamber via a skimmer of 4,3 or 2 mm diameter (see chapter 1). This sampling step cools down the molecules and provides a low pressure environment for probing. When coupling a nozzle with a skimmer, one must pay attention to the potential creation of shock waves which could affect the sampling of the flow and possibly destroy any weakly bound complexes. The nozzle sampling conditions were verified using a rotational diagram with vinyl cyanide (VCN). The pressure in the skimmer chamber during the experiment was also compared to the predicted one to further attest to the usability of the nozzle. An example of a rotational diagram for the nitrogen 38 K nozzle coupled with a 4 mm skimmer is shown in figure 4.2. The other rotational diagram for the argon nozzle is available in figure 3.3. A chirp between 73 and 78 GHz and LO of 74 GHz was used to probe the various VCN transitions (provided in appendix A.2). The pressure inside the skimmer chamber was 8 µbar and corresponds with the predicted one. The analysis gave a rotational temperature of $\sim$ 15 K for the nitrogen nozzle and $\sim$ 9 K for the argon nozzle.

The complexation reaction is followed over time by changing the reservoir position relative

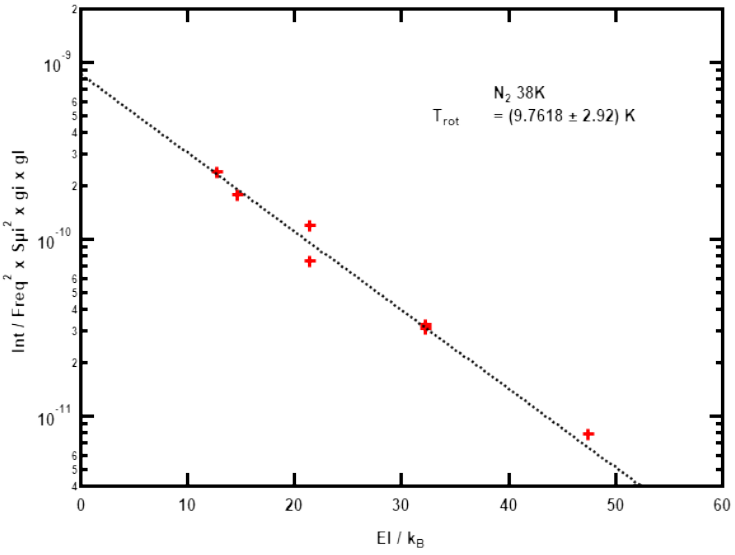

Figure 4.2: Rotational diagram acquired with 0.2 g/h of vinyl cyanide in the flow. The flow of the nitrogen 38 K nozzle was sampled using a 4mm skimmer. $P_{reservoir}$ = 470 mbar and $P_{chamber}$ = 0.39 mbar $P_{skimmer}$= 8 µbar. Probing: 200 ns chirp between 73-78 GHz with 250 000 accumulations, LO = 74 GHz.

to the probing region (figure 4.3). Since the gas in the isentropic core has a constant velocity (v), the corresponding reaction time can be defined as

$$t = \frac{x}{v} \tag{4.2}$$

Where x is the distance between the end of the nozzle and the entrance of the skimmer chamber.

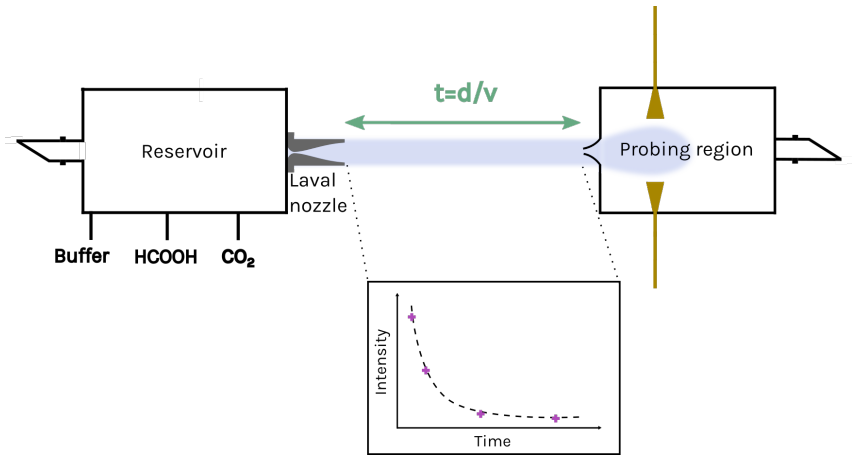

Figure 4.3: Schematic of the experimental setup for rate coefficient measurement of heterodimer formation.

The total time for the reaction kinetics study is determined by the nozzle's total hydrodynamic

time. As the measurements are performed under pseudo-first order conditions, only the slope of the second-order plot is necessary to extract the final rate coefficient. Therefore, the time inside the nozzle does not need to be taken into account as the formation of complexes in this part will not affect this slope under pseudo-first order conditions.

While the isentropic region of the Laval nozzle is quite uniform, there is still some slight variation in the temperature and density conditions. This effect can be observed by looking at the Pitot map discussed in chapter 2 section 2.2.2. These variations will affect the signal intensity depending on the reservoir position. To correct this effect, each nozzle was characterised by measuring the signal variation in the function of the reservoir position. For this normalisation procedure N_2O signal intensity was used. An example of signal variation is shown in figure 4.4. Here the 38 K nozzle was characterised between 16 and 52 cm with 2 cm steps. The scans were acquired with a density of N_2O in the flow of 8×10^{13} cm^{-3}. A 170 µs single frequency pulse was used to follow the transition at 75 369 MHz ($3 \leftarrow 2$). These data were then used to correct the reactant or product signal intensity. This test was also used to determine the minimal distance between the nozzle and the probing region. If the nozzle is too close to the skimmer holder, this can cause perturbation in the flow, possibly due to problems in effective conductance, which could therefore affect the sampling of the flow.

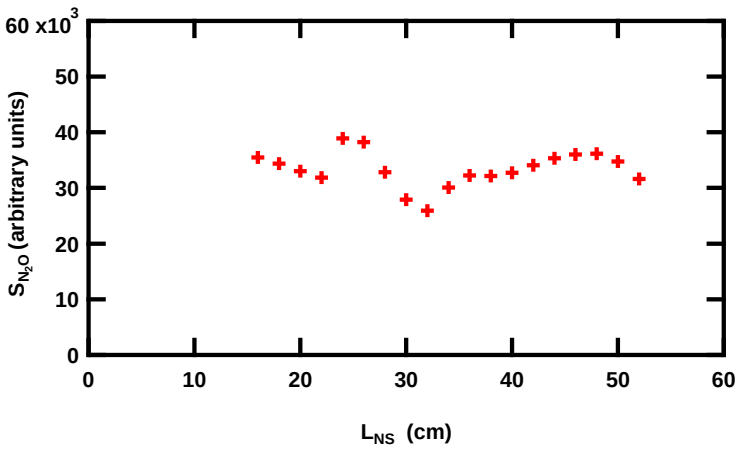

Figure 4.4: N_2O (8×10^{13} cm^{-3} in the flow) signal intensity as a function of the reservoir position. Probing conditions: 75 369 MHz frequency, pulse length = 170 µs with 10,000 accumulations, LO=74 GHz. Acquired in nitrogen 38 K nozzle with 4 mm skimmer. Reservoir between 16 and 52 cm with 2 cm steps.

Based on the acquisition scheme described above and in chapter 2 section 2.4.4, the kinetics of dimerisation was measured either following the formic acid decay using a single frequency pulse with the 67 291 MHz transition ($3_{0,3} \leftarrow 2_{0,2}$) or by following the complex FA-CO_2 line at 65 738 MHz ($5_{(5)} \leftarrow 4_{(4)}$). For each scan, the number of acquisitions is adjusted as a function of the SNR which depends on the nozzle and probed molecule. The maximum acquisition number is 1 million which gives an acquisition time of ∼16 minutes at ∼2 kHz repetition rate.

4.2.2 Experimental procedure and analysis method for the FA-CO_2 system

The heterodimer formation reaction is a termolecular association which follows the Lindemann Hinshelwood mechanism (see chapter 1 section 1.2). The reaction can be written as follows

$$FA + CO_2 \rightleftharpoons FA\cdot\cdot CO_2^* + M \longrightarrow FA\cdot\cdot CO_2 + M \tag{4.3}$$

The measurement of the rate coefficient was performed under the pseudo-first order conditions, as described in chapter 1 section 1.2. One of the reactants is introduced in excess compared to the other one to simplify the rate law. Here, CO_2 was chosen to be in excess as the FA homodimer has a stronger binding energy (4974 cm^{-1} [Kalescky et al., 2014]) compared with the CO_2 homodimer (455 cm^{-1} [Illies et al., 1987]). Since FA-CO_2 has a higher binding energy (1420 cm^{-1} [Vigorito et al., 2015]) than CO_2 dimer, the heterodimer formation will be favoured in these conditions. The rate law for the reaction can be written as

$$[FA]_t = [FA]_0 exp(-kt[CO_2]) \tag{4.4}$$

The rate coefficient k of dimerisation can be determined in two ways. Firstly by following the decay of FA signal either as a function of time at a fixed [CO_2] or as a function of [CO_2] at a fixed time. The signal from this plot can be fitted to derive the pseudo-first order rate coefficient. This measurement is repeated for different values of the other variable, [CO_2] concentrations or time respectively. The final rate coefficient can be extracted with linear fit of the different pseudo-first order rate coefficients. For this work, the measurement of the pseudo-first order rate was performed at a fixed time (fixed reservoir position) and variable concentration of CO_2. These measurements were repeated for various reservoir positions to extract the final rate. Under these pseudo-first order conditions, the rate law becomes

$$[FA]_t = [FA]_0 exp(-k'[\mathrm{CO_2}]) \tag{4.5}$$

where $k' = kt$.

Another method consists of following the appearance of the FA-CO_2 complex as a function of time. The same principle applies but here another equation is needed to fit the data. This model has to take into account both the appearance of the complex and the potential destruction pathways. In this work, a first simple model was used to fit the data and take into account the formation of the homodimer and its destruction with a reaction with CO_2. The reaction scheme is as follows

$$\mathrm{FA} + \mathrm{CO_2} \xrightarrow{k_1} \mathrm{FA\cdot\cdot CO_2} + \mathrm{CO_2} \xrightarrow{k_2} \mathrm{P}$$

The rate law can be expressed as

$$\begin{aligned}\frac{d[FA\cdot\cdot CO_2]}{dt} &= k_1[FA][\mathrm{CO_2}] - k_2[FA\cdot\cdot CO_2][\mathrm{CO_2}] \\ &= k_1[\mathrm{CO_2}][FA]_0 e^{-k_1[\mathrm{CO_2}]t} - k_2[FA\cdot\cdot CO_2][\mathrm{CO_2}]\end{aligned} \tag{4.6}$$

This differential equation can be solved using Laplace transformation. The concentration of FA-CO_2 complex can finally be derived as

$$[FA \cdot \cdot CO_2] = \frac{k_1[FA]_0}{k_2 - k_1}(e^{-k_1[\mathrm{CO_2}]t} - e^{-k_2[\mathrm{CO_2}]t}) \tag{4.7}$$

It is worth noting that formic acid presents two conformers, the cis and the trans. The energy gap between these two conformations is 1365 cm^{-1} [Hocking, 1976] which gives a relative population of 100:0.1, the most stable conformer being the trans-FA. The interconversion barrier between the two conformers is 4827 cm^{-1}. The most stable FA-CO_2 complex is formed with trans-FA as its structure forms a pseudo-six-membered ring, making it very stable. Figure 4.5 presents the spectrum of the cis and trans formic acid observed in the argon 35 K nozzle. Comparing the intensity between trans and cis-FA, the same 100:0.1 ratio was found.

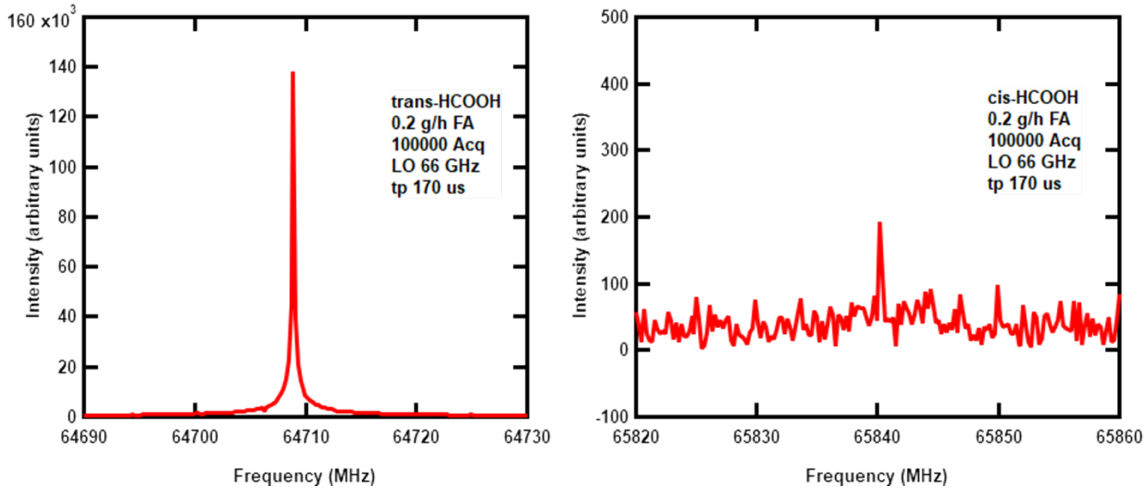

Figure 4.5: Frequency spectrum of trans (left panel) and cis (right panel) formic acid. Acquired in argon 35 K nozzle.

Establishing the experimental conditions

To be able to measure the dimerisation rate of FA and CO_2, the right experimental conditions have to be established in order to avoid potential cross-reactions that could affect the reactant/product signals. In particular, the homodimerisation of CO_2 and FA has to be avoided as well as the formation of heterodimers with the buffer gas. These homodimers lack a dipole moment and thus cannot be probed directly using rotational spectroscopy.

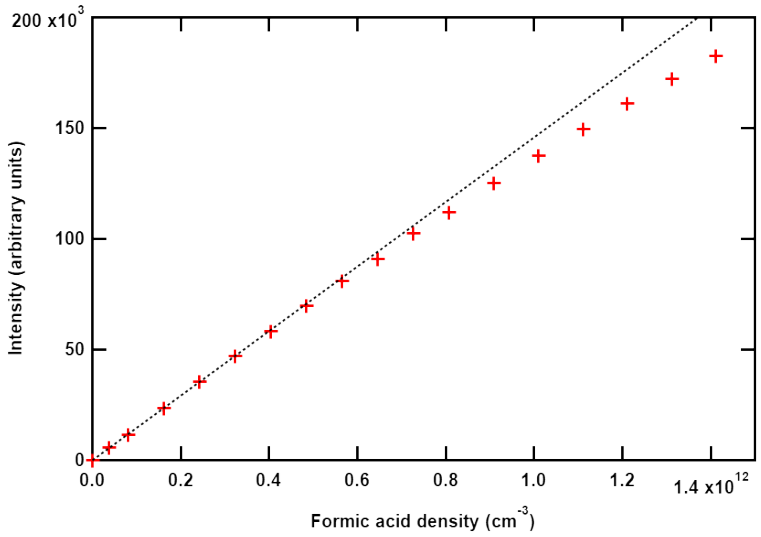

Figure 4.6: Signal intensity as a function of the formic acid density. Probing conditions: 67 291 MHz transition ($3_{0,3} \leftarrow 2_{0,2}$), pulse length = 170 µs with 100,000 accumulations, LO = 68 GHz. Acquired in argon 52 K nozzle with 3 mm skimmer.

As mentioned above, the FA-FA dimer is quite stable with a binding energy of 4974 cm^{-1} [Kalescky et al., 2014]. This dimer presents a pseudo-eight-member ring stabilised by resonance with the hydrogen bond. At room temperature, the dimer is already present in the reservoir, however, given the high binding energy, the dimer is not supposed to dissociate and interfere with the measurement. The possible FA densities to be used in the flow were determined with a cluster test by following the formic acid signal as a function of FA density. The deviation from linearity of the signal gave the maximum density of formic acid for a given nozzle. Figure 4.6 shows an example of a formic acid clustering test in the argon 52 K nozzle.

The same consideration goes for the formation of CO_2-CO_2 homodimers. However, the CO_2 molecule does not have a dipole moment, thus it cannot be probed using chirped pulse microwave spectroscopy. To determine the maximum density of CO_2, the N_2O molecule was used instead as a proxy to estimate the start of the complexation of CO_2. N_2O was chosen as it is a triatomic linear molecule with a similar molar mass and presents the same homodimer slipped-parallel geometry [Walker et al., 2008]. Its binding energy (598 cm^{-1} [Berner et al., 2009]) is slightly higher than the CO_2 dimer (455 cm^{-1} [Illies et al., 1987]) and thus ensure an overestimation of the CO_2 homodimerisation. Figure 4.7 shows an example of cluster test using N_2O in the argon 52 K nozzle.

The complexation of either FA or CO_2 with the buffer gas might also affect the reaction by impacting the FA decay or opening another pathway for the FA-CO_2 complex formation. The FA-Ar complex has been studied by Ioannou and Kuczkowski [1994] using rotational spectroscopy. They estimate the complex binding energy to be 126.3 cm^{-1}. Despite research using single-frequency pulses, the FA-Ar complex was not observed down to 35 K, providing further evidence that this complex might not be formed in the uniform flow. The FA-N_2 complex has not been studied using rotational spectroscopy, thus its presence in the uniform flow could not be confirmed. The complex of CO_2-Ar has also been studied using rotational spectroscopy

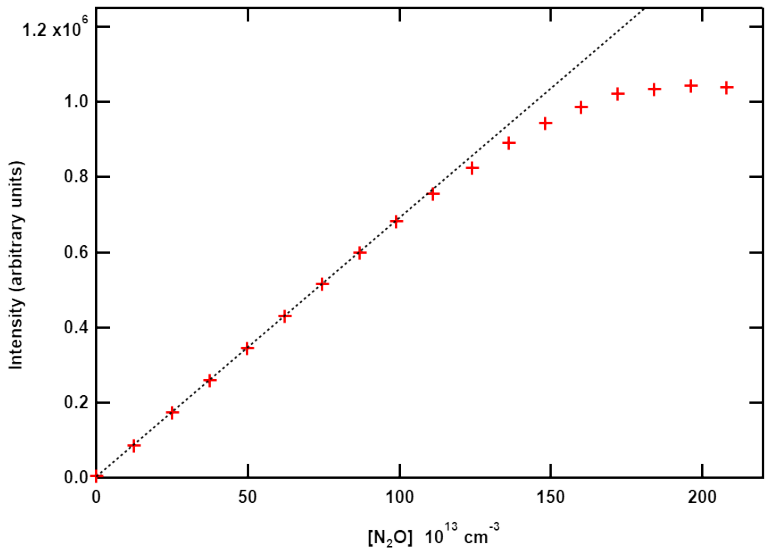

Figure 4.7: Signal intensity as a function of the formic acid density. Probing conditions: 75 369 MHz (3 ← 2), pulse length = 170 µs with 100,000 accumulations, LO = 74 GHz. Acquired in argon 52 K nozzle with 3 mm skimmer.

by Mäder et al. [1996] and Bohac et al. [1992] measured a binding energy value of 166 cm^{-1} for the complex. Finally, the CO_2-N_2 complex have been studied with microwave spectroscopy by Frohman et al. [2010]. They calculated a binding energy of 323 cm^{-1}. The complex of CO_2 with argon or nitrogen has not been detected to date in any nozzle flow.

4.3 Results and discussion

At 52 K, both the decay of FA and the appearance of the FA-CO_2 complex were followed with various CO_2 concentrations. Figure 4.8 presents the FA decay for which CO_2 density was varied between 0 and 1.6×10^{15} cm^{-3} and FA density was fixed at 8×10^{11} cm^{-3}. These measurements were repeated for seven reservoir positions between 12 and 32 cm. The first 1 points were not taken into account in the exponential decay fit as the pseudo-first order conditions were not achieved. The linear fit from the second-order kinetic plot gave a rate coefficient of (1.9 ± 0.06) 10^{-12} cm^{-3} s^{-1}. The full dataset is provided in appendix C.2.

Figure 4.9 presents the appearance of FA-CO_2 complex, acquired with the same conditions used to follow the FA decay. These measurements were repeated for five reservoir positions between 12 and 28 cm, all plots are provided in appendix C.3. The data were fitted using equation 4.7 which accounts for the complex formation and destruction with CO_2. In this fit, the pseudo-first-order rate coefficient for the complex apparition was fixed using the value measured with the FA decay presented above. This first simple model shows agreement between the measurement of the dimerisation rate coefficient from the FA decay and dimer apparition. However, a better model accounting for other destruction pathways is needed to provide a better fit, such as destruction with formic acid for instance.

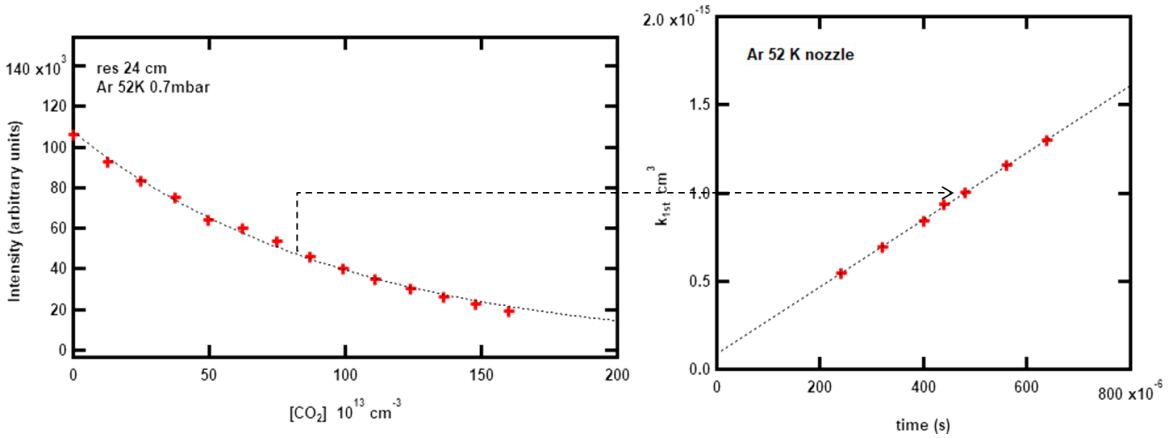

Figure 4.8: Kinetics data obtained in argon nozzle at 52 K with a 3 mm skimmer. The left panel shows the formic acid decay at a 24 cm position fit with a single exponential decay function (black dotted line). The right panel shows the second-order kinetics plot where the pseudo-first order rate coefficients are plotted as a function of CO_2 concentration. The black dotted line shows the fit yielding the second-order rate coefficient.

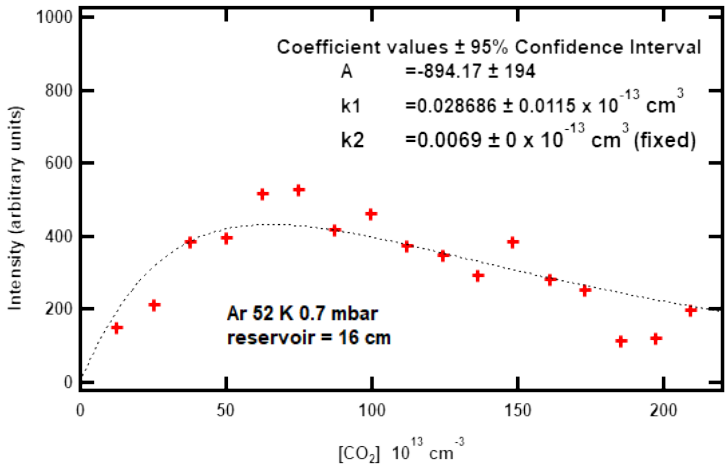

Figure 4.9: Kinetics data obtained in argon nozzle at 52 K with a 3 mm skimmer showing the FA-CO_2 complex growth at a 16 cm position and fitted using equation 4.5 (black dotted line). Probing: single frequency pulse at 65 738 MHz, 170 ns, LO = 68 GHz, 250 000 accumulations, FA density = 8×10^{11} cm^3.

A measurement of the rate at 38 K was also attempted in a nitrogen nozzle. The formic acid decay is shown in figure 4.10. Six measurement points were taken between 8 and 52 cm with a 5 cm step. The FA density was fixed at 8.8×10^{11} cm^{-3} and CO_2 density was varied between 0 and 6×10^{13} cm^{-3}. The first 3 points were not taken into account in the exponential decay fit as the pseudo-first order conditions were not achieved. The linear fit from the second-order kinetic plot gave a rate coefficient of (3.4 ± 0.8) 10^{-11} cm^{-3} s^{-1}. This value is one order of magnitude faster than the rate coefficient measured in the argon nozzle. Despite the slight temperature difference, such a difference would not be expected. From table 4.1, the calculated Gibbs energy

for FA-N_2 dimer formation was found to be lower than for the other complexes. This suggests that FA-N_2 is formed faster than the other complexes but as it is less stable, it will further react with CO_2 to form the FA-CO_2 complex. These calculations and the experimental measurement provide evidence that the FA-CO_2 complex has two formation pathways, either with FA-N_2 + CO_2 or with FA + CO_2 which are in competition. This highlights the difficulty of working with a nitrogen nozzle to measure the dimerisation of FA and CO_2. At higher temperatures, the formation of FA-N_2 might not be favourable anymore which would allow the study of the reaction in nitrogen nozzles.

Table 4.1: Summary of calculated Gibbs energies and equilibrium constant calculated with CBS-QB3 thermochemistry method. Calculations performed by Sándor Demes.

reaction	ΔG (kJ.mol^{-1})		K_p	
	38 K and 0.39 mbar	35 K and 0.28 mbar	39 K and 0.39 mbar	35 K and 0.28 mbar
FA··N_2 + CO_2 ↔ FA··CO_2 + N_2	-9.6588	-13.065	49.3	194
FA + FA ↔ FA··FA	-53.6011	-54.4695	2.4×10^{9}	3.5×10^{9}
FA + N_2 ↔ FA··N_2	-0.6754	-	1.31	-
FA + Ar ↔ FA··Ar	-	+1.9009	-	0.464
FA + CO_2 ↔ FA··CO_2	-10.3342	-11.1544	64.7	90.1

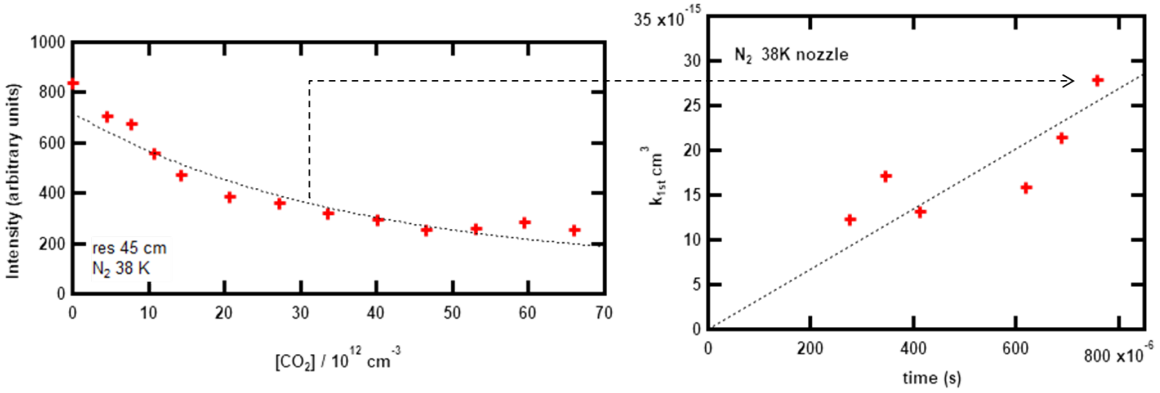

Figure 4.10: Kinetics data obtained in N_2 nozzle at 38 K with a 4 mm skimmer. The left panel shows the formic acid decay at a 45 cm position fit with a single exponential decay function (black dotted line). The right panel shows the second-order kinetics plot where the pseudo-first order rate coefficients are plotted as a function of CO_2 concentration. The black dotted line shows the fit yielding the second-order rate coefficient.

4.4 Conclusion

The absolute rate coefficient of dimerisation of formic acid and CO_2 was measured for the first time using chirped pulse microwave spectroscopy in CRESU flows. In this work, the rate coefficient was directly measured by following the reactant decay under pseudo-first order conditions at 52 K. The product evolution over time was also followed and was found to be in agreement with the measured rate.

The main challenge with complexation rate measurement relies on avoiding other complexation processes, such as the formation of homodimers from the reactants and the formation of heterodimers with the buffer gas. The formation of homodimers can be avoided by introducing the reactants in the appropriate density. This maximum density can be determined with a cluster test by following the signal intensity evolution of the molecule of interest (or a proxy if the molecule does not have a dipole moment) for different molecular densities. This represents however an experimental limit as the maximum densities need to be large enough to ensure proper rate measurements. The formation of heterodimers with the buffer gas on the other hand will be influenced by the flow conditions and the nature of the buffer gas. Therefore they might be avoided by playing with the nozzle in use. The influence of the complex formed with the buffer was observed in this work with a nitrogen nozzle at 38 K. The measured rate coefficient was one order of magnitude faster than in the argon nozzle at 52 K. Despite the slightly different flow conditions, this seems unlikely. Calculations of Gibbs energy for the formation of this complex were performed and provide further evidence of a chaperon mechanism where a first complex with formic acid and nitrogen is formed before reacting with CO_2.

This first study coupling CRESU flows with chirped pulse microwave spectroscopy shows the capabilities of this setup towards absolute rate coefficient measurements. The detection technique used here has the advantage of being highly specific and thus allows to distinguish the different isomers of the dimer. In this work, the cis and trans formic acid were detected in the flow. These two isomers can form a dimer with CO_2 but will have different configuration and might thus follow different kinetics. Perhaps it would be interesting to measure the cis formic acid kinetics to see the difference with the trans form in the future.

The future direction for this work would be to perform more measurements at different temperatures and to explore the pressure dependence of the dimerisation process by measuring the rate coefficient with nozzles of the same temperature and different pressures. This could imply using different buffer gases since the complex formed with buffer gas could open a new pathway for the FA-CO_2 complex formation. Finally, some theoretical calculations are under going to model these experimental measurements.

Chapter 5

Conclusion and perspectives

La beauté de la science réside dans sa capacité à éclairer les coins les plus sombres de l'univers.

– Lisa Randall

The determination of branching ratio and rate coefficients were explored in this work for the reaction of CN and propene and the dimerisation reaction of formic acid and CO_2 respectively using CRESU flows coupled with chirped-pulse microwave spectroscopy.

The branching fraction of the vinyl cyanide channel for the CN and propene reaction was measured for the first time below room temperature. It was found to be the major product down to 35 K, with a similar fraction than previous room temperature measurements, which suggests a non-temperature dependence. The upper limits for the other products were determined to be around 20% with the current spectrometer sensitivity. These experimental results were further supported with theoretical calculations using the MESMER software package. In particular, these results predict the cyanopropene product channels to be each less than 10%, which would explain the impossibility of detecting the product with the current experimental setup. The measurement of the vinyl cyanide fraction could still be performed using a calibration reaction. This technique remains however very limited for branching fraction measurements in general. It implies finding a reaction that possesses a channel giving 100% of the target product, which is not so common as the size of the molecule increases. Comparing two scans one after the other might also contribute to the final error in the measured fraction due to experimental fluctuations.

The main objective of coupling CRESU flows with chirped-pulse microwave spectroscopy is to take advantage of the broadband characteristic of this detection method in order to avoid the necessity of a calibration reaction. From this work, the main limitation to fulfil this goal is to improve the sensitivity of the technique. As mentioned throughout this thesis, the main factor contributing to the diminution of the signal is the pressure broadening. While the SKISURF setup has helped to increase the sensitivity by decoupling the probing and the reaction re-

gion using a skimmer, it has also reduced the number of molecules which are probed within the microwave radiation. The biggest skimmer used for this setup has a 4 mm diameter, however, the excimer laser can achieve a larger diameter, which means that the number of photolyzed molecules participating in the reaction could be increased (figure 5.1). Furthermore, the SKISURF setup is more susceptible to alignment and diffusion issues which also contributes to the loss of signal. The maximum diameter of the skimmer is defined by the pumping capacity of the setup which also constrains the accessible conditions for a Laval nozzle.

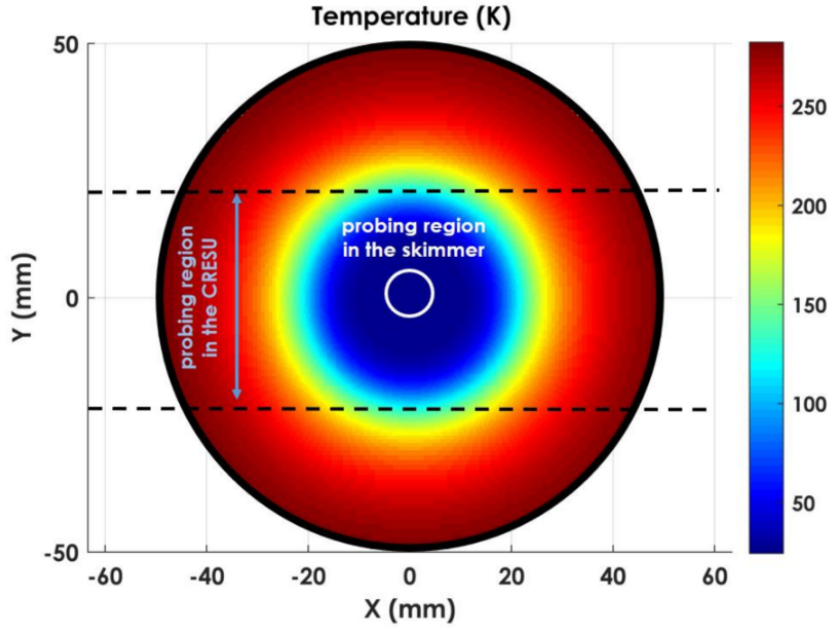

Figure 5.1: 2D radial temperature profile of the nitrogen 23.5 K nozzle ($P_{reservoir}$ = 773.5 mbar and $P_{chamber}$ = 0.12 mbar). Obtained using CFD simulation with Ansys Fluent. The probing region of a 4 mm diameter skimmer is represented in white. The two black dashed lines show the region covered by the horn antennas in the CRESU environment. From Abdelkader Khedaoui [2022].

Perhaps, the way to further increase the sensitivity could be to increase the effective pumping capacity which will give access to new possibilities in the flow conditions and skimmer sizes. This can be achieved using pulsed Laval nozzles, for which the average flows are smaller.

Various versions of pulsed CRESU flows have been developed throughout the years. Two main types of design can be distinguished, first, the one employing pulsed valves [Atkinson and Smith, 1995, Lee et al., 2000] and secondly the one using an aerodynamic chopper to pulse the flow [Jiménez et al., 2015, Morales, 2009]. For the design of this new pulsed system, the aerodynamic chopper method was chosen with a slightly different approach than the previous setups. Beforehand, the disk was sandwiched inside the Laval nozzle, which introduced various constraints on the disk. To overcome this problem, in the current design the disk was placed in the reservoir before the nozzle throat. This simplifies the mechanical setup and allows the use of all nozzles previously designed for continuous flows. Thicker disks can also be used which limits buckling due to inertial forces of rotation.

The design of the pulsed system is described in Abdelkader Khedaoui [2022]. In particular, the disk geometry was chosen to ensure a gain of ∼10 on the pressure and flow rate. A nozzle was specifically designed for this setup to operate at 6 K with helium as buffer gas. The setup was installed in CRESU-LIF chamber (another chamber connected to CRESUCHIRP chamber, as described in 2) to characterise this new nozzle with 1 and 2D Pitot maps. The pressure sensor described in section 2.2.2 was replaced with a rapid pressure sensor (Kulite pressure transducer XCQ-062) given the repetition rate of the gas pulses. The signal from the sensor is then amplified with an EFS 0582 conditioner.

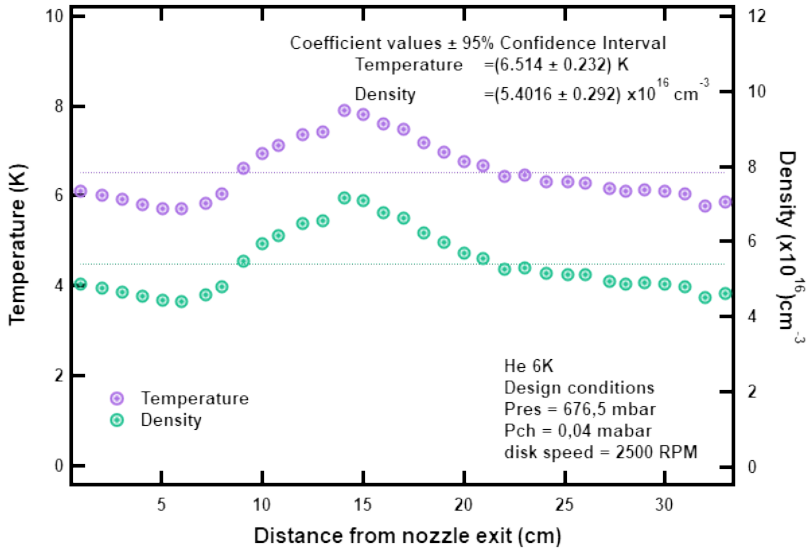

Figure 5.2: 1D temperature and density measurement along flow axis using a Pitot probe of He 6 K nozzle ($P_{reservoir}$ = 676.5 mbar and $P_{chamber}$ = 0.04 mbar, motor speed = 2500 RPM)

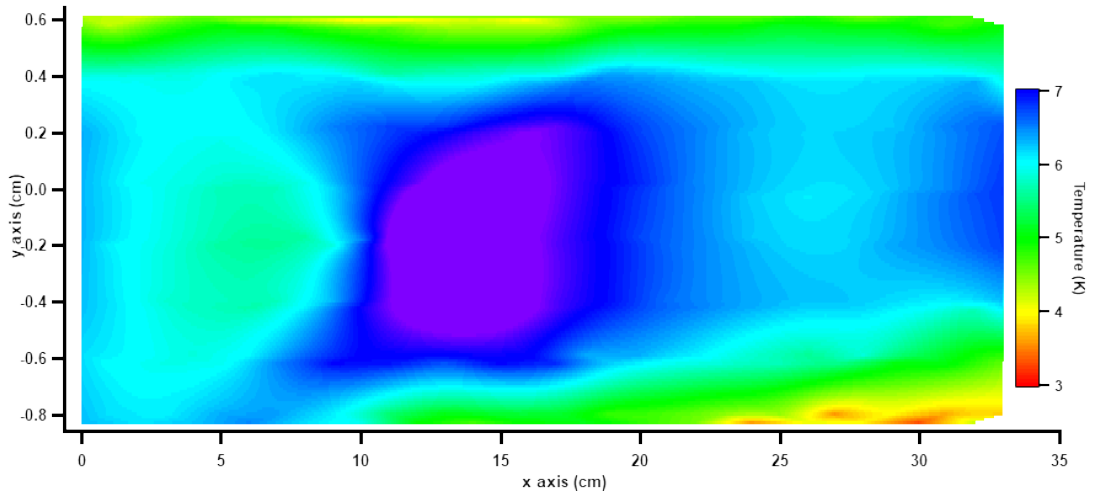

Figure 5.3: 2D temperature measurement along flow axis using a Pitot probe of He 6 K nozzle ($P_{reservoir}$ = 676.5 mbar and $P_{chamber}$ = 0.04 mbar, motor speed = 2500 RPM)

The 1 and 2D profiles are provided in figure 5.2 and 5.3 respectively. For this first test, the measurements were performed with the nozzle's designed conditions. Here the two maps show an under-expanded flow. This will be corrected in the future by adjusting the pressure of the chamber to ensure better uniform conditions. Nevertheless, this first test provides evidence of the future usability of this nozzle which can achieve a temperature of 6 K without initial pre-cooling of the reservoir.

The next step before coupling this new pulsed system with the spectrometer consists of implementing two main upgrades in the setup. Firstly, an optic fiber is under installation in order to measure the true repetition rate of the disk. The signal of the optic fiber will also be used to trigger the delay generator in order to synchronise the gas pulses with the laser and electronic devices. Secondly, an electronic actuator is being installed in order to move the disk from outside of the chamber. Both these new additions will allow a proper characterisation of the system before being able to use it for kinetics experimental measurements. In particular, the consistency of the nozzle conditions with the wear of the sealing gasket which connects the Laval nozzle to the rotating disk needs to be characterised before coupling the system to the chirped-pulse. Furthermore, the system was designed to reach the maximum repetition rate of the excimer laser at 100 Hz but this point needs to be characterised as well with the installation of the optic fiber. Finally, the pulsed system needs to be installed and coupled with the spectrometer in order to characterise the gain on the molecular signal. Figure 5.4 shows a picture of the pulsed system during the installation of the optic fiber and the actuator.

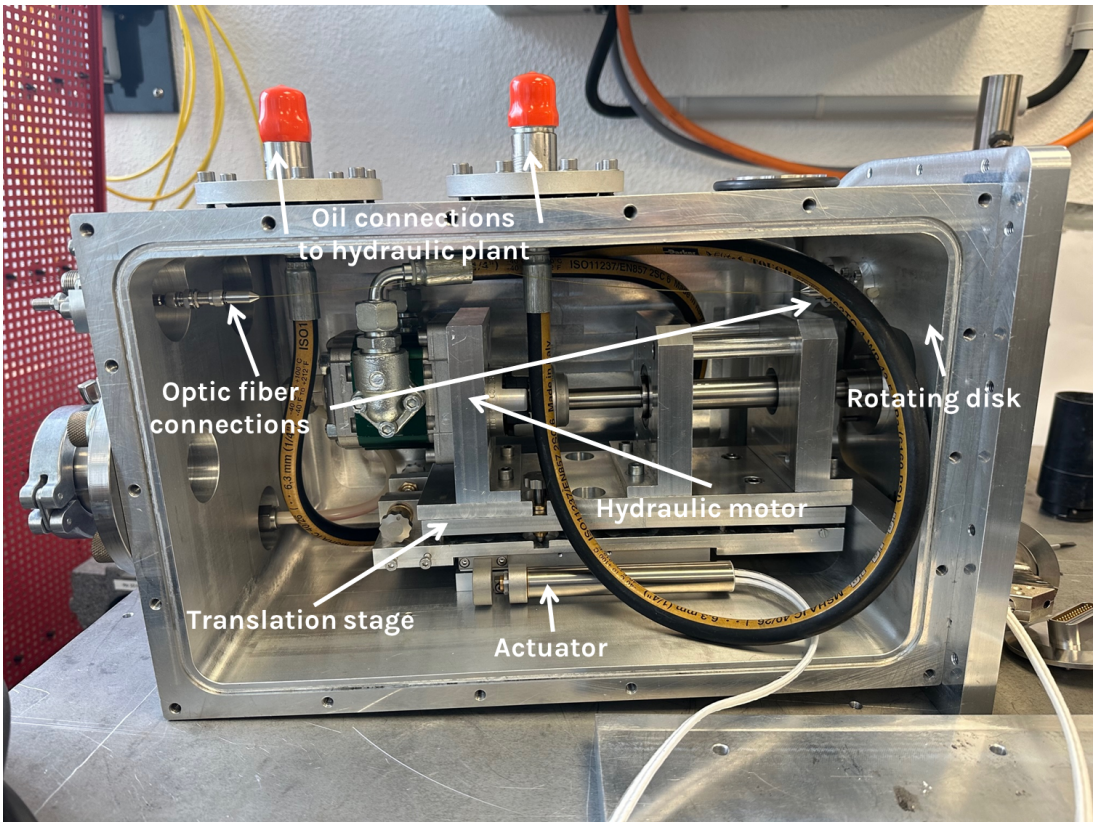

Figure 5.4: Picture of the inside of the pulsed system reservoir.

The second part of this thesis was dedicated to the rate coefficient measurement of the heterodimer formation of formic acid and CO_2. This work provides the first absolute rate coefficient measurement coupling CRESU flows with chirped pulse microwave spectroscopy. This benchmark system provides a method to study the formation of heterodimers for other molecules of atmospheric and astrochemical interest. The main challenge for these kinds of measurements is to avoid the formation of other complexes, in particular, the homodimers of the reactants and heterodimers formed with the buffer gas. These cross-reactions could affect the mechanism for the reaction of interest and impact the final rate coefficient.

The chirped pulse technique has the advantage of being highly specific, which means that every molecule as long as it possesses a dipole moment, even conformers can be distinguished. This aspect can be useful as differences in the conformation of the molecules could result in different kinetics. This aspect can be useful for the study of the first step of the nucleation process which remains elusive to date.

The results on the dimerisation of formic acid and CO_2 presented here are preliminary and more measurements are planned to characterise the temperature and pressure dependence of the rate coefficient. Theoretical calculations are also ongoing to model these experimental results. In the future, other dimerisation reactions of astrochemical interest could be studied such as heterodimer formation with PAHs which would be of interest for Titan's atmosphere for instance.

Overall, this thesis has presented two applications for the kinetics characterisations of reactive systems using CRESU flows coupled with chirped-pulse microwave spectroscopy. Firstly for the branching ratios measurements of neutral-neutral reactions. Secondly, for rate coefficient measurements of dimerisation processes. These two different kinds of chemical processes need experimental measurements in order to build accurate chemical models and unravel the chemistry of astrophysical environments. As for all experimental setups, it has its sets of advantages and drawbacks. Here some paths of improvement are proposed to further push these limits and meet the challenges of experimental astrochemistry.

Bibliography

Abdelkader Khedaoui, O. (2022). *Improving the sensitivity of mm-wave rotational spectroscopy in uniform supersonic flows for laboratory astrophysics applications*. PhD thesis, Université de Rennes, Rennes.

Abeysekera, C., Joalland, B., Ariyasingha, N., Zack, L. N., Sims, I. R., Field, R. W., and Suits, A. G. (2015). Product Branching in the Low Temperature Reaction of CN with Propyne by Chirped-Pulse Microwave Spectroscopy in a Uniform Supersonic Flow. *The Journal of Physical Chemistry Letters*, 6(9):1599–1604.

Abeysekera, C., Zack, L. N., Park, G. B., Joalland, B., Oldham, J. M., Prozument, K., Ariyasingha, N. M., Sims, I. R., Field, R. W., and Suits, A. G. (2014). A chirped-pulse Fourier-transform microwave/pulsed uniform flow spectrometer. II. Performance and applications for reaction dynamics. *The Journal of Chemical Physics*, 141(21):214203.

Agúndez, M., Cabezas, C., Tercero, B., Marcelino, N., Gallego, J. D., De Vicente, P., and Cernicharo, J. (2021). Discovery of the propargyl radical (CH_2CCH) in TMC-1: One of the most abundant radicals ever found and a key species for cyclization to benzene in cold dark clouds. *Astronomy & Astrophysics*, 647:L10.

Atkinson, D. B. and Smith, M. A. (1995). Design and characterization of pulsed uniform supersonic expansions for chemical applications. *Review of Scientific Instruments*, 66(9):4434–4446.

Balucani, N. (2009). Elementary Reactions and Their Role in Gas-Phase Prebiotic Chemistry. *International Journal of Molecular Sciences*, 10(5):2304–2335.

Barnum, T. J., Siebert, M. A., Lee, K. L. K., Loomis, R. A., Changala, P. B., Charnley, S. B., Sita, M. L., Xue, C., Remijan, A. J., Burkhardt, A. M., McGuire, B. A., and Cooke, I. R. (2022). A Search for Heterocycles in GOTHAM Observations of TMC-1. *The Journal of Physical Chemistry A*, 126(17):2716–2728.

Bartis, J. T. and Widom, B. (1974). Stochastic models of the interconversion of three or more chemical species. *The Journal of Chemical Physics*, 60(9):3474–3482.

Becker, R. and Döring, W. (1935). Kinetische Behandlung der Keimbildung in übersättigten Dämpfen. *Annalen der Physik*, 416(8):719–752.

Berner, G. M., East, A. L. L., Afshari, M., Dehghany, M., Moazzen-Ahmadi, N., and McKellar, A. R. W. (2009). Nitrous oxide dimer: An *ab initio* coupled-cluster study of isomers, interconversions, and infrared fundamental bands, and experimental observation of a new fundamental for the polar isomer. *The Journal of Chemical Physics*, 130(16):164305.

Berné, O., Martin-Drumel, M.-A., Schroetter, I., Goicoechea, J. R., Jacovella, U., Gans, B., Dartois, E., Coudert, L., Bergin, E., Alarcon, F., Cami, J., Roueff, E., Black, J. H., Asvany, O., Habart, E., Peeters, E., Canin, A., Trahin, B., Joblin, C., Schlemmer, S., Thorwirth, S., Cernicharo, J., Gerin, M., Tielens, A., Zannese, M., Abergel, A., Bernard-Salas, J., Boersma,

C., Bron, E., Chown, R., Cuadrado, S., Dicken, D., Elyajouri, M., Fuente, A., Gordon, K. D., Issa, L., Kannavou, O., Khan, B., Lacinbala, O., Languignon, D., Le Gal, R., Maragkoudakis, A., Meshaka, R., Okada, Y., Onaka, T., Pasquini, S., Pound, M. W., Robberto, M., Röllig, M., Schefter, B., Schirmer, T., Sidhu, A., Tabone, B., Van De Putte, D., Vicente, S., and Wolfire, M. G. (2023). Formation of the Methyl Cation by Photochemistry in a Protoplanetary Disk. *Nature*, pages 1–3.

Biennier, L., Sabbah, H., Chandrasekaran, V., Klippenstein, S. J., Sims, I. R., and Rowe, B. R. (2011). Insights into the role of polycyclic aromatic hydrocarbon condensation in haze formation in Jupiter's atmosphere. *Astronomy & Astrophysics*, 532:A40. Publisher: EDP Sciences.

Biver, N., Russo, N. D., Opitom, C., and Rubin, M. (2022). Chemistry of comet atmospheres. arXiv:2207.04800 [astro-ph].

Bjork, B. J., Bui, T. Q., Heckl, O. H., Changala, P. B., Spaun, B., Heu, P., Follman, D., Deutsch, C., Cole, G. D., Aspelmeyer, M., Okumura, M., and Ye, J. (2016). Direct frequency comb measurement of OD + CO $\rightarrow$ DOCO kinetics. *Science*, 354(6311):444–448.

Bohac, E. J., Marshall, M. D., and Miller, R. E. (1992). The vibrational predissociation of Ar–CO2 at the state-to-state level. I. Vibrational propensity rules. *The Journal of Chemical Physics*, 97(7):4890–4900.

Bourgalais, J., Durif, O., Le Picard, S. D., Lavvas, P., Calvo, F., Klippenstein, S. J., and Biennier, L. (2019). Propane clusters in Titan's lower atmosphere: insights from a combined theory/laboratory study. *Monthly Notices of the Royal Astronomical Society*, 488(1):676–684.

Bourgalais, J., Jamal-Eddine, N., Joalland, B., Capron, M., Balaganesh, M., Guillemin, J.-C., Le Picard, S. D., Faure, A., Carles, S., and Biennier, L. (2016a). Elusive anion growth in Titan's atmosphere: Low temperature kinetics of the C3N + HC3N reaction. *Icarus*, 271:194–201.

Bourgalais, J., Roussel, V., Capron, M., Benidar, A., Jasper, A., Klippenstein, S., Biennier, L., and Le Picard, S. (2016b). Low Temperature Kinetics of the First Steps of Water Cluster Formation. *Physical Review Letters*, 116(11):113401.

Bouwman, J., Fournier, M., Sims, I. R., Leone, S. R., and Wilson, K. R. (2013). Reaction Rate and Isomer-Specific Product Branching Ratios of C2H + C4H8: 1-Butene, cis-2-Butene, trans-2-Butene, and Isobutene at 79 K. *The Journal of Physical Chemistry A*, 117(24):5093–5105.

Broderick, B. M., Suas-David, N., Dias, N., and Suits, A. G. (2018). Isomer-specific detection in the UV photodissociation of the propargyl radical by chirped-pulse mm-wave spectroscopy in a pulsed quasi-uniform flow. *Physical Chemistry Chemical Physics*, 20(8):5517–5529.

Brown, G. G., Dian, B. C., Douglass, K. O., Geyer, S. M., Shipman, S. T., and Pate, B. H. (2008). A broadband Fourier transform microwave spectrometer based on chirped pulse excitation. *Review of Scientific Instruments*, 79(5):053103.

Cami, J., Bernard-Salas, J., Peeters, E., and Malek, S. E. (2010). Detection of C60 and C70 in a Young Planetary Nebula. *Science*, 329(5996):1180–1182.

Carl, T., Wirström, E. S., Bergman, P., Charnley, S. B., Chuang, Y.-L., and Kuan, Y.-J. (2023). Deep search for glycine conformers in Barnard 5. *Monthly Notices of the Royal Astronomical Society*, page stad2017.

Carstensen, H.-H. and Dean, A. M. (2007). Chapter 4 The Kinetics of Pressure-Dependent Reactions. In Carr, R. W., editor, *Comprehensive Chemical Kinetics*, volume 42 of *Modeling of Chemical Reactions*, pages 101–184. Elsevier.

Cernicharo, J., Fuentetaja, R., Cabezas, C., Agúndez, M., Marcelino, N., Tercero, B., Pardo, J. R., and De Vicente, P. (2022). Discovery of five cyano derivatives of propene with the QUIJOTE line survey. *Astronomy & Astrophysics*, 663:L5.

Choi, N., Blitz, M., McKee, K., Pilling, M., and Seakins, P. (2004). H atom branching ratios from the reactions of CN radicals with C2H2 and C2H4. *Chemical Physics Letters*, 384(1-3):68–72.

Cooke, I. R., Gupta, D., Messinger, J. P., and Sims, I. R. (2020). Benzonitrile as a Proxy for Benzene in the Cold ISM: Low-temperature Rate Coefficients for CN + C6H6. *The Astrophysical Journal Letters*, 891(2):L41.

Dias, N., Joalland, B., Ariyasingha, N. M., Suits, A. G., and Broderick, B. M. (2018). Direct versus Indirect Photodissociation of Isoxazole from Product Branching: A Chirped-Pulse Fourier Transform mm-Wave Spectroscopy/Pulsed Uniform Flow Investigation. *The Journal of Physical Chemistry A*, 122(38):7523–7531.

Dobrijevic, M., Ollivier, J. L., Billebaud, F., Brillet, J., and Parisot, J. P. (2003). Effect of chemical kinetic uncertainties on photochemical modeling results: Application to Saturn's atmosphere. *Astronomy & Astrophysics*, 398(1):335–344.

Dubois, D., Carrasco, N., Petrucciani, M., Vettier, L., Tigrine, S., and Pernot, P. (2019). In situ investigation of neutrals involved in the formation of Titan tholins. *Icarus*, 317:182–196.

Elsila, J. E., Glavin, D. P., and Dworkin, J. P. (2009). Cometary glycine detected in samples returned by Stardust. *Meteoritics & Planetary Science*, 44(9):1323–1330. _eprint: https://onlinelibrary.wiley.com/doi/pdf/10.1111/j.1945-5100.2009.tb01224.x.

Evans, M. G. and Polanyi, M. (1935). Some applications of the transition state method to the calculation of reaction velocities, especially in solution. *Transactions of the Faraday Society*, 31:875.

Eyring, H. (1935). The Activated Complex in Chemical Reactions. *The Journal of Chemical Physics*, 3(2):107–115.

Faure, A., Vuitton, V., Thissen, R., and Wiesenfeld, L. (2009). A Semiempirical Capture Model for Fast Neutral Reactions at Low Temperature. *The Journal of Physical Chemistry A*, 113(49):13694–13699.

Favre, C., Fedele, D., Semenov, D., Parfenov, S., Codella, C., Ceccarelli, C., Bergin, E. A., Chapillon, E., Testi, L., Hersant, F., Lefloch, B., Fontani, F., Blake, G. A., Cleeves, L. I., Qi, C., Schwarz, K. R., and Taquet, V. (2018). First Detection of the Simplest Organic Acid in a Protoplanetary Disk. *The Astrophysical Journal*, 862:L2. ADS Bibcode: 2018ApJ...862L...2F.

Felps, W. S., Rupnik, K., and McGlynn, S. P. (1991). Electronic spectroscopy of the cyanogen halides. *The Journal of Physical Chemistry*, 95(2):639–656.

Fournier, M., Le Picard, S. D., and Sims, I. R. (2017). Low-temperature Chemistry in Uniform Supersonic Flows.

Freeman, A. and Millar, T. J. (1983). Formation of complex molecules in TMC-l.

Frisch, M. J., Trucks, G. W., Schlegel, H. B., Scuseria, G. E., Robb, M. A., Cheeseman, J. R., Scalmani, G., Barone, V., Mennucci, B., Petersson, G. A., Nakatsuji, H., Caricato, M., Li, X., Hratchian, H. P., Izmaylov, A. F., Bloino, J., Zheng, G., Sonnenberg, J. L., Hada, M., Ehara, M., Toyota, K., Fukuda, R., Hasegawa, J., Ishida, M., Nakajima, T., Honda, Y., Kitao, O., Nakai, H., Vreven, T., Montgomery, Jr., J. A., Peralta, J. E., Ogliaro, F., Bearpark, M., Heyd, J. J., Brothers, E., Kudin, K. N., Staroverov, V. N., Kobayashi, R., Normand, J., Raghavachari, K., Rendell, A., Burant, J. C., Iyengar, S. S., Tomasi, J., Cossi, M., Rega, N., Millam, J. M., Klene, M., Knox, J. E., Cross, J. B., Bakken, V., Adamo, C., Jaramillo, J., Gomperts, R., Stratmann, R. E., Yazyev, O., Austin, A. J., Cammi, R., Pomelli, C., Ochterski, J. W., Martin, R. L., Morokuma, K., Zakrzewski, V. G., Voth, G. A., Salvador, P., Dannenberg, J. J., Dapprich, S., Daniels, A. D., Farkas, , Foresman, J. B., Ortiz, J. V., Cioslowski, J., and Fox, D. J. (2009). Gaussian09 Revision E.01.

Frohman, D. J., Contreras, E. S., Firestone, R. S., Novick, S. E., and Klemperer, W. (2010). Microwave spectra, structure, and dynamics of the weakly bound complex, N2 CO2. *The Journal of Chemical Physics*, 133(24):244303.

Gannon, K. L., Glowacki, D. R., Blitz, M. A., Hughes, K. J., Pilling, M. J., and Seakins, P. W. (2007). H Atom Yields from the Reactions of CN Radicals with C_2H_2, C_2H_4, C_3H_6, *trans* -2-C_4H_8, and *iso* -C_4H_8. *The Journal of Physical Chemistry A*, 111(29):6679–6692.

Gerlich, D. and Rox, T. (1989). Association reactions with state selected ions at meV collision energies: CO+ (v=0,j) + 2 CO $\rightarrow$ (CO)2++CO. *Zeitschrift für Physik D Atoms, Molecules and Clusters*, 13(3):259–268.

Glowacki, D. R., Liang, C.-H., Morley, C., Pilling, M. J., and Robertson, S. H. (2012). MESMER: An Open-Source Master Equation Solver for Multi-Energy Well Reactions. *The Journal of Physical Chemistry A*, 116(38):9545–9560.

Gobrecht, D., Plane, J. M. C., Bromley, S. T., Decin, L., Cristallo, S., and Sekaran, S. (2022). Bottom-up dust nucleation theory in oxygen-rich evolved stars - I. Aluminium oxide clusters. *Astronomy & Astrophysics*, 658:A167. Publisher: EDP Sciences.

Gu, X., Zhang, F., and Kaiser, R. I. (2008). Reaction Dynamics on the Formation of 1- and 3-Cyanopropylene in the Crossed Beams Reaction of Ground-State Cyano Radicals (CN) with Propylene (C_3H_6) and Its Deuterated Isotopologues. *The Journal of Physical Chemistry A*, 112(39):9607–9613.

Guillaume, T. (2021). *Construction of an E-band chirped-pulse spectrometer and application to the measurement of low temperature collisional processes of astrochemical interest.* PhD thesis, Université de Rennes, Rennes.

Gupta, D. (2021). *Rate Coefficients and Branching Ratio Measurements for Reactions of Astrochemical Relevance Involving CN Radicals*. PhD thesis, Université de Rennes, Rennes.

Gurusinghe, R. M., Dias, N., Krueger, R., and Suits, A. G. (2022a). Uniform supersonic flow sampling for detection by chirped-pulse rotational spectroscopy. *The Journal of Chemical Physics*, 156(1):014202.

Gurusinghe, R. M., Dias, N., Mebel, A. M., and Suits, A. G. (2022b). Radical–Radical Reaction Dynamics Probed Using Millimeterwave Spectroscopy: Propargyl + NH2/ND2. *The Journal of Physical Chemistry Letters*, 13(1):91–97.

Hadidi, R., Božanić, Ganjitabar, H., Garcia, G. A., Powis, I., and Nahon, L. (2021). Conformer-dependent vacuum ultraviolet photodynamics and chiral asymmetries in pure enantiomers of gas phase proline. *Communications Chemistry*, 4(1):1–14.

Hamon, S., Le Picard, S. D., Canosa, A., Rowe, B. R., and Smith, I. W. M. (2000). Low temperature measurements of the rate of association to benzene dimers in helium. *The Journal of Chemical Physics*, 112(10):4506–4516.

Hays, B. M., Guillaume, T., Hearne, T. S., Cooke, I. R., Gupta, D., Abdelkader Khedaoui, O., Le Picard, S. D., and Sims, I. R. (2020). Design and performance of an E-band chirped pulse spectrometer for kinetics applications: OCS – He pressure broadening. *Journal of Quantitative Spectroscopy and Radiative Transfer*, 250:107001.

Heard, D. E. (2018). Rapid Acceleration of Hydrogen Atom Abstraction Reactions of OH at Very Low Temperatures through Weakly Bound Complexes and Tunneling. *Accounts of Chemical Research*, 51(11):2620–2627.

Hearne, T. S., Abdelkader Khedaoui, O., Hays, B. M., Guillaume, T., and Sims, I. R. (2020). A novel Ka-band chirped-pulse spectrometer used in the determination of pressure broadening coefficients of astrochemical molecules. *The Journal of Chemical Physics*, 153(8):084201.

Herbst, E. and Van Dishoeck, E. F. (2009). Complex Organic Interstellar Molecules. *Annual Review of Astronomy and Astrophysics*, 47(1):427–480.

Hickson, K. M. and Bergeat, A. (2012). Low temperature kinetics of unstable radical reactions. *Physical Chemistry Chemical Physics*, 14(35):12057.

Hocking, W. H. (1976). The Other Rotamer of Formic Acid, cis-HCOOH1. *Zeitschrift für Naturforschung A*, 31(9):1113–1121. Publisher: De Gruyter.

Huang, C. H., Kaiser, R. I., and Chang, A. H. H. (2009). Theoretical Study on the Reaction of Ground State Cyano Radical with Propylene in Titan's Atmosphere. *The Journal of Physical Chemistry A*, 113(45):12675–12685.

Hébrard, E., Dobrijevic, M., Bénilan, Y., and Raulin, F. (2006). Photochemical kinetics uncertainties in modeling Titan's atmosphere: A review. *Journal of Photochemistry and Photobiology C: Photochemistry Reviews*, 7(4):211–230.

Illies, A. J., McKee, M. L., and Schlegel, H. B. (1987). Ab initio study of the carbon dioxide dimer and the carbon dioxide ion complexes [(CO2)2+ and (CO2)3+]. *The Journal of Physical Chemistry*, 91(13):3489–3494. Publisher: American Chemical Society.

Ioannou, I. I. and Kuczkowski, R. L. (1994). Microwave Spectrum and Structure of the Argon-Formic Acid van der Waals Complex. *The Journal of Physical Chemistry*, 98(9):2231–2235.

Jiménez, E., Ballesteros, B., Canosa, A., Townsend, T. M., Maigler, F. J., Napal, V., Rowe, B. R., and Albaladejo, J. (2015). Development of a pulsed uniform supersonic gas expansion system based on an aerodynamic chopper for gas phase reaction kinetic studies at ultra-low temperatures. *Review of Scientific Instruments*, 86(4):045108.

Joalland, B., Jamal-Eddine, N., Papanastasiou, D., Lekkas, A., Carles, S., and Biennier, L. (2019). A mass-selective ion transfer line coupled with a uniform supersonic flow for studying ion–molecule reactions at low temperatures. *The Journal of Chemical Physics*, 150(16):164201.

Kaiser, R. I., Zhao, L., Lu, W., Ahmed, M., Evseev, M. M., Azyazov, V. N., Mebel, A. M., Mohamed, R. K., Fischer, F. R., and Li, X. (2022). Gas-phase synthesis of racemic helicenes and their potential role in the enantiomeric enrichment of sugars and amino acids in meteorites. *Physical Chemistry Chemical Physics*, 24(41):25077–25087.

Kalescky, R., Kraka, E., and Cremer, D. (2014). Accurate determination of the binding energy of the formic acid dimer: The importance of geometry relaxation. *The Journal of Chemical Physics*, 140(8):084315.

Kalikmanov, V. I. and Hagmeijer, R. (2019). Cluster Formation at Extreme Supersaturations: Nucleation versus Barrierless Transition. *The Journal of Physical Chemistry B*, 123(50):10890–10895.

Kamp, I., Henning, T., M. Arabhavi, A., Bettoni, G., Christiaens, V., Gasman, D., L. Grant, S., Morales-Calderón, M., Tabone, B., Abergel, A., Absil, O., Argyriou, I., Barrado, D., Boccaletti, A., Bouwman, J., Garatti, A. C. o., Dishoeck, E. F. v., Geers, V., M. Glauser, A., Güdel, M., Guadarrama, R., Jang, H., Kanwar, J., Lagage, P.-O., Lahuis, F., Mueller, M., Nehmé, C., Olofsson, G., Pantin, E., Pawellek, N., Perotti, G., P. Ray, T., Rodgers-Lee, D., Samland, M., Scheithauer, S., Schreiber, J., Schwarz, K., Temmink, M., Vandenbussche, B., Vlasblom, M., Waelkens, C., M. Waters, L. B. F., and Wright, G. (2023). The chemical inventory of the inner regions of planet-forming disks – the JWST/MINDS program. *Faraday Discussions*.

Langevin, P. (1905). A fundamental formula of kinetic theory. *Ann. Chim. Phys*, 5(0365-1444):245–288.

Lattelais, M., Ellinger, Y., Matrane, A., and Guillemin, J.-C. (2010). Looking for heteroaromatic rings and related isomers as interstellar candidates. *Physical Chemistry Chemical Physics*, 12(16):4165.

Lavvas, P., Griffith, C., and Yelle, R. (2011). Condensation in Titan's atmosphere at the Huygens landing site. *Icarus*, 215(2):732–750.

Lebonnois, S. (2005). Benzene and aerosol production in Titan and Jupiter's atmospheres: a sensitivity study. *Planetary and Space Science*, 53(5):486–497.

Lee, S., Hoobler, R. J., and Leone, S. R. (2000). A pulsed Laval nozzle apparatus with laser ionization mass spectroscopy for direct measurements of rate coefficients at low temperatures with condensable gases. *Review of Scientific Instruments*, 71(4):1816–1823.

Leger, A. and Puget, J. L. (1984). Identification of the Unidentified Infrared Emission Features of Interstellar Dust. *Astronomy and Astrophysics*, 137:L5–L8. ADS Bibcode: 1984A&A...137L...5L.

Li, C., Krohn, J., Lippe, M., and Signorell, R. (2021). How volatile components catalyze vapor nucleation. *Science Advances*, 7(3):eabd9954.

Li, C. and Signorell, R. (2021). Understanding vapor nucleation on the molecular level: A review. *Journal of Aerosol Science*, 153:105676.

Liu, Y., Qi, H., and Lei, M. (2022). Elastic Image Pair Method for Finding Transition States on Potential Energy Surfaces Using Only First Derivatives. *Journal of Chemical Theory and Computation*, 18(8):5108–5115.

Loomis, R. A., Burkhardt, A. M., Shingledecker, C. N., Charnley, S. B., Cordiner, M. A., Herbst, E., Kalenskii, S., Lee, K. L. K., Willis, E. R., Xue, C., Remijan, A. J., McCarthy, M. C., and McGuire, B. A. (2021). An investigation of spectral line stacking techniques and application to the detection of HC11N. *Nature Astronomy*, 5(2):188–196.

Lopes, R. M. C., Wall, S. D., Elachi, C., Birch, S. P. D., Corlies, P., Coustenis, A., Hayes, A. G., Hofgartner, J. D., Janssen, M. A., Kirk, R. L., LeGall, A., Lorenz, R. D., Lunine, J. I., Malaska, M. J., Mastroguiseppe, M., Mitri, G., Neish, C. D., Notarnicola, C., Paganelli, F., Paillou, P., Poggiali, V., Radebaugh, J., Rodriguez, S., Schoenfeld, A., Soderblom, J. M., Solomonidou, A., Stofan, E. R., Stiles, B. W., Tosi, F., Turtle, E. P., West, R. D., Wood, C. A., Zebker, H. A., Barnes, J. W., Casarano, D., Encrenaz, P., Farr, T., Grima, C., Hemingway, D., Karatekin, O., Lucas, A., Mitchell, K. L., Ori, G., Orosei, R., Ries, P., Riccio, D., Soderblom, L. A., and Zhang, Z. (2019). Titan as Revealed by the Cassini Radar. *Space Science Reviews*, 215(4):33.

Marcelino, N., Cernicharo, J., Agúndez, M., Roueff, E., Gerin, M., Martín-Pintado, J., Mauersberger, R., and Thum, C. (2007). Discovery of Interstellar Propylene (CH_2CHCH_3): Missing Links in Interstellar Gas-Phase Chemistry. *The Astrophysical Journal*, 665(2):L127–L130.

Marquette, J.-B. (1988). *Une Approche Expérimentale de l'astrochimie : La Méthode CRESU, Principes et Applications*. PhD thesis, Paris 7.

McCarthy, M. C., Lee, K. L. K., Loomis, R. A., Burkhardt, A. M., Shingledecker, C. N., Charnley, S. B., Cordiner, M. A., Herbst, E., Kalenskii, S., Willis, E. R., Xue, C., Remijan, A. J., and McGuire, B. A. (2021). Interstellar detection of the highly polar five-membered ring cyanocyclopentadiene. *Nature Astronomy*, 5(2):176–180.

McGuire, B. A. (2022). 2021 Census of Interstellar, Circumstellar, Extragalactic, Protoplanetary Disk, and Exoplanetary Molecules. *The Astrophysical Journal Supplement Series*, 259(2):30.

McGurk, J. C., Schmalz, T. G., and Flygare, W. H. (1974). Fast passage in rotational spectroscopy: Theory and experiment. *The Journal of Chemical Physics*, 60(11):4181–4188.

McKellar, A. (1940). EVIDENCE FOR THE MOLECULAR ORIGIN OF SOME HITHERTO UNIDENTIFIED INTERSTELLAR LINES. *Publications of the Astronomical Society of the Pacific*, 52(307):187.

Messinger, J. P., Gupta, D., Cooke, I. R., Okumura, M., and Sims, I. R. (2020). Rate Constants of the CN + Toluene Reaction from 15 to 294 K and Interstellar Implications. *The Journal of Physical Chemistry A*, 124(39):7950–7958.

Miller, J. A. and Klippenstein, S. J. (2006). Master Equation Methods in Gas Phase Chemical Kinetics. *The Journal of Physical Chemistry A*, 110(36):10528–10544.

Miller, S. L. and Urey, H. C. (1959). Organic compound synthesis on the primitive earth. *Science (New York, N.Y.)*, 130(3370):245–251.

Morales, S. (2009). *Le hacheur aérodynamique : un nouvel instrument dédié aux processus réactionnels à ultra-basse température*. These de doctorat, Rennes 1.

Morales, S. B., Le Picard, S. D., Canosa, A., and Sims, I. R. (2010). Experimental measurements of low temperature rate coefficients for neutral–neutral reactions of interest for atmospheric chemistry of Titan, Pluto and Triton: Reactions of the CN radical. *Faraday Discussions*, 147:155.

Mourits, F. M. and Rummens, F. H. A. (1977). A critical evaluation of Lennard–Jones and Stockmayer potential parameters and of some correlation methods. *Canadian Journal of Chemistry*, 55(16):3007–3020. Publisher: NRC Research Press.

Mäder, H., Heineking, N., and Yunjie, W. J. (1996). Rotational spectrum of the isotopicalIy substituted van der WaaIs complex Ar-CU, investigated with a molecular beam Fourier transform microwave spectrometer. *J. Chem. Soc. Faraday Trans.*, 97(6):901–905.

Müller, H. S., Schlöder, F., Stutzki, J., and Winnewisser, G. (2005). The Cologne Database for Molecular Spectroscopy, CDMS: a useful tool for astronomers and spectroscopists. *Journal of Molecular Structure*, 742(1-3):215–227.

Neeman, E. M., González, D., Blázquez, S., Ballesteros, B., Canosa, A., Antiñolo, M., Vereecken, L., Albaladejo, J., and Jiménez, E. (2021). The impact of water vapor on the OH reactivity toward CH3CHO at ultra-low temperatures (21.7–135.0 K): Experiments and theory. *The Journal of Chemical Physics*, 155(3):034306.

Nixon, C. A., Jennings, D. E., Bézard, B., Vinatier, S., Teanby, N. A., Sung, K., Ansty, T. M., Irwin, P. G. J., Gorius, N., Cottini, V., Coustenis, A., and Flasar, F. M. (2013). DETECTION OF PROPENE IN TITAN'S STRATOSPHERE. *The Astrophysical Journal*, 776(1):L14.

Oldham, J. M., Abeysekera, C., Joalland, B., Zack, L. N., Prozument, K., Sims, I. R., Park, G. B., Field, R. W., and Suits, A. G. (2014). A chirped-pulse Fourier-transform microwave/pulsed uniform flow spectrometer. I. The low-temperature flow system. *The Journal of Chemical Physics*, 141(15):154202.

Olkhov, R. V. and Smith, I. W. M. (2007). Rate coefficients for reaction and for rotational energy transfer in collisions between CN in selected rotational levels (XΣ+2, v=2, N=, 1, 6, 10, 15, and 20) and C2H2. *The Journal of Chemical Physics*, 126(13):134314.

O'Halloran, M. A., Joswig, H., and Zare, R. N. (1987). Alignment of CN from 248 nm photolysis of ICN: A new model of the Ã continuum dissociation dynamics. *The Journal of Chemical Physics*, 87(1):303–313.

Park, G. B., Steeves, A. H., Kuyanov-Prozument, K., Neill, J. L., and Field, R. W. (2011). Design and evaluation of a pulsed-jet chirped-pulse millimeter-wave spectrometer for the 70-102 GHz region. *The Journal of Chemical Physics*, 135(2):024202.

Pickett, H. M. (1991). The fitting and prediction of vibration-rotation spectra with spin interactions. *Journal of Molecular Spectroscopy*, 148(2):371–377.

Pickett, H. M., Cohen, E. A., Drouin, B. J., and Pearson, J. C. (2003). Submillimeter, Millimeter, and Microwave Spectral Line Catalog.

Reizer, E., Viskolcz, B., and Fiser, B. (2022). Formation and growth mechanisms of polycyclic aromatic hydrocarbons: A mini-review. *Chemosphere*, 291:132793.

Roberts, F. C., Lewandowski, H. J., Hobson, B. F., and Lehman, J. H. (2020). A rapid, spatially dispersive frequency comb spectrograph aimed at gas phase chemical reaction kinetics. *Molecular Physics*, 118(16):e1733116.

Rowe, B. R., Dupeyrat, G., Marquette, J. B., and Gaucherel, P. (1984). Study of the reactions N+2+2N2→N+4+N2 and O+2+2O2→O+4+O2 from 20 to 160 K by the CRESU technique. *The Journal of Chemical Physics*, 80(10):4915–4921.

Sabbah, H., Biennier, L., Klippenstein, S. J., Sims, I. R., and Rowe, B. R. (2010). Exploring the Role of PAHs in the Formation of Soot: Pyrene Dimerization. *The Journal of Physical Chemistry Letters*, 1(19):2962–2967. Publisher: American Chemical Society.

Sanz-Novo, M., Alonso, J. L., Rivilla, V. M., McGuire, B. A., León, I., Mata, S., Jimenez-Serra, I., and Martín-Pintado, J. (2022). Laboratory detection and astronomical study of interstellar acetohydroxamic acid, a glycine isomer. *Astronomy & Astrophysics*, 666:A134.

Satterthwaite, L., Koumarianou, G., Carroll, P. B., Sedlik, R. J. J., Wang, I., McCarthy, M. C., and Patterson, D. (2023). Low-Temperature Gas-Phase Kinetics of Ethanol–Methanol Heterodimer Formation. *The Journal of Physical Chemistry A*, 127(18):4096–4102. Publisher: American Chemical Society.

Schuhmann, M., Altwegg, K., Balsiger, H., Berthelier, J.-J., De Keyser, J., Fiethe, B., Fuselier, S. A., Gasc, S., Gombosi, T. I., Hänni, N., Rubin, M., Tzou, C.-Y., and Wampfler, S. F. (2019). Aliphatic and aromatic hydrocarbons in comet 67P/Churyumov-Gerasimenko seen by ROSINA. *Astronomy & Astrophysics*, 630:A31.

Schwendeman, R. H. (1978). Transient Effects in Microwave Spectroscopy. *Annual Review of Physical Chemistry*, 29(1):537–558. _eprint: https://doi.org/10.1146/annurev.pc.29.100178.002541.

Sims, I. R. (2013). Tunnelling in space. *Nature Chemistry*, 5(9):734–736.

Sims, I. R., Queffelec, J.-L., Travers, D., Rowe, B. R., Herbert, L. B., Karthäuser, J., and Smith, I. W. (1993). Rate constants for the reactions of CN with hydrocarbons at low and ultra-low temperatures. *Chemical Physics Letters*, 211(4-5):461–468.

Smith, I. W. M. (2006). Reactions at Very Low Temperatures: Gas Kinetics at a New Frontier. *Angewandte Chemie International Edition*, 45(18):2842–2861.

Smith, I. W. M., Sage, A. M., Donahue, N. M., Herbst, E., and Quan, D. (2006). The temperature-dependence of rapid low temperature reactions: experiment, understanding and prediction. *Faraday Discussions*, 133:137.

Soorkia, S., Liu, C.-L., Savee, J. D., Ferrell, S. J., Leone, S. R., and Wilson, K. R. (2011). Airfoil sampling of a pulsed Laval beam with tunable vacuum ultraviolet synchrotron ionization quadrupole mass spectrometry: Application to low-temperature kinetics and product detection. *Review of Scientific Instruments*, 82(12):124102.

Stoecklin, T., Dateo, C. E., and Clary, D. C. (1991). Rate constant calculations on fast diatom–diatom reactions. *Journal of the Chemical Society, Faraday Transactions*, 87(11):1667–1679.

Suas-David, N., Thawoos, S., and Suits, A. G. (2019). A uniform flow–cavity ring-down spectrometer (UF-CRDS): A new setup for spectroscopy and kinetics at low temperature. *The Journal of Chemical Physics*, 151(24):244202.

Swings, P. and Rosenfeld, L. (1937). Considerations Regarding Interstellar Molecules. *The Astrophysical Journal*, 86:483–486.

Thawoos, S., Hall, G. E., Cavallotti, C., and Suits, A. G. (2023). Kinetics of CN ($v = 1$) reactions with butadiene isomers at low temperature by cw-cavity ring-down in a pulsed Laval flow with theoretical modelling of rates and entrance channel branching. *Faraday Discussions*.

Trevitt, A. J., Goulay, F., Meloni, G., Osborn, D. L., Taatjes, C. A., and Leone, S. R. (2009). Isomer-specific product detection of CN radical reactions with ethene and propene by tunable VUV photoionization mass spectrometry. *International Journal of Mass Spectrometry*, 280(1-3):113–118.

Trevitt, A. J., Soorkia, S., Savee, J. D., Selby, T. S., Osborn, D. L., Taatjes, C. A., and Leone, S. R. (2011). Branching Fractions of the CN + C_3H_6 Reaction Using Synchrotron Photoionization Mass Spectrometry: Evidence for the 3-Cyanopropene Product. *The Journal of Physical Chemistry A*, 115(46):13467–13473.

Vasyunin, A. I., Semenov, D., Henning, T., Wakelam, V., Herbst, E., and Sobolev, A. M. (2008). Chemistry in Protoplanetary Disks: A Sensitivity Analysis. *The Astrophysical Journal*, 672(1):629.

Vigorito, A., Gou, Q., Calabrese, C., Melandri, S., Maris, A., and Caminati, W. (2015). How CO2 Interacts with Carboxylic Acids: A Rotational Study of Formic Acid–CO2. *ChemPhysChem*, 16(14):2961–2967. Publisher: John Wiley & Sons, Ltd.

Vuitton, V., Yelle, R. V., and Anicich, V. G. (2006). The Nitrogen Chemistry of Titan's Upper Atmosphere Revealed. *The Astrophysical Journal*, 647(2):L175.

Waite, J. H., Young, D. T., Cravens, T. E., Coates, A. J., Crary, F. J., Magee, B., and Westlake, J. (2007). The Process of Tholin Formation in Titan's Upper Atmosphere. *Science, New Series*, 316(5826):870–875.

Walker, N. R., Minei, A. J., Novick, S. E., and Legon, A. C. (2008). Microwave spectrum and structure of the polar N2O dimer. *Journal of Molecular Spectroscopy*, 251(1):153–158.

Wang, M., Xiao, M., Bertozzi, B., Marie, G., Rörup, B., Schulze, B., Bardakov, R., He, X.-C., Shen, J., Scholz, W., Marten, R., Dada, L., Baalbaki, R., Lopez, B., Lamkaddam, H., Manninen, H. E., Amorim, A., Ataei, F., Bogert, P., Brasseur, Z., Caudillo, L., De Menezes, L.-P., Duplissy, J., Ekman, A. M. L., Finkenzeller, H., Carracedo, L. G., Granzin, M., Guida, R., Heinritzi, M., Hofbauer, V., Höhler, K., Korhonen, K., Krechmer, J. E., Kürten, A., Lehtipalo, K., Mahfouz, N. G. A., Makhmutov, V., Massabò, D., Mathot, S., Mauldin, R. L., Mentler, B., Müller, T., Onnela, A., Petäjä, T., Philippov, M., Piedehierro, A. A., Pozzer, A., Ranjithkumar, A., Schervish, M., Schobesberger, S., Simon, M., Stozhkov, Y., Tomé, A., Umo, N. S., Vogel, F., Wagner, R., Wang, D. S., Weber, S. K., Welti, A., Wu, Y., Zauner-Wieczorek, M., Sipilä, M., Winkler, P. M., Hansel, A., Baltensperger, U., Kulmala, M., Flagan, R. C., Curtius, J., Riipinen, I., Gordon, H., Lelieveld, J., El-Haddad, I., Volkamer, R., Worsnop, D. R., Christoudias, T., Kirkby, J., Möhler, O., and Donahue, N. M. (2022). Synergistic HNO3–H2SO4–NH3 upper tropospheric particle formation. *Nature*, 605(7910):483–489. Number: 7910 Publisher: Nature Publishing Group.

Werner, H.-J., Knowles, P. J., Knizia, G., Manby, F. R., and Schütz, M. (2012). Molpro: a general-purpose quantum chemistry program package. *WIREs Computational Molecular Science*, 2(2):242–253. _eprint: https://onlinelibrary.wiley.com/doi/pdf/10.1002/wcms.82.

West, N. A., Millar, T. J., Sande, M. V. d., Rutter, E., Blitz, M. A., Decin, L., and Heard, D. E. (2019). Measurements of Low Temperature Rate Coefficients for the Reaction of CH with CH2O and Application to Dark Cloud and AGB Stellar Wind Models. *The Astrophysical Journal*, 885(2):134.

Ye, L., Georgievskii, Y., and Klippenstein, S. J. (2015). Pressure-dependent branching in the reaction of 1CH2 with C2H4 and other reactions on the C3H6 potential energy surface. *Proceedings of the Combustion Institute*, 35(1):223–230.

Zhang, D. and Willitsch, S. (2017). Cold Ion Chemistry. In Dulieu, O. and Osterwalder, A., editors, *Cold Chemistry: Molecular Scattering and Reactivity Near Absolute Zero*, page 0. The Royal Society of Chemistry.

Zhang, R., Khalizov, A., Wang, L., Hu, M., and Xu, W. (2012). Nucleation and Growth of Nanoparticles in the Atmosphere. *Chemical Reviews*, 112(3):1957–2011. Publisher: American Chemical Society.

Zuckerman, B., Ball, J. A., and Gottlieb, C. A. (1971). Microwave Detection of Interstellar Formic Acid. *The Astrophysical Journal*, 163:L41. ADS Bibcode: 1971ApJ...163L..41Z.

Appendix A

Laval nozzles

Argon 35K

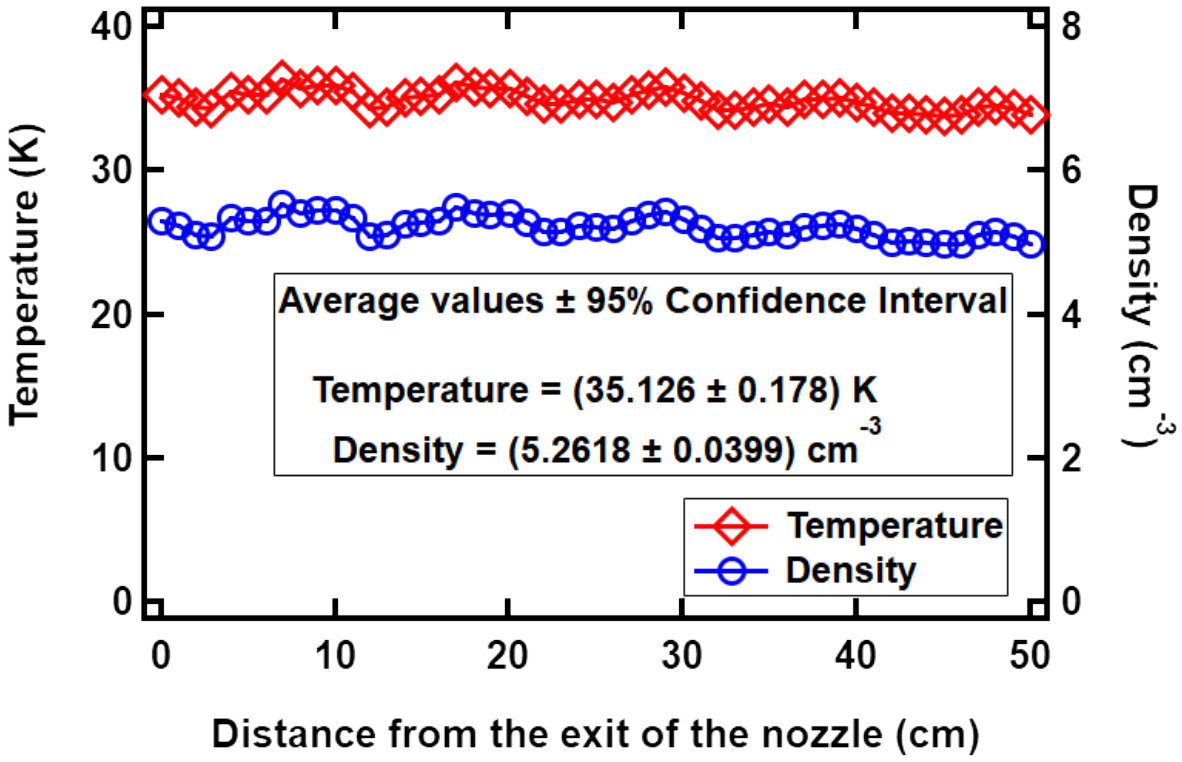

Figure A.1: 1D temperature and density measurement along flow axis using a Pitot probe of Ar 35K nozzle (see conditions in table A.1)

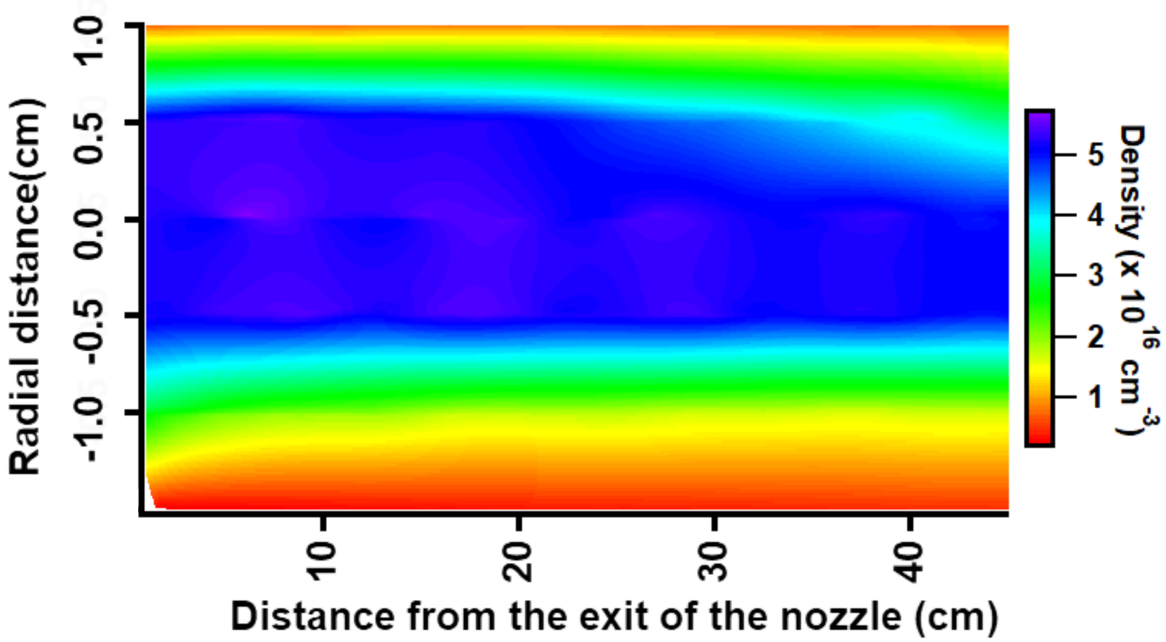

Figure A.2: 2D density measurement along and lateral to the flow axis using a Pitot probe of Ar 35K nozzle (see conditions in table A.1)

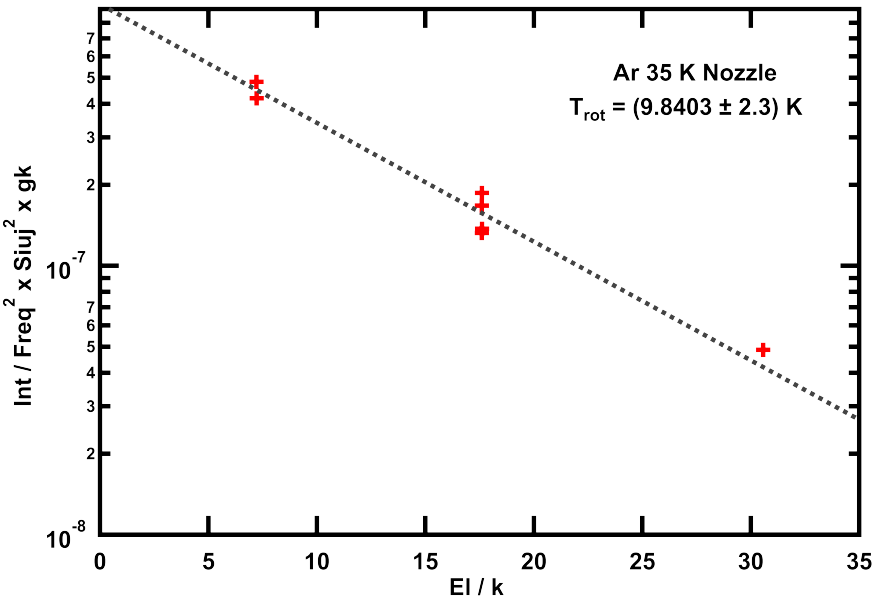

Figure A.3: Rotation diagram using the line intensities of the vinyl cyanide spectrum for the argon 35 K nozzle. Probing: 200 ns chirp between 73-78 GHz with 250 000 accumulations, LO=74 GHz, Flow VCN = 0.2g/h.

Ar 50K 0.3

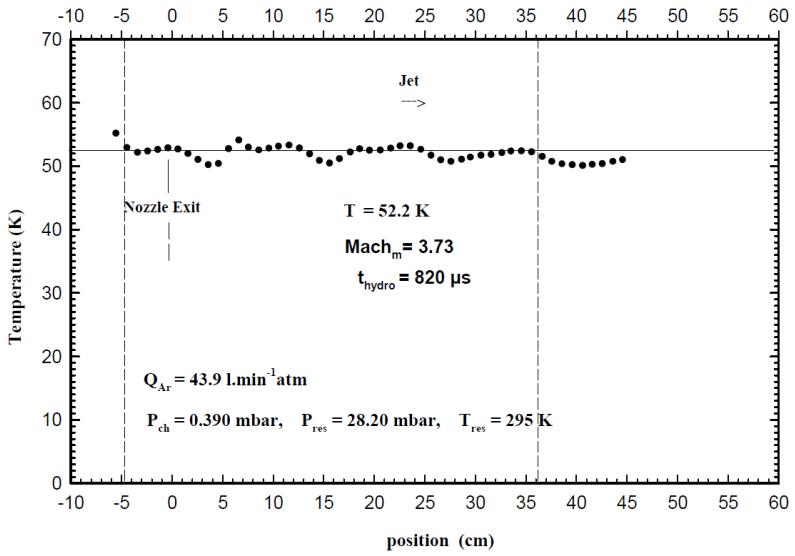

Figure A.4: 1D temperature measurement along flow axis using a Pitot probe of Ar 50K 0.3 nozzle (see conditions in table A.1)

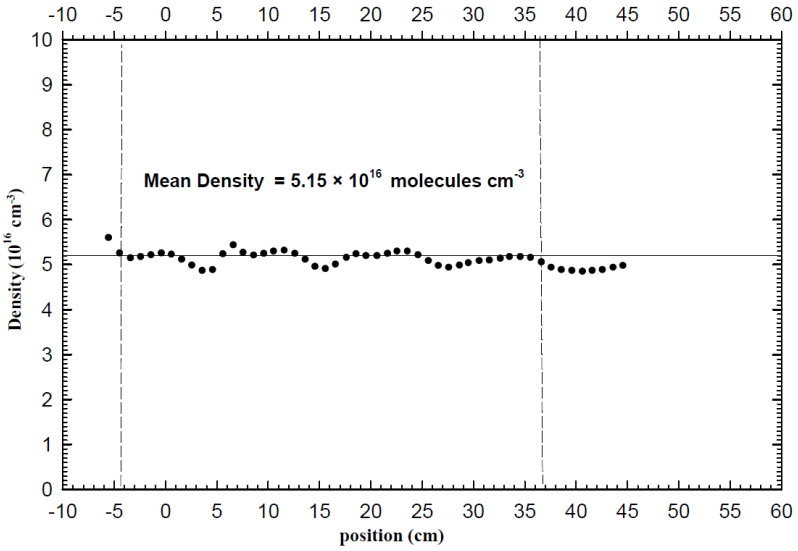

Figure A.5: 1D density measurement along flow axis using a Pitot probe Ar 50K 0.3 nozzle (see conditions in table A.1)

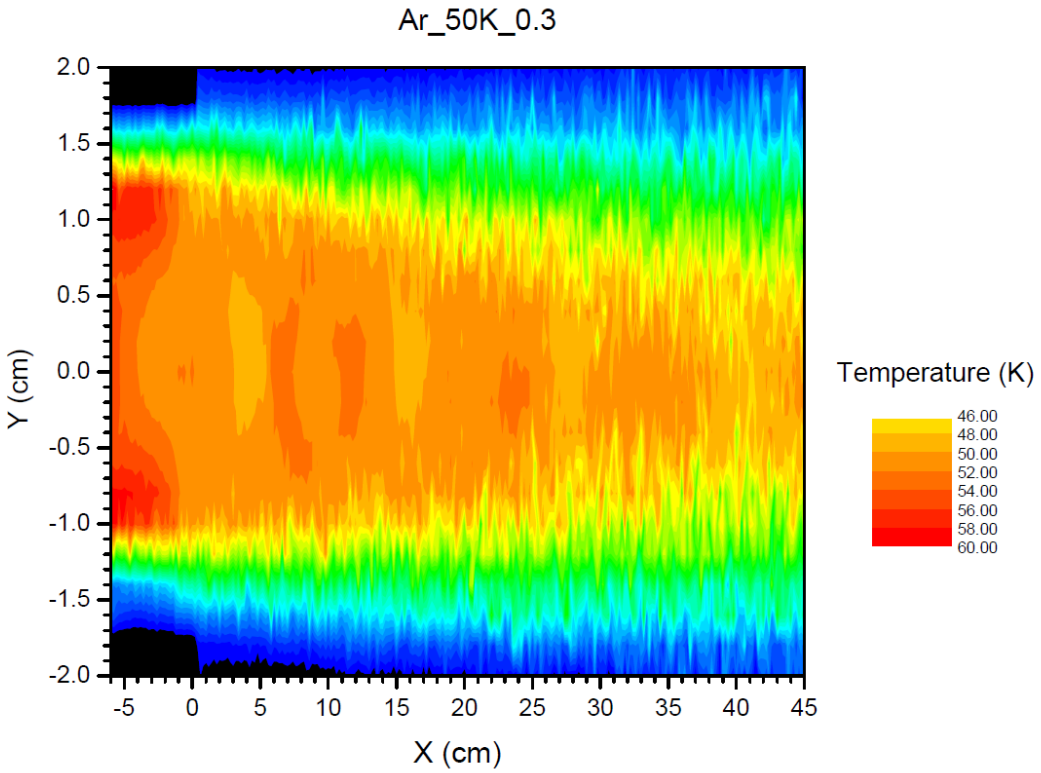

Figure A.6: 2D temperature measurement along and lateral to the flow axis using a Pitot probe Ar 50K 0.3 nozzle (see conditions in table A.1)

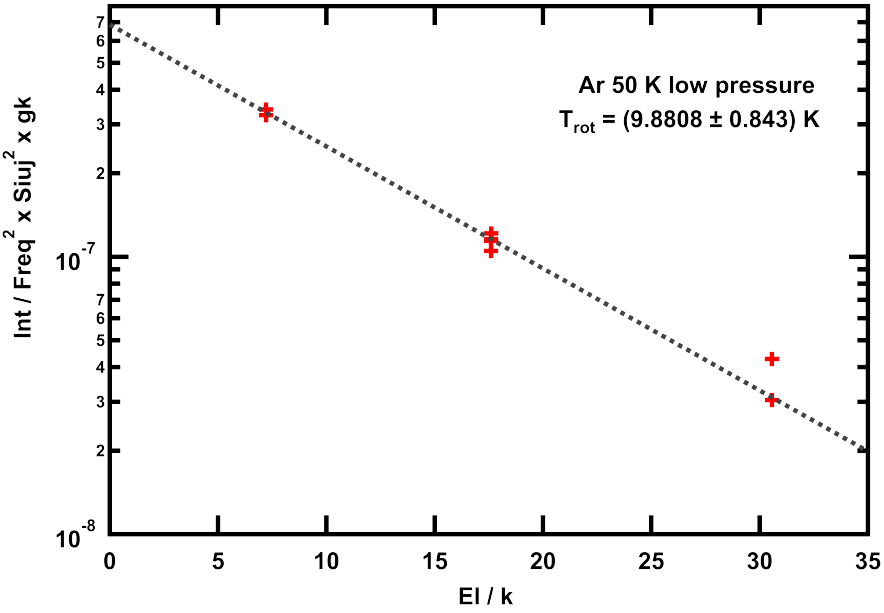

Figure A.7: Rotation diagram using the line intensities of the propene spectrum for argon 52 K low pressure nozzle. Probing: chirp 73-78 GHz, duration 200 ns, LO=74GHz, Flow VCN = 0.2g/h.

Ar50K 0.7

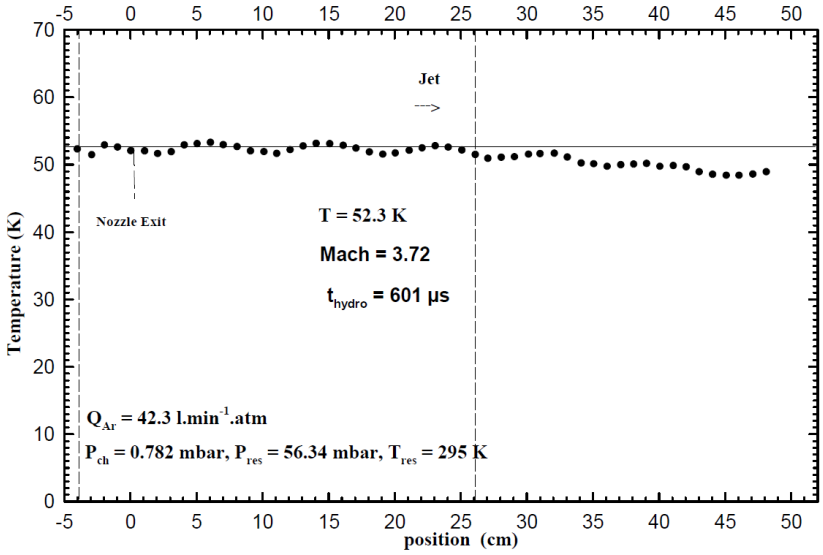

Figure A.8: 1D temperature measurement along flow axis using a Pitot probe Ar 50K 0.7 nozzle (see conditions in table A.1)

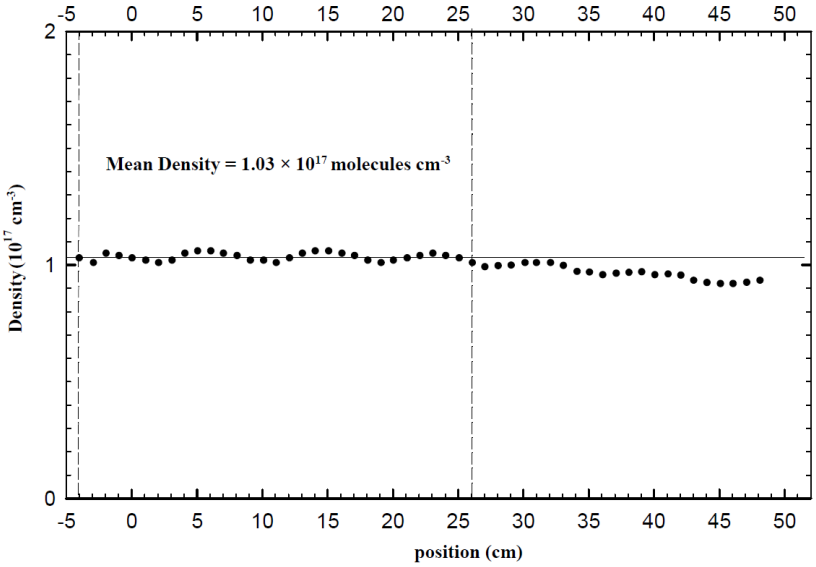

Figure A.9: 1D density measurement along flow axis using a Pitot probe Ar 50K 0.7 nozzle (see conditions in table A.1)

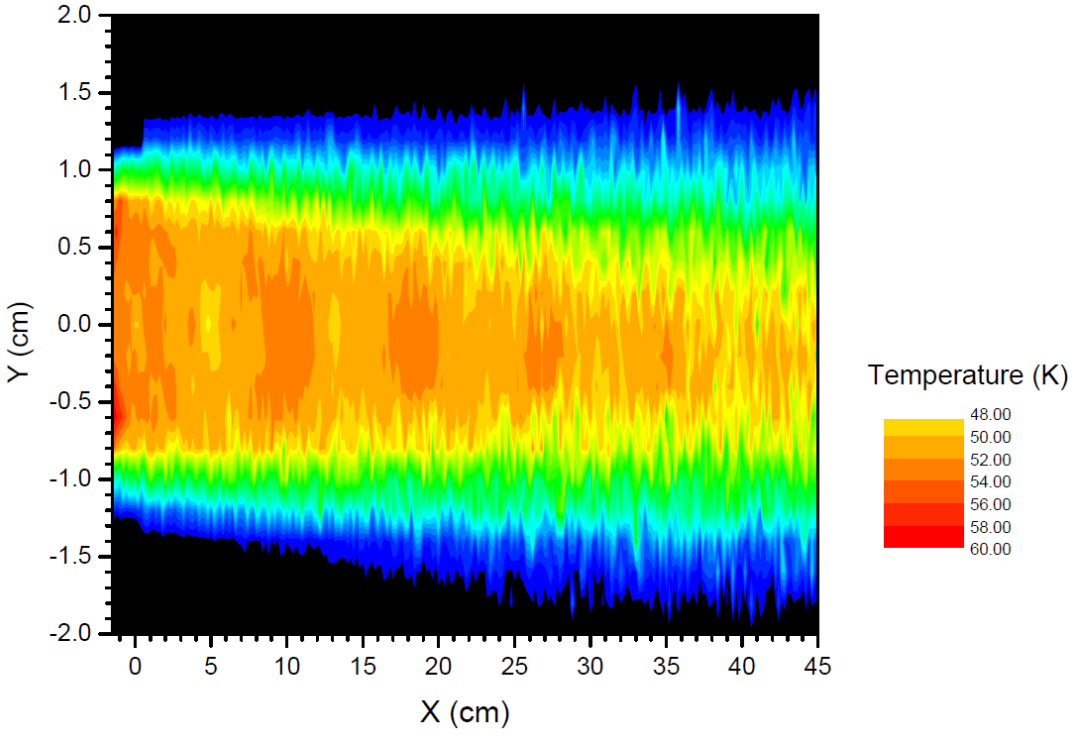

Figure A.10: 2D temperature measurement along and lateral to the flow axis using a Pitot probe Ar 50K 0.7 nozzle (see conditions in table A.1)

N2 38K

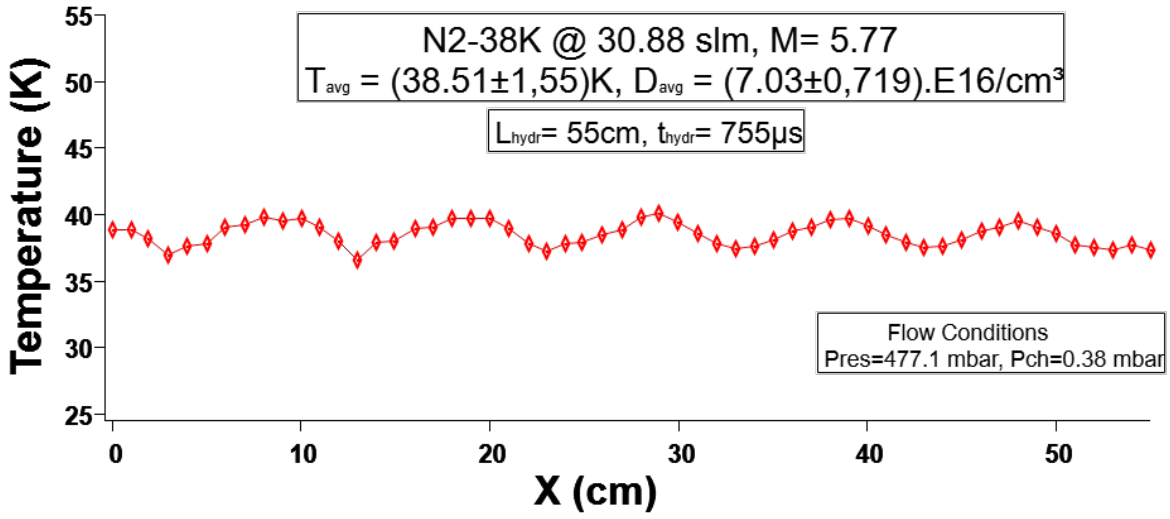

Figure A.11: 1D temperature measurement along flow axis using a Pitot probe N2 38K nozzle (see conditions in table A.1)

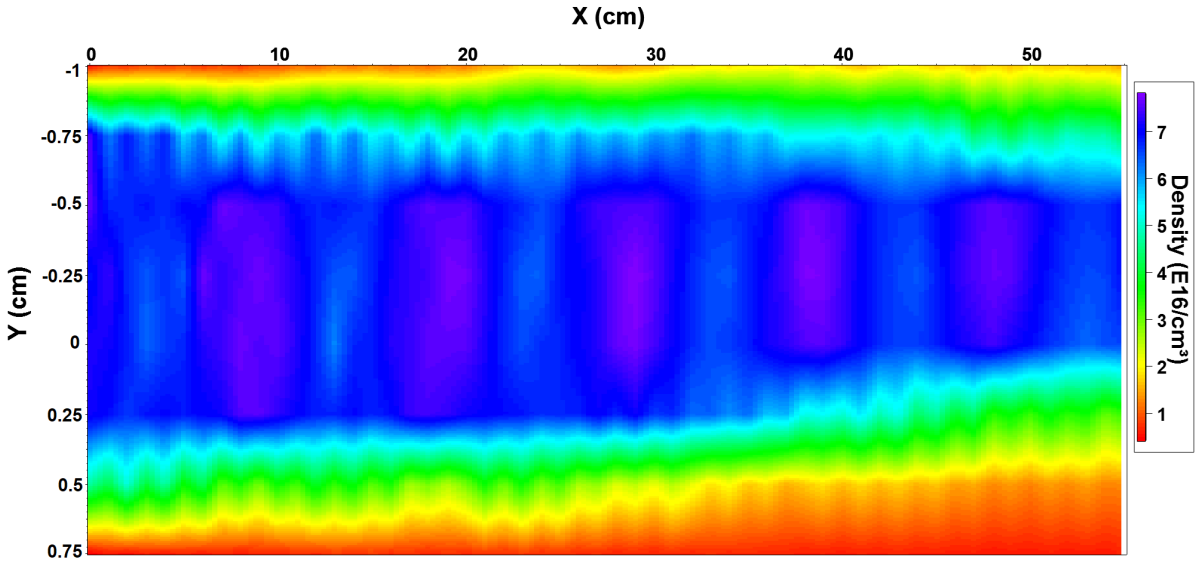

Figure A.12: 2D density measurement along and lateral to the flow axis using a Pitot probe N2 38K nozzle (see conditions in table A.1)

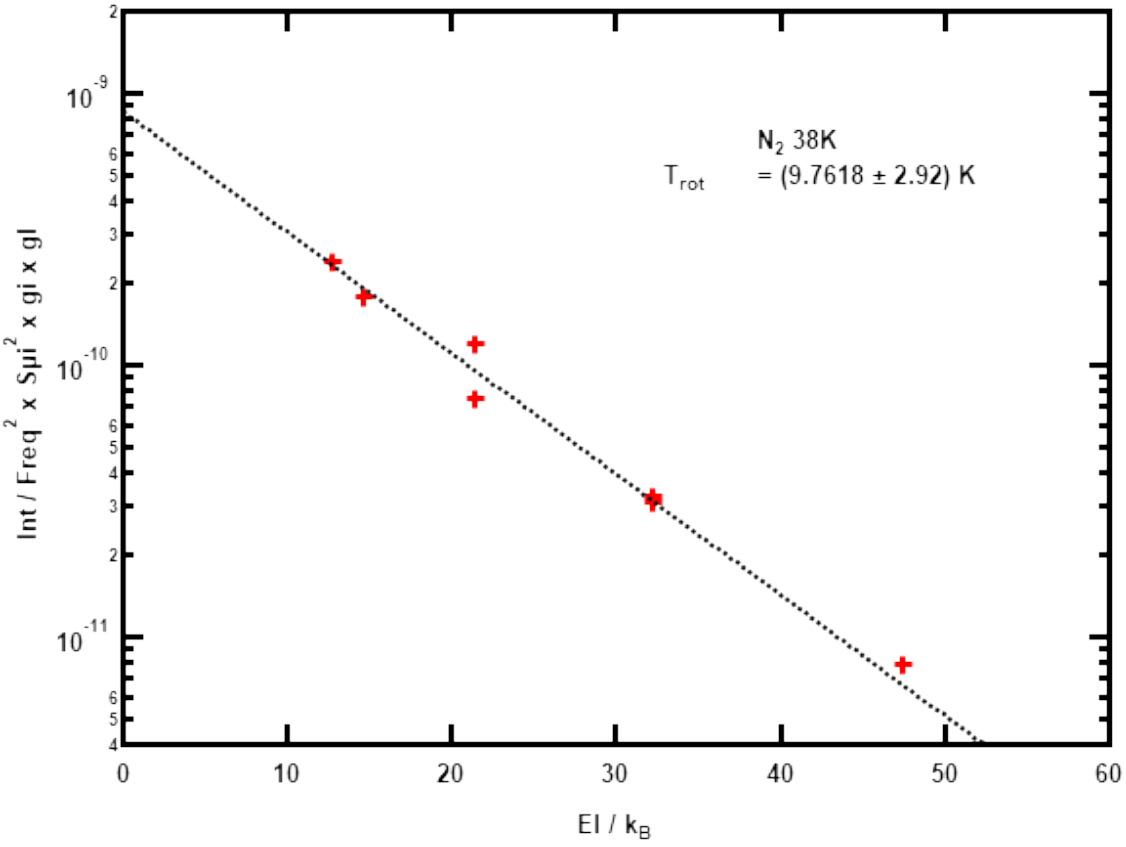

Figure A.13: Rotation diagram using the line intensities of the propene spectrum for nitrogen 38 K nozzle. Probing: chirp 73-78 GHz, duration 200 ns, LO = 74 GHz.

Table A.1: Nozzle conditions.

Name	Gas	Flow (SLM)	Reservoir pressure (mbar)	Temperature of the flow (K)	Chamber pressure (mbar)	Density (10^{16}cm^{-3})	Mach number	Velocity (m.s^{-1})	hydro-dynamic time (µs)	hydro-dynamic length (cm)
Ar 35K	Ar	20.51	52.7	35.12	0.28	5.26	4.72	521	949.24	55
Ar 50K 0.3	Ar	43.9	28.2	52.2	0.39	5.15	3.73	502	817	41 + 4
Ar 50K 0.7	Ar	42.3	56.34	52.3	0.782	10.3	3.72	501	599	30
N2 38K	N2	30.88	470.04	38.51	0.39	7.02	5.77	730	753	55

Rotational diagram

Table A.2: Vinyl cyanide line list used for rotational diagram analysis

Transition ($J_{Ka,Kc} \leftarrow J'_{Ka',Kc'}$))	**Frequency (MHz)**
$8_{0,8} \leftarrow 7_{0,7}$	75 585.6522
$8_{2,7} \leftarrow J'_{2,6}$	75 838.9230
$8_{4,5} \leftarrow J'_{4,4}$	75 922.1739
$8_{4,4} \leftarrow J'_{4,3}$	75 921.7391
$8_{5,3} \leftarrow J'_{5,2}$	75 926.7391
$8_{3,6} \leftarrow J'_{3,5}$	75 927.8261
$8_{3,5} \leftarrow J'_{3,4}$	75 931.9565
$8_{2,6} \leftarrow J'_{2,5}$	76 128.9130

Appendix B

CN + propene

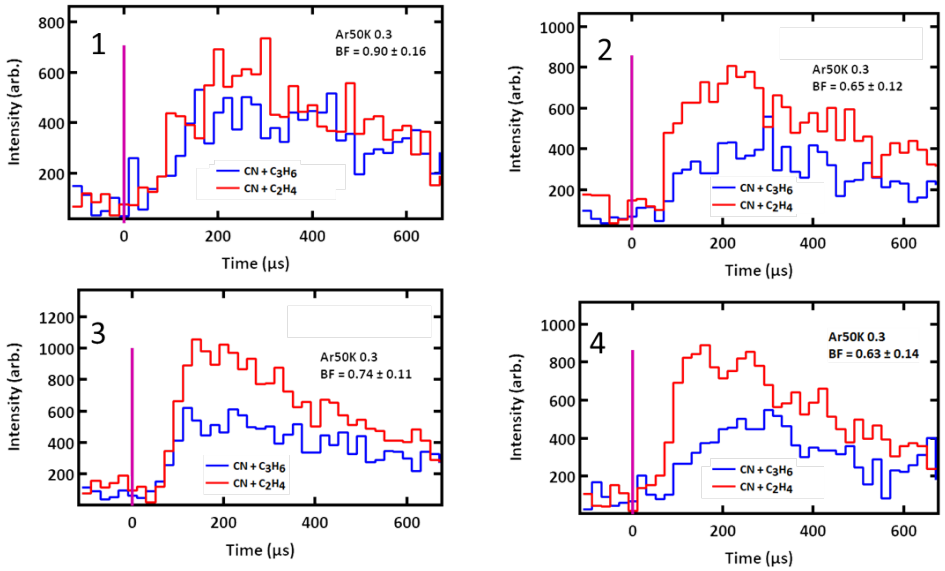

Figure B.1: Ar 50 K low pressure data.

Table B.1: Experimental conditions for the CN radical and propene reaction in argon 52 K nozzle. Propene density 1×10^{14} cm^{-3}, total flow density 5.15×10^{16} cm^{-3}. Experimental uncertainties are estimated at the $\pm 2\sigma$ level.

Run n°	**1**	**2**	**3**	**4**
Laser Fluence (photons pulse^{-1} cm^{-2}) $\times 10^{16}$	6.81	6.81	8.9	8.9
ICN$_{propene}$ $\times 10^{12}$	2.31 ± 0.22	2.24 ± 0.01	1.50 ± 0.11	1.60 ± 0.05
ICN$_{ethene}$ $\times 10^{12}$	2.23 ± 0.10	2.38 ± 0.14	1.67 ± 0.10	1.55 ± 0.10
Branching fraction	0.90±0.16	0.65±0.12	0.74±0.11	0.63±0.14

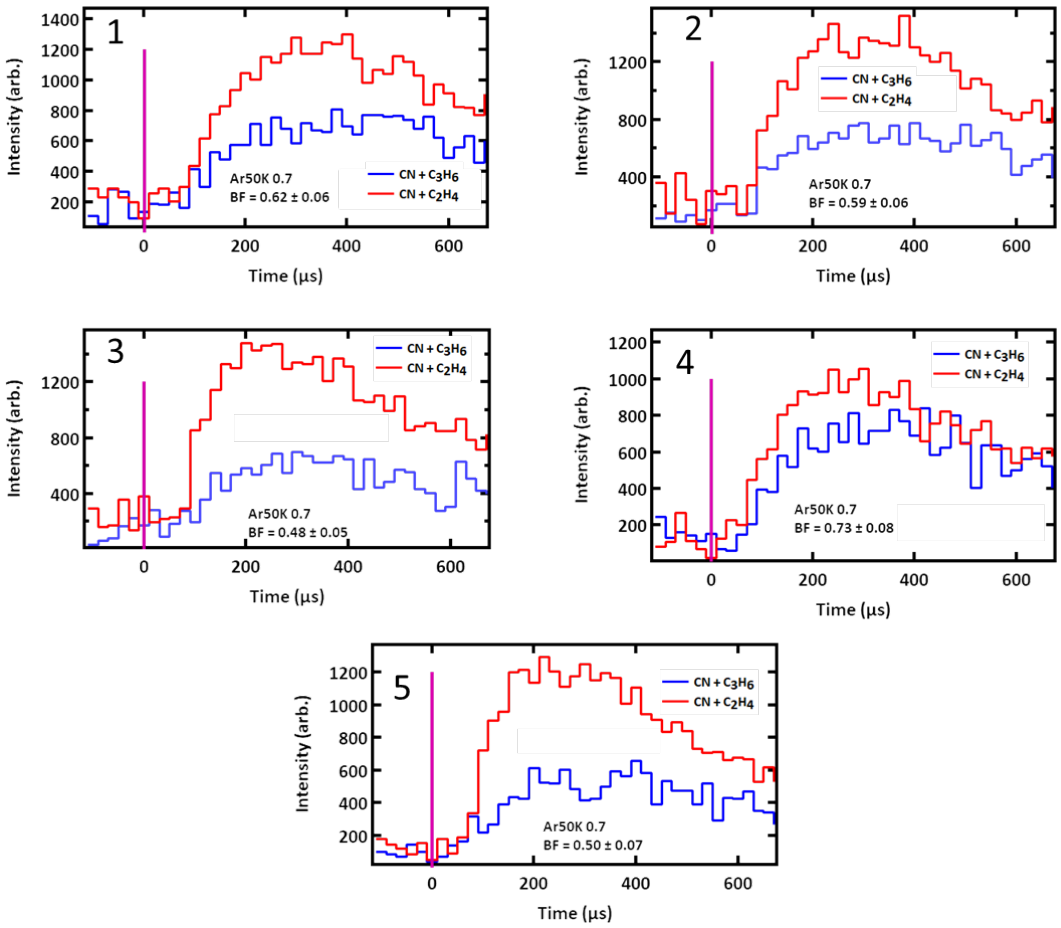

Figure B.2: Ar 50 K high pressure data.

Table B.2: Experimental conditions for the CN radical and propene reaction with argon 52 K high pressure. Propene density 5×10^{13} cm^{-3}, total flow density 10.3×10^{16} cm^{-3}. Experimental uncertainties are estimated at the $\pm 2\sigma$ level.

Run n°	**1**	**2**	**3**	**4**	**5**
Laser Fluence (photons pulse^{-1} cm^{-2}) $\times 10^{16}$	6.48	6.8	6.8	6.2	6.2
ICN$_{propene}$ $\times 10^{12}$	3.44 ± 0.002	2.89 ± 0.005	2.95 ± 0.02	4.09 ± 0.12	3.84 ± 0.11
ICN$_{ethene}$ $\times 10^{12}$	3.73 ± 0.05	2.96 ± 0.03	2.89 ± 0.02	4.14 ± 0.05	3.94 ± 0.06
Branching fraction	0.62±0.06	0.59±0.06	0.48±0.05	0.73±0.08	0.50±0.07

B.1 Full data sets

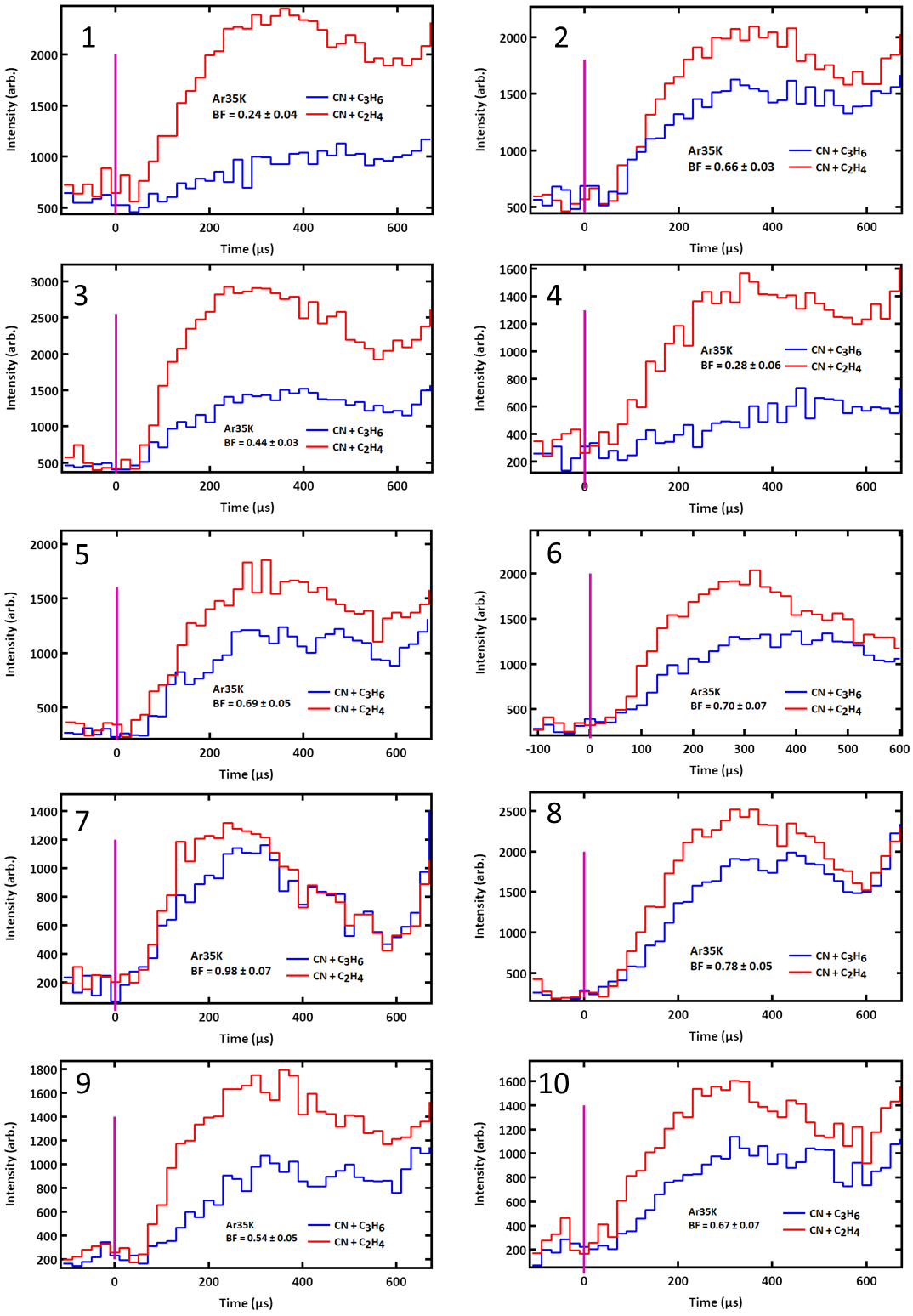

Figure B.3: Ar 35 data.

Table B.3: Experimental conditions for the CN radical and propene reaction with argon 35 K nozzle. Propene density 5×10^{13} cm^{-3}, total flow density 5.26×10^{16} cm^{-3}. Experimental uncertainties are estimated at the $\pm 2\sigma$ level.

Run n°	**1**	**2**	**3**	**4**	**5**	**6**	**7**	**8**	**9**	**10**
Laser Fluence (photons $pulse^{-1}$ cm^{-2}) $\times 10^{16}$	7.66	7.66	7.66	6.81	6.81	6.81	5.84	6.18	5.84	5.84
$ICN_{propene}$ (cm^{-3}) $\times 10^{12}$	4.39 ± 0.15	4.29 ± 0.49	4.50 ± 0.16	3.83 ± 0.19	4.00 ± 0.01	4.00 ± 0.35	1.47 ±0.04	4.72 ± 0.21	4.47 ± 0.66	4.58 ± 0.21
ICN_{ethene} (cm^{-3}) $\times 10^{12}$	4.09 ± 0.23	4.34 ± 0.43	3.20 ± 0.33	3.66 ± 0.24	4.03 ± 0.12	4.42 ± 0.18	1.58 ± 0.03	4.03 ± 0.09	4.43 ± 0.02	3.55 ± 0.39
Branching fraction	0.24±0.04	0.66±0.03	0.44±0.03	0.28±0.06	0.69±0.05	0.70±0.07	0.98±0.07	0.78±0.05	0.54±0.05	0.67±0.07

B.2 Igor Pro code for branching ratio calculation

```
function branching_ratio_MD(run_reac,run_cal,xstart,xend,startbg,endbg)

// This program is designed to calculate the branching fraction using a
//calibration reaction.
//In this first version the user can choose the start zone of analysis.
//The end is defined by the hydrodynamic time

//run_cal = name of the time dep of the calibration scan
//run_reac = name of the time dep of the reaction scan

// WARNING : NEED TO CORRECT THE RAW DATA BEFORE COMPARING THEM
//(CN concentration, laser fluence, etc)

wave run_reac,run_cal
variable xstart,xend,endbg,startbg
variable n,numpts,x,m,bf,i,s,sdevnum_list,p,temp,numlist,sigdev,conflim,num_bg
variable bg_reacmoy, bg_calmoy
String name,namerun
wave coef1,coef2,temprun_cal


//inisialisation of the parameters and creation of necessary waves

num_list=xend-xstart+1
num_bg=endbg-startbg+1


make /O /N=(numpnts(run_cal)) temprun_cal
make /O /N=(num_list) individual_bf=2

bg_reac=0
p=0

//BG calculation for reaction
        for(m=startbg;m<=endbg;m+=1)
                                bg_reac=bg_reac+run_reac[m]
        endfor
                bg_reacmoy=bg_reac/num_bg

//BG calculation for reaction and calibration
                for(m=startbg;m<=endbg;m+=1)
                                bg_cal=bg_cal+run_cal[m]
                endfor

                bg_calmoy=bg_cal/num_bg

//BF calculation for each individual point
for(m=xstart;m<=xend;m+=1)
```

```
        individual_bf[p] = abs((run_reac[m]-bg_reacmoy)/(run_cal[m]-bg_calmoy))
        p=p+1

endfor

//Calculation of the average BF

for(p=0;p<num_list;p+=1)
        bf=bf+individual_bf[p]
endfor

bf=bf/num_list

print "branching fraction =",bf
killwaves temprun_cal

//Calculation of the standard deviation and the 95% confidence limit
for (n=0;n<num_list;n+=1)
        s=s+(individual_bf[n]-bf)^2
endfor

sdev=sqrt(s/(num_list-1))

sigdev=sdev/(sqrt(num_list-1))

conflim= 2.086 * sigdev

print sdev, sigdev, conflim

end
```

B.3 VAR and INT files for the cyanopropene isomers

Trans 1-cyanopropene

VAR File

```
TRANSCROTONILE
 11 5967   11    5    0.0000E+000    1.1000E+001    1.0000E+000 1.0000000000
a 1  1 0,50,  ,  ,     ,     ,  ,  , 0 ,
                10000  3.805400000000010E+004 -0.000000000 /A
                20000  2.297075046224000E+003 -0.000000 /B
                30000  2.195186936220000E+003 -0.000000 /C
                  200 -0.287435000000000E-003  0.0000E-03 /Delta_J
                 2000 -1.573881133000000E-027  0.000000000E-27 /Delta_K
                 1100  1.877211400000000E-002 -0.000000 /Delta_JK
                40100 -0.011993847000000E-021 -0.000000000E-21 /-del_J
                41000 -0.012129138000000E-021 -0.000000000E-21 /-del_K
         110010000 -3.721621900000000E+000  0.00000 /chi_aa
         110020000  1.820480000000000E+000 -0.000 /chi_bb
```

INT File

```
Trans-crotonitrile
 0000   52023 350.6547,  0, 100, -10.0,-9.0, 100, 9.375
 001  4.35
 002  1.91
 003  0.00
```

Cis 1-cyanopropene

VAR File

```
CIS-CROTONITRILE                    June 18 2021
  11  110   11    5    0.0000E+000    1.1000E+001    1.0000E+000 1.0000000000
a 1  1 0,50,  ,  ,     ,     ,  ,  , 0 ,
         10000  1.185444941000000E+004 1.00000000E+000 /A
         20000  3.524697711450000E+003 1.00000000E+000 /B
         30000  2.759742937300000E+003 1.00000000E+000 /C
           200 -2.731538400000000E-003 1.00000000E+000 /-DJ
          2000 -6.580159000000000E-002 1.00000000E+000 /-DK
          1100  1.821065300000000E-002 1.00000000E+000 /-DJK
         40100 -8.747154000000000E-004 1.00000000E+000 /-dJ
         41000 -5.252616700000000E-003 1.00000000E+000 /-dK
                   300  5.204930000000000E-009 1.00000000E+000 /PhiJ
                  2100 -2.322000000000000E-007 1.00000000E+000 /PhiKJ
                 40200  2.287820000000000E-009 1.00000000E+000 /phiJ
          10010000 -1.895849000000000E+000 1.00000000E+000 /Eaa
          10020000 -1.055650000000000E-001 1.00000000E+000 /Ebb
          10030000  2.001365000000000E+000 1.00000000E+000 /Ecc
```

INT File

```
Cis-crotonitrile
 0000    52023 452.8271,   0, 100, -10.0,-9.0, 9.375, 9.375
 001   3.74
 002   1.63
 003   0.00
```

2-cyanopropene

VAR File

```
METHYLACRYLONITRILE                        Tue Apr 27 16:43:01 2021
   10    72    11     5     0.0000E+000     1.1000E+001     1.0000E+000 1.0000000000
a 1  1 0,50,  ,  ,     ,     ,  ,  , 0 ,
         10000   9.291324977556440E+003 4.66236548E-003 /A
         20000   4.166448682858881E+003 8.26250192E-004 /B
         30000   2.924654929756764E+003 6.90669987E-004 /C
           200  -7.676389874441016E-004 5.22670792E-007 /-DJ
          1100  -1.389770959049683E-002 3.06113272E-006 /-DJK
          2000   4.700599161140623E-003 5.40901091E-005 /-DK
         40100  -2.668232996953333E-004 2.06865504E-007 /-dJ
         41000  -8.686024920440348E-003 8.18225567E-006 /-dK
         41100   7.496758037499224E-008 7.20280775E-009 /phiJK
         42000  -5.078897253379590E-007 3.10731439E-008 /phiK
-0.1030495-0.2811527-0.2714869 0.1464661-0.0689840-0.3012532-0.0842112-0.5936081
-0.7437152 0.8369451 0.3108118 0.1473492 0.1450987-0.1010872-0.2387689-0.0637013
 0.2894396 0.4093451-0.2066193-0.7442433 0.3419929 0.6440407 0.6203302-0.0668460
-0.3420082-0.1268511-0.4087383-0.7871693-0.2223470-0.1344943 0.3749455 0.3289043
-0.3978997 0.6391557-0.0945755 0.8942523-0.4719640-0.0768522-0.0891396 0.1408744
-0.0075963 0.3691262-0.2068336-0.0696206 0.3258235 0.3068415 0.2342517-0.1204939
-0.0402437-0.4632691-0.4137628-0.5732712-0.4421152 0.9454306-1.0000000
```

INT File

```
Methylacrylonitrile
 0000    52023 457.1044,   0, 100, -10.0,-9.0, 100, 9.375
 001   3.940
 002   0.265
 003   0.000
```

Cis 3-cyanopropene

VAR File

```
CIS-ALLYCYANIDE                            June 18 2021
12 124    11     5     0.0000E+000     1.1000E+001     1.0000E+000 1.0000000000
a 1  1 0,50,  ,  ,     ,     ,  ,  , 0 ,
         10000   1.132298370000000E+004 1.00000000E+000 /A
```

```
20000   3.739346620000000E+003 1.00000000E+000 /B
30000   2.858532640000000E+003 1.00000000E+000 /C
  200  -3.067490000000000E-003 1.00000000E+000 /-DJ
 1100   1.839000000000000E-002 1.00000000E+000 /-DJK
 2000  -5.319880000000000E-002 1.00000000E+000 /-DK
40100  -1.015730000000000E-003 1.00000000E+000 /-dJ
41000  -5.171700000000000E-003 1.00000000E+000 /-dK
  300   6.300000000000000E-009 1.00000000E+000 /PhiJ
 1200  -4.727000000000000E-008 1.00000000E+000 /PhiJK
 2100  -1.323700000000000E-007 1.00000000E+000 /PhiKJ
40200   2.730000000000000E-009 1.00000000E+000 /phiJ
```

INT File

```
Cis-allylcyanide
 0000    52023 442.0675,  0, 100, -10.0,-9.0, 100, 9.375
 001   3.26
 002   2.16
 003   0.00
```

Gauche 3-cyanopropene

VAR File

```
GAUCHE-ALLYLCYANIDE  Demaison et al. 1991
  14  114    11    0    0.0000E+000    1.1000E+001    1.0000E+000 1.0000000000
Thu Oct 15 14:02:52 2020
s   1   1   0  50,  ,  ,     ,     ,  ,  , 0 ,
        10000   1.970758400000000E+004 1.00000000E+000 /A
        20000   2.619786480000000E+003 1.00000000E+000 /B
        30000   2.497566570000000E+003 1.00000000E+000 /C
          200  -1.810620000000000E-003 1.00000000E+000 /-DJ
         1100   8.032620000000000E-002 1.00000000E+000 /-DJK
         2000  -1.266510000000000E+000 1.00000000E+000 /-DK
        40100  -1.874500000000000E-004 1.00000000E+000 /-dJ
        41000   2.569900000000000E-002 1.00000000E+000 /-dK
          300   1.004400000000000E-008 1.00000000E+000 /PhiJ
         1200  -1.983000000000000E-007 1.00000000E+000 /PhiJK
         2100  -6.220500000000000E-006 1.00000000E+000 /PhiKJ
        40200   3.551000000000000E-009 1.00000000E+000 /phiJ
        41100  -2.900000000000000E-007 1.00000000E+000 /phiJK
        42000   1.252000000000000E-005 1.00000000E+000 /phiK
```

INT File

```
Gauche-allylcyanide
 0000    000 428.1232,  0, 100, -10.0,-9.0, 100, 9.375
 001   3.69
 002   1.11
 003   0.98
```

B.4 Optimized geometries

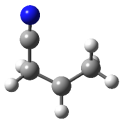

C1b-1

Cartesian Coordinate

Atom	X	Y	Z
C	1.15163	0.507134	-0.285917
C	-0.173274	1.030678	0.174588
C	1.60806	-0.852088	0.095066
H	2.497706	-1.140924	-0.460661
H	1.855675	-0.909922	1.1634
H	0.829228	-1.59655	-0.084812
H	1.856644	1.231861	-0.664335
H	-0.149789	1.306817	1.237608
H	-0.451837	1.930399	-0.374125
C	-1.24705	0.045781	0.013003
N	-2.067689	-0.744387	-0.11393

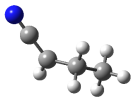

C1-2

Cartesian Coordinate

Atom	X	Y	Z
C	-0.94901296	-0.4226854	0.40851067
C	0.1909151	0.52967038	0.27931749
C	-2.1686669	0.03737164	-0.39140797
H	-1.93502486	0.09329926	-1.45371903
H	-2.99691294	-0.65640815	-0.25772811
H	-2.49680686	1.02411507	-0.06440925
H	-0.633038	-1.41613882	0.09374096
H	0.02597915	1.58745358	0.43333812
C	1.48565609	0.11662293	-0.01791193
N	2.55800908	-0.24267445	-0.26980143
H	-1.223608	-0.49947703	1.46633776

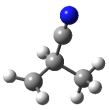

C3-1

Cartesian Coordinate

Atom	X	Y	Z
C	0.39581391	0.06995234	0.4073549
C	0.94513871	1.34372735	-0.15327427
C	1.1333953	-1.1619046	-0.12779771
H	0.71855444	-2.07755561	0.2881964
H	1.04936251	-1.20600284	-1.21290372
H	2.18695523	-1.09423729	0.13783647
H	0.4687897	0.09190158	1.49716291
H	0.80291739	2.27608243	0.36961651
H	1.2602729	1.36727121	-1.18582021
C	-1.04141201	-0.02960806	0.09375365
N	-2.15492394	-0.09863738	-0.17347254

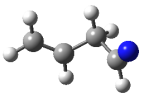

C5-1b

Cartesian Coordinate

Atom	X	Y	Z
C	-1.14339487	0.41819382	-0.15564507
C	0.10906212	0.29691983	0.65974395
C	-2.12130985	-0.4722242	-0.1516101
H	-3.00797784	-0.33945221	-0.75595211
H	-2.06709185	-1.36508321	0.45936089
H	-1.22253287	1.30049683	-0.78376005
H	0.20696409	1.16207482	1.32189697
H	0.09516512	-0.60238718	1.27247094
C	1.34154113	0.27016487	-0.22826203
N	2.20372015	-0.61819312	-0.18747202
H	1.45404113	1.09337688	-0.94707301

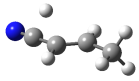

TS 1a-1

	Cartesian Coordinate		
Atom	X	Y	Z
C	-0.88587498	-0.40146204	0.10657587
C	0.11914903	0.46209004	-0.13889181
C	-2.32246997	-0.05716302	-0.05665015
H	-2.81992091	-0.77934585	-0.70626438
H	-2.83342404	-0.09751229	0.9082648
H	-2.45101395	0.93902009	-0.47569089
H	-0.64108399	-1.38258814	0.49594963
H	-0.06612494	1.40862417	-0.63069457
H	0.25706089	1.54880062	1.4030385
C	1.49248003	0.05004304	-0.06096381
N	2.59068603	-0.27972096	-0.01357481

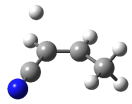

TS1b-1

	Cartesian Coordinate		
Atom	X	Y	Z
C	1.15208804	0.53340514	-0.13546102
C	-0.12786498	0.95853606	-0.09545488
H	2.2367991	-1.18924772	-0.75568234
H	2.20483519	-0.93774597	0.9785657
H	0.76090717	-1.55481893	0.1568717
H	1.91755899	1.2870462	-0.27569196
C	1.60048913	-0.86828987	0.07066175
H	-0.45580489	1.49286978	1.68659622
H	-0.38326705	1.97932308	-0.34271271
C	-1.22492792	0.030865	-0.04893095
N	-2.09710488	-0.71493205	-0.027548

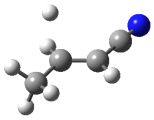

TS1a-2b

	Cartesian Coordinate		
Atom	X	Y	Z
C	-0.85477281	0.34616503	-0.11723802
C	0.15681019	-0.50351902	0.1321728
C	-2.29336982	-0.06199694	-0.10056791
H	-2.42946679	-1.01013399	0.41610401
H	-2.91224576	0.69365303	0.38023222
H	-2.65170393	-0.17348483	-1.12592289
H	-0.90822562	1.33351186	1.58660209
H	-0.0287228	-1.51198405	0.47868072
C	1.52108819	-0.11412203	0.0005487
N	2.62420918	0.19212395	-0.10064038
H	-0.61763383	1.32440807	-0.52070694

TS1b-2b

	Cartesian Coordinate		
Atom	X	Y	Z
C	-1.11743698	0.52322807	-0.08296271
C	0.15050698	0.9712932	-0.12958173
C	-1.51225382	-0.91856798	-0.05855267
H	-0.68943075	-1.55101588	0.26858735
H	-2.3678958	-1.07877205	0.59482134
H	-1.80366079	-1.22838003	-1.06446666
H	-1.530936	0.85703307	1.82103628
H	0.37186986	2.02430022	-0.22867376
C	1.26831407	0.09398833	-0.01253271
N	2.16988515	-0.61340557	0.0793443
H	-1.90392406	1.25102398	-0.24493572

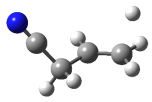

TS2-1

Cartesian Coordinate

Atom	X	Y	Z
C	-0.97876406	-0.11079705	0.50703388
C	0.16519893	-0.79810406	-0.18538614
C	-2.10416209	0.2396449	-0.11662408
H	-2.92796408	0.68284091	0.42489394
H	-1.77780816	2.06110588	-0.85946517
H	-2.28434513	-0.03419114	-1.14886806
H	-0.83216102	0.12758199	1.55325587
H	0.34826496	-1.78057904	0.25646689
H	-0.05763512	-0.9471711	-1.24186012
C	1.40651692	-0.02781703	-0.07275322
N	2.37127291	0.58183599	0.03170771

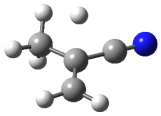

TS3-1

Cartesian Coordinate

Atom	X	Y	Z
C	0.38780496	0.11926174	0.06741192
C	0.93501447	1.34244452	-0.08821201
C	1.16348547	-1.16684757	-0.09276894
H	0.79055305	-1.93812542	0.57703902
H	1.06106948	-1.52719955	-1.11689795
H	2.2165505	-0.99249199	0.11627723
H	0.3144886	-0.04340221	1.89683892
H	0.32553383	2.23350176	-0.10789312
H	2.00899952	1.45293909	-0.14249884
C	-1.05154308	-0.00474469	-0.0005503
N	-2.18939512	-0.13227223	-0.07687848

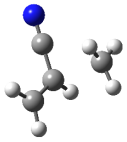

TS4-1

Cartesian Coordinate

Atom	X	Y	Z
C	-0.31864001	-0.45632618	0.46344106
C	-0.9684379	-1.42804223	-0.22860498
C	-1.10674021	1.55321876	-0.14761188
H	-0.52188928	2.18768079	0.50315315
H	-0.8318792	1.54545982	-1.19154887
H	-2.1543042	1.43383164	0.08558611
H	-0.61435805	-0.21154725	1.47432107
H	-1.91911987	-1.80294834	0.11931499
H	-0.58263686	-1.80093215	-1.16564799
C	1.03393696	-0.10497003	0.11984209
N	2.11192493	0.18073909	-0.15251089

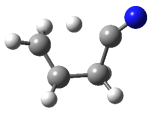

TS5-1a

Cartesian Coordinate

Atom	X	Y	Z
C	-1.29088112	0.47447293	-0.20618897
C	0.03696885	1.00111292	0.21143014
C	-1.49906101	-0.84606517	0.10737867
H	-2.29343398	-1.4097231	-0.36412147
H	0.003281	-1.11023796	-0.25403944
H	-1.18342096	-1.23197041	1.07363155
H	-1.84946618	0.9720221	-0.98530982
H	0.35832677	1.88860709	-0.32842562
H	0.09999086	1.20981663	1.2814332
C	1.03296993	-0.15256194	-0.0453572
N	2.16924895	-0.45432383	-0.11810631

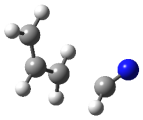

TS5-1b

	Cartesian Coordinate		
Atom	X	Y	Z
C	1.2449378	0.402306	0.23201575
C	0.1028689	0.78692661	-0.54275559
C	1.97292779	-0.70134616	-0.00555757
H	2.81596371	-0.96810284	0.61515167
H	1.73553385	-1.35571661	-0.83491023
H	1.50745774	1.02699546	1.07994843
H	-0.22495207	1.81837464	-0.5125542
H	-0.06852802	0.2782241	-1.48112632
C	-1.51000024	0.04720624	0.47757765
N	-2.18580919	-0.6450041	-0.18127603
H	-1.32921632	0.50469776	1.43474142

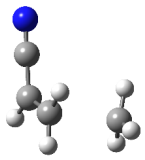

TS4-2b

	Cartesian Coordinate		
Atom	X	Y	Z
C	-0.75140388	0.87427419	0.44758879
C	0.31900319	0.79964986	-0.37300608
C	-2.2149172	-0.83988255	-0.14048017
H	-1.5317234	-1.66452568	-0.010288
H	-2.96828825	-0.68600329	0.61758073
H	-2.45245302	-0.54459061	-1.15031823
H	-0.71859709	0.4304933	1.43217085
H	0.35401241	1.33353874	-1.31209014
C	1.42354197	-0.04808736	-0.08138187
N	2.31309279	-0.73993253	0.15053431
H	-1.5319447	1.59489035	0.25288062

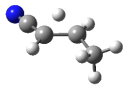

TS1a-2a

	Cartesian Coordinate		
Atom	X	Y	Z
C	0.9334379	-0.45242279	-0.15150013
C	-0.18411609	0.5281902	-0.11047888
C	2.31902688	-0.00141991	0.15876817
H	2.47397177	0.0676297	1.24102921
H	3.06120291	-0.68673577	-0.245008
H	2.51073592	0.99010024	-0.25538145
H	0.6587369	-1.4962258	-0.12570153
H	0.05530289	1.56513814	0.07407252
H	0.33066801	0.14261459	-1.18992297
C	-1.52742311	0.11349816	0.03734584
N	-2.61945312	-0.24422787	0.1280146

	Cartesian Coordinate		
Atom	X	Y	Z

B.5 Direct mechanisms for CN and propene reaction

Direct mechanisms:

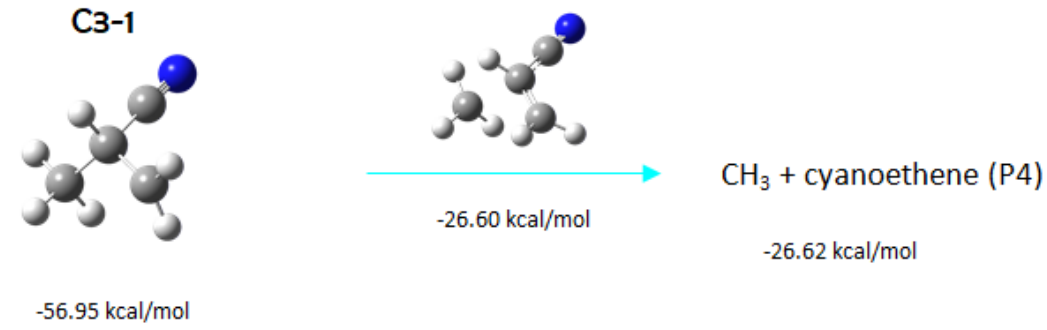

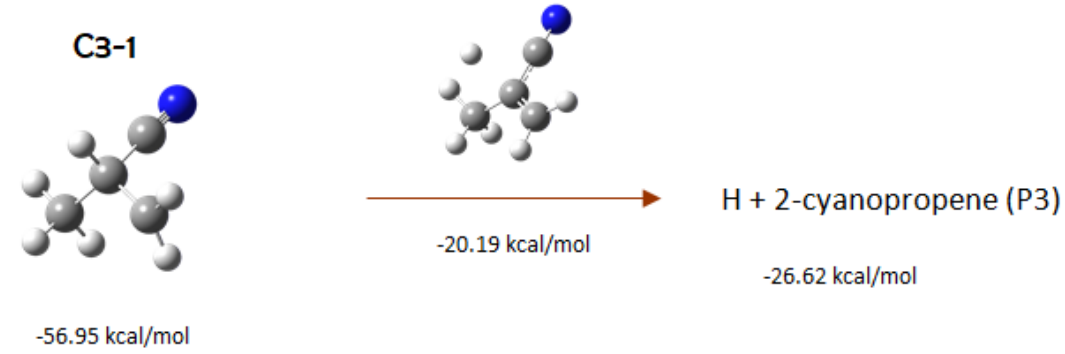

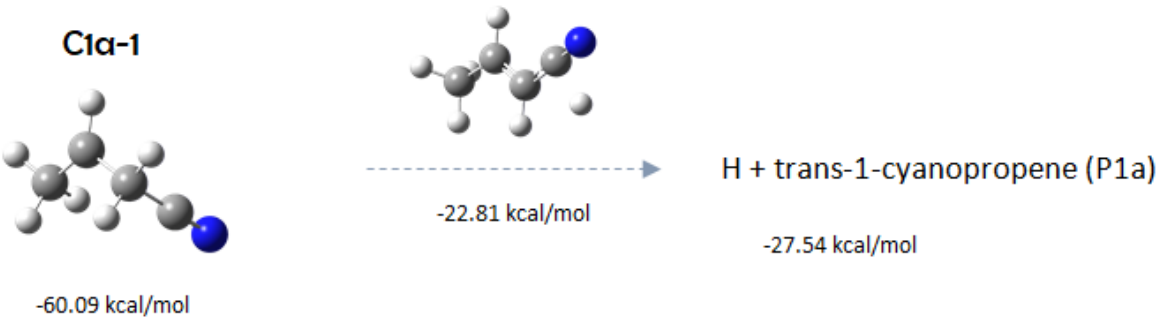

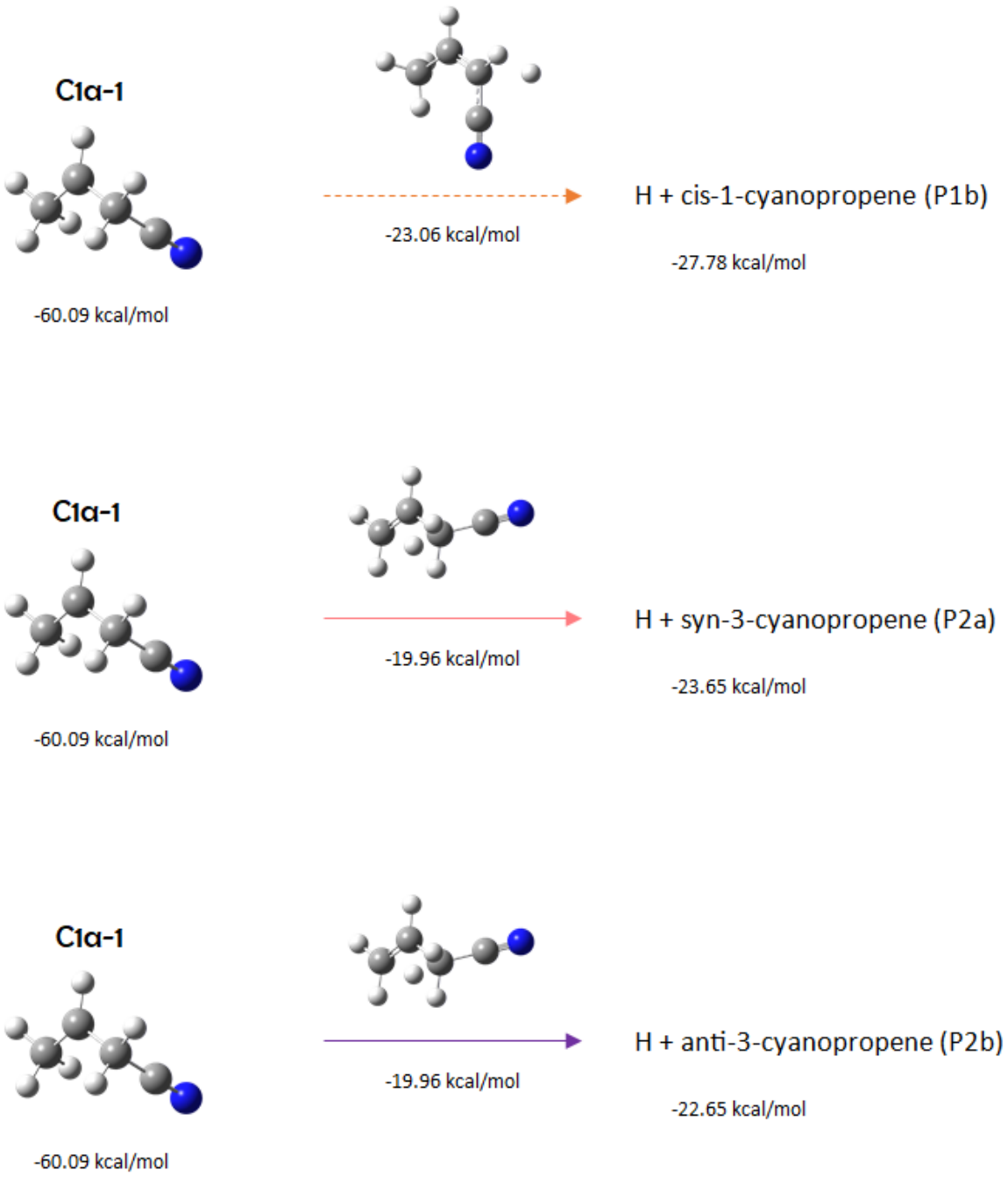

Complex mechanisms:

CH_3 + 2-cyanopropene (P4)

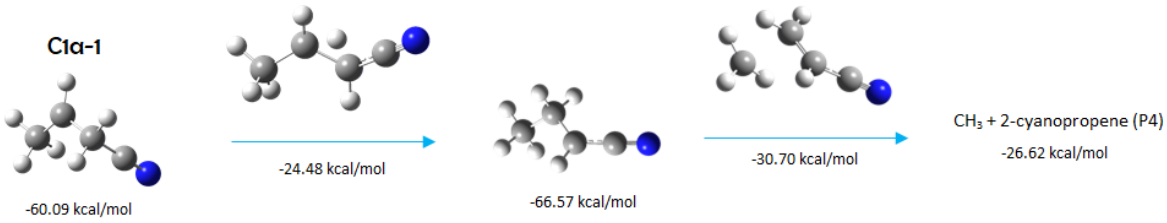

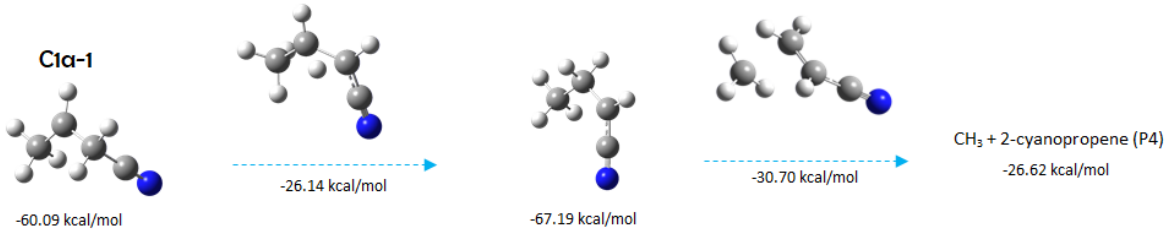

H + trans-1-cyanopropene (P1a)

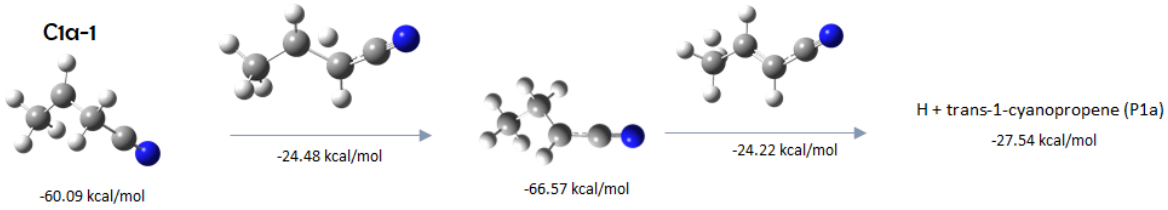

H + cis-1-cyanopropene (P1b)

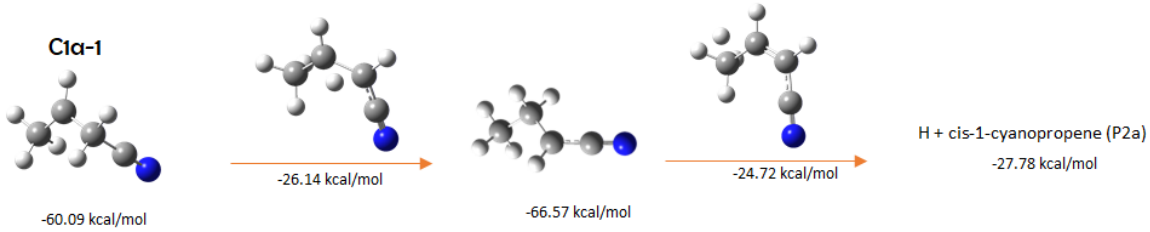

HCN + C3H5

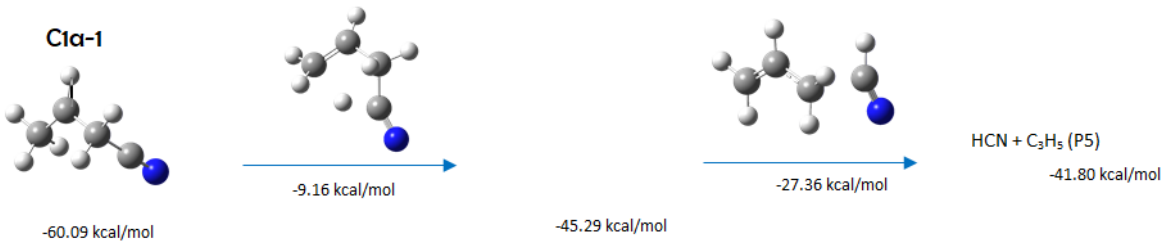

Appendix C

Formic acid and CO_2 dimerisation

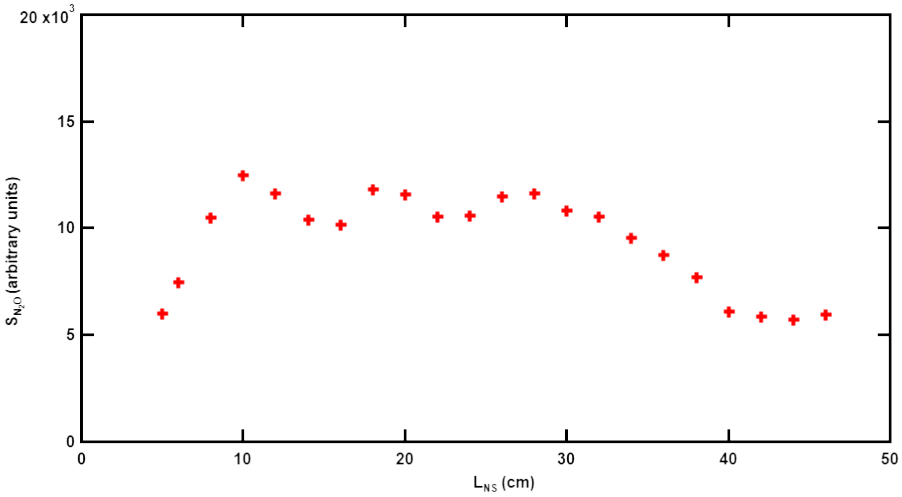

Figure C.1: NO_2 (5 sccm) signal intensity in function of the reservoir position. Probing conditions: 75 369 MHz conditions, pulse length = 170 µs with 10,000 accumulations, LO=74 GHz. Acquired in argon 52 K nozzle with 3mm skimmer. reservoir between 8 and 52 cm with 2 cm steps.

C.1 Argon 52K data set

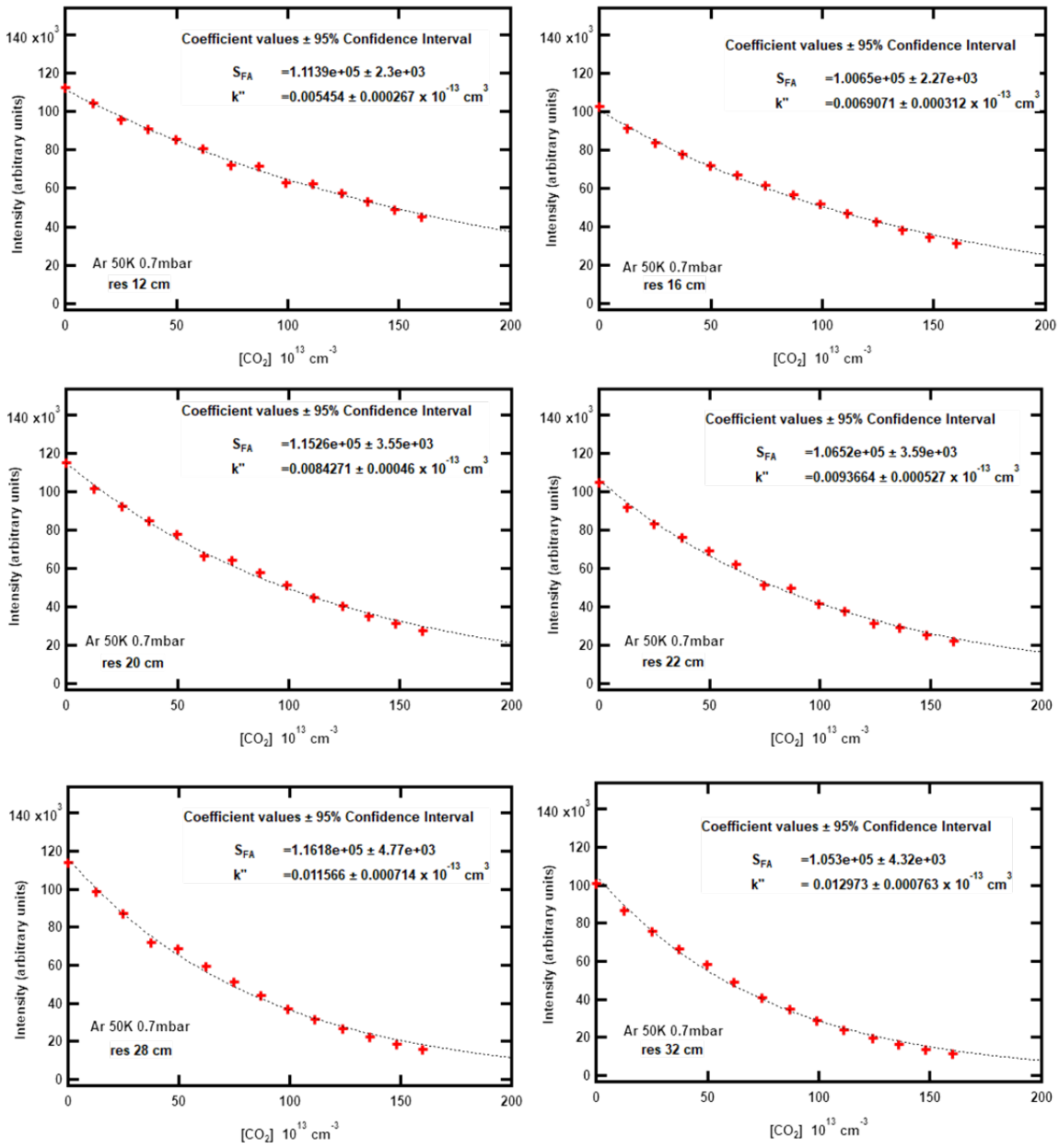

Figure C.2: Kinetics data obtained in argon nozzle at 52 K with a 3 mm skimmer. Formic acid decay fitted with a single exponential decay function (black dotted line).

reservoir (cm)	12	16	20	22	28	32
time (µs)	240	319	399	439	559	639
k_{1st} (cm^3)	5.45×10^{-16}	6.91×10^{-16}	8.43×10^{-16}	9.37×10^{-16}	1.16×10^{-15}	1.29×10^{-15}

Table C.1: Ar 52 K data set. Fitting range for k_{1st} determination: $[CO_2]$ = 1.4×10^{14}–1.6×10^{15} cm^{-3}.

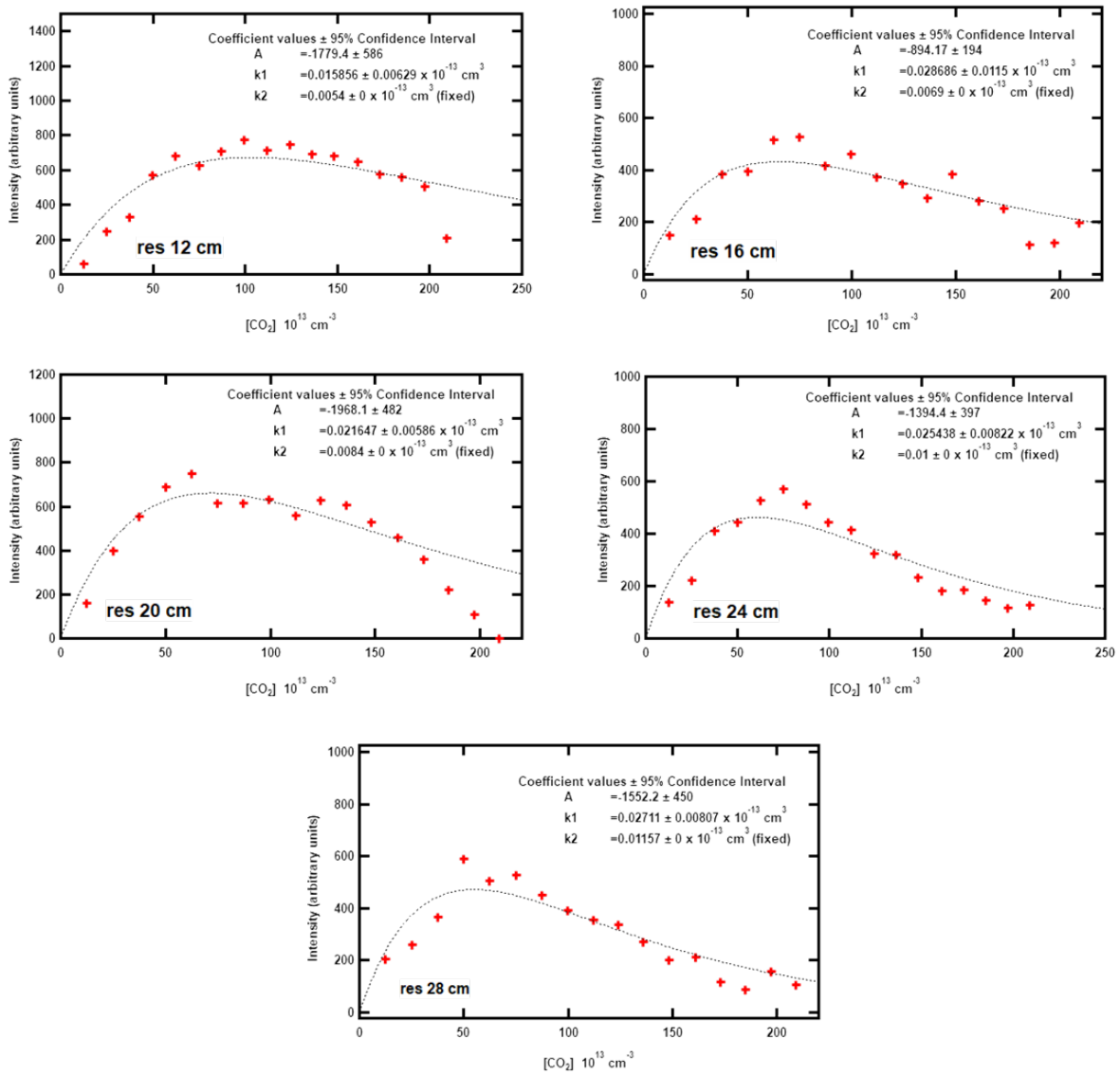

Figure C.3: Kinetics data obtained in argon nozzle at 52 K with a 3 mm skimmer. Formic acid-CO_2 complex signal fitted with a model described in chapter 4 (black dotted line).

C.2 Nitrogen 38K data set

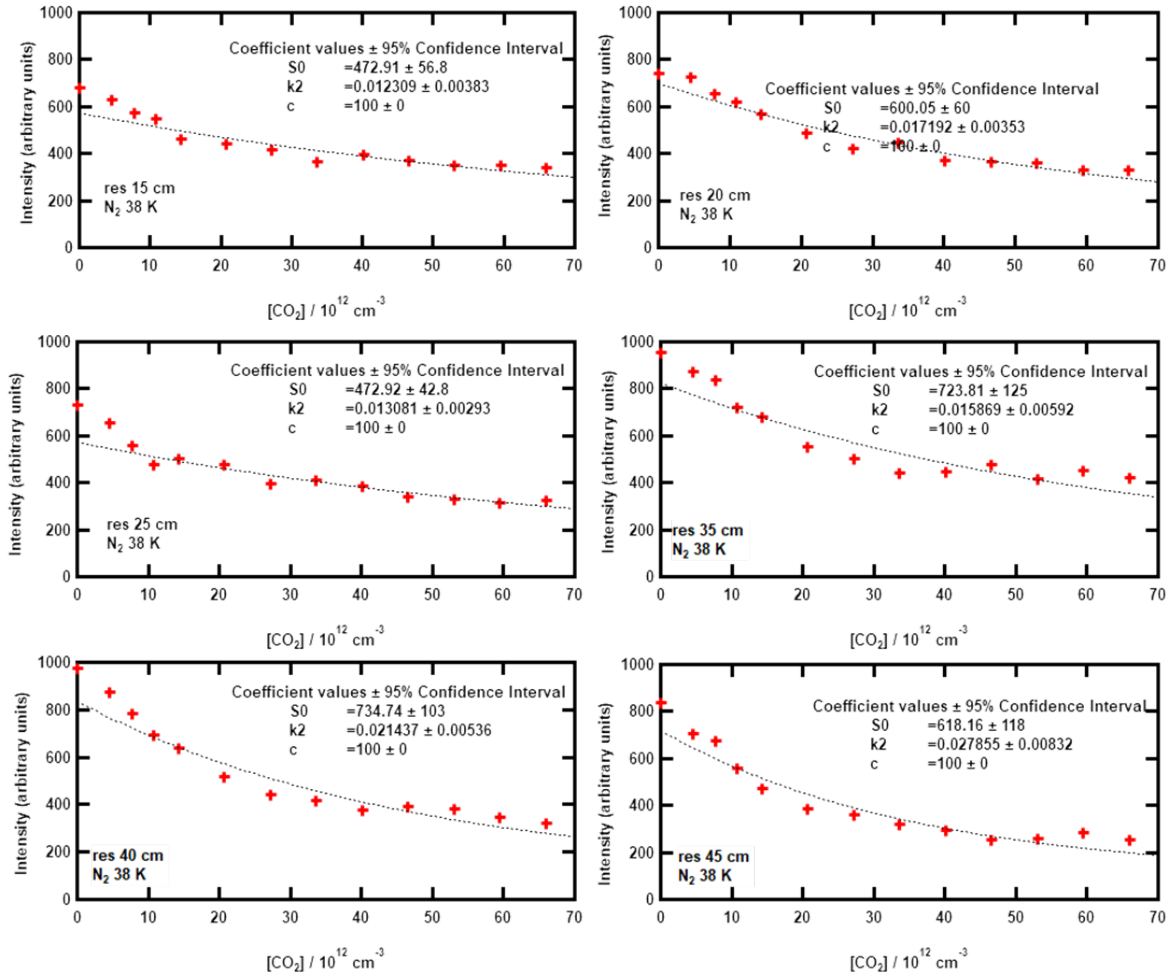

Figure C.4: Kinetics data obtained in nitrogen nozzle at 38 K with a 4 mm skimmer. Formic acid decay fitted with a single exponential decay function (black dotted line).

reservoir (cm)	15	20	25	35	40	45
time (μs)	207	275	344	482	551	620
k_{1st} (cm^3)	1.23×10^{-14}	1.72×10^{-14}	1.31×10^{-14}	1.59×10^{-14}	2.14×10^{-14}	2.78×10^{-14}

Table C.2: Nitrogen 38 K data set. Fitting range for k_{1st} determination: $[CO_2] = 1\times10^{13}$–6.5×10^{13} cm^{-3}.

COLLEGE SCIENCES DE LA MATIERE
DOCTORAL DES MOLECULES
BRETAGNE ET MATERIAUX

Université de Rennes

Titre: Mesures de Cinétique à Basse Température pour des Réactions d'Interêt Astrochimique

Mot clés : CRESU, Spectroscopie micro-onde à impulsion chirpées, Astrochimie, Rapport de branchement, Constante de vitesse, Réactions en phase gazeuse

Résumé : Cette thèse présente un travail expérimental réalisé pour mesurer la cinétique à basse température de réactions d'intérêt astrochmique. La technique CRESU (Cinétique de réaction en écoulement supercomic uniforme) a été combinée à la spectroscopie micro-onde à impulsions chirpées pour éffectuer des mesures de coefficient de vitesse et de rapport de branchement à basse température. Ces mesures ont été effectuées avec l'appareil SKISURF (SKImmed uniform SUpeRsonic Flow). Ici, la région de réaction dans le flux uniforme, a été découplée de la région de détection. La première partie présente la détermination du rapport de branchement de la réaction entre le radical CN et propène. Le rapport de branchement du produit majoritaire a été mesuré à 35 et 52 K. Ces mesures sont étayées par des calculs théoriques de rapport de branchement effectués avec MESMER. La deuxième partie présente une étude cinétique de la formation d'hétérodimères d'acide formique et de CO_2. Le coefficient de vitesse de cette réaction a été mesuré en suivant le réactif et le produit à 52 K. Ces résultats préliminaires ouvrent la voie à de futures études sur la formation d'hétérodimères qui est considérée comme l'étape déterminante dans les milieux sursaturés. Ce travail met en évidence la nécessité d'améliorer la sensibilité du dispositif expérimental. La principale voie d'amélioration implique le développement d'un système de gaz pulsé qui est actuellement en cours de caractérisation.

Title: Low Temperature Kinetics Measurements for Reactions of Astrochemical Relevance

Keywords: CRESU, Chirped pulse microwave spectroscopy, Astrochemistry, Branching ratio, Rate coefficient, Gas-Phase reactions

Abstract: This thesis presents experimental work performed to measure low-temperature kinetics of reactions relevant to astrophysical media. In this study, the CRESU (Reaction kinetics in uniform supersonic flow) technique was combined with chirped-pulse microwave spectroscopy to make rate coefficient and branching ratio measurements at low temperatures. These measurements were performed using the SKISURF (SKImmed uniform SUpeRsonic Flow) setup. Here the reaction region, in the uniform flow, was decoupled from the probing region. The first part presents the branching ratio determination of the CN radical and propene reaction. The main reaction channel was determined at 35 and 52 K and the measurements are further supported by theoretical calculation of branching ratio performed using MESMER. The second part presents the kinetics study of heterodimer formation of formic acid and CO_2. The rate coefficient for this reaction was measured both following the reactant and the product at 52 K. These preliminary results pave the way for future study for heterodimer formation which is thought to be the rate-determining step of condensation under highly supersaturated conditions. Overall, this work highlights the need to improve the sensitivity of the experimental setup. The main path of improvement involves the development of a pulsed gas system which is currently under characterisation.